Synchrotron Electron Beam Control

Sandira Gayadeen
St. Hugh's College
University of Oxford

A thesis submitted in partial fulfilment
of the requirements for the degree of
Doctor of Philosophy at the University of Oxford

Trinity Term, 2014

Acknowledgements

I would like to express my deepest gratitude to my DPhil supervisor, Professor Stephen Duncan for his support, guidance, patience and understanding throughout my doctoral research. It was a great pleasure to work with him.

I would also like to thank members of Diamond Light Source, in particular Mark Heron, Michael Abbott, Isa Uzun, Chris Christou, Marco Apollonio and Guenther Rehm, all of whom have been tremendously generous with their time and knowledge.

I also wish to acknowledge the contribution of James Rowland towards my research. James' constant involvement and enthusiasm resulted in the successful implementation of the controllers at Diamond Light Source. He was a great friend and mentor.

The substantial financial support of Diamond Light Source, the Department of Engineering Science, the Institute of Engineering and Technology and St. Hugh's College for this work is greatly acknowledged.

Finally I would like to thank my mother, my sister and Khouler for their continuous love and support.

Abstract

SYNCHROTRON ELECTRON BEAM CONTROL

SANDIRA GAYADEEN, ST. HUGH'S COLLEGE

DOCTOR OF PHILOSOPHY

TRINITY TERM, 2014

This thesis develops techniques for the design and analysis of controllers to achieve sub-micron accuracy on the position of electron beams for the optimal performance of synchrotrons. The techniques have been applied to Diamond Light Source, the UK's national synchrotron facility. Electron beam motion in synchrotrons is considered as a large-scale, two-dimensional process and by using basis functions, controllable modes of the process are identified which are independent and allow the design to be approached in terms of a family of single-input, single-output transfer functions. In this thesis, loop shaping concepts for dynamical systems are applied to the two-dimensional frequency domain to meet closed loop specifications. Spatial uncertainties are modelled by complex Fourier matrices and the closed loop robust stability, in the presence of spatial uncertainties is analysed within an Integral Quadratic Constraint framework. Two extensions to the unconstrained, single-actuator array controller design are considered. The first being anti-windup augmentation to give satisfactory performance when rate limit constraints are imposed on the actuators and the second being a strategy to account for two arrays of actuators with different dynamics. The resulting control schemes offer both stability and performance guarantees within structures that are feasible for online computation in real time.

Contents

List of Figures

List of Tables

Notation

$\mathbb{R}$	Real numbers
$\mathbb{R}^M$	M-dimensional vectors with real entries
$\mathbb{R}^{M\times N}$	M by N matrices with real entries
$\mathbb{Z}$	Integer numbers
$\mathbb{C}$	Complex numbers
$\mathbb{C}^M$	Complex M-dimensional vectors
$\mathbb{C}^{M\times N}$	Complex M by N matrices
j	the imaginary unit i.e. $j = \sqrt{-1}$
$\mathbf{0}$	Zero matrix of compatible dimensions
$\mathbf{I}$	Identity matrix of compatible dimensions
$\mathbf{M}^{\mathrm{T}}$	Transpose of matrix $\mathbf{M}$
$\mathbf{M}^*$	Conjugate transpose of matrix $\mathbf{M}$
$\mathbf{M}^{-1}$	Inverse of matrix $\mathbf{M}$
$\mathrm{diag}_{m=1,\ldots,M}\{a_m\}$	Diagonal matrix with M diagonal elements, $a_1, \ldots, a_M$
$\mathbf{M}_{ij}$	ith row and jth column of matrix $\mathbf{M}$
$\|\cdot\|_2$	2-norm:
	of a vector $v \in \mathbf{C}^M : \|v\|_2 := \sqrt{\sum_i^M \|v_i\|^2}$
	of a matrix $\mathbf{M} \in \mathbf{C}^{M\times N} : \|\mathbf{M}\|_2 := \sqrt{\sigma^2_{\max}(\mathbf{M}^*\mathbf{M})}$
	where $\sigma^2_{\max}$ is the largest eigenvalue of $\mathbf{M}$
	of a discrete function $u[k] : \mathbb{Z} \mapsto \mathbb{C}^n$, $\|u[k]\|_2 := \sqrt{\sum_{k=-\infty}^{\infty} u[k]^* u[k]}$

$\|\cdot\|_\infty$	∞-norm:
	of a vector $v \in \mathbf{C}^M$: $\|\mathbf{M}\|_\infty := \max_i \lvert v_i \rvert$
	of a matrix $\mathbf{M} \in \mathbf{C}^{M\times N}$: $\|\mathbf{M}\|_\infty := \max_i \sum_j^M \lvert m_{ij} \rvert$
	of a discrete function $u[k] : \mathbb{Z} \mapsto \mathbb{C}^n$, $\|u[k]\|_\infty := \sup_{k\in\mathbb{Z}} \lvert u[k] \rvert$
	of a discrete operator $G(z^{-1})$, $\|G\|_\infty := \text{ess sup}_{\omega\in[-\pi,\pi]} \sigma_{max}(G(e^{j\omega}))$
	where $\sigma_{max}(\cdot)$ indicate the largest singular value
l_2	Space of discrete functions $f[k] : \mathbb{Z} \mapsto \mathbb{C}^n$ satisfying $\|f\|_2 < \infty$
CD	Cross-direction
BPM	Beam Position Monitor
FOFB	Fast Orbit Feedback
FPGA	Field-programmable gate array
IMC	Internal Model Control
IQC	Integral Quadratic Constraint
LMI	Linear Matrix Inequality
LTI	Linear Time Invariant
MD	Machine-direction
MIMO	Multiple-Input Multiple-output
MISO	Multiple-Input Single-output
RF	Radio-frequency
RMS	Root-Mean-Square
SISO	Single-Input Single-output
SVD	Singular Value Decomposition

Chapter 1

Introduction

Synchrotrons are accelerators where electrons travelling at nearly the speed of light follow a circular path which causes them to lose energy in the form of light. The light spans the electromagnetic spectrum from infrared, through visible and ultraviolet (UV) light to X-rays and is referred to as synchrotron light. The synchrotron light, in the form of a photon beam, is channelled into photon beamlines where it is used for a wide variety of academic and industrial research, such as rational drug design, non-destructive techniques in palaeontology and for the development of novel materials for engineering applications [Materlik, 2013].

The electron beam travels around the synchrotron in a vacuum vessel that is surrounded by magnets which induce a magnetic field within the vacuum vessel. The magnetic field is used to bend the electron beam in the circular path and to focus it in order to maintain properties required for operation. The desired properties of the light and quality of the experiments place extreme requirements on the stability of the electron beam which is subjected to external disturbances ranging from long-term disturbances, such as changes in air temperature during the day, to higher frequency disturbances such as vibrations arising from cooling water pumps. Instability of the electron beam degrades the quality of the photon beam used in synchrotron experiments and in turn, degrades the quality of the experiments carried out at synchrotrons. The electron beam cross-section is elliptical, with typical vertical beam sizes being 5μm and the generally accepted target for stability is to keep the root-mean-square (RMS) variation of the position to 10% of the beam size. This means that sub-micron accuracy is necessary for the position of the electron beam in order to maintain the quality of the photon beam and to achieve this, electron beam stabilisation control systems are required.

Although beam stabilisation systems have been applied to synchrotrons in the past, they have been relatively simple and have not addressed control issues such as robustness or constraints. There are over 40 synchrotrons worldwide and the closed loop performance requirements and controller design are usually bespoke to each facility. Furthermore, because orbit feedback systems typically operate at sampling rates of 10kHz or faster and use 100's of sensors and actuators, computationally inexpensive control methods have been used at the expense of optimality. Efforts for a tractable controller design for electron beam stabilisation has concentrated in model diagonalisation. This is suitable for this class of control problem because the response of the array of the actuators can be modelled as the product of a matrix, describing the steady state or spatial response of the actuators, and a scalar dynamic term describing the temporal response of the actuators. By pre- and post- multiplying the plant model by orthogonal matrices, a diagonal transfer function matrix remains and the control design proceeds in terms of a family of independent single-input single-output (SISO) transfer functions, where each SISO loop is associated with a *spatial frequency* or *spatial mode* [Duncan, 1989, Duncan and Bryant, 1997, Featherstone et al., 2000, Heath, 1996, Stewart, 2000].

The steady state response matrix is usually ill-conditioned for synchrotron accelerators and this property makes the multivariable plant difficult to control and sensitive to modelling errors [Skogestad and Postlethwaite, 2005]. This is because satisfying performance specifications of the closed loop process in all directions leads to a controller applying a large control signal in the low-gain directions of the plant which can lead to actuator saturation. Moreover, controlling all directions of an ill-conditioned process is especially vulnerable to stability problems caused by model uncertainty [Duncan and Bryant, 1997]. The approach for electron orbit control has traditionally been to either discard the low-gain modes or detune the controller in these weakly controllable modes. However, there is a lack of analysis of the effect on closed loop performance and stability when applying either method. This is mainly because robust stability of the closed loop in the presence of model uncertainty is not explicitly considered in the design of the electron orbit controller. The controller design is usually based on an ideal model of the accelerator which can deviate significantly from the real machine and while this is recognised within the synchrotron community, the approach to address this uncertainty, is to calibrate the components of the accelerator regularly so that the measured response matches the ideal model as best as possible. It is common on synchrotrons to have rate limiters on the actuators for safe operation, however these rate limits are usually relaxed and if the limits are violated, it is considered to be abnormal conditions and the electron beam cannot be sustained. However future changes to the operation of synchrotrons that require significantly better beam stability, may cause the system to be constrained more often than is currently observed. To the best of the author's knowledge there is no study on the effect of actuator constraints on closed loop stability and how to address performance deterioration in the presence of these constraints.

The goal of this thesis is to provide systematic design techniques and analysis tools for controller designs that capture the majority of closed loop performance and stability specifications within the synchrotron community.

1.1 Aims and Contributions

It is the goal of this thesis to adapt standard control frameworks to design electron beam stabilisation controllers that explicitly consider performance and robustness tradeoffs. The main contributions to meet this goal are discussed below.

Firstly, in this thesis, an Internal Model Control (IMC) structure is used for control, whereas Proportional only or Proportional-Integral (PI) control are the only other controllers used on synchrotrons. An IMC controller is appropriate for electron orbit control since the open loop process is subject to significant delays [Morari and Zafiriou, 1989] and does not significantly increase the amount of online computation over the traditional PI controllers that are used. Furthermore, an IMC structure allows for explicit design tradeoffs. Traditional approaches to reduce computation have been to apply the same PI controller to each spatial mode but detune the gains on each mode. In this thesis, the former approach is compared to one where different controller dynamics (in the form of an IMC controller) are designed on a mode by mode basis. By considering the power of the underlying disturbances in each spatial and dynamic (temporal) frequency, the closed loop sensitivity is shaped in both dimensions. The resulting controller has two degrees of freedom, relating to spatial and dynamic control respectively, and it is demonstrated how the choice of each parameter influences performance and robustness of the closed loop.

Secondly, robust stability of the closed loop in the presence of uncertainty is explicitly addressed within an Integral Quadratic Constraint (IQC) framework, where the uncertainties satisfy IQCs defined by particular multipliers, which depend on the structure of the uncertainty. By using the theory of IQCs and the Kalman-Yakubovich-Popov (KYP) lemma, a robust stability test is developed in the form of a linear matrix inequality (LMI). This method may be computationally intractable due to the large size of the system, so an uncertainty description that allows the stability test to be decoupled on a mode by mode basis is presented. This is achieved by the Fourier analysis of the closed orbit which also allows the robust stability margins to be interpreted in terms of meaningful, physical parameters of the accelerator and electron beam.

Thirdly, the effect of actuator rate limit constraints on closed loop performance and stability is addressed in this thesis. Augmentation of the unconstrained controller to provide anti-windup compensation when the rate limits are violated is presented. The choice to use anti-windup compensation rather than a Model Predictive Control (MPC) framework was made because of the computational burden of implementing an MPC controller on such a large and fast system. Furthermore, the aim is to make use of the existing IMC structure for practical reasons and as such, augmentation of the IMC controller is considered. The IMC structure is well-suited since it can be easily modified to include anti-windup compensation without significantly increasing the computational burden of the online controller implementation.

The underlying assumption that all actuators have the same dynamics is the reason the process model can be represented as the product of a steady state matrix and a scalar dynamic term. However this assumption is not valid for all synchrotrons, where two arrays of actuators with differing dynamics are used for electron beam control [Chiu et al., 2013, Hubert et al., 2009, Plouvier et al., 2011, Steier et al., 2004]. Typically one array of actuators has strong magnetic fields that are limited in bandwidth, while the second array of actuators is faster in order to compensate for high frequency disturbances. The faster actuators however are amplitude limited and can easily become saturated. The final aim of this thesis is to provide a suitable controller structure and design heuristic to address the problem of the two arrays of actuators which takes advantage of the different actuator dynamic characteristics. While framing the control problem as an optimal control problem is an attractive approach, the main consideration for the design was one that minimised online computation.

The outcomes of the research in this thesis have been implemented and tested on the Diamond Light Source synchrotron. Diamond's accelerators are largely unconstrained and therefore the unconstrained controller has been implemented on the main accelerator at Diamond and is currently used for electron orbit control during operation of the facility. The emerging techniques from this work, such mode by mode control and constrained control was implemented on a test accelerator, the booster synchrotron, to assess the performance of these control strategies and to evaluate the impact on computation before implementation on the main accelerator. In this thesis, real machine data from both the main accelerator and the booster is presented to demonstrate the controller performance. Diamond's accelerators use a single array of actuators, therefore a simulation study for the multi-array controller structure is presented for the booster.

To summarise, the novel contributions of this thesis are:

- The use of an IMC controller structure for electron orbit stabilisation to make explicit the design tradeoffs. This work is presented in [Gayadeen and Duncan, 2014, Napier et al., 2011].

- The use of a two-dimensional frequency design process to select electron orbit feedback controller dynamics based on the distribution of the power of the disturbance in both spatial and dynamic frequency domains. This work is presented in [Gayadeen and Duncan, 2014, Gayadeen et al., 2011, 2013b].

- The use of an IQC framework to develop closed loop robust stability tests in the presence of uncertainties and nonlinearities for this application. This work is presented in [Gayadeen and Duncan, 2012, 2014].

- The use of Fourier analysis to model spatial uncertainties that maintain direct physical interpretations for this application. This work is presented in

[Gayadeen and Duncan, 2012, 2014].

- The augmentation of the IMC controller structure to provide anti-windup compensation and robust stability in the presence of rate constrained actuators. This work is presented in [Gayadeen and Duncan, 2013].
- The novel augmentation of the IMC controller structure to accommodate multiple arrays of actuators with different dynamics. This work is presented in [Gayadeen et al., 2013a].
- The successful implementation of the unconstrained IMC controller structure on the Diamond storage ring where the same controller dynamics are applied to each spatial mode but the gains are selected to tradeoff performance and robust stability. This work is presented in [Gayadeen and Duncan, 2014, Gayadeen et al., 2013b].
- The successful implementation of the unconstrained IMC structure on the Diamond booster where the different controller dynamics are applied to each spatial mode using the two-dimensional design process to tradeoff performance and robust stability. This work is presented in [Gayadeen and Duncan, 2014, Gayadeen et al., 2013b].
- The successful implementation of the IMC anti-windup augmentation structure on the Diamond booster when rate limits on the actuators are introduced to provide acceptable constrained performance and robust stability. This work is presented in [Gayadeen and Duncan, 2013].

1.2 Thesis Outline

Below, the contents of each chapter are summarised and the contributions are listed. The necessary background material and relevant literature are presented at the beginning of each chapter.

- In Chapter 2, the fundamentals of the operation of synchrotrons are introduced and necessary background on linear beam optics are reviewed. The main contribution of this chapter is the development of both a dynamic and spatial model which is used for the design of the controller in subsequent chapters.

- In Chapter 3, electron beam orbit stability requirements are presented and the conditions under which the proposed design techniques are based, are discussed. A general structure is presented for the class of discretised, spatially distributed process models under consideration. The use of modal decomposition of the spatial response matrix to identify controllable modes is discussed and the implications to the controller design and structure are outlined. The similarities to some common and emerging two-dimensional control problems are discussed. The outcome of this chapter is the identification of the closed loop performance and robustness requirements, in the two-dimensional (spatial and temporal) frequency domain.

- In Chapter 4, a controller design for the unconstrained system using an IMC structure is proposed. It is demonstrated how a two-dimensional loop shaping technique can be used to select appropriate parameters to guarantee closed loop performance specifications. A robust stability test is developed using IQCs to determine closed loop stability in the presence of plant uncertainty. A comparison of modal truncation and filtering of the high order modes is presented. Furthermore, it is demonstrated how an H_∞ control design can be used to tune the IMC controller. The design of controllers on both the storage ring and booster accelerators at Diamond are presented and machine data from both are used to demonstrate the performance of the controllers.

- In Chapter 5, Fourier analysis of the closed orbit is used to develop a realistic uncertainty model leading to robust design. The developed uncertainty description decouples the various sources of uncertainty, where each uncertainty can be expressed in a diagonally structured form. This allows the robust stability condition developed in Chapter 4 to be decomposed on a mode by mode basis and thereby reduce the computation involved. It is demonstrated how this uncertainty description is used to interpret closed loop stability in terms of physical beam parameters by applying the technique to the storage ring.

- In Chapter 6, the effect of a rate limit constraint on the closed loop performance is shown and anti-windup compensation techniques developed for saturating constraints within an IMC framework, are adapted for the rate constraint case. A technique using Riccati equations to design an anti-windup compensator is reformulated for the IMC structure and the equivalence between the two is demonstrated. The rate limiter is not l_2 stable and is modified so that closed loop stability in the presence of both uncertainty and the rate limits can be determined within an IQC framework. Performance and stability results from the booster implementation are presented.

- In Chapter 7, the control design is extended to systems where there are two arrays of actuators with differing dynamic characteristics. A technique to determine the overlapping controllable subspaces of both arrays is utilised and the control problem is decomposed into decoupled SISO loops or two-input, single output (TISO) loops. A design heuristic is presented for choosing appropriate control directions and it is demonstrated how the design meets stability criteria. Furthermore, a controller design for the TISO case is presented in which mid-ranging control is employed. A simulation study of the booster is presented.

- Conclusions and future directions are discussed in Chapter 8.

Chapter 2

Introduction to Synchrotrons

In this chapter the basic operation of synchrotrons and the main components that make up the synchrotron accelerators and are used to generate synchrotron light are described. A simplified overview of the electron beam steering and focusing is introduced. Components of the process to be controlled are presented and a suitable model for electron beam orbit control is identified.

2.1 Operation of Synchrotrons

In the mid 1940s, circular accelerators, namely betatrons and cyclotrons, were built and optimised for high energy physics experiments [Wilson, 2001]. These machines accelerated electrons to relativistic speeds and in order to follow a circular orbit, the path of the electrons was bent by a magnetic field that caused the electrons to lose energy in the form of light. In 1947, this visible light was observed for the first time at the 70MeV synchrotron built at General Electric Co., Schenectady, and is now known as synchrotron light or synchrotron radiation [Elder et al., 1947, Wille, 1996]. Initially, the synchrotron light produced by these machines was considered to be a nuisance but as the potential for using synchrotron radiation as a research

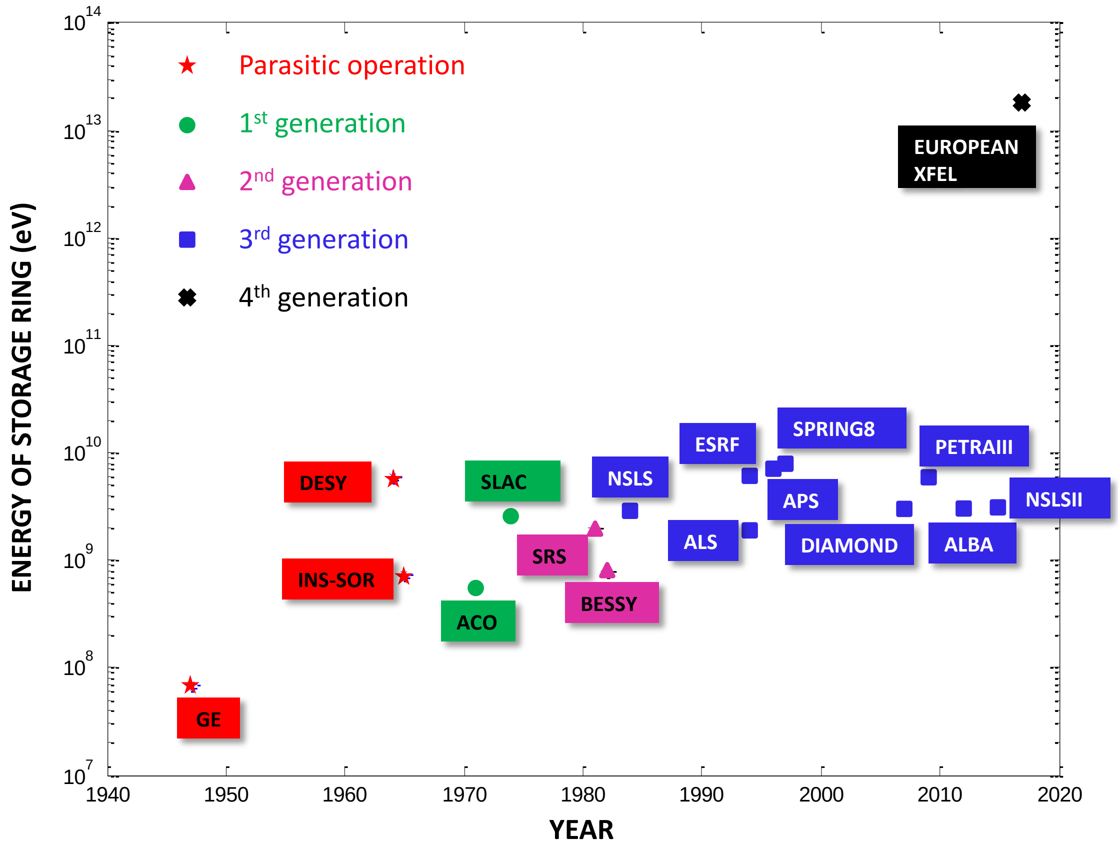

Fig. 2.1: Development of synchrotrons from parasitic operation on high energy physics experiments (first generation) to modern (third generation) facilities which provide brighter and tunable synchrotron light. The free electron laser, considered as a fourth generation light source candidate, is also shown.

tool was recognised, synchrotron light experiments were performed parasitically on the first generation of synchrotrons that had been built primarily for high-energy physics experiments. This led to the construction of a second generation of synchrotrons that was dedicated to the production of synchrotron light and synchrotron light experiments, the first of which was built at Daresbury, UK in 1980. Modern synchrotrons, referred to as third generation synchrotrons, are dedicated light sources that use special arrays of magnets called *insertion devices* to produce even more intense and tunable beams of light. There are now over 40 light sources around the world and Fig. 2.1 traces the progress of the field from 1947 to present, in which fourth generation light sources are included. The energy of the electrons

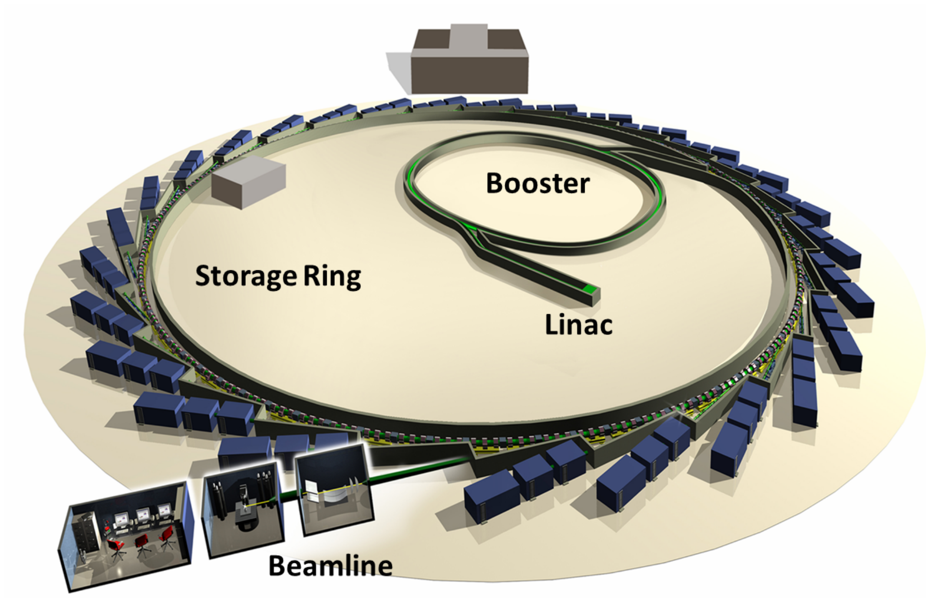

Fig. 2.2: Schematic of Diamond Light Source showing the linear accelerator (Linac), the booster and the main storage ring as well as an expanded view of one photon beamline.

are measured in units of ‘electron Volt’ (eV) which is equal to the kinetic energy gained by an electron while being accelerated in the field between two electrodes with a potential difference of 1V. Fourth generation light sources are considered to be those which exceed the performance of third generation sources by an order of magnitude or more, in parameters such as brightness and coherence or pulse duration. Candidates for fourth generation light sources currently include lower emittance rings and free electron lasers (FEL) [Winick, 1997].

At synchrotrons, three main techniques are employed to use the light in a wide range of academic and industrial experiments: diffraction, spectroscopy and imaging. X-ray diffraction and scattering techniques are used to produce diffraction patterns which are caused when X-rays pass through a crystal and are reflected off the regular arrangement of planes of atoms that make up the crystal. For example, diffraction techniques are used in rational drug design to fight cancer by looking at the structure of biological samples. Spectroscopic experiments allow researchers to reveal elemental composition, chemical state and physical properties of both inorganic material and biological systems and aid in the development of novel materials for engineering applications. Imaging and microscopy techniques are used to give resolutions down to two nanometres, enabling researchers to see structures, such as the iron particles used in magnetic recording or the particles of a catalyst that speeds up a chemical reaction and are employed in the investigation of effects of human activities on global environments and in non-destructive techniques in palaeontology.

Diamond Light Source, a third generation light source, is the UK's national synchrotron science facility, which generates synchrotron radiation for research. The layout of the Diamond facility is shown in Fig. 2.2 where the linear accelerator (linac), the booster and the storage ring are depicted. To establish and sustain an electron beam in these accelerators, many components such as magnets, ultra-high vacuum systems, radio-frequency (RF) systems, injector systems and beam measurement and control systems are required. The nature and functioning of the major components are discussed in Sections 2.1.1 to 2.1.7.

2.1.1 Storage Ring

A storage ring is a circular accelerator where after injection, electrons circulate for several hours at a constant energy i.e. the electrons are 'stored' and therefore serve as a source of continuous synchrotron radiation. At Diamond, the storage ring has a circumference of 561.6m. The electrons are injected into the storage ring vacuum chamber through an injection system and various magnets are arranged around the ring to confine and bend the electron beam. An RF source is used to maintain the energy of the particles which lose energy as a result of passing through a bending magnet or insertion device. Fig. 2.3 shows one section of the Diamond storage ring where dipole magnets (green), quadrupole magnets (red) and sextupole magnets (yellow) are arranged along a support girder. The vacuum chamber is installed

Fig. 2.3: Diamond Light Source cell showing magnets that make up magnetic lattice mounted on a support girder.

along the centre of the magnets. All other main components, such as the RF cavity and insertion devices are installed along the closed loop that defines the orbit along which the electrons travel as demonstrated in Fig. 2.4 [Wiedemann, 2002].

2.1.2 Magnets

The electron beam in the storage ring and booster are confined by strong magnetic fields generated by various magnets. Bending magnets are used to deflect the electron beam and are placed in a carefully ordered arrangement that forces the electron beam to follow a closed path. The location of the bending magnets defines the geometry of the storage ring and although it is considered to be a circular accelerator, the storage ring is a series of arc sections (bending magnets) interrupted by straight sections, for example, at Diamond, the storage ring consists of 24 straight sections angled together. Quadrupole magnets are placed in the straight sections

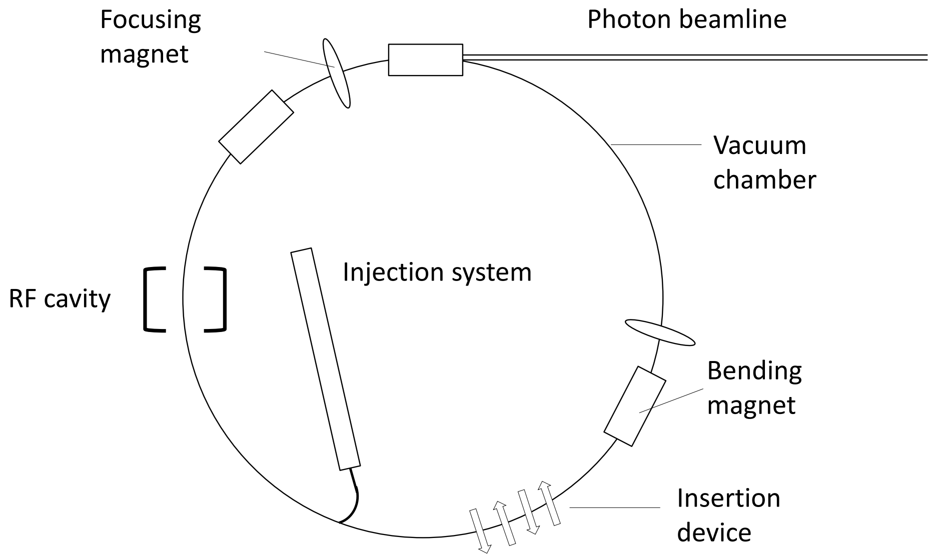

Fig. 2.4: Schematic of components required for storage rings that are installed along the closed loop which defines the beam orbit.

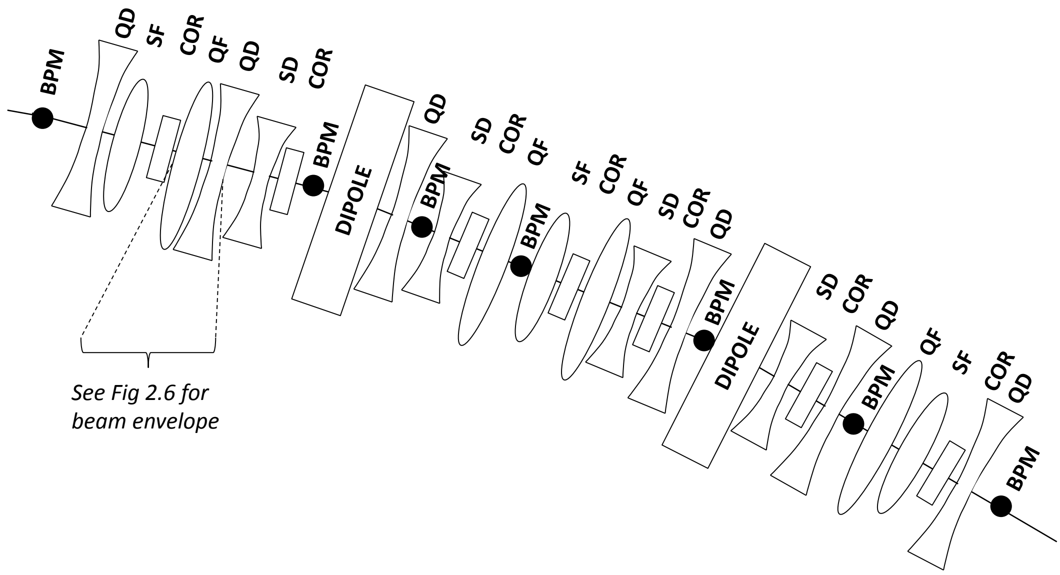

Fig. 2.5: A cell of the Diamond storage ring showing magnets that make up the magnetic lattice which are focusing (QF) and defocusing (QD) quadrupoles, focusing (SF) and defocusing (SD) sextupoles, dipoles, corrector magnets (COR) and also shown are sensors called beam position monitors (BPM). The magnet pattern is repeated to form the closed path of the storage ring.

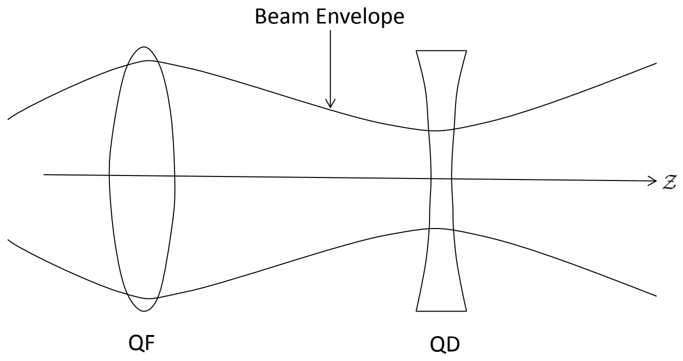

Fig. 2.6: Beam envelope created by alternating focusing (QF) and defocusing (QD) quadrupole magnets.

between the bending magnets to prevent particles deviating from the orbital path by focusing the electron beam. Some electrons may not be at the nominal energy of the ring (3GeV at Diamond) and will be deflected at a different angle from those at nominal energy, so sextupole magnets are used to focus these off-energy particles. The pattern of bending and focusing magnets is called the magnetic lattice and is shown for one cell of the Diamond storage ring in Fig. 2.5. The alternating focusing and defocusing magnets within the cell create a beam envelope as shown in Fig. 2.6. In addition to these magnets, small dipole magnets called corrector magnets are used to adjust the position of the electron beam.

2.1.3 Vacuum Chamber

An electron beam travelling through air will quickly lose electrons as the electrons collide with air molecules and either lose energy or become scattered, so to maintain the electron beam circulating in the storage ring, the chamber the electrons travel in must be kept at a very high vacuum. At Diamond the pressure in the vacuum chamber is $< 10^{-9}$mbar and to sustain this vacuum, the chamber walls are a stainless steel alloy (316LN) to ensure good thermal and mechanical properties. A vacuum system achieves and maintains the low pressure by using vacuum pumps along the circular path of the storage ring.

2.1.4 Radio-Frequency System

Although the particle energy is kept constant, energy is lost into synchrotron radiation and must be compensated by equivalent acceleration. On each rotation around the ring, the electron beam passes through a cavity containing electromagnetic fields oscillating at a radio frequency which provides an energy boost and allows the beam to maintain a fixed orbit around the storage ring [Wiedemann, 2002]. The electric field oscillates at a frequency of 499.7MHz at Diamond and the desired acceleration occurs only when the electrons pass through the cavity at a specific time. For this reason the circulating electron beam is composed of bunches of electrons where the distance between the bunches is any integer multiple of the RF wavelength. As a result, the circumference of the ring also must be an integer multiple of the RF wavelength.

2.1.5 Injection System

Electrons are generated by an electron gun, where a high voltage cathode is heated under vacuum conditions, giving the electrons in the material sufficient thermal energy to 'evaporate' from the surface and escape (thermionic emission). These liberated electrons are then accelerated by an earthed anode, producing a stream of electrons with an energy of 90keV. The linear accelerator (linac) is used to accelerate the electrons to an extreme relativistic energy of 100MeV using RF cavities and electrons with an energy of 100MeV are injected from the linac into the booster. The booster at Diamond has a circumference of 158.4m and is designed to operate at a repetition rate of 5Hz. Here the electrons follow an 'athletics track' shaped trajectory with two straight sections joined together with semicircular curves. Thirty six dipole bending magnets are used to curve the electrons around the bends and an RF voltage source is used to accelerate the electrons in one of the straight sections.

To maintain a fixed radius of curvature, the magnetic field produced by the bending magnets is increased (up to a maximum of 0.8T) as the electron energy rises up to a final extraction energy of 3GeV. At Diamond, the booster supplies beam to the storage ring every 200ms to accumulate the storage ring current for users and the current is then topped up every 10 minutes to make up any lost electrons.

2.1.6 Insertion Devices

Synchrotron radiation emitted from bending magnets does not always meet all requirements of the users and in order to provide the desired radiation, insertion devices are placed in the magnet free sections along the orbit. In order not to perturb the ring geometry, these magnets are composed of more than one pole with opposing polarities such that the total beam deflection in the insertion device is zero. Two main types of insertion devices are employed at Diamond:

- A wiggler which consists of an array of magnets which cause the electron beam to follow a 'wiggling' path. This causes the light to be produced in a wide cone, spanning a broad spectrum of X-rays. Wigglers are used in beamlines where the priority is for very high energy X-ray and a continuous spectrum.
- Undulators are the more common type of insertion device at Diamond and produce very bright light in a discontinuous spectrum. The energy that is generated is selected by varying the separation of the magnet arrays. Undulators produce very bright X-rays over a continuous frequency range; this is essential for crystallography and microfocus spectroscropy experiments.

2.1.7 Photon Beamlines

The photon beamlines are placed tangentially to the storage ring to guide the narrow beams of light to experimental stations, where the light is focused for use in

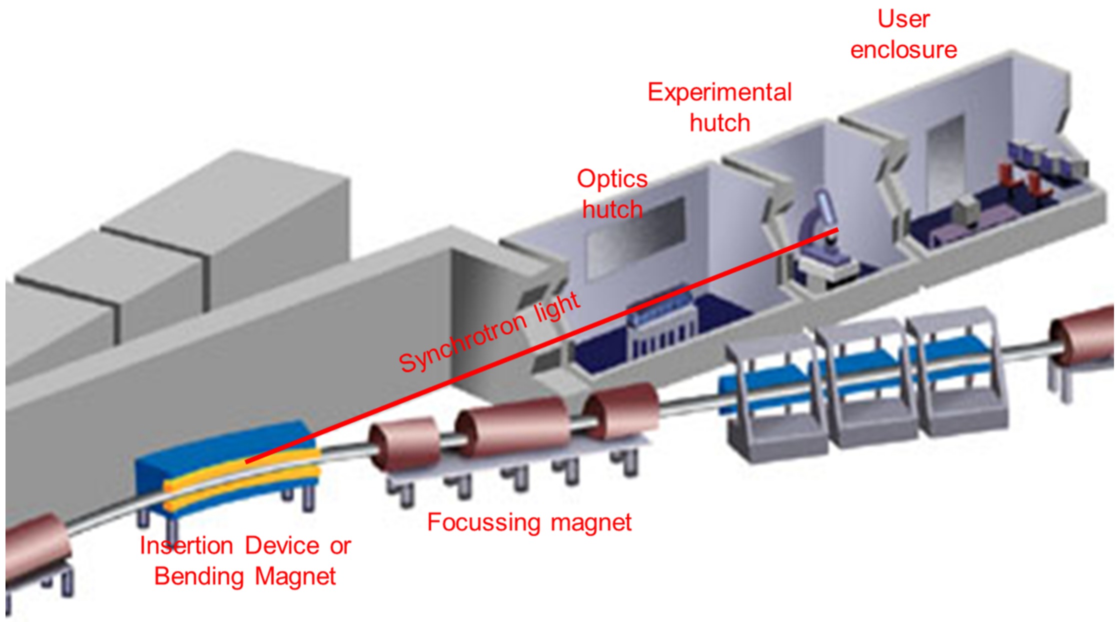

Fig. 2.7: Schematic of photon beamline showing the bending magnet used to generate the synchrotron light, the optics hutch, the experimental hutch and the user enclosure. In the case of an insertion device beamline, the insertion device is located in the storage ring upstream of the bending magnet.

experiments. A beamline has four major sections as shown in Fig. 2.7:

- A front end where light is extracted from the storage ring.
- An optics hutch where certain wavelengths of light are selected and focussed.
- An experimental hutch where the focused synchrotron light interacts with samples and detectors gather experimental data.
- A user enclosure where the scientific team monitors and controls the experiment and takes data.

2.2 Linear Beam Optics

Charged particles can be manipulated using magnetic lenses and by analogy with the manipulation of light with optical lenses, electron beam steering and focusing is referred to as *beam optics*. In Sections 2.2.1 and 2.2.2, linear beam optics are

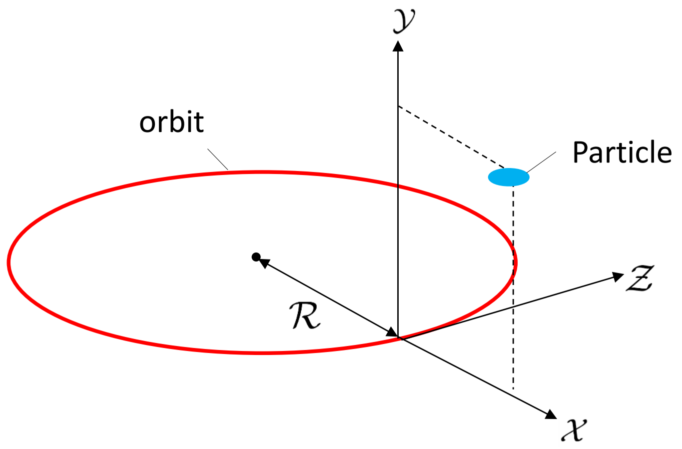

Fig. 2.8: Rotated co-moving coordinate system showing a particle in the vicinity of a nominal trajectory.

defined and associated concepts are discussed.

2.2.1 Equation of Motion in a Co-moving Coordinate System

A Cartesian coordinate system $(\mathcal{X}, \mathcal{Y}, \mathcal{Z})$ shown in Fig. 2.8 whose origin moves along the trajectory of the beam, can be used to describe the motion of a particle in the vicinity of the ideal trajectory (referred to as the *orbit*), where $\mathcal{Z}$ is the axis along the beam direction, $\mathcal{X}$ is the horizontal axis and $\mathcal{Y}$ is the vertical axis. For simplicity the following assumptions are made:

1. velocity, $\mathcal{V} = (0, 0, \mathcal{V}_{\mathcal{Z}})$ i.e. particles move parallel to the $\mathcal{Z}$-direction
2. the magnetic field, $\mathcal{P} = (\mathcal{P}_{\mathcal{X}}, \mathcal{P}_{\mathcal{Y}}, 0)$ i.e. only has transverse components (i.e. in the $\mathcal{X}$ and $\mathcal{Y}$ directions).

For a particle moving in the horizontal plane through the magnetic field, there is a balance between the Lorentz force given by

$$\mathcal{F}_{\mathcal{X}} = -\mathcal{E}\mathcal{V}_{\mathcal{Z}}\mathcal{P}_{\mathcal{Y}} \tag{2.1}$$

Multipole	Definition	Effect
dipole	$\frac{1}{\mathcal{R}} = \frac{\mathcal{E}}{\mathcal{W}\mathcal{V}_{\mathcal{Z}}}\mathcal{P}_{\mathcal{Y}0}$	beam steering
quadrupole	$\mathcal{K} = \frac{\mathcal{E}}{\mathcal{W}\mathcal{V}_{\mathcal{Z}}}\frac{d\mathcal{P}_{\mathcal{Y}}}{d\mathcal{X}}$	beam focusing
sextupole	$\mathcal{K}' = \frac{\mathcal{E}}{\mathcal{W}\mathcal{V}_{\mathcal{Z}}}\frac{d^2\mathcal{P}_{\mathcal{Y}}}{d\mathcal{X}^2}$	chromaticity compensation

Table 2.1: Multipoles and their principle effects on beam motion.

and the centrifugal force given by

$$\mathcal{F}_r = \mathcal{W}\mathcal{V}_{\mathcal{Z}}^2/\mathcal{R} \tag{2.2}$$

where $\mathcal{E}$ is the charge of the particle, $\mathcal{W}$ is the particle mass and $\mathcal{R}$ is the radius of curvature of the trajectory [Wille, 1996]. Balancing the two forces leads to the relation

$$\frac{1}{\mathcal{R}} = \frac{\mathcal{E}}{\mathcal{W}\mathcal{V}_{\mathcal{Z}}}\mathcal{P}_{\mathcal{Y}} \tag{2.3}$$

and since the transverse dimensions of the beam are small compared to the radius of curvature of the particle trajectory, the magnetic field can be expanded in the vicinity of the nominal trajectory (using a Taylor series expansion):

$$\mathcal{P}_{\mathcal{Y}}(\mathcal{X}) = \mathcal{P}_{\mathcal{Y}_{\mathcal{X}_0}} + \frac{d\mathcal{P}_{\mathcal{Y}}}{d\mathcal{X}}\mathcal{X} + \frac{1}{2!}\frac{d^2\mathcal{P}_{\mathcal{Y}}}{d\mathcal{X}^2}\mathcal{X}^2 + \dots \tag{2.4}$$

and multiplying by $\frac{\mathcal{E}}{\mathcal{W}\mathcal{V}_{\mathcal{Z}}}$ gives

$$\begin{aligned}\frac{\mathcal{E}}{\mathcal{W}\mathcal{V}_{\mathcal{Z}}}\mathcal{P}_{\mathcal{Y}}(\mathcal{X}) &= \frac{\mathcal{E}}{\mathcal{W}\mathcal{V}_{\mathcal{Z}}}\mathcal{P}_{\mathcal{Y}_{\mathcal{X}_0}} + \frac{\mathcal{E}}{\mathcal{W}\mathcal{V}_{\mathcal{Z}}}\frac{d\mathcal{P}_{\mathcal{Y}}}{d\mathcal{X}}\mathcal{X} + \frac{1}{2!}\frac{\mathcal{E}}{\mathcal{W}\mathcal{V}_{\mathcal{Z}}}\frac{d^2\mathcal{P}_{\mathcal{Y}}}{d\mathcal{X}^2}\mathcal{X}^2 + \dots \\ &= \frac{1}{\mathcal{R}} + \mathcal{K}\mathcal{X} + \frac{1}{2!}\mathcal{K}'\mathcal{X}^2 \\ &= \text{dipole} + \text{quadrupole} + \text{sextupole} + \dots\end{aligned} \tag{2.5}$$

The magnetic field around the beam is therefore regarded as the sum of multipoles, each of which has a different effect on the path of the particle, which is summarised in Table 2.1 [Wille, 1996]. For example, in a dipole the bending force is constant and is described by the radius $\mathcal{R}$ and in a quadrupole the bending force increases linearly with the transverse displacement from the ideal trajectory and is described by the quadrupole strength $\mathcal{K}$. Therefore if only dipoles and quadrupoles are used for beam steering in an accelerator, then *linear* beam optics apply and the linear equations of motion for a particle travelling through the magnetic structure of an accelerator are given by

$$\begin{gathered}\mathcal{X}''(\mathcal{Z}) + \left(\frac{1}{\mathcal{R}^2(\mathcal{Z})} - \mathcal{K}(\mathcal{Z})\right)\mathcal{X}(\mathcal{Z}) = \frac{1}{\mathcal{R}(\mathcal{Z})}\frac{\Delta\mathcal{W}\mathcal{V}_Z}{\mathcal{W}\mathcal{V}_Z} \\ \mathcal{Y}''(\mathcal{Z}) + \mathcal{K}(\mathcal{Z})\mathcal{Y}(\mathcal{Z}) = 0\end{gathered} \tag{2.6}$$

where $\mathcal{K}$ is the quadrupole strength, $\frac{\Delta\mathcal{W}\mathcal{V}_Z}{\mathcal{W}\mathcal{V}_Z}$ represents the relative momentum deviation and the terms $\mathcal{X}''(\mathcal{Z})$ and $\mathcal{Y}''(\mathcal{Z})$ represent derivatives with respect to the spatial parameter $\mathcal{Z}$ i.e. $\mathcal{X}''(\mathcal{Z}) = \frac{d^2\mathcal{X}}{d\mathcal{Z}^2}$ and $\mathcal{Y}''(\mathcal{Z}) = \frac{d^2\mathcal{Y}}{d\mathcal{Z}^2}$ [Wille, 1996, Wilson, 2001]. These equations are referred to as Hill's differential equation of motion.

2.2.2 Transfer Matrices

To understand particle trajectories through the various magnets, the solution of (2.6) is considered. In a dipole and quadrupole magnet there is no coupling between the horizontal and vertical motion of the particle [Wille, 1996] so it is sufficient to consider only one plane and the horizontal plane is considered here. There are some assumptions to be made for a solution:

1. The field begins and ends abruptly at the beginning and end of the magnet.
2. Within the magnet, the field is constant along the beam axis.
3. The particles have nominal energy.

These assumptions are made since beam optics are always calculated for the nominal case which is of importance in this thesis. If assumptions (1) and (2) are no longer

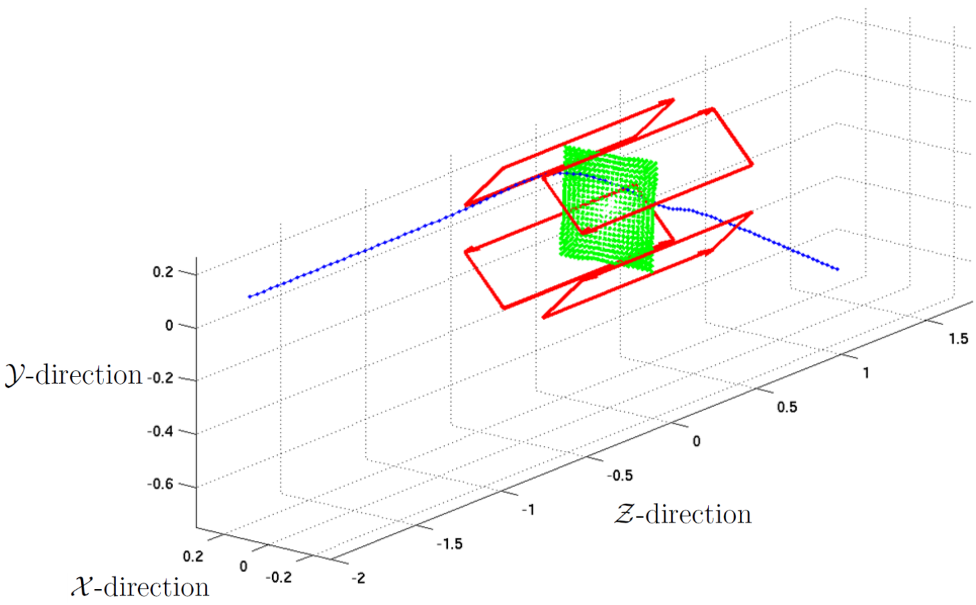

Fig. 2.9: Effect of magnetic field (green) induced within a quadrupole magnet (poles shown in red) on electron beam (blue).

met, then 'edge focusing' [Wilson, 2001] can be introduced. Likewise, if a real beam with particular momentum distribution is used (assumption(3)) then the 'dispersion function' [Wille, 1996] is introduced. However these concepts are beyond the scope of this thesis. The trajectory of an electron beam through a quadrupole is shown in Fig. 2.9 i.e. there is no bending of the beam horizontally ($1/\mathcal{R} = 0$) therefore (2.6) simplifies to

$$\mathcal{X}''(\mathcal{Z}) - \mathcal{K}\mathcal{X}(\mathcal{Z}) = 0 \tag{2.7}$$

where $\mathcal{K}$ is constant. This homogeneous and linear second order differential equation has the form of a normal oscillation equation which is directly solved analytically. The trajectory of an electron beam through a dipole is shown in Fig. 2.10 i.e. there is a constant bending radius $\mathcal{R}$ but the nominal energy of particles is assumed ($\frac{\Delta\mathcal{W}\mathcal{V}_Z}{\mathcal{W}\mathcal{V}_Z} = 0$) and (2.6) simplifies to

$$\mathcal{X}''(\mathcal{Z}) + \frac{1}{\mathcal{R}^2(\mathcal{Z})}\mathcal{X}(\mathcal{Z}) = 0 \tag{2.8}$$

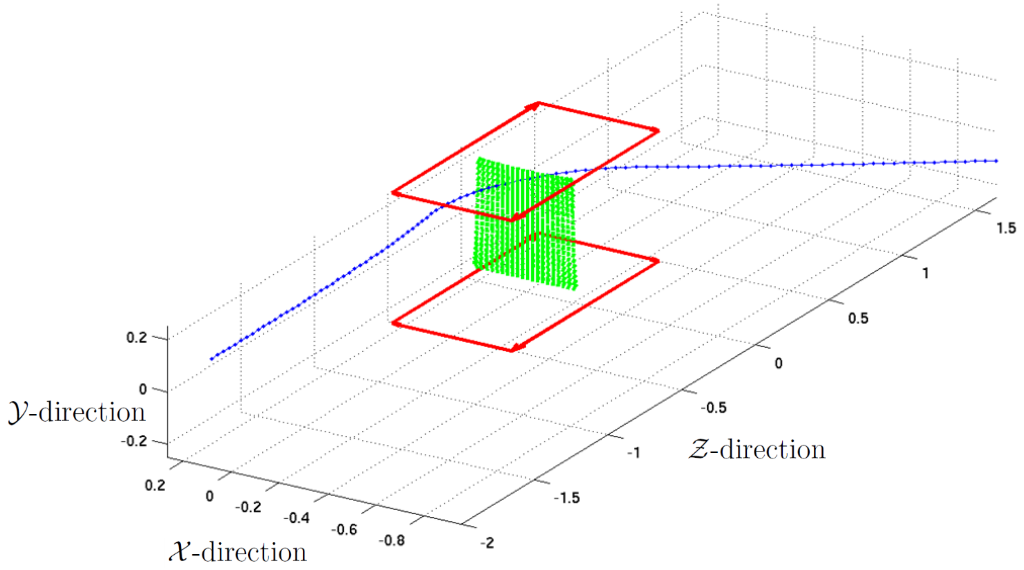

Fig. 2.10: Effect of magnetic field (green) induced within a dipole magnet (poles shown in red) on electron beam (blue).

The solution of (2.7) and (2.8) is given in the form

$$\begin{bmatrix} \mathcal{X}(\mathcal{Z}) \\ \mathcal{X}'(\mathcal{Z}) \end{bmatrix} = \boldsymbol{\mathcal{M}} \begin{bmatrix} \mathcal{X}_0 \\ \mathcal{X}'_0 \end{bmatrix} \tag{2.9}$$

with initial conditions $\mathcal{X}(0) = \mathcal{X}_0$, $\mathcal{X}'(0) = \mathcal{X}'_0$ and are found for the cases where $\mathcal{K} < 0$, $\mathcal{K} > 0$ and $\mathcal{K} = 0$ which are listed below:

1. $\mathcal{K} < 0$ i.e. horizontally focusing quadrupole:

$$\boldsymbol{\mathcal{M}}_{QF} = \begin{pmatrix} \cos\theta_{\mathcal{K}} & \frac{1}{\sqrt{|\mathcal{K}|}}\sin\theta_{\mathcal{K}} & 0 & 0 \\ -\sqrt{|\mathcal{K}|}\sin\theta_{\mathcal{K}} & \cos\theta_{\mathcal{K}} & 0 & 0 \\ 0 & 0 & \cosh\theta_{\mathcal{K}} & \frac{1}{\sqrt{|\mathcal{K}|}}\sinh\theta_{\mathcal{K}} \\ 0 & 0 & \sqrt{|\mathcal{K}|}\sinh\theta_{\mathcal{K}} & \cosh\theta_{\mathcal{K}} \end{pmatrix} \tag{2.10}$$

2. $\mathcal{K} > 0$ i.e. vertically focusing quadrupole:

$$\boldsymbol{\mathcal{M}}_{QD} = \begin{pmatrix} \cosh\theta_{\mathcal{K}} & \frac{1}{\sqrt{\mathcal{K}}}\sinh\theta_{\mathcal{K}} & 0 & 0 \\ \sqrt{\mathcal{K}}\sinh\theta_{\mathcal{K}} & \cosh\theta_{\mathcal{K}} & 0 & 0 \\ 0 & 0 & \cos\theta_{\mathcal{K}} & \frac{1}{\sqrt{\mathcal{K}}}\sin\theta_{\mathcal{K}} \\ 0 & 0 & -\sqrt{\mathcal{K}}\sin\theta_{\mathcal{K}} & \cos\theta_{\mathcal{K}} \end{pmatrix} \tag{2.11}$$

3. $\mathcal{K} = 0$ i.e. zero-field drift region:

$$\boldsymbol{\mathcal{M}}_{drift} = \begin{pmatrix} 1 & \mathcal{Z} & 0 & 0 \\ 0 & 1 & 0 & 0 \\ 0 & 0 & 1 & \mathcal{Z} \\ 0 & 0 & 0 & 1 \end{pmatrix} \tag{2.12}$$

4. $\mathcal{K} = 0, \mathcal{R} > 0$ i.e. dipole magnet:

$$\boldsymbol{\mathcal{M}}_{dipole} = \begin{pmatrix} \cos\frac{\mathcal{Z}}{\mathcal{R}} & \mathcal{R}\sin\frac{\mathcal{Z}}{\mathcal{R}} & 0 & 0 \\ -\frac{1}{\mathcal{R}}\sin\frac{\mathcal{Z}}{\mathcal{R}} & \cos\frac{\mathcal{Z}}{\mathcal{R}} & 0 & 0 \\ 0 & 0 & 1 & \mathcal{Z} \\ 0 & 0 & 0 & 1 \end{pmatrix} \tag{2.13}$$

where $\theta_{\mathcal{K}} = \sqrt{|\mathcal{K}|}\mathcal{Z}$. To describe the behaviour of an entire composite beam (still assumming that $1/\mathcal{R} = 0$ and nominal energy of particles), the general solution of the Hill's equations must be considered, which can be expressed in the form

$$\begin{aligned} \mathcal{X}(\mathcal{Z}) &= \sqrt{\mathcal{U}}\sqrt{\beta(\mathcal{Z})}\cos\left(\eta(\mathcal{Z}) + \theta_0\right) \\ \mathcal{X}'(\mathcal{Z}) &= -\frac{\sqrt{\mathcal{U}}}{\sqrt{\beta(\mathcal{Z})}}\left[\alpha(\mathcal{Z})\cos\left(\eta(\mathcal{Z}) + \theta_0\right) + \sin\left(\eta(\mathcal{Z}) + \theta_0\right)\right] \end{aligned} \tag{2.14}$$

where

$$\begin{aligned}\eta(\mathcal{Z}) &= \int_0^{\mathcal{Z}} \frac{d\mathcal{Z}}{\beta(\mathcal{Z})} \\ \alpha(\mathcal{Z}) &= -\frac{\beta'(\mathcal{Z})}{2}\end{aligned} \tag{2.15}$$

These equations describe the path taken by the electron where $\mathcal{U}$ and θ_0 are constants of a particular trajectory and $\beta(\mathcal{Z})$ has a periodicity of the circumference of an equilibrium orbit. The motion is a distorted sine wave with varying amplitude $\sqrt{\mathcal{U}\beta(\mathcal{Z})}$ which is modulated in proportion to the root of the beta function, $\beta(\mathcal{Z})$ and with a phase $(\eta(\mathcal{Z}) + \theta_0)$ which advances with $\mathcal{Z}$ at a varying rate proportional to $1/\beta$ [Sands, 1970]. The beam size depends on the magnetic lattice, defined by the beta function $\beta(\mathcal{Z})$ and the beam itself, defined by the emittance $\mathcal{U}$. The emittance is invariant around the ring while the beta function changes around the ring. The betatron phase, $\eta(\mathcal{Z})$ does not advance linearly with time and distance around the ring, although the beta function and phase have the same periodicity as the lattice. For a beam of particles with the nominal energy, the beam size (i.e. cross-section at a given point) is given by

$$\mathcal{S}(\mathcal{Z}) = \sqrt{\beta(\mathcal{Z})\mathcal{U}} \tag{2.16}$$

and for the Diamond storage ring the emittance is 2.74nm.rad and the beta function is shown in Fig. 2.11. The pattern of $\beta(\mathcal{Z})$ in Fig. 2.11 reflects the 24 cells that make up the closed ring but the pattern also shows that there is not true 6-fold symmetry as the beta function was modified for particular cells (evident just before 300m position on the x-axis). The position of the insertion devices is associated with the minimum points of the beta function. This is desirable since a minimum beta function is associated with minimum emittance which is required at the point where light is extracted for use in the beamlines.

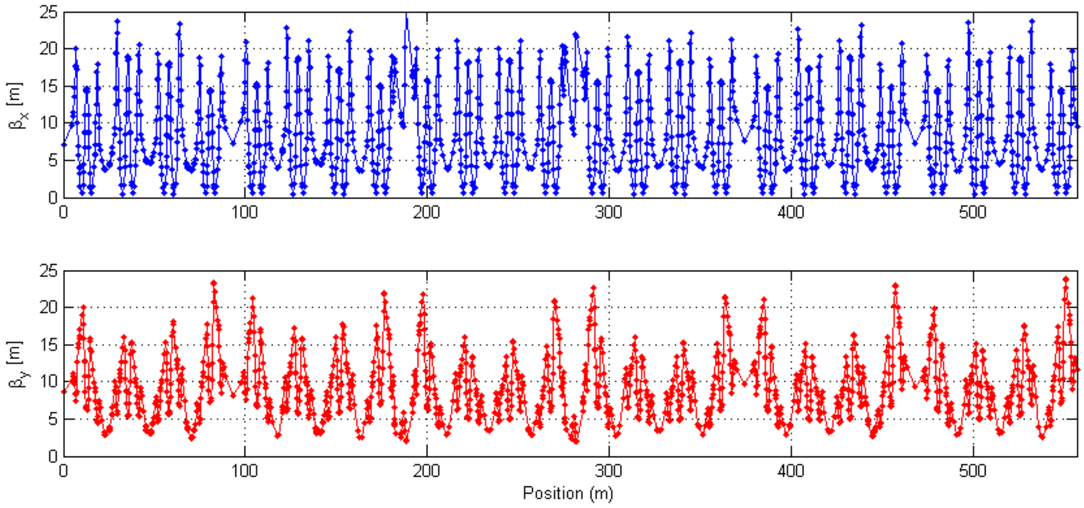

Fig. 2.11: Horizontal (blue) and vertical (red) beta functions for the Diamond storage ring along the entire circumference of 561.6m.

With initial conditions $\beta(0) = \beta_0$, $\alpha(0) = \alpha_0$ and $\eta(0) = 0$ then

$$\begin{aligned} \cos\theta_0 &= \frac{\mathcal{X}_0}{\sqrt{\mathcal{U}\beta_0}} \\ \sin\theta_0 &= -\frac{1}{\sqrt{\mathcal{U}}}\left(\mathcal{X}_0'\sqrt{\beta_0} + \frac{\alpha_0\mathcal{X}_0}{\sqrt{\beta_0}}\right) \end{aligned} \tag{2.17}$$

Inserting this into (2.14) gives

$$\boldsymbol{\mathcal{M}} = \begin{pmatrix} \sqrt{\frac{\beta(\mathcal{Z})}{\beta_0}}\left(\cos\eta(\mathcal{Z}) + \alpha_0\sin\eta(\mathcal{Z})\right) & \sqrt{\beta(\mathcal{Z})\beta_0}\sin\eta(\mathcal{Z}) \\ \frac{(\alpha_0-\alpha(\mathcal{Z}))\cos\eta(\mathcal{Z})-(1+\alpha_0\alpha(\mathcal{Z}))\sin\eta(\mathcal{Z})}{\sqrt{\beta(\mathcal{Z})\beta_0}} & \sqrt{\frac{\beta_0}{\beta(\mathcal{Z})}}\left(\cos\eta(\mathcal{Z}) - \alpha(\mathcal{Z})\sin\eta(\mathcal{Z})\right) \end{pmatrix} \tag{2.18}$$

where the transfer matrix $\boldsymbol{\mathcal{M}}$ describes the transformation of the beam properties through a component from some initial point. The trajectory of a particle through a beam transport system can be determined by repeated multiplication of transfer matrices through each individual elements of the beam line [Wiedemann, 2007]. So that a full one-turn map at the entrance of the first element of the ring through to N_E elements is given by,

$$\boldsymbol{\mathcal{M}}_{0|N_E} = \boldsymbol{\mathcal{M}}_{N_E}\ \ldots\ \boldsymbol{\mathcal{M}}_3\ \boldsymbol{\mathcal{M}}_2\ \boldsymbol{\mathcal{M}}_1 \tag{2.19}$$

	Storage Ring	Booster
Circumference (m)	561.6	158
Energy (GeV)	3	0.1
Beam Current (mA)	300	1(max)
Beam size (μm)	$\mathcal{X}$: 123	$\mathcal{X}$: 300
	$\mathcal{Y}$: 6	$\mathcal{Y}$: 200
No. of actuators	172	22
No. of sensors	172	22

Table 2.2: Comparison of the storage ring and booster properties (when the booster is operated in stored beam mode).

where $\boldsymbol{\mathcal{M}}_i$ is the i^{th} element transfer matrix and is defined by any of the matrices given in (2.10) to (2.13). Using this relationship, the beta function and phase advance contribution at each element can be determined and for a full revolution,

$$\mathcal{M}_{\mathcal{Z}|\mathcal{Z}+2\pi\mathcal{R}} = \begin{pmatrix} \cos 2\pi\mathcal{Q} + \alpha(\mathcal{Z})\sin 2\pi\mathcal{Q} & \beta(\mathcal{Z})\sin 2\pi\mathcal{Q} \\ \frac{1+\alpha^2(\mathcal{Z})}{\beta(\mathcal{Z})}\sin 2\pi\mathcal{Q} & \cos 2\pi\mathcal{Q} - \alpha(\mathcal{Z})\sin 2\pi\mathcal{Q} \end{pmatrix} \tag{2.20}$$

where the tune of the machine, $\mathcal{Q}$ represents the number of free oscillations a particle makes in one revolution.

2.3 Storage Ring and Booster Test Platforms

In this thesis, the design of electron orbit controllers are considered for both the Diamond storage ring and booster. While electron orbit control is mainly utilised on storage rings and is necessary for the operation of storage rings, this is not generally the case for boosters. Boosters are designed to deliver a given charge at a given energy to storage rings. At Diamond, during each 200ms cycle, beam is injected on-axis from a 100MeV linac, and dipoles and quadrupoles are ramped to accelerate the beam to 3GeV before extraction and insertion into the storage ring. To advance

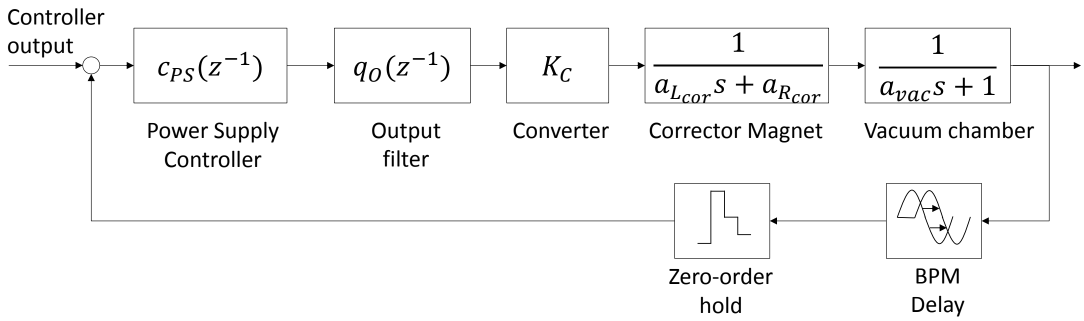

Fig. 2.12: Schematic of components that make up the process.

the evaluation and optimization of new control algorithms for orbit stability for the storage ring, it was decided to use the booster as a test platform by operating it in DC mode at 100MeV i.e. operating as a storage ring with nominal energy 100MeV [Christou et al., 2011]. In stored beam mode, the booster operates in a similar manner as the storage ring but uses significantly less actuators and sensors which eases online computation for the control system. The properties of the two accelerators are compared in Table 2.2 where the electron beam in the storage ring has a much higher beam current and is considerably smaller than the beam in the booster.

2.4 Electron Beam Orbit Control System

A feedback control system, referred to as Fast Orbit Feedback (FOFB) is used to control the location of the electron beam. FOFB controllers use beam position monitors (BPMs) to detect the electron beam position around the ring and vary the current to corrector magnets which change the induced magnetic field and therefore the position of the electron beam. The FOFB controller provides the setpoint to the system depicted in Fig. 2.12 and receives positional data from the discretised signal from the BPMs. The individual components of the process to be controlled are discussed in Sections 2.4.1 to 2.4.6.

	Storage Ring		Booster	
	Horizontal	Vertical	Horizontal	Vertical
K_p	22	22	0.76	1.32
K_i	20.94	20.94	560	578

Table 2.3: Power supply PI parameters of storage ring and booster.

2.4.1 Power Supply Unit

A power supply controller unit, $C_{PS}(z^{-1})$ is used to control the current setpoint to the corrector magnets and protect the semiconductors from large changes in current. The power supply unit at Diamond is shown in Fig. 2.13 and comprises five major sections:

- The voltage ratings of the power supply are considerably higher than needed for the maximum current in the load therefore a limiter for the reference value is needed. The saturation limit is combined with a low pass filter to limit the rate of change of the reference value. The rate limit is variable to allow small signal currents to propagate. When the difference between the power supply setpoint and the measured current, i_{diff} is small, the rate limit is relaxed and for larger values of i_{diff}, a smaller rate limit is applied. Fig. 2.14 shows how the rate limit changes with i_{diff}.

- The measured values are filtered using a low pass filter, and the error between the reference and the filtered signal is fed into a PI controller given by

$$c_{PI}(z^{-1}) = K_p \left(1 + K_i \frac{T_s z^{-1}}{1 - z^{-1}}\right) \tag{2.21}$$

  where the sample rate $T_s = 100\mu$s and the parameters K_p and K_i for the storage ring and booster are given in Table 2.3.

- DC link voltage variations influence the converter output voltage which will

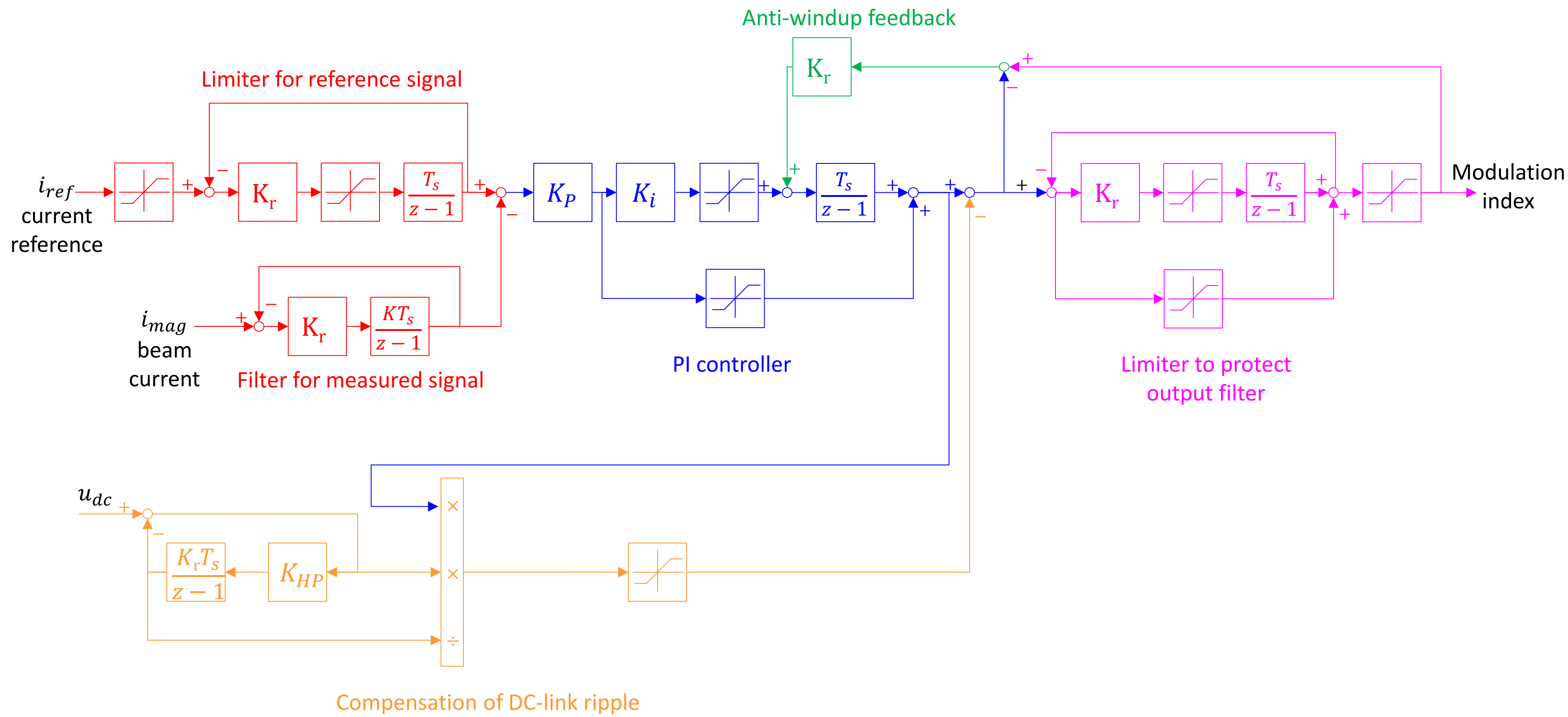

Fig. 2.13: Components of the Diamond storage ring power supply controller unit showing the input (red) and output (magenta) rate limiters, the PI controller (blue), DC-link ripple compensation (yellow) and the anti-windup feedback loop (green).

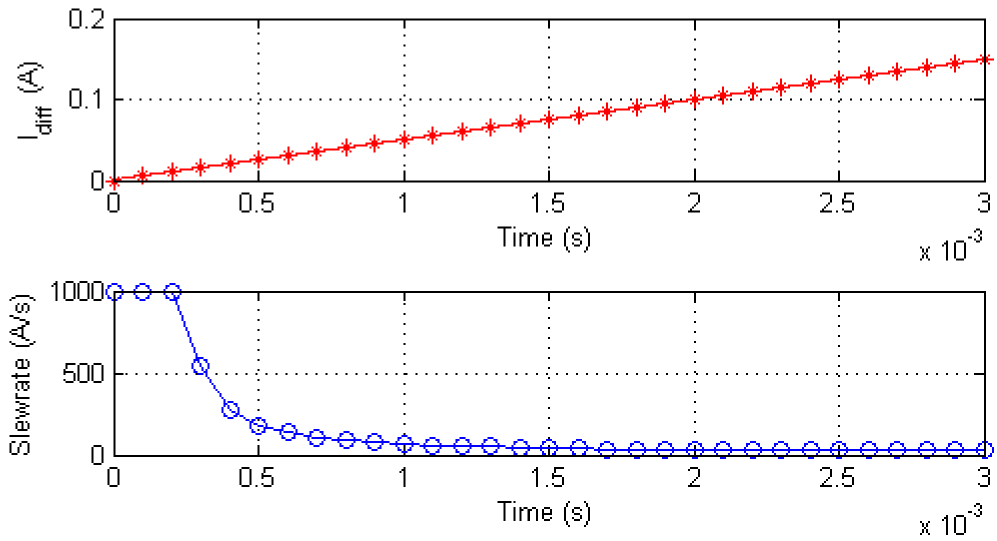

Fig. 2.14: Power supply controller slew rate operation showing how the rate limit changes with i_{diff}.

cause variations of the load current which will be corrected by the controller but delayed. Voltage fluctuations of a medium speed are particularly critical: fast pulses are filtered by the output filter while slow fluctuations are well corrected by the control loop. With an appropriate voltage feed forward, the influence of DC-link voltage pulsations on the converter output can be reduced.

- A second rate limiter is included to protect an output filter since the resistors of the output filter can be destroyed with over current.
- An anti-windup feedback loop is also included for constrained operation.

2.4.2 Pulse Width Modulation Converter and Output filter

An output filter, $q_O(z^{-1})$ in the form of a parallel damped filter, uses an output resistor to reduce the output peak impedance of the filter at a cutoff frequency of 3kHz. The frequency response of the filter is shown in Fig. 2.15. A converter at the output of the filter is used to convert the pulse-width modulation index to a voltage at 100kHz and is modelled as a gain of $K_C = 24$.

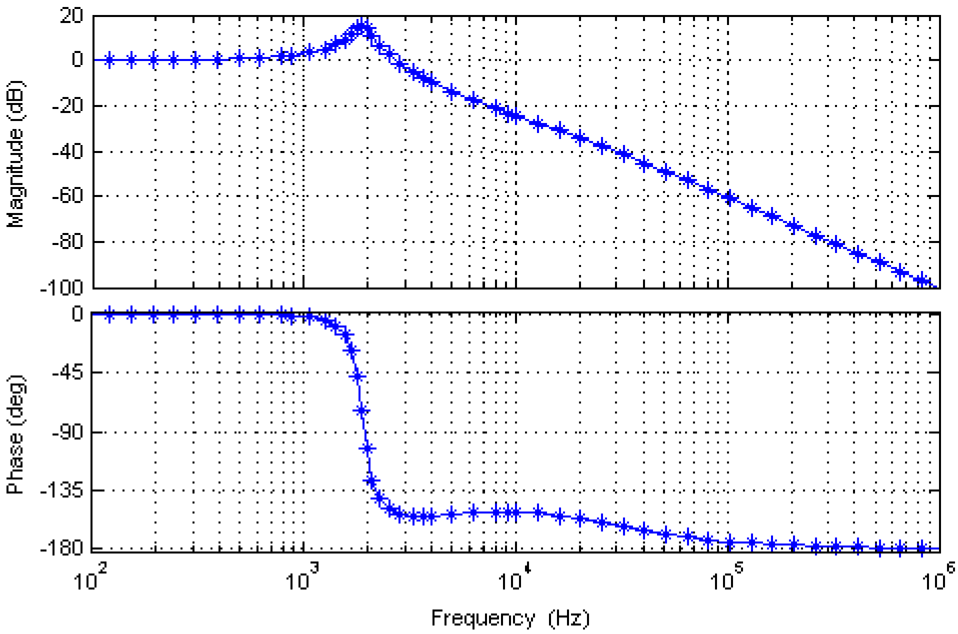

Fig. 2.15: Frequency response of output filter on booster.

2.4.3 Corrector Magnets (Actuators)

In addition to the magnets that are used for beam focusing and confinement, small dipole magnets called corrector magnets are used to change the beam position, the locations of which are shown in Fig. 2.5 for a single cell. It is important to have a good model of the electrical behaviour of the corrector magnets and it is known that the resistive and inductive part of their impedances show strong frequency dependence, while the effects of hysteresis losses and eddy currents in the core can be modelled with a frequency dependent ohmic part of the coil. Therefore a corrector magnet is modelled as a RL series filter such that the coil transfer function is

$$\frac{1}{a_{L_{cor}}s + a_{R_{cor}}} \tag{2.22}$$

where $a_{L_{cor}}$ is the magnet inductance, $a_{R_{cor}}$ is the magnet resistance and s is the Laplace transform variable. These properties have been measured on the storage ring and booster and are recorded in Table 2.4.

	Storage Ring		Booster	
	Horizontal	Vertical	Horizontal	Vertical
Resistance, $a_{R_{cor}}$ (Ω)	2.78	2.81	0.660	1.16
Inductance, $a_{L_{cor}}$ (mH)	210	168	7.7	12.6

Table 2.4: Resistance and inductance of storage ring and booster corrector magnets for both horizontal and vertical planes.

2.4.4 Vacuum Chamber

In addition to the DC ohmic losses in the coils, there are AC losses (eddy current loses) in the stainless steel walls of the vacuum chamber. For a circular chamber, the time constant of the magnetic field decay due to eddy current losses can be expressed as

$$\frac{1}{a_{vac}s + 1} \tag{2.23}$$

where $a_{vac} = \frac{1}{2} v_{per} v_{con} a_{rad} a_{wall}$ for vacuum permeability $v_{per} = 4\pi \times 10^{-7}$H.m^{-1} and 316LN stainless steel conductivity $v_{con} = 1.3514 \times 10^6$ Ωm with radius of the vacuum chamber a_{rad} and wall thickness, a_{wall} given in metres. The vacuum chambers of the storage ring and booster at Diamond are, in fact, elliptical with parameters in Table 2.5. However this estimate of the time constant is reasonable, as the procedure for calculating the losses in elliptical chambers given in [Kim., 2001] rely on approximations with Mathieu functions and the resulting time constant difference is negligible.

2.4.5 Beam Position Monitors (Sensors)

The beam position is detected by sensors called beam position monitors (BPMs). Each BPM consists of an electrostatic button in the vacuum vessel with four pickup electrodes surrounding the electron beam, that pick up electric fields corresponding to the electron beam position as modulations of the machine RF (of frequency

	Storage Ring	Booster
Major diameter (mm)	52	47
Minor diameter(mm)	24	18.2
Thickness (mm)	1	1

Table 2.5: Diamond vacuum chamber dimensions of storage ring and booster.

499.65MHz) as shown in Fig. 2.16. The four button signals are fed by coaxial cables to a BPM processor where the amplitudes of the signals are processed and used to compute the electron beam position and beam current as follows

$$\begin{aligned}\mathcal{X} &= K_{B_\mathcal{X}} \frac{A_1 - A_2 - A_3 + A_4}{A_1 + A_2 + A_3 + A_4} + \mathcal{X}_{B_0} \\ \mathcal{Y} &= K_{B_\mathcal{Y}} \frac{A_1 + A_2 - A_3 - A_4}{A_1 + A_2 + A_3 + A_4} + \mathcal{Y}_{B_0} \\ \mathcal{I} &= K_{B_\mathcal{I}} \frac{A_1 + A_2 + A_3 + A_4}{K_{RF}}\end{aligned} \tag{2.24}$$

where $K_{B_\mathcal{X}}$ and $K_{B_\mathcal{Y}}$ are scaling factors determined by button geometry and $\mathcal{X}_{B_0}$ and $\mathcal{Y}_{B_0}$ are measured beam offsets. The beam current $\mathcal{I}$ is also calculated from a scaling factor $K_{B_\mathcal{I}}$ that is calibrated against the DC current transformer and the RF gain K_{RF} [Abbott et al., 2009].

Significant data processing and signal conditioning within the BPM field-programmable gate array (FPGA) is also performed on the measured signal which is depicted in Fig. 2.17. Firstly, an RF board passes the four signals through a cross-bar switch into four parallel analogue channels where they are undersampled by ADCs at approximately 117MHz, labelled as first turn data in Fig. 2.17. The raw sampled signal is processed by an FPGA and the signals are filtered by repeated stages of digital down conversion to reduce the sample frequencies and each stage is shown in Fig. 2.17. An FIR filter which has a 3dB point at 2kHz and the first null frequency at 5kHz is designed to decimate the turn by turn data stream to 10kHz for the fast orbit feedback system. This is referred to as the fast acquisition data stream. Beam

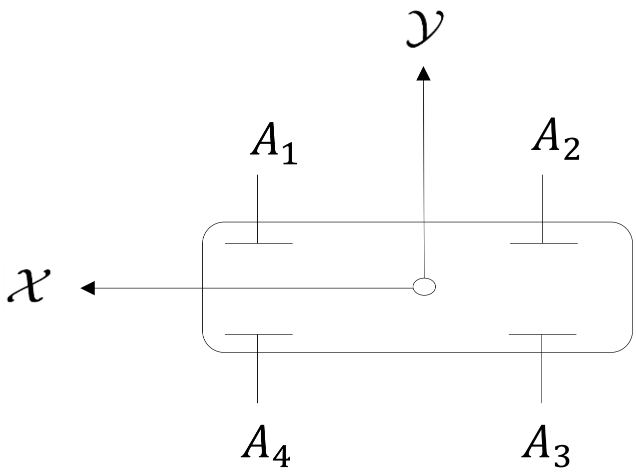

Fig. 2.16: Structure of BPM which consists of a button block in the vacuum vessel with four pickup electrodes surrounding the electron beam.

positions at approximately 10Hz are also made available. This is the slow acquisition data stream which is made available through the control software, Experimental Physics and Industrial Control System (EPICS) over the computer network [Abbott et al., 2009]. Signal conditioning in the BPMs eliminates low frequency drift in measured position but at the cost of high levels of noise at the frequency at which the final measured button signal is produced (referred to as the switching frequency) [Abbott et al., 2009]. The effect of the switching noise is seen in Fig. 2.18 where the lowest switching frequency is at 1.6kHz. Notch filters are therefore included to remove switching noise from the fast acquisition at 1.6kHz given by

$$\frac{121362 - 122735z^{-1} + 121362z^{-2}}{131072 - 122735z^{-1} + 111652z^{-2}} \tag{2.25}$$

and 3.2kHz given by

$$\frac{121362 - 118600z^{-1} + 121362z^{-2}}{131072 - 11860z^{-1} + 111652z^{-2}} \tag{2.26}$$

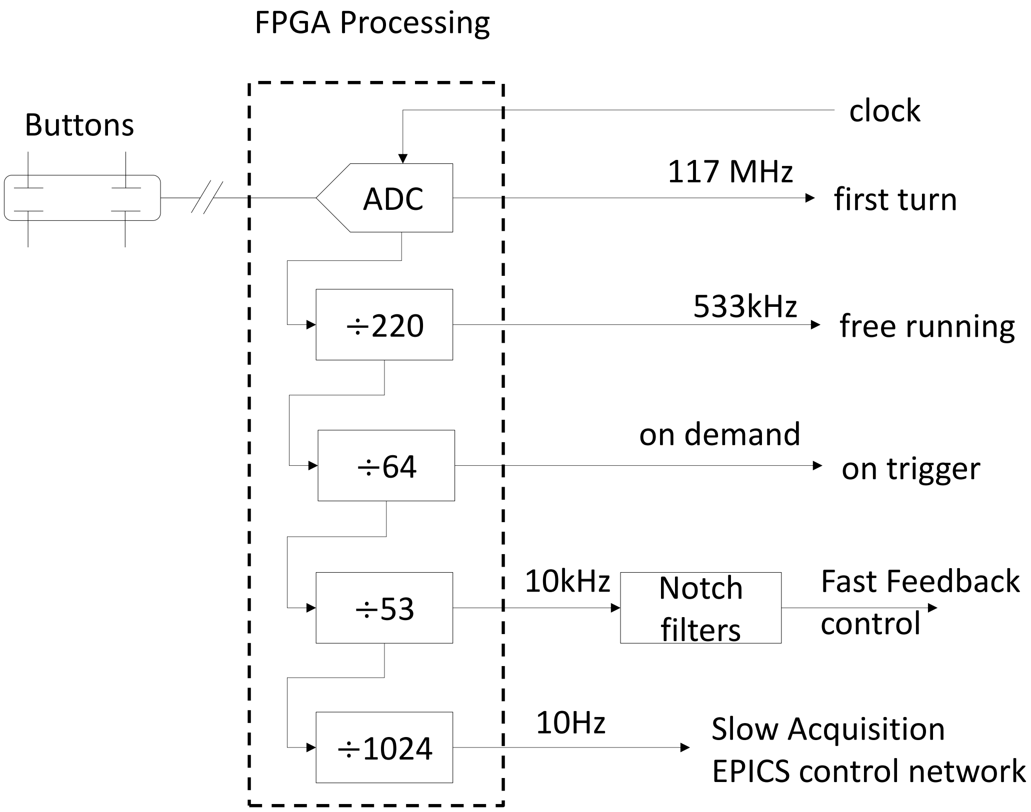

Fig. 2.17: Diamond storage ring BPM FPGA data processing.

2.4.6 Control Communication Network

For the FOFB system, a Motorola MVME5500 VME processor with VxWorks real-time operating system is used and one feedback processor in each of the 24 cells of the storage ring (or each of the 4 cells of the booster) runs the feedback algorithm using the position values from all 172 BPMs for the storage ring (or 22 for the booster). Therefore beam positions from all BPMs around the ring need to be distributed to all 24 feedback processors. A communication controller, implemented in VHSIC hardware description language (VHDL), is used to transfer horizontal and vertical positional and control data from all BPMs to each of the 24 computation nodes for the storage ring. The network topology is shown in Fig. 2.19. In the communication scheme, time is divided into 'time frames' of equal length. In the beginning of each time frame, each BPM injects its own beam position values to the FOFB network, and then starts a forwarding or discarding process of the BPM

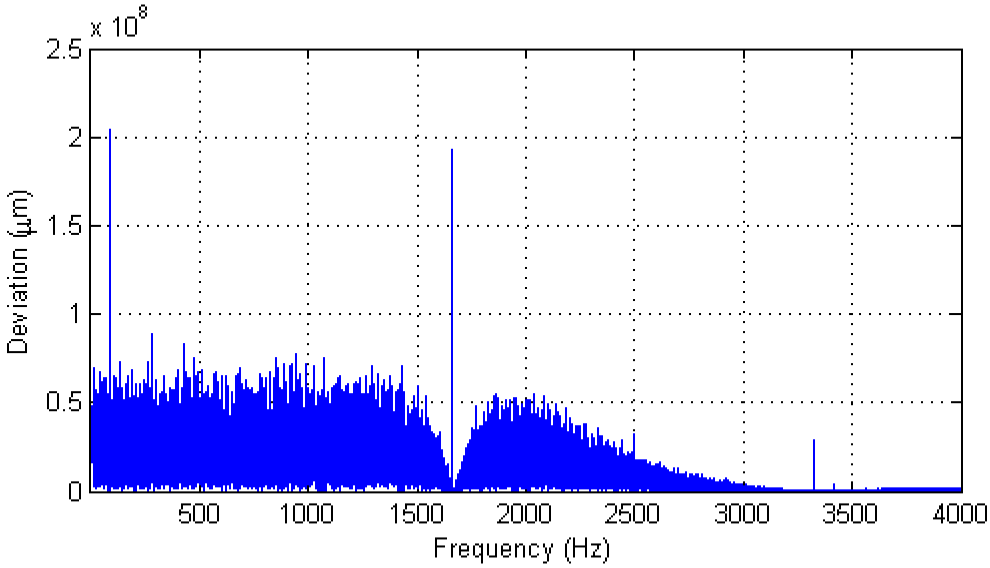

Fig. 2.18: Booster frequency response showing the effect of BPM switching noise at 1.6kHz and 3.2kHz.

values that it receives. Each BPM position value has to propagate to all BPMs and 24 computation nodes before the end of the time frame [Heron et al., 2009]. Each computation node receives the data from all BPMs and uses the dedicated VME processor to calculate the control action corresponding to all corrector magnets for that cell. The controller dynamics are then implemented as IIR filters using difference equations. The new power supply controller demand values are written via a dedicated 1Mbps point-to-point link from each computation node to the power supply controllers for that cell. The FOFB communication network is implemented by fast, serial RocketIO links. The links between BPMs in the diagnostic rack in each cell have been implemented using electrical high speed copper patch cables. A fibre optic infrastructure is installed from each of the cells to the Control Systems Computer Room (CSCR) which consists of a mixture of single-mode and multi-mode fibres. The links between 'primary' BPMs and the computation modes in the same cell are implemented with fibre patch cables. These BPMs in each cell are connected to the patch panel in the CSCR where the connections between the cells are implemented using single mode fibres.

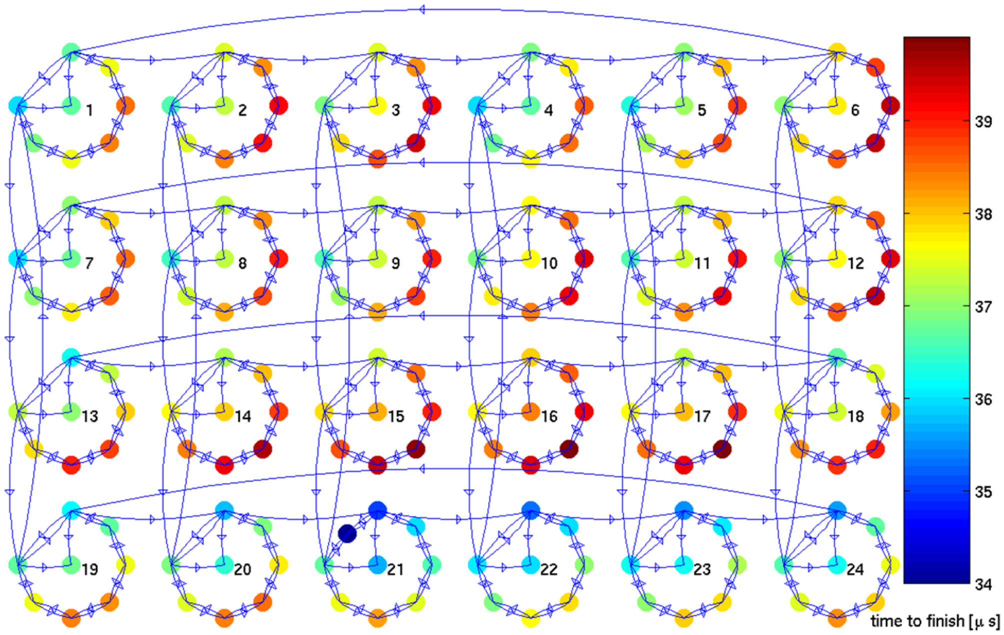

Fig. 2.19: Communication network topology with each circle being one cell consisting of seven BPMs and a computational node in the centre, showing propagation delays between 34μs and 40μs.

2.5 Cross-directional Control

Web forming processes such as paper manufacturing, plastic film extrusion, metal rolling and coating can be considered as distributed parameter or two-dimensional systems [Featherstone et al., 2000]. This is because variations in web characteristics occur in two dimensions: in the direction of travel of the web (referred to as the machine direction (MD)) and in the direction perpendicular to this, the cross-direction (CD). These variations are continuous in both time and space but are measured at discrete intervals in time [Corscadden and Duncan, 2000]. The response of the array of CD actuators $\mathbf{G}(s)$, is usually modelled as the product of a matrix describing the spatial response of the actuators $\mathbf{R}$ and a scalar dynamic term $g(s)$ describing the dynamics of the actuators [Wilhelm, 1984] i.e.

$$\mathbf{G}(s) = g(s)\mathbf{R} \tag{2.27}$$

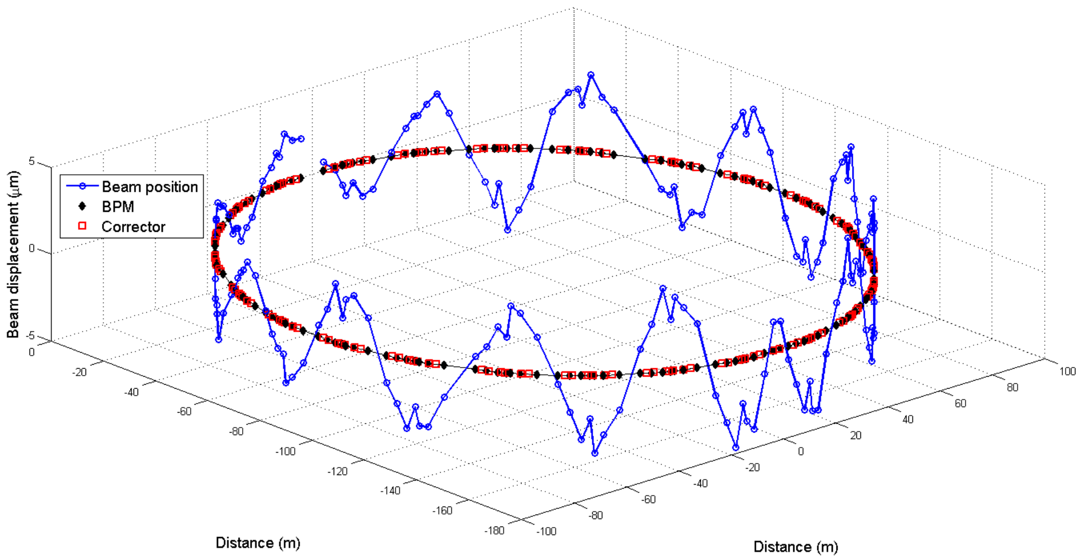

Fig. 2.20: Electron beam position ('o' blue) on storage ring measured from 172 BPMs ('◇' black) and corrected by corrector magnets ('□' red).

where it is assumed that all actuators have the same dynamics and the dynamics are independent of position. However spatial coupling exists between the CD actuator responses such that a change in the control variable of one actuator influences web parameters over some distance at both sides of the actuator and is time invariant. The dynamics can usually be modelled by a first order response plus a transport delay between the control action and its effect observed at the sensors.

Variations in the electron beam position also occur in two dimensions: in time (MD) and in space (CD). Fig. 2.20 shows the vertical beam position at a single time instant in the storage ring which is measured by BPMs. The corrector magnets, shown in Fig. 2.20 are used as actuators for electron beam control and are distributed around the ring and have the same dynamics. Furthermore there is spatial coupling between the corrector magnets. The goal of the feedback controller is to maintain the horizontal and vertical position of the electron beam to a zero orbit (i.e. zero deviation from the ideal orbit) over time. Therefore the control of the electron beam position can be considered as a cross-directional problem. In Sections 2.6 and

2.7, the models for the dynamic response ($g(s)$) and the spatial response ($\mathbf{R}$) are identified and discussed.

2.6 Dynamic Process Model

To determine the process response, a sinusoidal excitation signal of amplitude 10mA with frequencies from 10Hz to 5kHz was applied to a single corrector magnet and the measured response at a single BPM on the storage ring and booster are shown in Fig. 2.21 and Fig. 2.22 respectively. The effect of the notch filter centered at 1.6kHz is evident and may affect an accurate estimate of the open loop frequency response, in particular the cutoff frequency. The notch filters were switched off and the open loop frequency response with the notch filters and without the notch filters were measured and are shown in Fig. 2.23 for the booster. While the notch filters affect the high frequency response, the cutoff frequency is not affected when the notches are turned on and therefore the open loop is characterised with the notch filters switched on.

When a 10mA excitation signal is used, the slew rate limit is set to 1000A/s which means that the signal is not constrained. However when a 50mA excitation signal is used, the rate limit is 67.5A.s^{-1} and since the input is sinusoidal, then $67.5 = 0.05\omega$ which means that the rate limit is active at 214Hz. The measured frequency response on the booster using a 10mA excitation and a 50mA excitation are compared in Fig. 2.24 and for the 50mA excitation, the cutoff frequency at 214Hz is evident. Since typical FOFB signals are below 10mA, the results using the 10mA excitation are used to model the process using a first order approximation with a delay τ_d, given by

$$g(s) = e^{-s\tau_d}\frac{a}{s+a} \tag{2.28}$$

where a is the bandwidth of the actuator response (in rad.s^{-1}).

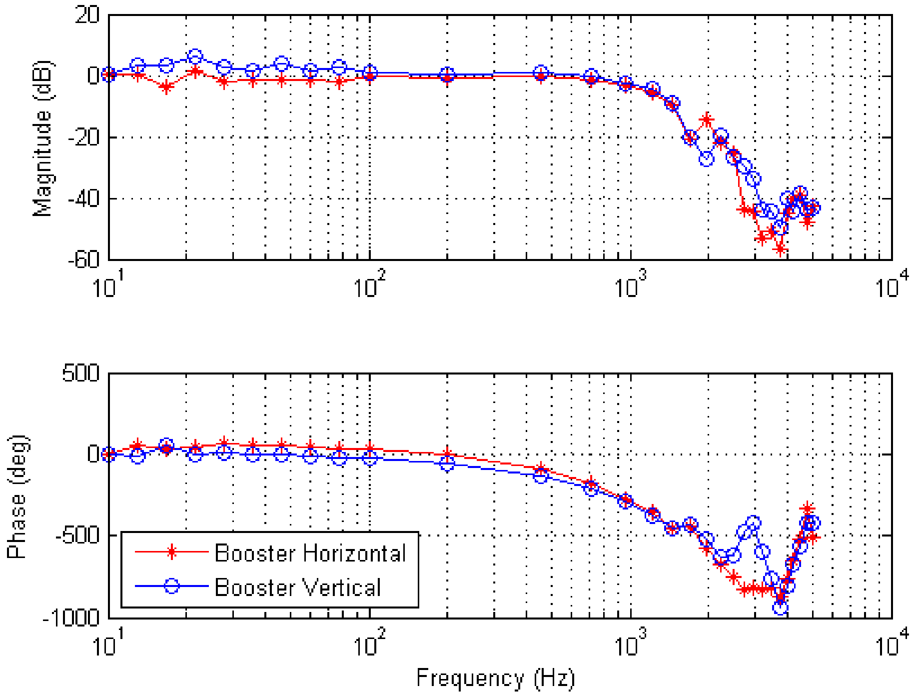

Fig. 2.21: Booster measured frequency response from sinusoid excitation of maximum amplitude 10mA for the horizontal ('$*$' red) and vertical ('o' blue) planes.

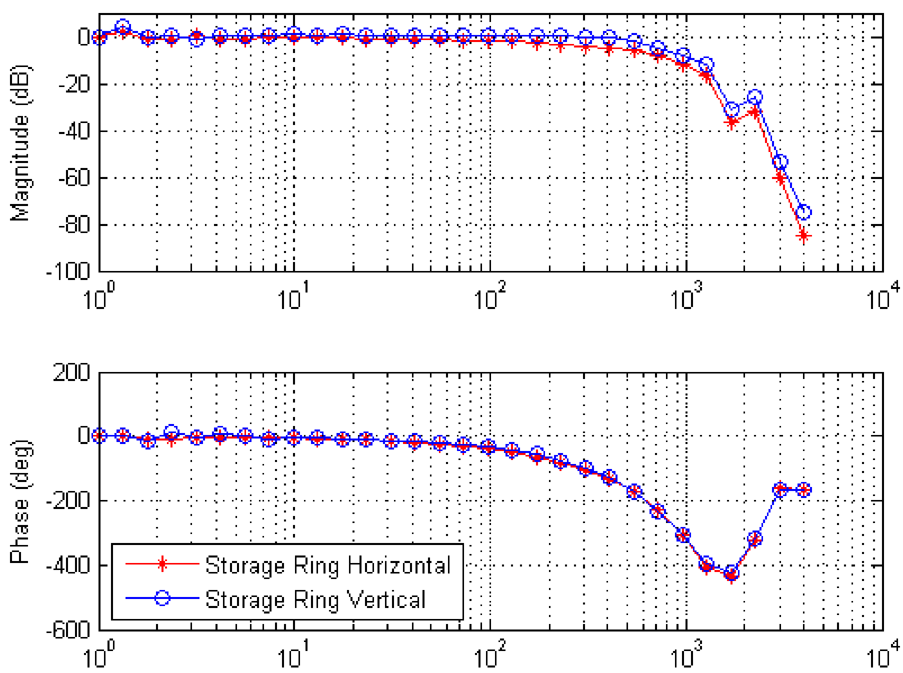

Fig. 2.22: Storage ring measured frequency response from sinusoid excitation of maximum amplitude 10mA for the horizontal ('$*$' red) and vertical ('o' blue) planes.

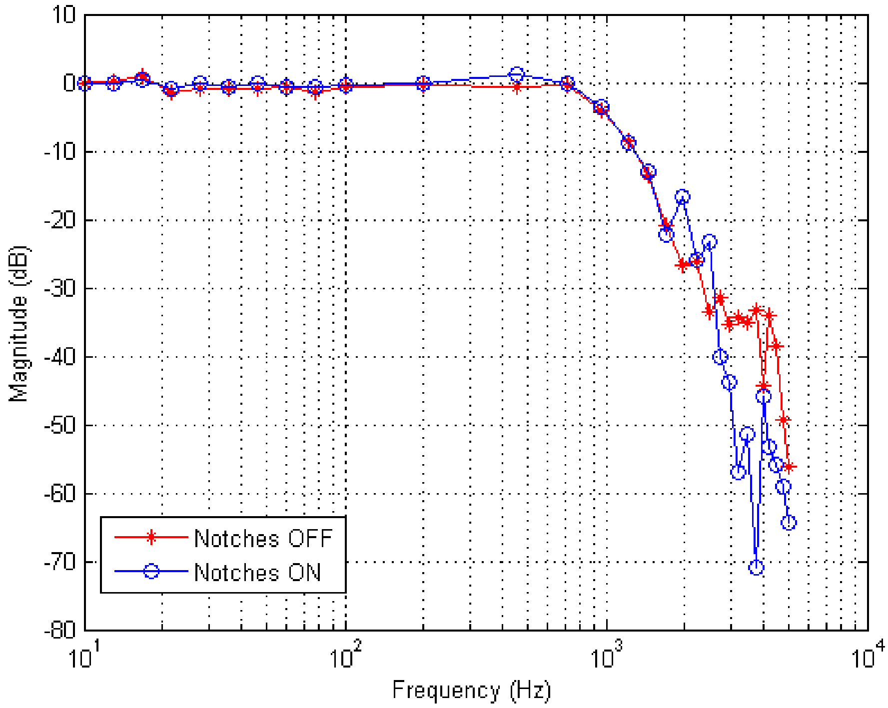

Fig. 2.23: Booster vertical magnitude frequency response with notch filters switched off ('∗' red) and with notch filters switched on ('o' blue).

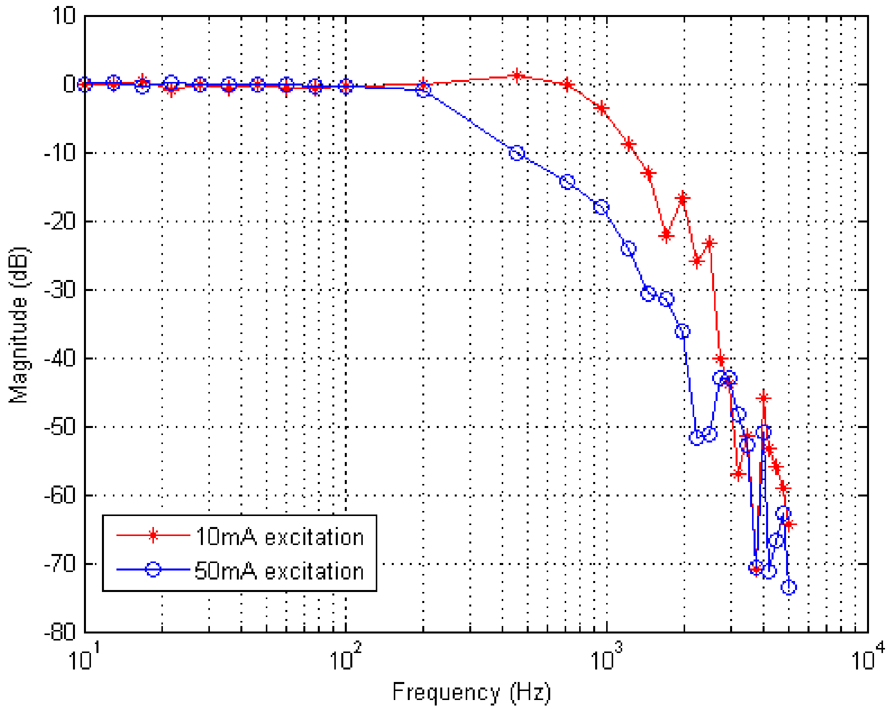

Fig. 2.24: Booster vertical frequency response with 10mA excitation signal ('∗' red) and with 50mA excitation signal ('o' blue).

	Booster		Storage Ring	
	Horizontal	Vertical	Horizontal	Vertical
a (rad.s^{-1})	$2\pi \times 1000$	$2\pi \times 1000$	$2\pi \times 700$	$2\pi \times 700$
τ_d (μs)	700	700	700	700

Table 2.6: Process parameters for the horizontal and vertical responses for the storage ring and booster.

The bandwidth, a can be estimated from the magnitude responses and the delay τ_d can be estimated from the phase responses in Fig. 2.21 and Fig. 2.22 and the parameters estimated for the model are summarised in Table 2.6. A total of approximately 500μs of the measured 700μs delay can be accounted for from each component of the system which is itemised in Table 2.7. The difference of 200μs between the measured and calculated latency comes from the power supply unit input filters and additional output filter that have been ignored in this thesis. For this reason the delay used for the process model will be taken from the measured open loop response from the machine. In Fig. 2.25 and Fig. 2.26 the measured responses are compared to the modelled responses for the booster and storage ring. These models are used in the design of the electron orbit stabilisation controller.

Source	Latency (μs)	
Group Delay FIR	148	Calculated
Simplified Power Supply Unit	200	Calculated
Control Action	50	Measured
Distribution of data around ring	50	Measured
DMA transfer to CPU	50	Measured
Total	498	

Table 2.7: Measured and calculated sources of latency in the process for the storage ring.

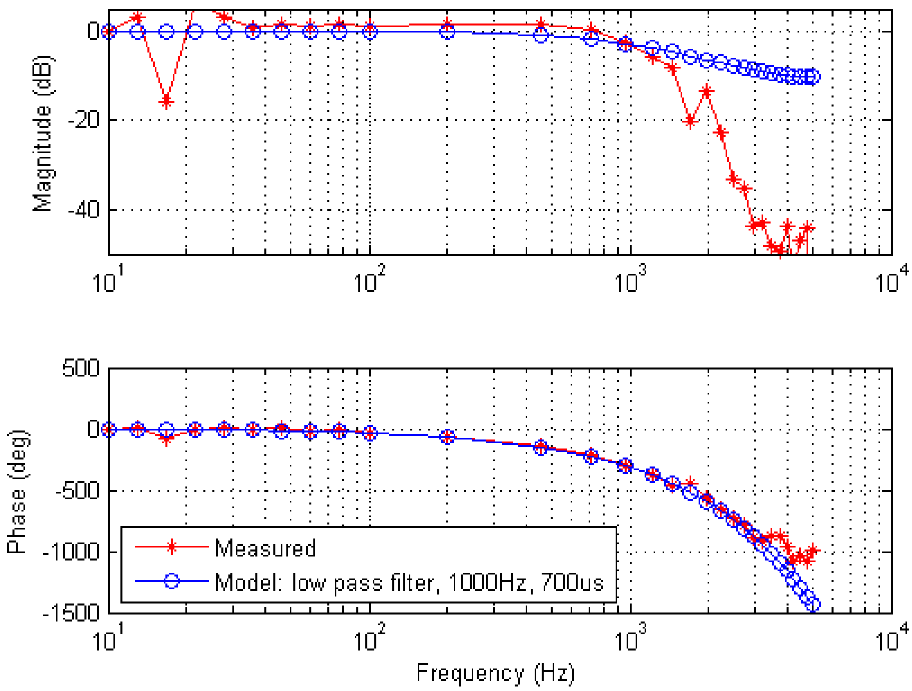

Fig. 2.25: Booster vertical measured frequency response ('∗' red) from sinusoid excitation of maximum amplitude 10mA compared to low pass filter model ('o' blue).

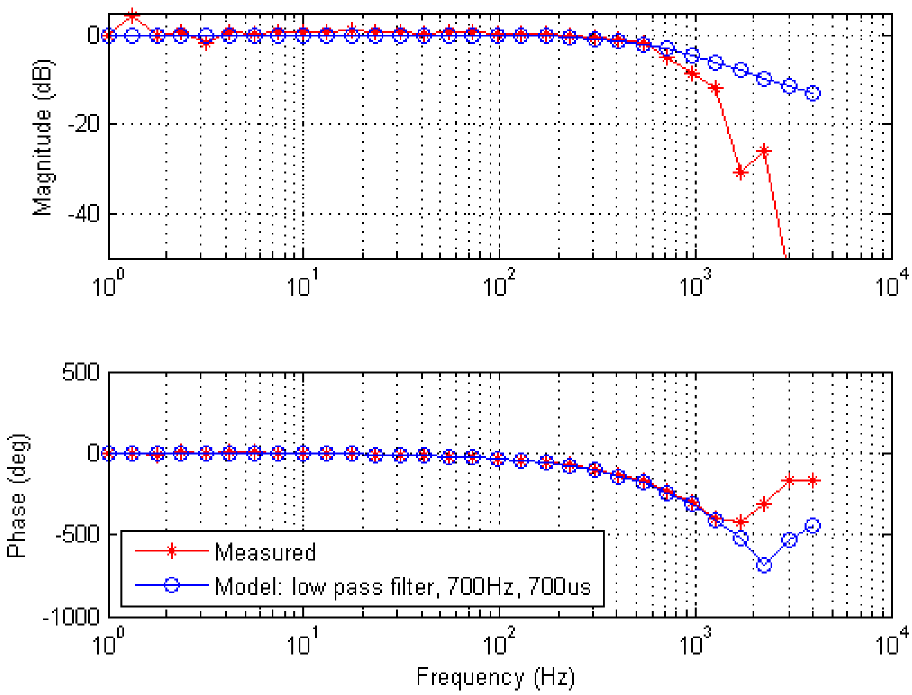

Fig. 2.26: Storage ring vertical measured frequency response ('∗' red) from sinusoid excitation of maximum amplitude 10mA compared to low pass filter model ('o' blue).

2.7 Spatial Process Model

So far, trajectories of electrons in a prescribed guided orbit have been considered and described by (2.14) which is repeated below

$$\mathcal{X}(\mathcal{Z}) = \sqrt{\mathcal{U}}\sqrt{\beta(\mathcal{Z})}\cos\left(\eta(\mathcal{Z}) + \theta_0\right) \tag{2.29}$$

Of interest is how will the trajectories be different if there are small deviations of the fields from the nominal field called field errors. Changes in the fields which cause the focussing functions $\mathcal{K}$ to differ from their nominal values will be called gradient errors. When there are field errors, the design orbit is no longer a possible trajectory. If the errors are small however, there will be another closed curve which is a possible orbit for an electron of the nominal energy. This is referred to as a disturbed closed orbit [Sands, 1970]. In passing through a field error which exists only in small interval, $\Delta\mathcal{Z}$ placed at $\mathcal{Z} = 0$, the displacement, $\mathcal{X}$ is unchanged but the slope $\mathcal{X}'$ is changed by an amount θ_c and the displacement of the disturbed closed orbit, $\mathcal{X}_c$ from the ideal one, caused by a field deviation θ_c, takes the form in (2.29) [Sands, 1970] such that

$$\mathcal{X}_c(\mathcal{Z}) = \frac{\theta_c\sqrt{\beta_0(\mathcal{Z})}}{2\sin\pi\mathcal{Q}}\sqrt{\beta(\mathcal{Z})}\cos\left(\eta(\mathcal{Z}) - \mathcal{Q}\pi\right) \tag{2.30}$$

Two interesting features of the disturbed closed orbit is that it is proportional everywhere to the strength θ_c of the field error and to $\sqrt{\beta_0(\mathcal{Z})}$, the magnitude of the betatron function at the location of the perturbation. Also, the denominator of (2.30) goes to 0 and $\mathcal{X}_c(\mathcal{Z})$ becomes large whenever the tune $\mathcal{Q}$ approaches an integer. The relationship in (2.30) can be generalised to give the closed orbit distortion for any arbitrary distribution θ_c of field errors around the ring. For an error at location $\mathcal{Z}_0$, (i.e. $\mathcal{Z} = 0$), $\eta(\mathcal{Z})$ is replaced by $\eta(\mathcal{Z}) - \eta_0(\mathcal{Z})$ in (2.30) to give

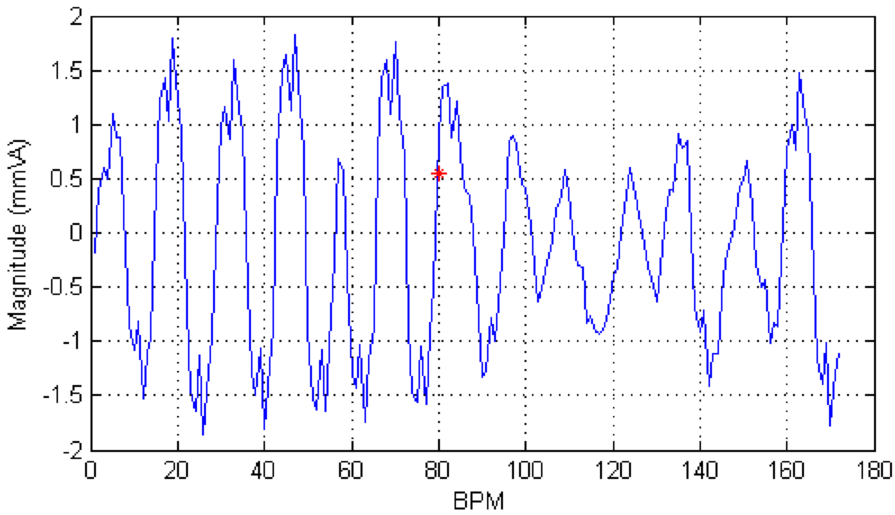

Fig. 2.27: Vertical storage ring response of the 80th corrector magnet observed at all BPMs.

$$\mathcal{X}_c(\mathcal{Z}) = \frac{\theta_c\sqrt{\beta_0(\mathcal{Z})}\sqrt{\beta(\mathcal{Z})}}{2\sin\pi\mathcal{Q}}\cos\left(\mathcal{Q}\pi - (|\eta(\mathcal{Z}) - \eta_0(\mathcal{Z})|)\right) \qquad (2.31)$$

If the deviation θ_c is known, then (2.31) will (with $\beta(\mathcal{Z})$ and $\mathcal{Q}$ taken as undisturbed values) give the form of the displaced closed orbit [Sands, 1970]. Therefore in order to map the disturbed closed orbit induced by transverse excitation at correctors located at $\mathcal{Z}_n$ and measured by BPMs at $\mathcal{Z}_m$, (2.31) may be written as

$$[\mathbf{R}]_{mn} = \frac{\sqrt{\beta_n(\mathcal{Z})}\sqrt{\beta_m(\mathcal{Z})}}{2\sin\pi\mathcal{Q}}\cos\left(\mathcal{Q}\pi - (|\eta_n(\mathcal{Z}) - \eta_m(\mathcal{Z})|)\right) \qquad (2.32)$$

where $\beta_m(\mathcal{Z})$ and $\beta_n(\mathcal{Z})$ are the magnitude of the beta functions at the BPM and corrector respectively and η_m and η_n are the phase advances at the BPM and corrector respectively and these parameters are derived from the transfer matrices for the individual elements. If a 1μrad change is made to a corrector magnet strength, the resulting response observed at all BPMs is shown in Fig. 2.27 for an arbitrary corrector magnet on the storage ring. The spatial response matrix $\mathbf{R}$, is composed of each of these responses observed for all M BPMs for perturbations made at all N corrector magnets.

If the linear optics in a ring are known then the closed orbit response matrix can be calculated from (2.32). The Linear Optics from Closed Orbits (LOCO) algorithm reverses this process; given a measured orbit response matrix the algorithm determines the actual linear optics of the ring. The optics model that best fits the measured data is determined by minimising the difference between between the measured data and the model i.e.

$$\sum_{m,n} \frac{[\mathbf{R}_{model}]_{mn} - [\mathbf{R}_{measured}]_{mn}}{\nu_m^2} \tag{2.33}$$

where ν_m is the noise level on the mth BPM [Safranek, 2007]. The standard fit parameters for LOCO are the quadrupole strengths, the BPM gains and the corrector magnet strengths and initial guesses for these parameters are required. LOCO fitting aims to solve a nonlinear least square problem with an iterative approach. A linear least square technique is applied in each iteration to move the solution toward the minimum - this approach is called the Gauss-Newton algorithm (GNA). GNA converges quickly if the initial solution is close to the minimum but in some situations an accurate initial guess is not available and the Levenberg-Marquardt non-linear least squares algorithm (LMA) [Moré, 1978] is more suitable. In such cases the GNA may fail because the solution it finds could lie outside the region where linearization of the model is valid but the LMA is a robust solver for general nonlinear least square problems and interpolates between the Gauss-Newton algorithm (GNA) (for a 'good' initial guess) and the method of gradient descent (when the guessed solution is not close enough to the minimum). Furthermore the LMA is based on the trust-region strategy i.e. the solution it finds is confined in the region where the linear model is valid.

Using LOCO, an ideal or 'golden' response matrix is formulated which is used for the design of the electron orbit controller and these ideal response matrices for the horizontal and vertical planes for the storage ring and booster are shown in

Fig. 2.28a, Fig. 2.28b, Fig. 2.29a and Fig. 2.29b respectively.

2.8 Conclusion

In this chapter, linear beam optics and models of the various components of synchrotrons were presented and used to build a process model of the system under consideration. The process model is decoupled into a dynamic component and spatial component and in Chapter 3, the structure and properties of both the dynamic and spatial models are used to define the control problem specifications.

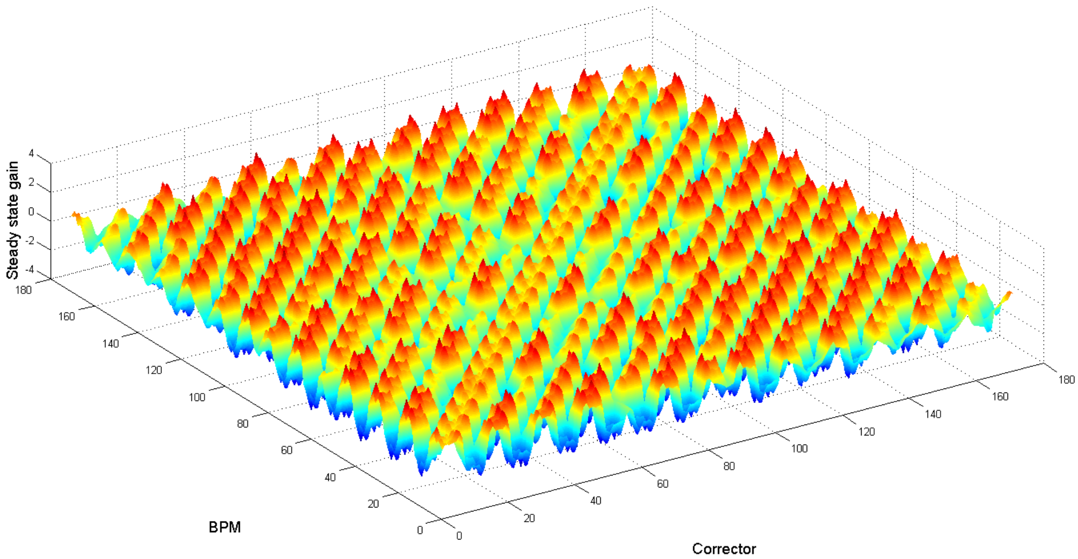

(a) Horizontal

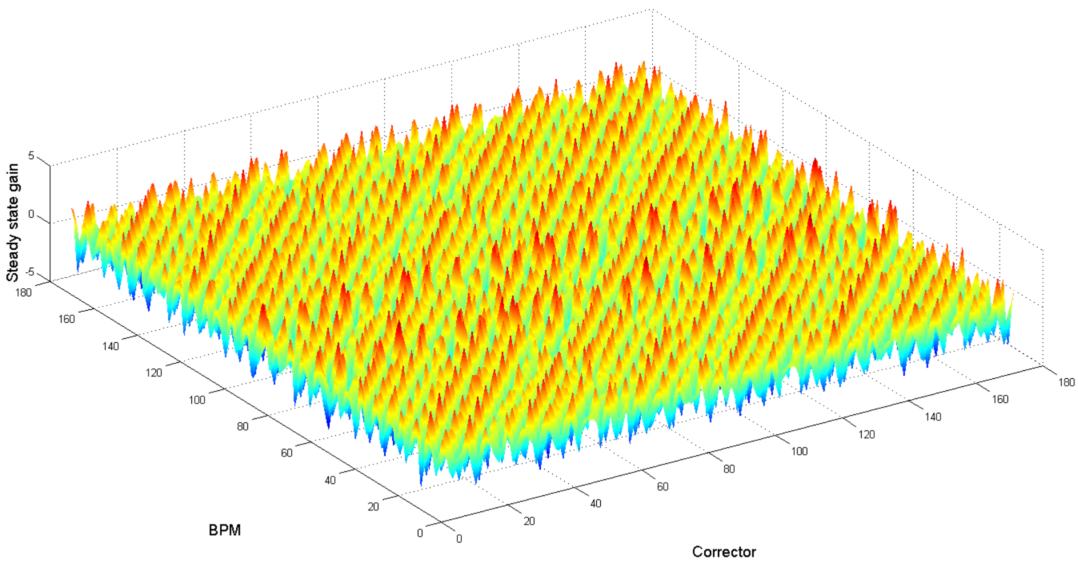

(b) Vertical

Fig. 2.28: Storage ring ideal response matrices.

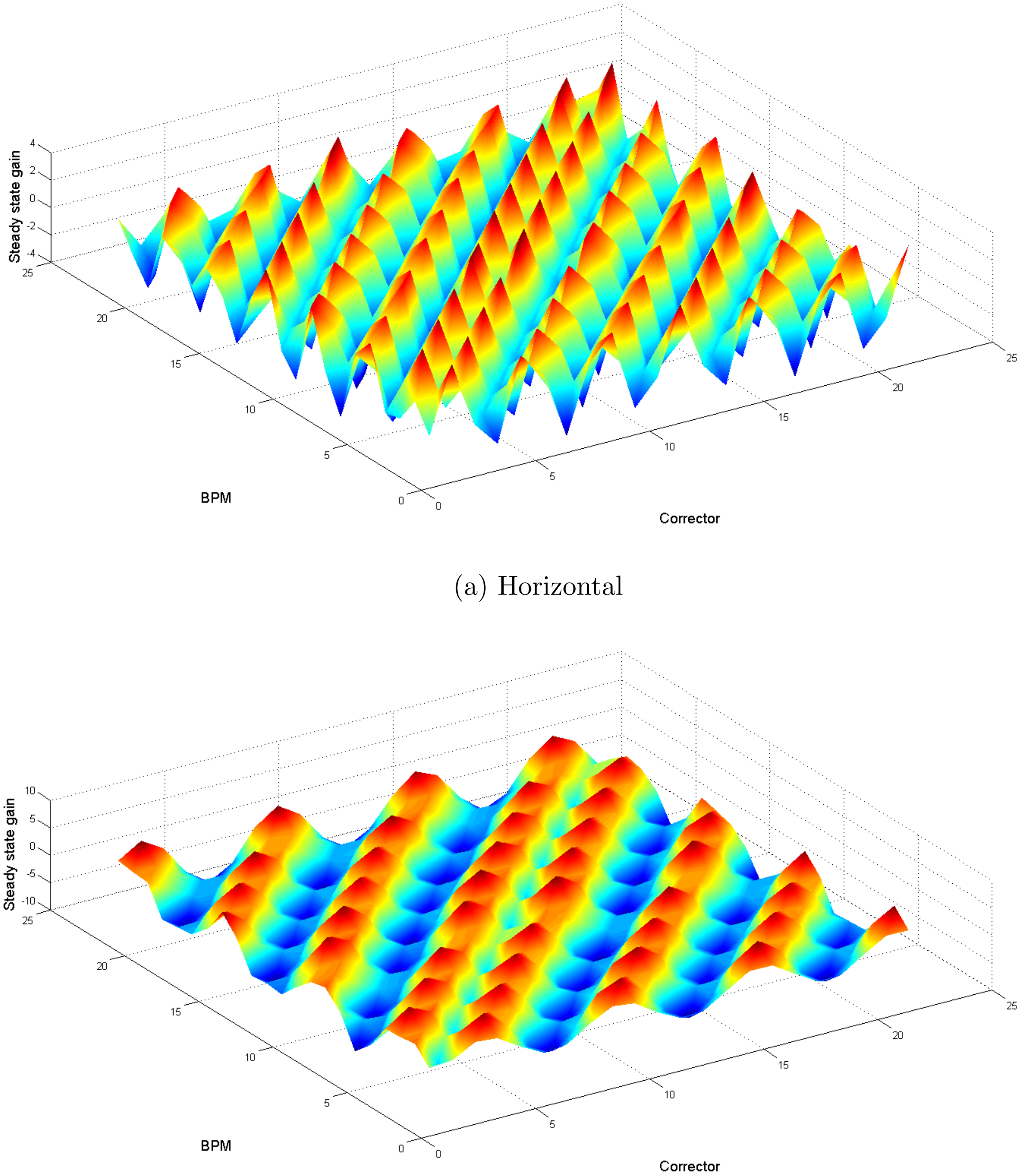

(a) Horizontal

(b) Vertical

Fig. 2.29: Booster ideal response matrices.

Chapter 3

Problem Specifications

3.1 Electron Beam Stability

At any instant a particle may be displaced horizontally by $\mathcal{X}$ and vertically by $\mathcal{Y}$ from the ideal position and may also have divergence angles horizontally $\mathcal{X}'$ and vertically $\mathcal{Y}'$ with respect to the orbit i.e. an angle between the tangent to the electron trajectory and the tangent to the ideal orbit. The turn by turn positions and angles of particle motion (from repeated rotations) lie on an ellipse shown in Fig. 3.1. The emittance is the phase space area occupied by an ensemble of particles and the transverse coordinates represent the size and the divergence of the beam (in RMS units) either in the horizontal or vertical directions.

Positional and angular stability of the electron beam at the source point of synchrotron light sources has been shown to be paramount to the preservation of low emittance generally found in third generation light sources [Rehm, 2013]. Although the position of the electron beam in the storage ring is maintained by the magnetic fields within the ring, the beam is subjected to disturbances from environmental effects that are coupled through the girders that support the magnets. There are also disturbances from the insertion devices that change the magnetic field as part of

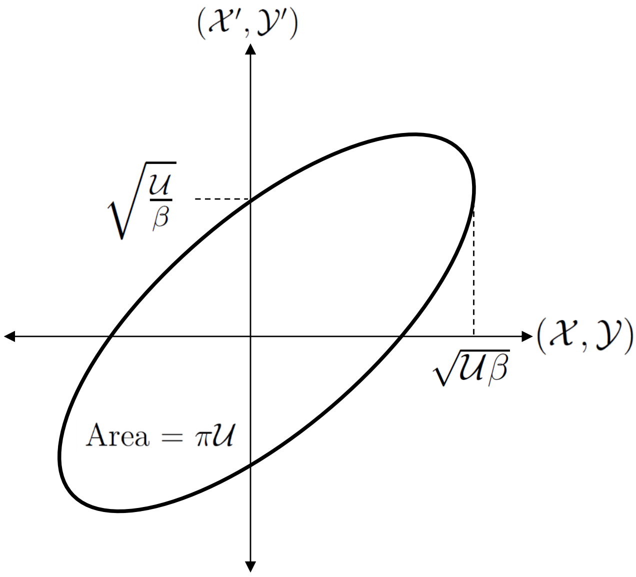

Fig. 3.1: Phase space ellipse of particle motion (decoupled case) where the axes represent either the horizontal or vertical motion.

a beamline experiment. Movement of the photon beam centroid may either 'smear out' the effective emittance, which has a deteriorating effect on the photon beam quality and/or lead to an increase in measurement noise [Steinhagen, 2007]. In order to minimise the effective emittance of the photon beam, a FOFB controller is used to control the location of the electron beam and to minimise any instability of the electron beam which may propagate into the photon beam. The accepted standard for electron beam orbit stability is to maintain the RMS variation of the electron beam position and angle to within 10% of the RMS beam size and divergence.

The relevant electron beam parameters at the source point of most current light sources provide vertical beam sizes which are now typically in the order of around 5μm. This is mainly the result of a general trend to lower the horizontal emittance, with the most recently built light sources now operating at around 1nm.rad. For Diamond, 10% beam stability corresponds to RMS variations listed in Table 3.1. But existing light sources are improving methods of reducing the emittance such that the vertical emittance values are as low as $1-2$pm.rad and can lead to vertical

Parameter	Motion(RMS)
$\Delta\mathcal{X}$	<12.3 μm
$\Delta\mathcal{Y}$	<0.6 μm
$\Delta\mathcal{X}'$	<2.4 μrad
$\Delta\mathcal{Y}'$	<0.4 μrad

Table 3.1: Accepted stability for beam size ($\Delta\mathcal{X}$,$\Delta\mathcal{Y}$) and angular divergence ($\Delta\mathcal{X}'$,$\Delta\mathcal{Y}'$)

beam sizes of just a few microns. On the other hand, horizontal beam sizes will remain one or two orders of magnitude larger than vertical beam sizes until the first of a new class of ultimate storage rings will be realised [Rehm, 2013]. As a result, even with the generally accepted target of keeping the RMS variation of electron beam position and pointing angle to 10% of RMS beam size and divergence, sub-micron stability is required for stabilisation in the vertical plane. The requirements for the horizontal plane are more relaxed and are thus easily met as a consequence of the efforts going into stabilisation of the vertical beam position and pointing angle. Table 3.2 lists some major existing facilities in order of increasing emittance. The PETRAIII facility is currently the brightest light source (lowest emittance), but the European Synchrotron Radiation Facility (ESRF) is undergoing an upgrade (indicated as ESRF-U) to achieve lower emittance of the beam. The new NSLSII ring which is scheduled to come into operation in 2015, will also achieve an emittance of less than 1nm.rad. From Table 3.2, it can be seen that the two rings without orbit feedback control (ALBA and ASLS) have significantly larger emittances than the machines utilising feedback control.

The typical figure of merit for FOFB performance is integrated beam motion given by

$$y_{IBM} = \sqrt{\sum_{f=0}^{F} \frac{2}{F^2} |\hat{y}_m[f]|^2} \tag{3.1}$$

where $\hat{y}_m[f]$ is the discrete Fourier transform of the time series positional data from

Facility	Year	FOFB	Energy	Cir.	Beam Current	$\mathcal{U}_\mathcal{X}$ $\mathcal{U}_\mathcal{Y}$	$\mathcal{S}_\mathcal{X}$ $\mathcal{S}_\mathcal{Y}$
			(GeV)	(m)	(mA)	(nm.rad)	(μm)
ESRF-U	2015	YES	6	844	200	0.2	24
						0.003	3.3
NSLS II	2015	YES	3	792	500	0.5	29.6
						0.008	3.1
Petra III	2009	YES	6	2304	100	1	141.5
						0.010	4.9
DLS-U	2018	YES	3	561.6	300	0.276	unknown
						0.008	unknown
DLS	2007	YES	3	561.6	300	2.75	123
						0.027	6.4
SLS	2001	YES	2.4	288	400	5.5	141.5
						0.003	4.9
Soleil	2007	YES	2.75	354	500	3.9	182
						0.039	8.1
ALBA	2010	NO	3	268.8	400	4.5	132
						0.033	5.2
ASLS	2007	NO	3	216	200	103	321
						0.120	17

Table 3.2: Comparison of synchrotron facilities listed in order of increasing emittance. The year of start of operation, whether Fast Orbit Feedback (FOFB) control is used, the nominal energy of the storage ring, the circumference of the storage ring, the nominal beam current, the horizontal and vertical emittances and beam sizes are listed. The facilities included are the upgraded European Synchrotron Radiation Facility (ESRF-U), France; the National Synchrotron Light Source (NSLSII), New York; PETRAIII, Germany; Diamond Light Source (DLS) and upgrade (DLS-U), UK; Swiss Light Source (SLS), Switzerland; Soleil, France; ALBA, Spain; Australian Synchrotron Light Source (ASLS), Australia.

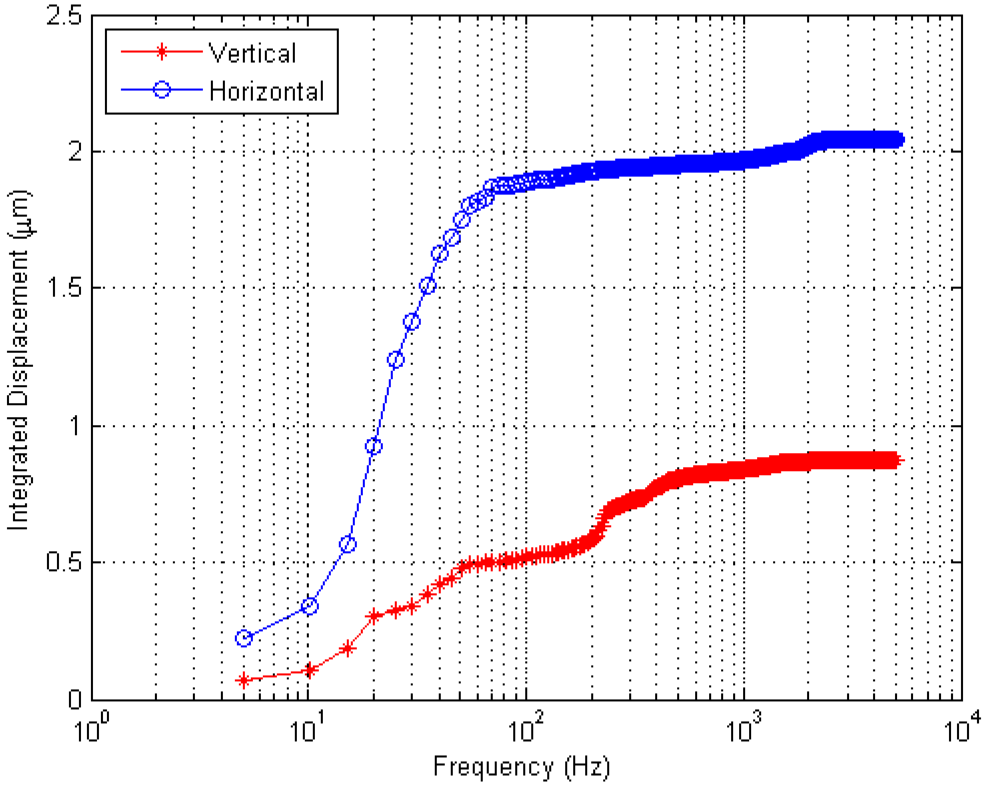

Fig. 3.2: Storage ring vertical ('$*$' red) and horizontal ('o' blue) integrated beam motion for an electron beam size of 123μm horizontally and 6.4μm vertically.

the mth BPM and F is the number of Fourier samples used. In Fig. 3.2, the integrated beam motion when there is no orbit control is shown for the horizontal and vertical movements. Up to 300Hz, the vertical integrated beam motion is about 0.7μm resulting in the RMS motion over the specification at 11%.

3.2 Two Dimensional Frequency Domain Process Model

The class of problems under consideration is modelled by linear dynamical systems distributed in a spatial dimension as described in Chapter 2 and discretised both dynamically and spatially. The control is effected through an array of identical corrector magnets and the process output is measured in the spatial domain at a number of discrete locations which, for the Diamond accelerators, are not evenly spaced. However the spacing of the corrector magnets and sensors within a single cell of the ring is repeated for all 24 cells that create the closed ring. Each location is assumed to be measured by an identical sensor.

The process response is further assumed to be invariant to shifts in space and time and the spatially invariant properties of the process are exploited in the work presented in this thesis. Analogous to time invariance in dynamical systems, the property of spatial invariance allows the design problem to be spatially decoupled. In particular, the spatial invariance allows the large-scale multivariable design problem to be decomposed into a family of independent SISO design problems, one for each spatial frequency or spatial mode [Bamieh et al., 2002, Hovd et al., 1997, Stewart et al., 2003], which simplifies the computational complexity of the controller synthesis.

The use of the two-dimensional frequency domain can be utilised at the specification stage where familiar concepts, such as loop shaping are presented in the two-dimensional frequency domain. For example, in dynamical systems the performance requirements are typically imposed at low temporal frequencies and robustness requirements are applied at high temporal frequencies [Stewart et al., 2003]. Similarly, for the broad class of two-dimensional systems it is found that high performance may be achieved at low spatial and temporal frequencies, while robustness requirements must be imposed at high spatial and temporal frequencies [Duncan and Bryant, 1997, Heath, 1996, Heath and Wills, 2004, Stewart et al., 2003].

In practice, the control system is implemented in 'sample and hold' mode where the sensor takes M beam position measurements $\mathbf{y}[k] \in \mathbb{R}^M$ at times $\{t = kT_s : k \in \mathbb{Z}^+\}$, with T_s being the sample interval so that $\mathbf{y}[k] = \mathbf{y}(kT_s)$ and the N actuator inputs, $\mathbf{u}[k] \in \mathbb{R}^N$, which are held constant over the time interval $t \in [kT_s, (k+1)T_s]$. The actuator dynamics, the process and the sensor spatial and dynamical responses will all be described by the linear transfer matrix model,

$$\mathbf{y}[k] = \mathbf{G}(z^{-1})\mathbf{u}[k] + \mathbf{h}[k] \tag{3.2}$$

where $\mathbf{h}[k] \in \mathbb{R}^M$ is the disturbance acting on the electron beam and $\mathbf{G}(z^{-1}) \in \mathbb{C}^{M\times N}$ is the process transfer matrix containing both the dynamical and spatial responses of the BPM array to the actuator array and can be factored into

$$\mathbf{G}(z^{-1}) = g(z^{-1})\mathbf{R} \tag{3.3}$$

where the response matrix $\mathbf{R} \in \mathbb{R}^{M\times N}$ is the steady state response of the actuators derived by (2.32) in Chapter 2 and $g(z^{-1})$ is the scalar dynamics and the starting assumption is that $g(z^{-1})$ is the same for all actuators since the same corrector magnets and power supplies are used around the ring. The dynamic response $g(z^{-1})$ is associated with the continuous function $g(s)$ in (2.28) derived in Chapter 2 and is given by

$$g(z^{-1}) = z^{-d}\frac{b_0 + b_1 z^{-1}}{1 - a_1 z^{-1}} \tag{3.4}$$

where d is the smallest integer satisfying $dT_s \geq \tau_d$ [Duncan, 2007] and

$$\begin{aligned} a_1 &= e^{-aT_s} \\ b_0 &= 1 - e^{-a(T_s-\tau^{'})} \\ b_1 &= e^{-a(T_s-\tau^{'})} - e^{-aT_s} \\ \tau^{'} &= \tau_d - (d-1)T_s \end{aligned} \tag{3.5}$$

and the sample time is given as $T_s = 100\mu$s.

3.3 Modal Decomposition

From (3.2) and (3.3), an open loop response in discrete time can be expressed as

$$\mathbf{y}[k] = g(z^{-1})\mathbf{R}\mathbf{u}[k] + \mathbf{h}[k] \tag{3.6}$$

The profile $\mathbf{y}[k]$ and response matrix $\mathbf{R}$ can be expressed in terms of some general orthonormal basis functions [Duncan et al., 1996]. A common orthonormal basis is derived from the Singular Value Decomposition (SVD) of the static response matrix, $\mathbf{R} \in \mathbb{R}^{M\times N}$, where $M \leq N$, decomposed as

$$\mathbf{R} = \mathbf{\Phi}\left[\mathbf{\Sigma}\;\; \mathbf{0}\right]\mathbf{\Psi}^{\mathrm{T}} \tag{3.7}$$

where $\mathbf{\Phi} \in \mathbb{R}^{M\times M}$ and $\mathbf{\Psi} \in \mathbb{R}^{N\times N}$ are respectively the left and right singular vectors and $\mathbf{\Sigma} \in \mathbb{R}^{M\times M}$ is a diagonal matrix containing the singular values, $\sigma_1 \geq \sigma_2 \geq \cdots \geq \sigma_M$. Additionally, the matrices $\mathbf{\Phi}$ and $\mathbf{\Psi}$ are orthogonal.

By partitioning $\mathbf{\Psi}$ as $[\mathbf{\Psi}_1\;\; \mathbf{\Psi}_2]$ where $\mathbf{\Psi}_1 \in \mathbb{R}^{N\times M}$ and $\mathbf{\Psi}_2 \in \mathbb{R}^{N\times(N-M)}$, the response matrix may be expressed as

$$\mathbf{R} = \mathbf{\Phi}\mathbf{\Sigma}\mathbf{\Psi}_1^{\mathrm{T}} \tag{3.8}$$

Alternately, for $N \leq M$,

$$\mathbf{R} = \mathbf{\Phi}_1\mathbf{\Sigma}\mathbf{\Psi}^{\mathrm{T}} \tag{3.9}$$

where $\mathbf{\Phi}$ is expressed as $[\mathbf{\Phi}_1\;\; \mathbf{\Phi}_2]$ where $\mathbf{\Phi}_1 \in \mathbb{R}^{M\times N}$ and $\mathbf{\Phi}_2 \in \mathbb{R}^{M\times(N-M)}$. For this thesis, the more common case at Diamond, $M \leq N$ is considered. Using the SVD decomposition, the open loop response in (3.6) can be written as

$$\mathbf{\Phi}^{\mathrm{T}}\mathbf{y}[k] = g(z^{-1})\mathbf{\Sigma}\mathbf{\Psi}_1^{\mathrm{T}}\mathbf{u}[k] + \mathbf{\Phi}^{\mathrm{T}}\mathbf{h}[k] \tag{3.10}$$

Defining

$$\begin{aligned}\bar{\mathbf{y}}[k] &= \mathbf{\Phi}^{\mathrm{T}}\mathbf{y}[k] \\ \bar{\mathbf{u}}[k] &= \mathbf{\Psi}_1^{\mathrm{T}}\mathbf{u}[k] \\ \bar{\mathbf{h}}[k] &= \mathbf{\Phi}^{\mathrm{T}}\mathbf{h}[k]\end{aligned} \tag{3.11}$$

projects the response into 'modal space', so that

$$\bar{y}_m[k] = g(z^{-1})\sigma_m \bar{u}_m[k] + \bar{h}_m[k] \tag{3.12}$$

where $\bar{y}_m[k]$, $\bar{u}_m[k]$ and $\bar{h}_m[k]$ are the mth elements of $\bar{\mathbf{y}}[k]$, $\bar{\mathbf{u}}[k]$ and $\bar{\mathbf{h}}[k]$. With this representation, $\mathbf{y}[k]$, $\mathbf{u}[k]$ and $\mathbf{h}[k]$ are written in terms of basis functions which are the columns of either $\mathbf{\Phi}$ or $\mathbf{\Psi}_1$ which are ordered according to the magnitude of the singular values and are classified as low or high frequency modes, using the terminology common in cross-directional control problems. This representation has two implications:

1. Each spatial mode (or spectral component) associated with a singular value can be controlled independently.

2. The high order spectral components or modes associated with $\sigma_m = 0$ are completely uncontrollable. This means that only low order modes are required for control, leading to considerable computational savings.

3. All low spectral components are controllable if and only if the space spanned by $\mathbf{\Sigma\Psi}^{\mathrm{T}}$ has dimension M. The dimension of the space spanned by $\mathbf{\Sigma\Psi}^{\mathrm{T}}$ is closely related to the number of actuators, so that the minimum number of actuators required to have the possibility to control all low spectral components can be determined Heath [1996].

The majority of synchrotron storage ring response matrices are ill-conditioned resulting from oversampling or inappropriate placement of sensors [Boge et al., 1999, Plouvier et al., 2013, Tian and Hua, 2011]. In other words, the condition numbers

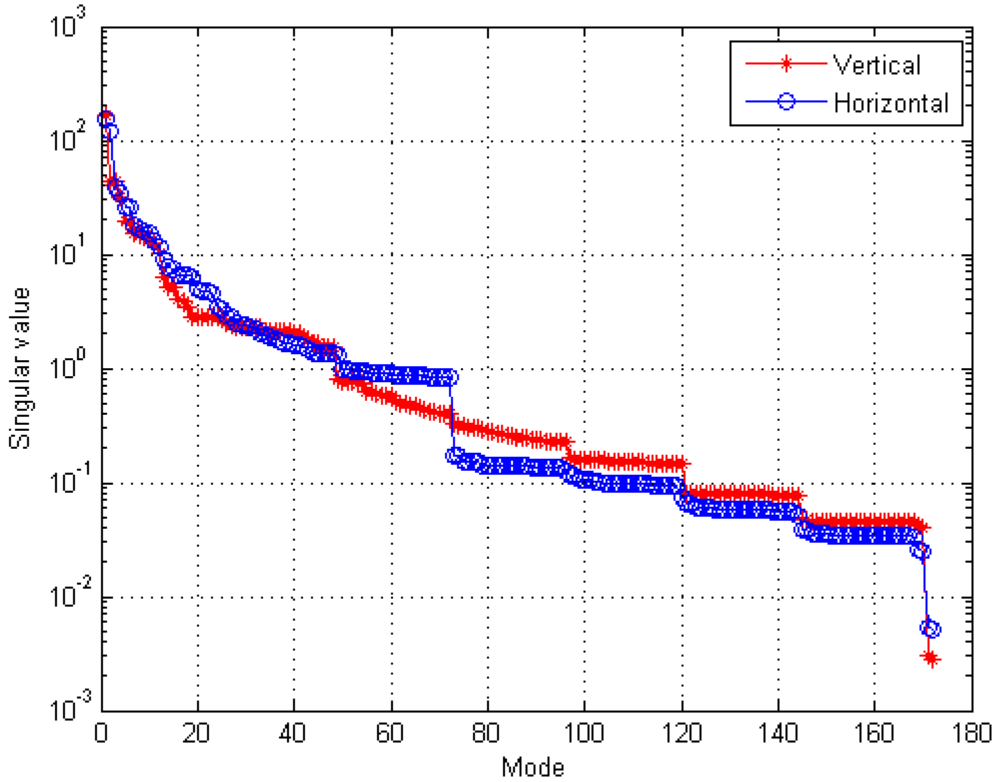

Fig. 3.3: Vertical ('$*$' red) and horizontal ('o' blue) storage ring singular values.

of the response matrices are large e.g. for the Diamond storage ring, the condition numbers are > 20000. From Fig. 3.3, in which the horizontal and vertical singular values for the storage ring are plotted, it is evident that the controller needs to provide larger control actions to remove disturbances that are aligned with the weakly controllable directions (i.e. low-gain directions). For this reason, ill-conditioned multivariable plants are considered to be difficult to control and are sensitive to modelling errors [Skogestad and Postlethwaite, 2005, Skogestad et al., 1988]. Full control requires the performance specifications to be satisfied for all directions of the closed loop process, leading to a controller applying a large control signal in the low-gain directions of the plant which can lead to actuator saturation. Additionally, it has been shown that the use of full control for ill-conditioned processes is especially vulnerable to stability problems caused by model uncertainty [Duncan and Bryant, 1997, Heath, 1996, Skogestad and Postlethwaite, 2005]. The combination of the

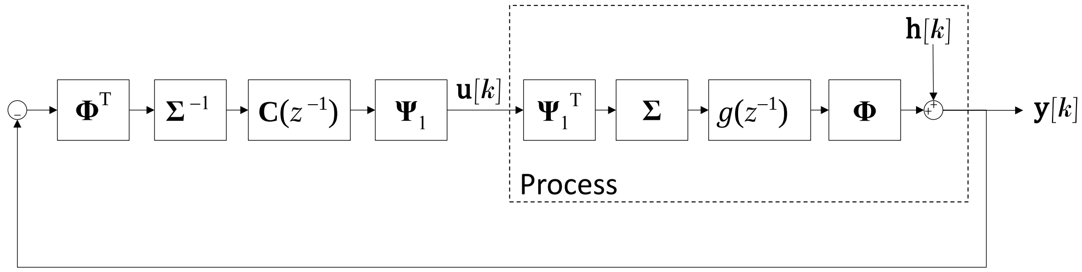

Fig. 3.4: Structure of controller in modal form.

large controller gain with a small plant gain reduces the tolerance of the closed loop system to model uncertainty [Stewart, 2000]. On the other hand, partial control means that the closed loop system satisfies performance specifications for a subset of the spatial modes, where the goal is to be aggressive in the low order modes (i.e. well-controllable directions) of the process, and conservative at the high order mode (i.e. weakly-controllable directions). Modal truncation strategies are a partial control scheme in which the controller is designed to act only on a limited number of modes of the process [Heath and Wills, 2004, Stewart, 2000], whereas another partial control approach is achieved by tuning the controller gain, such that it is low, but not zero, in the high order modes of the process. One method for detuning the controller in this way is described in Chapter 4 and the performance of this approach is compared to a modal truncation method.

In modal form the controller can be considered to belong to a class of controllers that have the form

$$\mathbf{\Phi}^{\mathrm{T}}\mathbf{\Sigma}^{-1}\mathbf{C}(z^{-1})\mathbf{\Psi}_1 \tag{3.13}$$

where $\mathbf{C}(z^{-1}) = \mathrm{diag}\{c_m(z^{-1})\}$ and $c_m(z^{-1})$ is a scalar transfer function describing the controller dynamics applied to each actuator. For electron orbit control, it is required to control the beam position to a zero orbit (or zero reference), so that the structure of the controller takes the form shown in Fig. 3.4. The plant input is

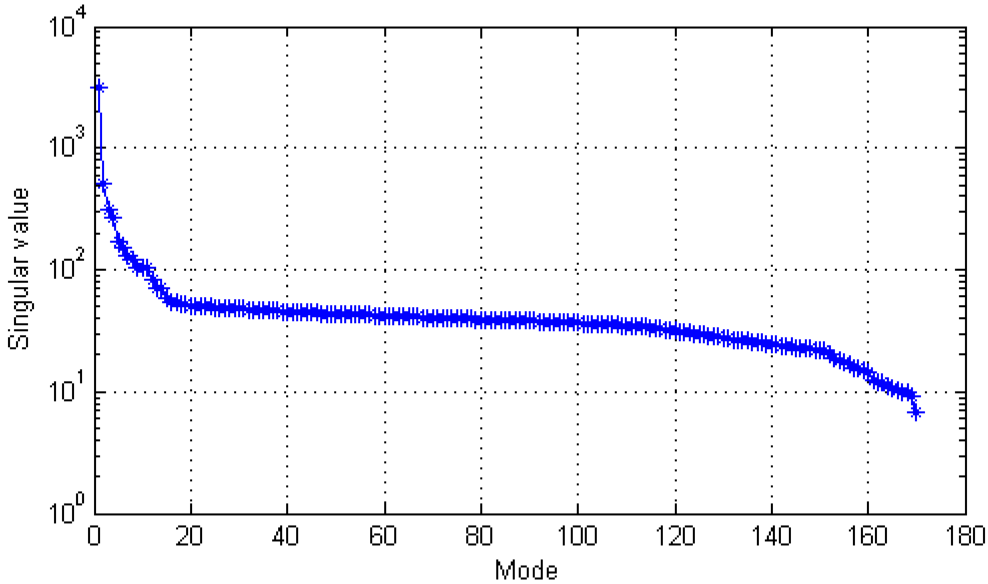

Fig. 3.5: Singular values of measured vertical position on the storage ring.

defined by

$$\mathbf{u}[k] = -\mathbf{\Psi}_1 \mathbf{\Sigma}^{-1} \mathbf{C}(z^{-1}) \mathbf{\Phi}^{\mathrm{T}} \mathbf{y}[k] \tag{3.14}$$

which can be represented in modal form,

$$\bar{\mathbf{u}}[k] = -\mathbf{\Sigma}^{-1} \mathbf{C}(z^{-1}) \bar{\mathbf{y}}[k] \tag{3.15}$$

and the output in mode space is given by

$$\bar{\mathbf{y}}[k] = \left[\mathbf{I} + \mathbf{C}(z^{-1}) g(z^{-1})\right]^{-1} \bar{\mathbf{h}}[k] \tag{3.16}$$

The sensitivity function, $\mathbf{S}(z^{-1})$ is the transfer function from the disturbance $\mathbf{h}[k]$ and the output $\mathbf{y}[k]$ described by (3.16) and because $\mathbf{C}(z^{-1})$ is diagonal, $\bar{y}_m[k] = s_m(z^{-1})\bar{h}_m[k]$ so that the sensitivity can be designed on a 'mode-by-mode' basis.

3.3.1 Signal and noise separation

Modal decomposition can also be used in analysing the contributions from *process* noise (or *orbit* noise) and *sensor* noise in the measured response, such that the output signal measured at M BPMs and over K_e samples can be represented as

$$\mathbf{Y} = \begin{bmatrix} y_{m=1}[1] & y_{m=1}[2] & \cdots & y_{m=1}[K_e] \\ y_{m=2}[1] & y_{m=2}[2] & \cdots & y_{m=2}[K_e] \\ \vdots & \vdots & \vdots & \\ y_{m=M}[1] & y_{m=M}[2] & \cdots & y_{m=M}[K_e] \end{bmatrix} \tag{3.17}$$

such that

$$\mathbf{Y} = \mathbf{\Phi}_y \mathbf{\Sigma}_y \mathbf{\Psi}_y^{\mathrm{T}} \tag{3.18}$$

The singular values, $\mathbf{\Sigma}_y$ are plotted in Fig. 3.5, which shows that the first 20 modes are the most significant and therefore a reasonable assumption is to define $\mathbf{\Sigma}_{orbit}$ as the first 20 modes and $\mathbf{\Sigma}_{bpm}$ as the remaining higher order modes, so that

$$\begin{aligned} \mathbf{y}[k] &= \mathbf{y}_{orbit}[k] + \mathbf{y}_{bpm}[k] \\ &= \begin{bmatrix} \mathbf{\Phi}_{orbit} & \mathbf{\Phi}_{bpm} \end{bmatrix} \begin{bmatrix} \mathbf{\Sigma}_{orbit} & \\ & \mathbf{\Sigma}_{bpm} \end{bmatrix} \begin{bmatrix} \mathbf{\Psi}_{orbit}^{\mathrm{T}} \\ \mathbf{\Psi}_{bpm}^{\mathrm{T}} \end{bmatrix} \end{aligned} \tag{3.19}$$

It is insightful to consider the frequency response of a single mode of $\mathbf{\Psi}_{orbit}$ and $\mathbf{\Psi}_{bpm}$ over all K_e samples, which are shown in Fig. 3.6. The frequency response associated with $\mathbf{\Psi}_{bpm}$ is identical to the measured response of the BPM when there is no beam in the vacuum chamber, which indicates that the higher order modes (>20) correspond to BPM noise rather than orbit disturbances. Furthermore given (3.19), the standard deviation at each BPM of $\mathbf{y}_{orbit}[k]$ and $\mathbf{y}_{bpm}[k]$ can be compared to $\mathbf{y}[k]$ and is shown in Fig. 3.7. There is a small contribution to the entire measured beam motion from the higher order modes. This means that only a small number

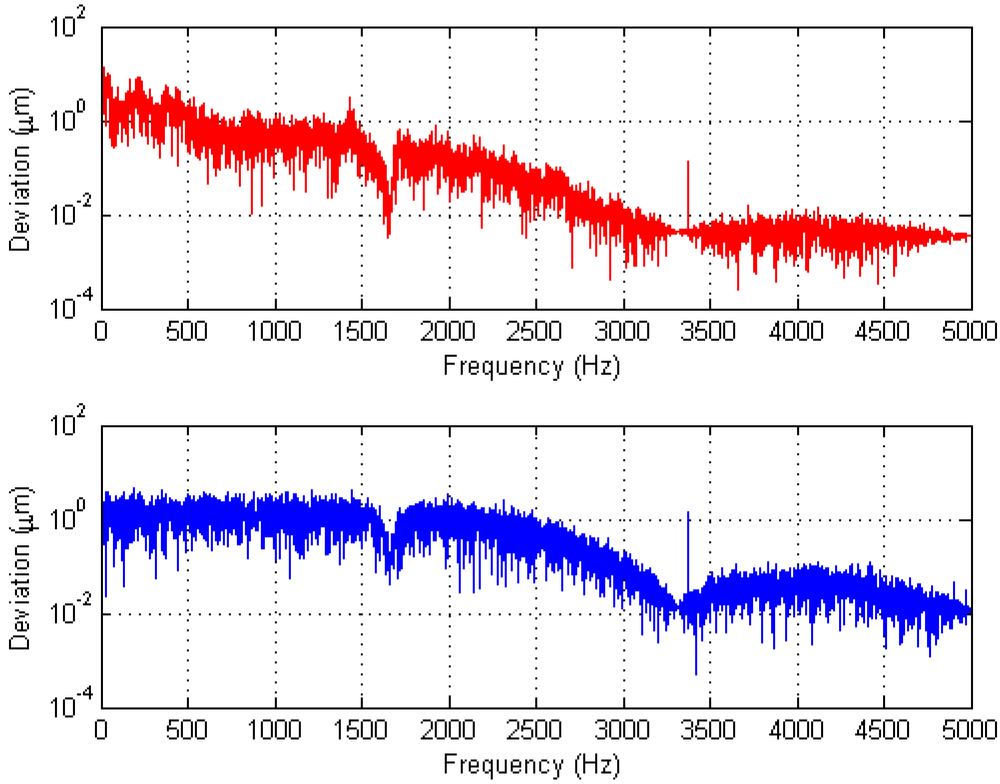

Fig. 3.6: Frequency response of a single mode of $\mathbf{\Psi}_{orbit}$ and $\mathbf{\Psi}_{bpm}$ for $K_e = 100000$ samples.

of modes relate to real process noise and the size of control problem can be reduced by selecting only the low order modes of $\mathbf{y}[k]$ for control.

3.4 Related applications

3.4.1 Web Processes

There are a number of industrial web processes that are similar to this application which include paper-making, metal rolling and plastic film extrusion. In each case the variations in sheet properties are controlled by an array of actuators. In these web processes though, the responses of the actuators near the edges of the sheet are not identical to the central actuator's response. Instead the actuators near

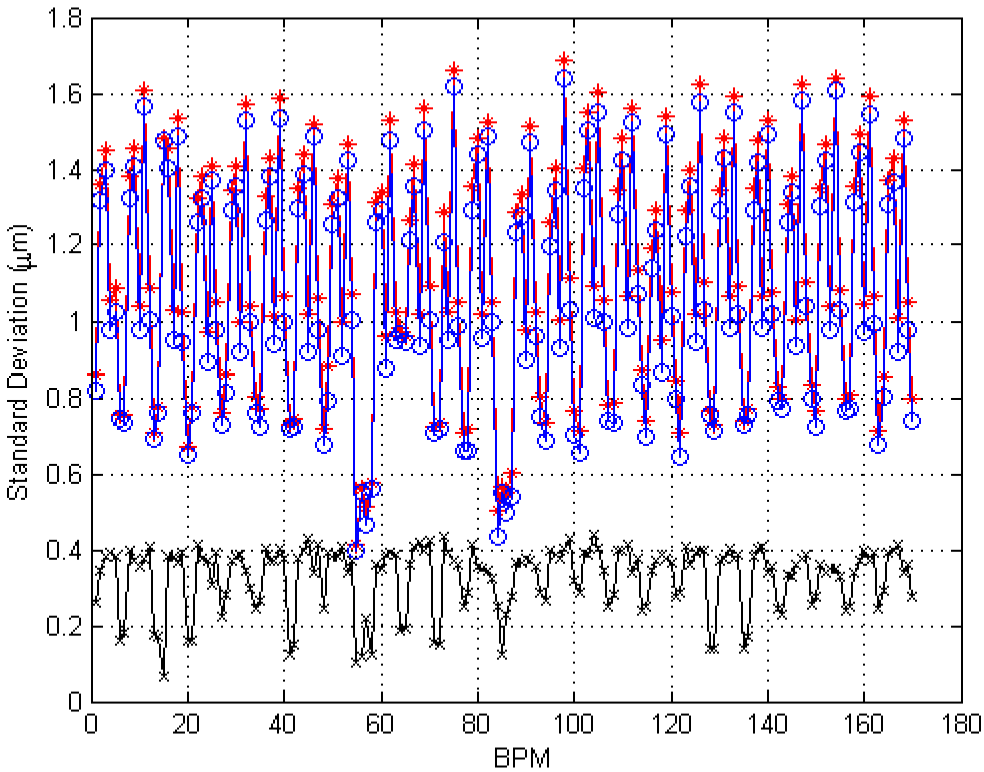

Fig. 3.7: Standard deviation at each BPM of $\mathbf{y}[k]$ ('$*$' red), $\mathbf{y}_{orbit}[k]$ ('o' blue) and $\mathbf{y}_{bpm}[k]$ ('x' black).

the edges are approximated as being circularly shifted from the central actuator's response [Featherstone et al., 2000, Stewart et al., 2003]. In other words the response matrices in web processes are spatially invariant *except for the edges*. This is the key difference between the electron beam motion control and most web processes since it is a circular process and the actuators at electron beam injection and extraction have the same response.

3.4.2 Plasma Shape Control

A similar application is plasma shape control in tokamaks that is used for nuclear fusion. In particular, for the Joint European Torus (JET) tokamak the controller regulates the plasma shape as specified in terms of plasma-wall distances and maintains this plasma shape in the presence of significant variations of critical plasma parameters, such as the plasma current [Ariola and Pironti, 2005]. The design procedure is based on the SVD of the plant steady state input-output matrix. Oversampling of the desired output shape is resolved by performing a SVD of the steady state response matrix and rather than removing the less significant outputs, so that the shape will be automatically adjusted to comply with the few degrees of freedom available to the control input [De Tommasi et al., 2011], a cost function that penalises how close inputs are to their saturation limits and how far the output is from the achievable steady state performance is built.

3.4.3 Free Electron Lasers

X-ray Free Electron Lasers which provide laser light with tunable wavelengths is the main candidate for the next generation of light sources. The process uses a linear particle accelerator which increases the energy of electrons by interaction with electromagnetic radio frequency (RF) fields inside high quality resonator cavities [Pfeiffer et al., 2011], much like the linacs and boosters used at synchrotrons. In order to reach wavelengths in the X-ray range it is required to control the electromagnetic field inside the cavities with extremely high precision. In [Pfeiffer et al., 2012], the multi-input, multi-output (MIMO) system is decoupled into a family of independent SISO systems by applying a two-dimensional special orthogonal group symmetry matrix of the process. This approach replaces the SVD method used for synchrotron electron beam control to decouple the input-output map. However the methodology for control is the same i.e. an orthogonal map is used to decouple the MIMO process to multiple SISO loops for control and then the orthogonal map is used to map the controller outputs to appropriate actuators. In this case the orthogonal basis is a rotation matrix determined by the phase of the RF signal to be controlled.

3.5 Two Dimensional Frequency Domain Performance

The electron beam is subjected to disturbances from environmental effects that are coupled through the girders supporting the magnets. Several external disturbances cause electron beam perturbations which range from long-term disturbances, such as changes in air temperature during the day, to re-injections of the electron beam, which typically occur in the frequency range below 0.01Hz. Most disturbances arise from ground vibrations and residual effects after feedforward correction of insertion device field changes that lie within the range 0.01Hz and 100Hz. Fig. 3.8 and Fig. 3.9 shows the frequency responses for the vertical and horizontal disturbances observed at a single BPM. The major peaks shown in Fig. 3.8 and Fig. 3.9 between 20Hz and 50Hz are associated with one of the resonant modes of the girders. Above 100Hz, the effects of vibration arising from cooling water pumps and girder cooling water flow resonances appear in the beam spectra [Duncan, 2007, Gayadeen and Duncan, 2012, 2013, Napier et al., 2011]. Given the smaller vertical beam size, the effect of the vibration is more prominent in the vertical spectrum shown in Fig. 3.8, where the bulk of these disturbances are concentrated between 20Hz and 250Hz.

As a comparison, the magnitude of the frequency response of the disturbances measured at all BPMs is shown in Fig. 3.10. The disturbances between 20Hz and 50Hz are easily distinguishable, however an important feature is the variation in the underlying disturbance observed at individual BPMs. It is reasonable then to expect significant variation in the disturbance content at individual modes and in Fig. 3.11 the average power (in dB) of the disturbance at each frequency within each of the spatial modes associated with singular values of the response matrix is shown. Since most of the resonant power is within the 20Hz and 50Hz range, a key requirement of the control design is to regulate the horizontal and vertical position of the beam in

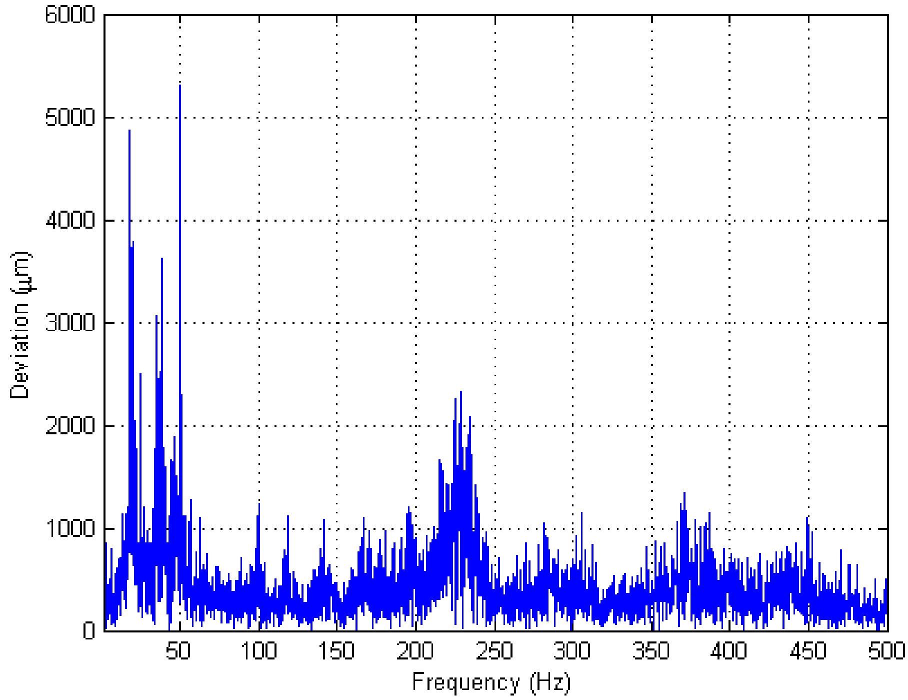

Fig. 3.8: Magnitude of frequency response of 5s of vertical variation observed at 1st vertical sensor on the storage ring.

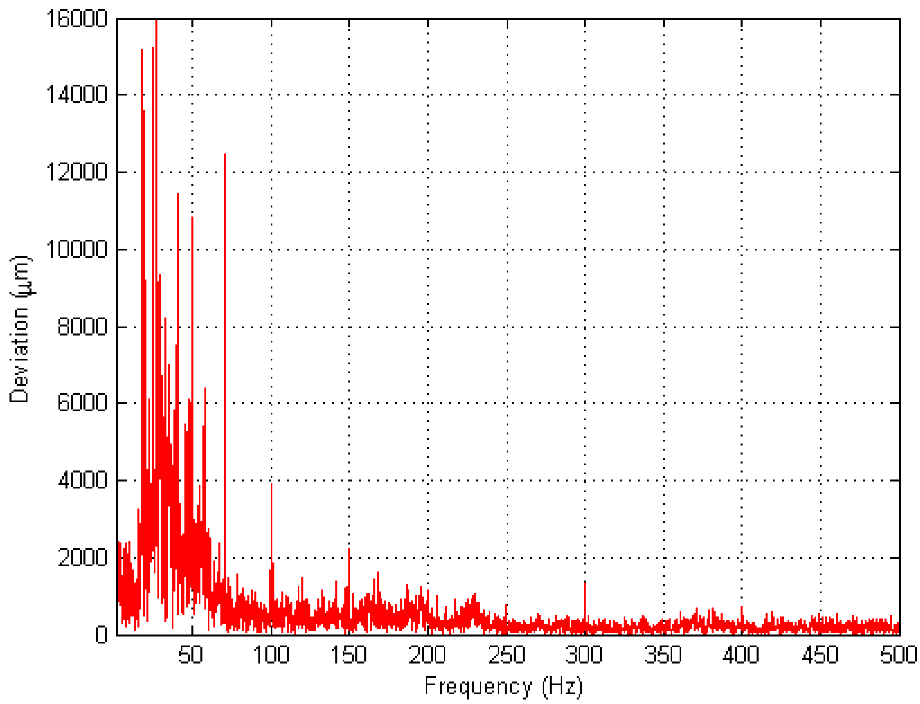

Fig. 3.9: Magnitude of frequency response of 5s of horizontal variation observed at 1st horizontal sensor on the storage ring.

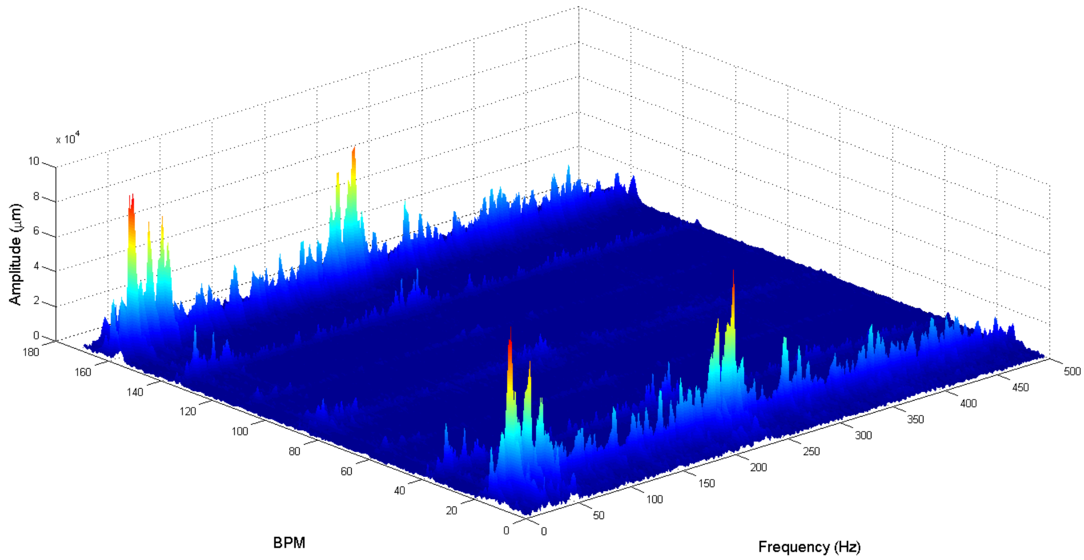

Fig. 3.10: Vertical storage ring frequency response for all BPMs.

the presence of disturbances in the range 1Hz to 100Hz, which includes the first three harmonics of the girder disturbance. From Fig. 3.11, it can also be seen that the power of these disturbances is concentrated at the lower order modes. However, not captured in Fig. 3.11, are the residual disturbances from the insertion devices, which are < 1Hz and affect all modes. The aim of the controller then, is to reduce the effect of the disturbances on the beam particularly at the low order modes for frequencies below 100Hz, while at the same time attenuating low frequency disturbance (< 1Hz) in all modes. In order to quantify the control action necessary at each mode, the average value of the power in the output is considered, which is given by

$$A_{ve}\|\mathbf{y}\,[k]\|_2^2 = \frac{1}{K_e}\sum_{k=0}^{K_e-1}\|\mathbf{y}\,[k]\|_2^2 \tag{3.20}$$

over a time duration of K_e samples. Since $\mathbf{\Phi}$ is an orthogonal matrix, $\|\bar{\mathbf{y}}[k]\|_2 = \|\mathbf{\Phi}\mathbf{y}[k]\|_2 = \|\mathbf{y}[k]\|_2$, so

$$A_{ve}\|\mathbf{y}[k]\|_2^2 = \frac{1}{K_e}\sum_{k=0}^{K_e-1}\|\bar{\mathbf{y}}[k]\|_2^2 \tag{3.21}$$

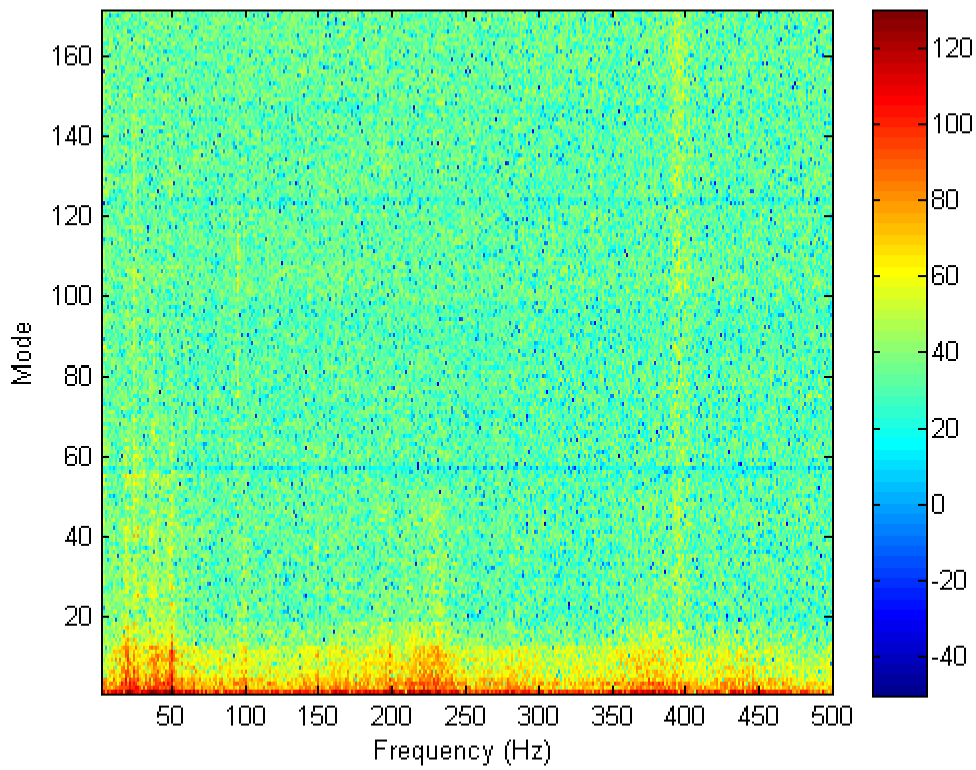

Fig. 3.11: Colormap of average power (dB) for each spatial mode against frequency (Hz).

Using the discrete Fourier transform (DFT) of $\bar{\mathbf{y}}[k]$

$$\bar{\mathbf{Y}}[f] = \sum_{k=0}^{K_e-1} \bar{\mathbf{y}}[k] e^{-j2\pi fk/K_e} \tag{3.22}$$

where $\{f = 0, 1, \ldots, K_e - 1\}$, then

$$\sum_{k=0}^{K_e-1} \|\bar{\mathbf{y}}[k]\|_2^2 = \frac{1}{K_e} \sum_{f=0}^{K_e-1} \|\bar{\mathbf{Y}}[f]\|_2^2 \tag{3.23}$$

and

$$A_{ve}\|\mathbf{y}[k]\|_2^2 = \frac{1}{K_e^2} \sum_{p=0}^{K_e-1} \|\bar{\mathbf{Y}}[f]\|_2^2 \tag{3.24}$$

Since

$$\|\bar{\mathbf{Y}}[f]\|_2^2 = \sum_{m=1}^{M} |\bar{Y}_m[f]|^2 \tag{3.25}$$

then, given the sensitivity function in (3.16),

$$\|\bar{\mathbf{Y}}[f]\|_2^2 = \sum_{m=1}^{M} |\bar{S}_m[f]|^2 |\bar{H}_m[f]|^2 \tag{3.26}$$

where $\bar{S}_m[f]$ is the frequency response of $s_m(z^{-1})$ and $\bar{H}_m[f]$, the frequency spectrum of each mode of the underlying disturbance such that

$$\bar{S}_m[f] = s_n(e^{-j2\pi fk/K_e}) \tag{3.27}$$

Combining (3.24) and (3.27) gives

$$A_{ve}\|\mathbf{y}[k]\|_2^2 = \frac{1}{K_e^2} \sum_{f=0}^{K_e-1} \sum_{m=1}^{M} |\bar{S}_m[f]|^2 |\bar{H}_m[f]|^2 \tag{3.28}$$

The relationship in (3.28) implies that given $\bar{H}_m[f]$ for each mode and $\bar{S}_m[f]$ (and hence $\bar{s}_m(z^{-1})$) designed on a 'mode-by-mode' basis, a specification on the average power observed across all sensors can be achieved [Duncan, 2007].

3.6 Uncertainty and Robustness

The tolerance of the closed-loop to model uncertainties is an essential part of the control system design, therefore in addition to reducing the effect of the disturbances at particular frequencies and modes, the control system also needs to be robust to uncertainties in the model that have the biggest effect when controlling the higher order modes. In general, the closed loop robust stability of the process is guaranteed by designing the controller such that the gain of the closed loop transfer matrix is sufficiently small. However a small loop gain is in direct conflict with the closed loop performance specifications. This is a fundamental trade-off in designing feedback control. A successful design is one in which the loop gain is high at those dynamical frequencies and spatial modes where the bulk of the disturbance is concentrated and small at those dynamical frequencies and modes for which robust stability is important.

3.7 Two-dimensional Closed Loop Specifications

With consideration of the spatial and dynamic performance and robustness specifications, the closed loop objectives are summarised below:

1. Disturbance attenuation requires the closed loop gain to be large where the process gain is large, typically at low spatial and temporal frequencies.
2. Limited control action requires the controller gain to be small where the process gain is small, typically at high spatial and temporal frequencies.
3. Robust stability requires the closed loop gain to be small at those temporal frequencies and modes where plant uncertainty is greatest.

Chapter 4

Electron Orbit Controller Design

In this chapter, a FOFB controller design is presented that meets the closed loop specifications identified in Chapter 3 and the tradeoffs between closed loop performance and robustness are discussed. An internal model control (IMC) structure is used for the design and the performance of the controllers on both the storage ring and booster at Diamond are presented.

4.1 Introduction to Internal Model Control

The IMC modal controller structure is shown in Fig. 4.1, where a parallel path containing a perfect model of the actual process is included and the reference for the output is zero (relating to the zero-orbit). The structure may be rearranged to the form in Fig. 4.2 and the closed loop equations are given by

$$
\begin{aligned}
\mathbf{u}[k] &= -\mathbf{\Psi}_1 \mathbf{Q}(z^{-1}) \mathbf{\Sigma}^{-1} \hat{\mathbf{h}}[k] \\
\hat{\mathbf{h}}[k] &= \mathbf{\Phi}^{\mathrm{T}} \mathbf{h}[k] \\
\mathbf{y}[k] &= \mathbf{h}[k] + \mathbf{\Phi} g(z^{-1}) \mathbf{\Sigma} \mathbf{\Psi}_1^{\mathrm{T}} \mathbf{u}[k]
\end{aligned}
\tag{4.1}
$$

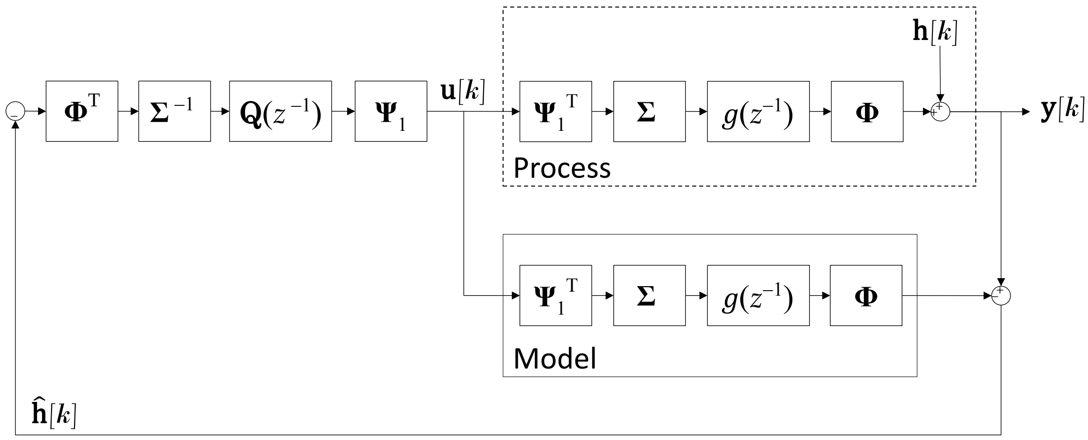

Fig. 4.1: Internal model control structure in modal form.

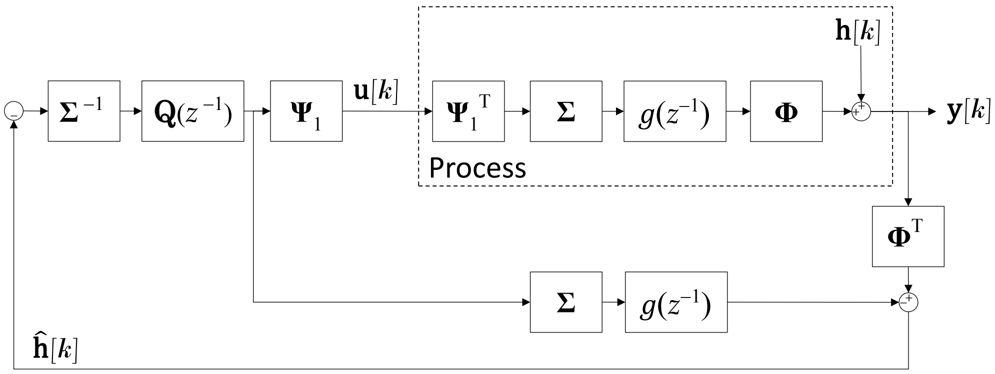

Fig. 4.2: Rearranged internal model control structure in modal form.

The signal, $\hat{\mathbf{h}}[k]$ expresses the uncertainty about the process - both model uncertainty and disturbances. In the absence of any uncertainty, the control system can be considered as operating in open-loop. The control law can be expressed in modal space as

$$\begin{aligned} \bar{\mathbf{u}}[k] &= -\mathbf{\Sigma}^{-1}\mathbf{Q}(z^{-1})\bar{\mathbf{h}}[k] \\ \bar{\mathbf{y}}[k] &= \bar{\mathbf{h}}[k] + g(z^{-1})\mathbf{\Sigma}\bar{\mathbf{u}}[k] \end{aligned} \tag{4.2}$$

where $\mathbf{Q}(z^{-1}) = \mathrm{diag}_{m=1,\ldots,M}\ \{q_m(z^{-1})\}$ and

$$\bar{\mathbf{y}}[k] = \left[\mathbf{I} - g(z^{-1})\mathbf{Q}(z^{-1})\right]\bar{\mathbf{h}}[k] \tag{4.3}$$

The implications of the IMC structure are as follows:

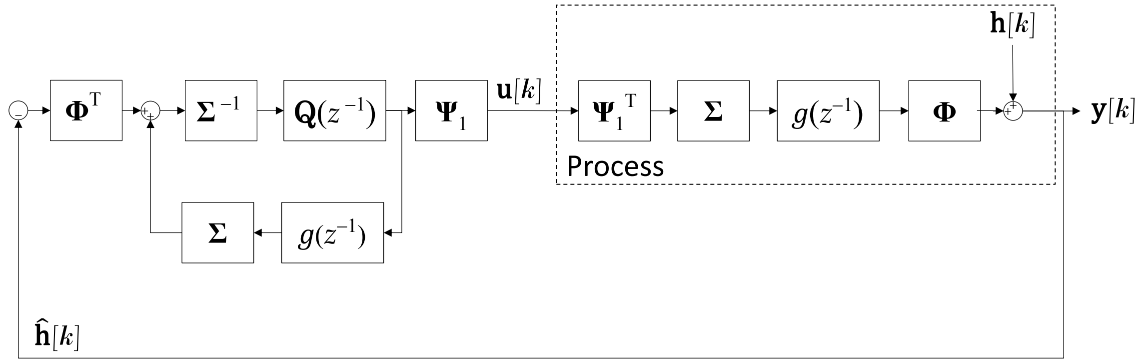

Fig. 4.3: Equivalent classic feedback structure of internal model control structure in modal form.

- Assuming a perfect model, the IMC closed loop is internally stable if and only if both the plant and controller are stable.
- The IMC structure is *entirely equivalent* [Morari and Zafiriou, 1989] to the classic feedback form with

$$\mathbf{C}(z^{-1}) = \mathbf{Q}(z^{-1})\left[1 - g(z^{-1})\mathbf{Q}(z^{-1})\right]^{-1} \tag{4.4}$$

  The IMC controller represented in a classic feedback form is shown in Fig. 4.3.

- From (4.3), the sensitivity and complementary sensitivity take simple forms,

$$\begin{aligned} \mathbf{S}(z^{-1}) &= \mathbf{I} - g(z^{-1})\mathbf{Q}(z^{-1}) \\ \mathbf{T}(z^{-1}) &= g(z^{-1})\mathbf{Q}(z^{-1}) \end{aligned} \tag{4.5}$$

Given these properties of the IMC structure, a 2 step design procedure is used [Morari and Zafiriou, 1989]:

1. *Nominal Performance*

   The controller for each mode, $\tilde{q}_m(z^{-1})$ is selected to yield a good system response for the input of interest, without regard for constraints and model uncertainty. Generally $\tilde{q}_m(z^{-1})$ is chosen such that it is $\mathcal{H}_2$ optimal where the

$\mathcal{H}_2$ optimal controller $\tilde{q}_m(z^{-1})$ minimizes

$$\min_{\tilde{q}_m} \left\| \left[1 - g(z^{-1})\tilde{q}_m(z^{-1})\right] \bar{h}_m(z^{-1}) \right\|_2 \tag{4.6}$$

subject to the constraint that each $\tilde{q}_m(z^{-1})$ is stable and causal. The problem in (4.6) reaches its absolute minimum for $\tilde{q}_m(z^{-1}) = [g(z^{-1})]^{-1}$. However this is only acceptable for minimum-phase systems. For the non-minimum phase system considered in this thesis, the exact inverse is unstable and/or noncausal, so the objective function cannot be made zero and an approximate inverse of $g(z^{-1})$ is found such that the weighted 2-norm of the sensitivity function is minimised [Morari and Zafiriou, 1989].

2. *Robust Stability and Robust Performance*

   The controller $\tilde{q}_m(z^{-1})$ is augmented by an IMC filter (usually a low pass filter) to achieve robust stability and robust performance, such that

$$q_m(z^{-1}) = f_{q_m}(z^{-1})\tilde{q}_m(z^{-1}) \tag{4.7}$$

   to provide the frequency roll-off necessary for robustness.

In Section 4.2, it is shown how this approach can be used to design the electron orbit controller.

4.2 Internal Model Control Design

In order to satisfy (4.6), the approximate inverse of $g(z^{-1})$ is required, so the non-minimum phase $g(z^{-1})$ given by (3.4), is expressed as

$$g(z^{-1}) = g^+(z^{-1})g^-(z^{-1}) \tag{4.8}$$

where the delay term is collected in $g^+(z^{-1})$. The controller that solves the weighted 2-norm in (4.6) is given by

$$\tilde{q}_m(z^{-1}) = \frac{1}{g^-(z^{-1})} \quad = \frac{1 - a_1 z^{-1}}{b_0 + b_1 z^{-1}} \tag{4.9}$$

The IMC design method for stable plants, allows the design of a controller that achieves a closed loop magnitude response exactly equal to that of a desired transfer function specified by the IMC filter $f_{q_m}(z^{-1})$, which contains a free parameter that tunes the closed-loop bandwidth. Therefore $\tilde{q}_m(z^{-1})$ is augmented with a low pass-filter for robust stability and performance such that

$$\begin{aligned} q_m(z^{-1}) &= f_{q_m}(z^{-1})\tilde{q}_m(z^{-1}) \\ &= \frac{1-\lambda_m}{1-\lambda_m z^{-1}} \frac{1 - a_1 z^{-1}}{b_0 + b_1 z^{-1}} \end{aligned} \tag{4.10}$$

where λ_m is the dominant closed-loop time constant when large enough and is chosen as $\lambda_m = e^{-\zeta_m T_s}$ where ζ_m is a tuning parameter which can be different for each mode [Morari and Zafiriou, 1989]. The pole at $z = -b_1/b_0$ lies on the negative real axis, causing damped oscillation in the inputs applied to the actuators that has a frequency equal to half the sampling frequency. Given that there is some degree of uncertainty in the exact value of the time constant of the actuator, this may also lead to the control signal 'ringing' due to the inexact cancellation of the pole with the corresponding zero in the transfer function of the process $g(z^{-1})$ [Dahlin, 1968]. In addition, it makes the system prone to instabilities caused by uncertainties in the response of the process at high frequencies. For this reason, it is better to use

$$q_m(z^{-1}) = \frac{1-\lambda_m}{1-\lambda_m z^{-1}} \frac{1 - a_1 z^{-1}}{b_0 + b_1} \tag{4.11}$$

where the scaling factor $(b_0 + b_1)$ ensures that the steady state gain of the controller is correct [Duncan, 2007].

The controller in Fig. 4.3 can be expressed as

$$\mathbf{C}(z^{-1}) = \mathbf{\Psi}_1 \mathrm{diag}\left\{\frac{1}{\sigma_m} c_m(z^{-1})\right\} \mathbf{\Phi}^{\mathrm{T}} \tag{4.12}$$

where the controller dynamics for each mode are given by

$$c_m(z^{-1}) = \frac{q_m(z^{-1})}{1 - g(z^{-1})q_m(z^{-1})} \tag{4.13}$$

substituting for $g(z^{-1})$ from (3.4) and $q_m(z^{-1})$ from (4.11) gives

$$c_m(z^{-1}) = \frac{1-\lambda_m}{b_0+b_1} \frac{1 - a_1 z^{-1}}{1 - \lambda_m z^{-1} - z^{-d}(1-\lambda_m)\tilde{B}(z^{-1})} \tag{4.14}$$

where

$$\tilde{B}(z^{-1}) = \tilde{b}_0 + \tilde{b}_1 z^{-1} = \frac{b_0 + b_1 z^{-1}}{b_0 + b_1} \tag{4.15}$$

Because $\tilde{b}_0 + \tilde{b}_1 = 1$, the second term in the denominator of (4.14) can be factored as

$$\begin{aligned} &1 - \lambda_m z^{-1} - z^{-d}(1-\lambda_m)\tilde{B}(z^{-1}) = \\ &(1 - z^{-1})\left[1 + (1-\lambda_m)z^{-1} + (1-\lambda_m)z^{-2} + \cdots + \tilde{b}_1 z^{-1}(1-\lambda_m)z^{-d}\right] \end{aligned} \tag{4.16}$$

and the presence of the $(1 - z^{-1})$ term ensures that the controller includes integral action and therefore takes the form of a Dahlin controller [Seborg et al., 2011].

As discussed in Chapter 3, the control system needs to be robust to uncertainties in the model which have the biggest effect when controlling the higher order modes and sometimes it is appropriate to discard these high order modes for control [Heath and Wills, 2004]. For the system at Diamond, some disturbances (such as those from insertion devices) affect all modes, so it is not desirable to use modal truncation. As an alternative, the controller gains determined by the inverse of the singular values can be augmented to ensure that control is limited at high order modes, by

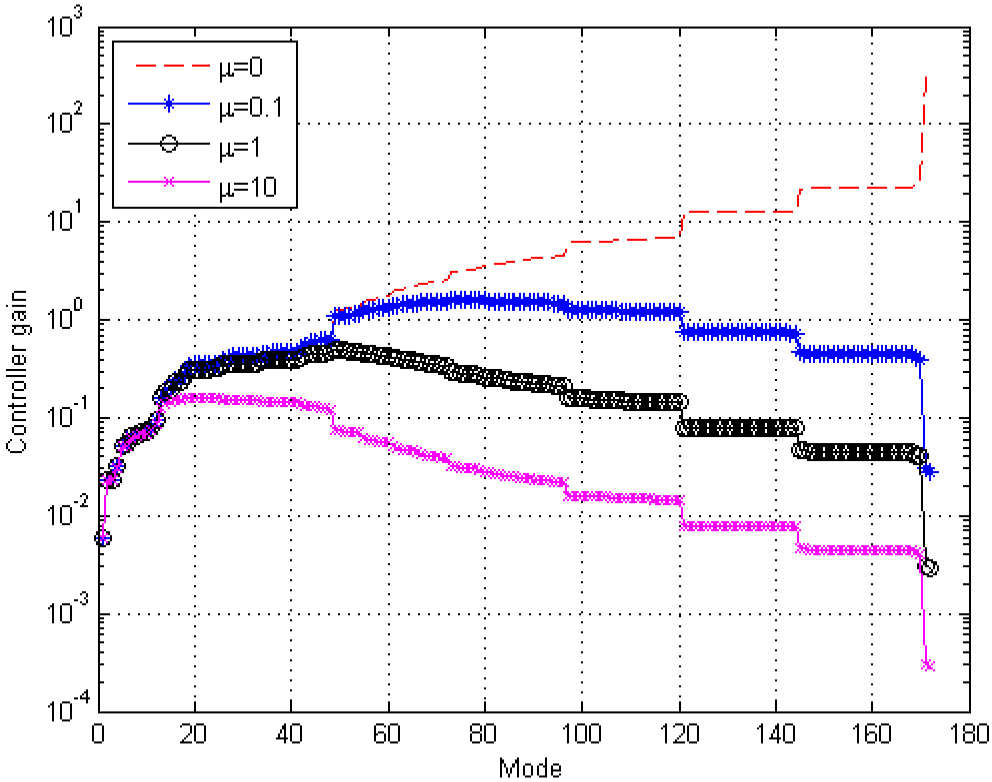

Fig. 4.4: The inverse singular values for the vertical response matrix of storage ring ('- -' red) (corresponding to $\mu = 0$) shown with the regularised controller gain, $p_m {\sigma_m}^{-1}$ for each mode where $\mu = 0.1$ ('$*$' blue), $\mu = 1$ ('o' black) and $\mu = 10$ ('x' magenta).

introducing the diagonal matrix $\mathbf{P} = \text{diag}\{p_m\}$, in which case the controller takes the form,

$$\mathbf{C}(z^{-1}) = \mathbf{\Psi}_1 \text{diag}\left\{\frac{p_m}{\sigma_m}\frac{1-\lambda_m}{b_0+b_1}\frac{1-a_1z^{-1}}{1-\lambda_m z^{-1} - z^{-d}p_m(1-\lambda_m)\tilde{B}(z^{-1})}\right\}\mathbf{\Phi}^{\mathrm{T}} \tag{4.17}$$

where the controller gain is now determined by an appropriate choice of p_m. One possible choice for the values of p_m is derived from the Tikhonov regularisation [Golub and Van Loan, 1999, Neumaier, 1998] where small singular values are filtered out, so that the controller gain becomes

$$\frac{p_m}{\sigma_m} = \frac{1}{\sigma_m}\frac{\sigma_m^2}{\sigma_m^2+\mu} \tag{4.18}$$

where the regularisation parameter, μ is chosen such that ${\sigma_m}^{-1}p_m \approx {\sigma_m}^{-1}$ when $\sigma_m^2 \gg \mu$ and ${\sigma_m}^{-1}p_m$ becomes small when $\sigma_m^2 \ll \mu$. This ensures that the optimal control action is applied to the low order modes, but the control action is 'switched off' for the high order modes where the effect of modelling uncertainties is greatest and the control actions tend to be large. When $\mu = 0$, the controller gain corresponds to the exact inverse singular value for each mode and by increasing μ, the controller gain observed at each mode is reduced. The effect of μ on the controller gain is demonstrated in Fig. 4.4 for the storage ring where for very large values of μ the controller gain approaches 0, effectively clamping these modes.

This type of filtering of the singular values is analogous to the effect of the low pass dynamic filter $f_{q_m}(z^{-1})$ in (4.10), which tunes the closed loop bandwidth for robust stability and performance. However, while the effect of μ on the controller gain is clear from Fig. 4.4, the "optimal" choice of μ is not obvious. The approach taken in this thesis, is to select μ to meet robust stability requirements and in Sections 4.3 and 4.4 it is demonstrated how the robust stability of the closed loop system is determined in the presence of plant uncertainty and how μ can be chosen to tradeoff performance and robustness.

4.3 Robust Stability Analysis

Comparisons of the measured response matrices to the ideal responses show that there are differences and in order to ensure robust stability of the closed loop in the presence of model uncertainty, these differences must be considered. So far, the model $g(z^{-1})\mathbf{R}$ has been assumed to be perfect, however to account for discrepancies between the process and the model, a norm bounded uncertainty operator, $\boldsymbol{\Delta}(z^{-1}) \in$

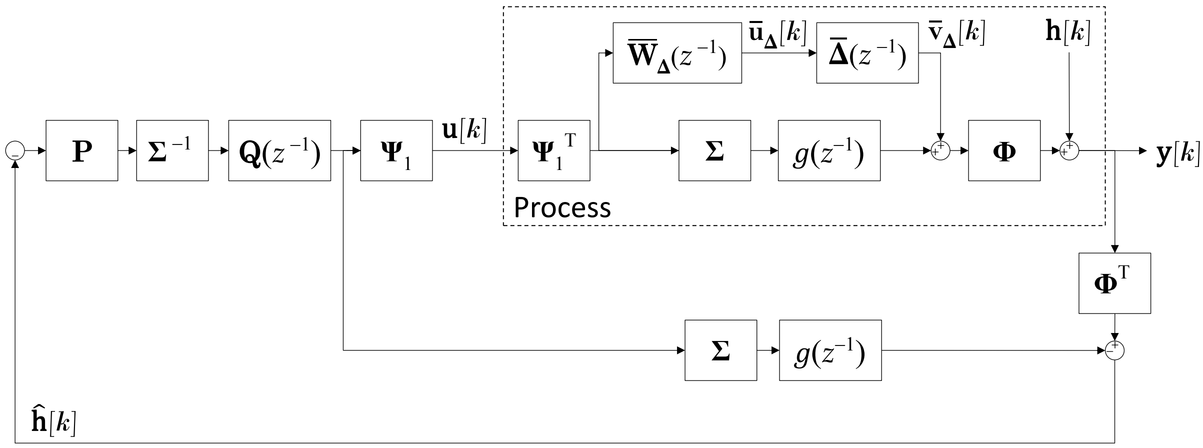

Fig. 4.5: The closed loop system showing uncertainty $\bar{\mathbf{\Delta}}(z^{-1})$ in modal space.

$\mathbb{C}^{M\times M}$ is introduced in the representation of the process, so that

$$\mathbf{y}[k] = \left[g(z^{-1})\mathbf{R} + \mathbf{W}_{\Delta}(z^{-1})\mathbf{\Delta}(z^{-1})\right]\mathbf{u}[k] + \mathbf{h}[k] \tag{4.19}$$

where uncertainty $\mathbf{\Delta}(z^{-1})$ is norm-bounded and $\mathbf{W}_{\Delta}(z^{-1})$ is a weighting introduced in order to normalise the perturbation so that $\|\mathbf{\Delta}\|_{\infty} \leq 1$. Assuming the modal decomposition of the process given by (3.8), then

$$\bar{\mathbf{y}}[k] = \left[g(z^{-1})\mathbf{\Sigma} + \bar{\mathbf{W}}_{\Delta}(z^{-1})\bar{\mathbf{\Delta}}(z^{-1})\right]\bar{\mathbf{u}}[k] + \bar{\mathbf{h}}[k] \tag{4.20}$$

where $\bar{\mathbf{W}}_{\Delta}(z^{-1})\bar{\mathbf{\Delta}}(z^{-1}) = \mathbf{\Phi}^{\mathrm{T}}\mathbf{W}_{\Delta}(z^{-1})\mathbf{\Delta}(z^{-1})\mathbf{\Psi}_1$ characterizes the uncertainty in modal space and as before, $\bar{\mathbf{W}}_{\Delta}(z^{-1})$ is a normalisation weight such that $\|\bar{\mathbf{\Delta}}\|_{\infty} \leq 1$. The closed loop system with modal uncertainty is shown in Fig. 4.5, however for stability analysis, it is advantageous to represent the closed loop in the standard feedback configuration in Fig. 4.6 [Megretski and Rantzer, 1997], so that the closed loop system is completely characterised by

$$\begin{aligned} \bar{\mathbf{v}}_{\Delta}[k] &= \bar{\mathbf{\Delta}}(z^{-1})\left(\bar{\mathbf{u}}_{\Delta}[k]\right) \\ \bar{\mathbf{u}}_{\Delta}[k] &= \mathbf{X}(z^{-1})\bar{\mathbf{v}}_{\Delta}[k] \end{aligned} \tag{4.21}$$

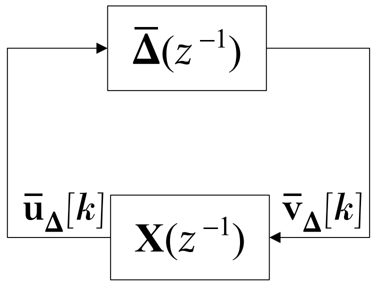

Fig. 4.6: The closed loop with uncertainty represented in the standard feedback configuration.

where $\mathbf{X}(z^{-1})$ is a known linear time invariant (LTI) transfer matrix, which for the closed loop structure in Fig. 4.5 is given as

$$\mathbf{X}(z^{-1}) = -\mathbf{P}\mathbf{\Sigma}^{-1}\mathbf{Q}(z^{-1})\bar{\mathbf{W}}_{\Delta}(z^{-1}) \tag{4.22}$$

From the measured and modelled frequency responses of the open loop system in Chapter 2, there is model mismatch at high frequencies (> 1kHz) in the dynamic response, but because the dynamic uncertainty lies well beyond the useful bandwidth of the controller, accounting for spatial uncertainty is considered of greater importance. The robust stability analysis in this thesis is motivated by the requirement to account for spatial model errors and therefore it is assumed that the dynamics are well-known, in which case the uncertain representation of the plant becomes

$$\bar{\mathbf{y}}[k] = g(z^{-1})\left[\mathbf{\Sigma} + \bar{\mathbf{W}}_{\Delta}\bar{\mathbf{\Delta}}\right]\bar{\mathbf{u}}[k] + \bar{\mathbf{h}}[k] \tag{4.23}$$

and this can be expressed in terms of (4.19) with $\mathbf{W}_{\Delta}(z^{-1}) = g(z^{-1})\mathbf{I}$. By comparing measured response matrices from the storage ring over a six month period, the spatial uncertainty can be measured and a suitable weighting matrix, $\bar{\mathbf{W}}_{\Delta}$ is constructed which takes the form shown in Fig. 4.7. The weighting matrix, $\bar{\mathbf{W}}_{\Delta}$ is diagonal and is chosen to scale the elements of the uncertainty so that $\|\bar{\mathbf{\Delta}}\|_{\infty} \leq 1$. The

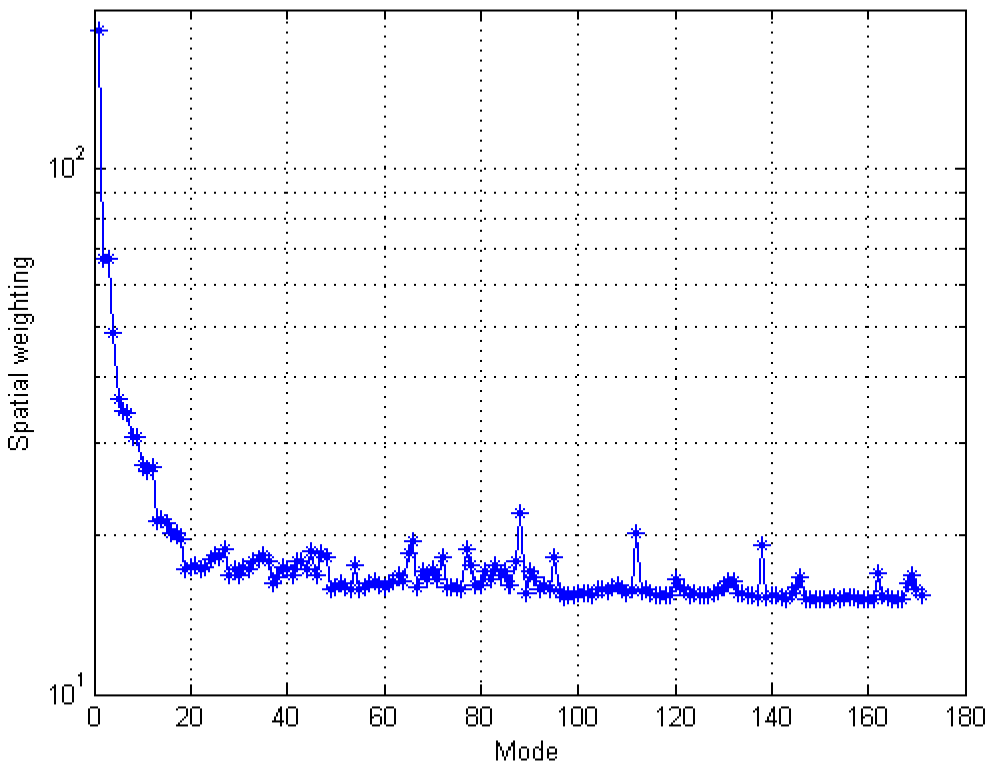

Fig. 4.7: Diagonal elements of storage ring uncertainty weighting $\bar{\mathbf{W}}_\Delta$ constructed from 10 measured vertical response matrices over a 6 month period.

weight matrix is chosen to accommodate the largest measured uncertainty from the dataset. If the modes are well-known, then $\bar{\mathbf{\Delta}}$ is diagonal and $\bar{\mathbf{W}}_\Delta$ is also diagonal. Uncertainty in the response matrix is not completely disregarded in this case, as it considers the uncertainty in the singular values of $\mathbf{R}$. However actuator and sensor inaccuracies are not included. If however the uncertainty, $\bar{\mathbf{\Delta}}$ is unstructured, then a broader class of uncertainties is taken into account. The uncertainty in the modes, as defined by the subspaces of the column and row spaces of $\mathbf{R}$ is accounted for.

For a given measured response matrix from the storage ring, the additive uncertainty in the spatial response, $\mathbf{\Delta}$ is shown in Fig. 4.8 which can be projected into modal space, shown in Fig. 4.9. The modal uncertainty $\bar{\mathbf{\Delta}}$ is unstructured because it takes into account modelling errors introduced by actuator errors and sensor misalignment. For the analysis in this chapter, a diagonal uncertainty description which considers only singular value errors is considered to develop the robust stability tests. However a more realistic uncertainty description is presented in Chapter 5.

4.3.1 Robust Stability Analysis using Integral Quadratic Constraints

Definition 1. ***Integral Quadratic Constraints*** *[Megretski and Rantzer, 1997]. Let Π be a bounded and self-adjoint operator. Then the uncertainty set $\Delta : l_2^M \mapsto l_2^M$ is said to satisfy the Integral Quadratic Constraint (IQC) defined by Π if*

$$\left\langle \begin{bmatrix} u \\ \Delta(u) \end{bmatrix}, \Pi \begin{bmatrix} u \\ \Delta(u) \end{bmatrix} \right\rangle \geq 0 \ \forall \ u = \Delta(u), \ \ u \in l_2^M \tag{4.24}$$

The operator Π is a multiplier that defines the IQC and the notation $\Delta \in IQC(\Pi)$ is used to mean that Δ satisfies the IQC defined by Π.

Robust stability analysis using IQCs involves two major steps for a system represented as a feedback interconnection of the LTI $\mathbf{X}(z^{-1})$ and the uncertain operator $\bar{\mathbf{\Delta}}$. The uncertainty $\bar{\mathbf{\Delta}}$ is first described by possible IQCs, and in many cases, such IQCs are readily available in literature [Megretski and Rantzer, 1997, Rantzer and Megretski, 1997], such as

$$\mathbf{\Pi} = \begin{bmatrix} \mathbf{\Gamma} & \\ & -\mathbf{\Gamma} \end{bmatrix} \tag{4.25}$$

where for a diagonally structured $\bar{\mathbf{\Delta}}$, $\mathbf{\Gamma} = \text{diag}\{\gamma_m\}$ where $\gamma_m > 0$ and is fixed [Megretski and Rantzer, 1997]. The second stage of the analysis requires a matrix function $\mathbf{\Pi}$ to be sought that satisfies (4.24). This search can be reduced to solving a system of linear matrix inequalities (LMIs). If a solution exists, the feedback system is stable, under the assumptions satisfied by $\mathbf{\Pi}$, $\bar{\mathbf{\Delta}}$ and $\mathbf{X}(z^{-1})$.

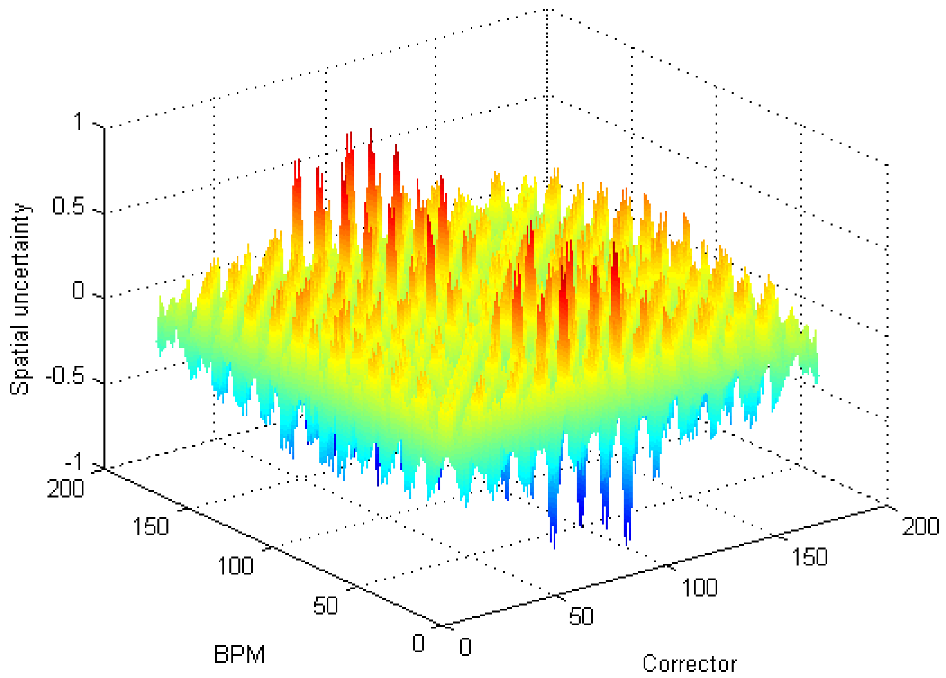

Fig. 4.8: Storage ring uncertainty $\mathbf{\Delta}$ between measured vertical response matrix and ideal vertical response matrix.

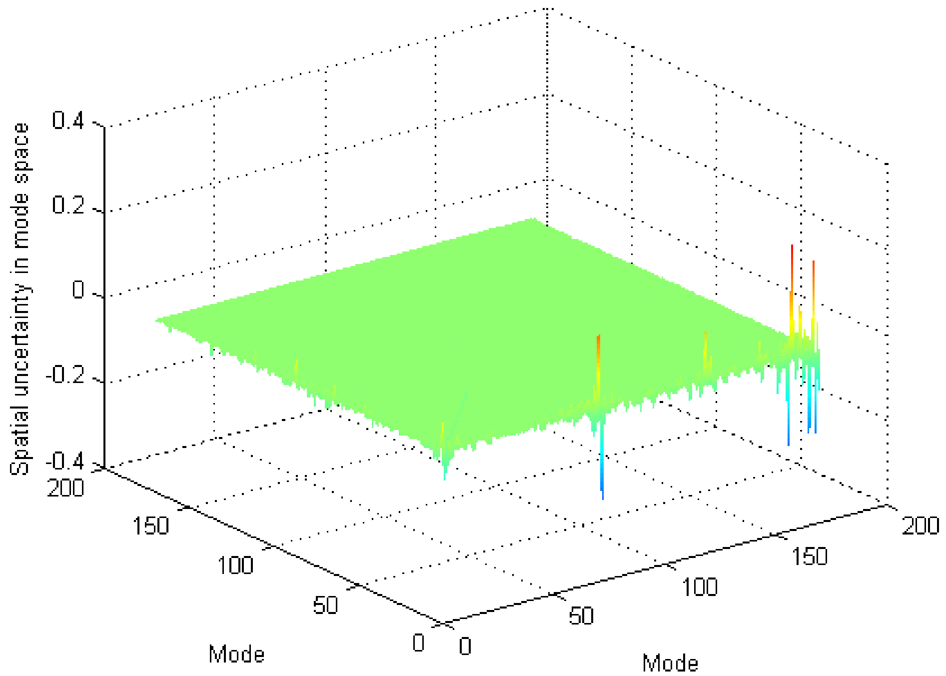

Fig. 4.9: Storage ring uncertainty $\bar{\mathbf{\Delta}}$ between measured vertical response matrix and ideal vertical response matrix in modal space.

Theorem 1 (IQC stability theorem)**.** *[Jonsson, 2001, Megretski and Rantzer, 1997]*

Assume that:

- *For* $\tau_\Delta \in [0,1]$ *the interconnection* $(X, \tau_\Delta \Delta)$ *is well-posed*
- *For* $\tau_\Delta \in [0,1]$, $\tau_\Delta \Delta \in IQC(\Pi)$
- *There exists* $\epsilon > 0$ *such that*

$$\begin{bmatrix} X(e^{j\omega}) \\ I \end{bmatrix}^* \Pi(e^{j\omega}) \begin{bmatrix} X(e^{j\omega}) \\ I \end{bmatrix} \leq -\epsilon I \tag{4.26}$$

Then the system is stable.

If $\mathbf{X}(z^{-1})$ is given by

$$\begin{bmatrix} X_{11}(z^{-1}) & \cdots & X_{1M}(z^{-1}) \\ \vdots & \ddots & \vdots \\ X_{M1}(z^{-1}) & \cdots & X_{MM}(z^{-1}) \end{bmatrix} \tag{4.27}$$

then the application of the IQC theorem guarantees stability of the closed loop provided that

$$\left[\begin{array}{ccc} X_{11}(e^{j\omega}) & \cdots & X_{1M}(e^{j\omega}) \\ \vdots & \ddots & \vdots \\ X_{M1}(e^{j\omega}) & \cdots & X_{MM}(e^{j\omega}) \\ \hline I & & \\ & \ddots & \\ & & I \end{array}\right]^* \mathbf{\Pi} \left[\begin{array}{ccc} X_{11}(e^{j\omega}) & \cdots & X_{1M}(e^{j\omega}) \\ \vdots & \ddots & \vdots \\ X_{M1}(e^{j\omega}) & \cdots & X_{MM}(e^{j\omega}) \\ \hline I & & \\ & \ddots & \\ & & I \end{array}\right] \leq -\epsilon \mathbf{I} \tag{4.28}$$

$\forall \omega \in [-\pi, \pi]$. Suppose that the uncertainty $\bar{\mathbf{\Delta}}$ is addressed by $\bar{\mathbf{\Delta}} \in \mathrm{IQC}(\mathbf{\Pi})$ and the IQC multiplier is static and is structured as follows

$$\begin{bmatrix} \mathbf{\Pi}_{11} & \mathbf{\Pi}_{12} \\ \mathbf{\Pi}_{21} & \mathbf{\Pi}_{22} \end{bmatrix} \tag{4.29}$$

where $\mathbf{\Pi}_{11} \geq 0$ and $\mathbf{\Pi}_{22} \leq 0$, then $\bar{\mathbf{\Delta}} \in \mathrm{IQC}(\mathbf{\Pi}) \Rightarrow \tau_\Delta \bar{\mathbf{\Delta}} \in \mathrm{IQC}(\mathbf{\Pi})$ $\forall \tau_\Delta \in [0,1]$

[Jonsson, 2001]. Given the state-space realization $\mathbf{X}(z^{-1}) = \boldsymbol{\mathcal{C}}_X(z^{-1}\mathbf{I} - \boldsymbol{\mathcal{A}}_X)^{-1}\boldsymbol{\mathcal{B}}_X + \boldsymbol{\mathcal{D}}_X$, then (4.28) can be formulated as

$$\begin{bmatrix} (e^{j\omega}\mathbf{I} - \boldsymbol{\mathcal{A}}_X)^{-1}\boldsymbol{\mathcal{B}}_X \\ \mathbf{I} \end{bmatrix}^* \tilde{\boldsymbol{\Pi}} \begin{bmatrix} (e^{j\omega}\mathbf{I} - \boldsymbol{\mathcal{A}}_X)^{-1}\boldsymbol{\mathcal{B}}_X \\ \mathbf{I} \end{bmatrix} \leq -\epsilon\mathbf{I} \ \forall\omega \in [-\pi, \pi] \tag{4.30}$$

where

$$\tilde{\boldsymbol{\Pi}} = \begin{bmatrix} \tilde{\boldsymbol{\Pi}}_{11} & \tilde{\boldsymbol{\Pi}}_{12} \\ \tilde{\boldsymbol{\Pi}}_{21} & \tilde{\boldsymbol{\Pi}}_{22} \end{bmatrix} \tag{4.31}$$

and

$$\begin{aligned} \tilde{\boldsymbol{\Pi}}_{11} &= \boldsymbol{\mathcal{C}}_X^{\mathrm{T}}\boldsymbol{\Pi}_{11}\boldsymbol{\mathcal{C}}_X \\ \tilde{\boldsymbol{\Pi}}_{12} &= \tilde{\boldsymbol{\Pi}}_{21}^* = \boldsymbol{\mathcal{C}}_X^{\mathrm{T}}\boldsymbol{\Pi}_{12} + \boldsymbol{\mathcal{C}}_X^{\mathrm{T}}\boldsymbol{\Pi}_{11}\boldsymbol{\mathcal{D}}_X \\ \tilde{\boldsymbol{\Pi}}_{22} &= \boldsymbol{\Pi}_{22} + \boldsymbol{\Pi}_{21}\boldsymbol{\mathcal{D}}_X + \boldsymbol{\mathcal{D}}_X^{\mathrm{T}}\boldsymbol{\Pi}_{12} + \boldsymbol{\mathcal{D}}_X^{\mathrm{T}}\boldsymbol{\Pi}_{11}\boldsymbol{\mathcal{D}}_X \end{aligned} \tag{4.32}$$

Lemma 1 (Discrete KYP Lemma)**.** *Assume the pair of matrices $(\mathcal{A}, \mathcal{B})$ is stabilizable and $\mathcal{A}$ has no eigenvalues on the imaginary axis. The following two statements are equivalent:*

1.

$$\begin{bmatrix} (e^{jw}I - \mathcal{A})^{-1}\mathcal{B} \\ I \end{bmatrix}^* \Pi \begin{bmatrix} (e^{jw}I - \mathcal{A})^{-1}\mathcal{B} \\ I \end{bmatrix} \leq 0 \qquad \forall\omega \in [-\pi, \pi] \tag{4.33}$$

2. There exists a matrix $\mathcal{G} = \mathcal{G}^{\mathrm{T}}$ such that

$$\Pi + \begin{bmatrix} \mathcal{A}^T\mathcal{G}\mathcal{A} - \mathcal{G} & \mathcal{A}^T\mathcal{G}\mathcal{B} \\ \mathcal{B}^T\mathcal{G}\mathcal{A} & \mathcal{B}^T\mathcal{G}\mathcal{B} \end{bmatrix} \leq 0 \tag{4.34}$$

Using the KYP lemma then (4.30) is equivalent to an LMI condition such that

$$\tilde{\boldsymbol{\Pi}} + \begin{bmatrix} \boldsymbol{\mathcal{A}}_X^{\mathrm{T}}\boldsymbol{\mathcal{G}}\boldsymbol{\mathcal{A}}_X - \boldsymbol{\mathcal{G}} & \boldsymbol{\mathcal{A}}_X^{\mathrm{T}}\boldsymbol{\mathcal{G}}\boldsymbol{\mathcal{B}}_X \\ \boldsymbol{\mathcal{B}}_X^{\mathrm{T}}\boldsymbol{\mathcal{G}}\boldsymbol{\mathcal{A}}_X & \boldsymbol{\mathcal{B}}_X^{\mathrm{T}}\boldsymbol{\mathcal{G}}\boldsymbol{\mathcal{B}}_X \end{bmatrix} \leq -\epsilon\mathbf{I} \tag{4.35}$$

where some matrix $\boldsymbol{\mathcal{G}}^{\mathrm{T}} = \boldsymbol{\mathcal{G}}$ exists [Jonsson, 2001, Megretski and Rantzer, 1997].

4.3.2 Decomposition of Robust Stability Test

Consider a single uncertainty in the singular values $\bar{\boldsymbol{\Delta}}$, where the closed loop system is characterised by

$$\mathbf{X}(z^{-1}) = -\mathbf{P}\boldsymbol{\Sigma}^{-1}\bar{\mathbf{W}}_{\Delta}\mathbf{Q}(z^{-1})g(z^{-1}) \tag{4.36}$$

Two cases are considered:

1. For an unstructured uncertainty, $\boldsymbol{\Gamma} = \gamma\mathbf{I}$ and it follows from (4.28) that there exists a $\gamma > 0$ and $\epsilon > 0$ such that

$$\mathbf{P}^2\boldsymbol{\Sigma}^{-2}\bar{\mathbf{W}}_{\Delta}^2\mathbf{Q}^*(z^{-1})\mathbf{Q}(z^{-1})g^*(z^{-1})g(z^{-1})\boldsymbol{\Gamma} - \boldsymbol{\Gamma} \leq \epsilon\mathbf{I} \tag{4.37}$$

for the system to be guaranteed stable. The inequality (4.37) is true if and only if

$$p_m^2\sigma_m^{-2}\bar{w}_{\Delta_m}^2 q_m^*(z^{-1})q_m(z^{-1})g^*(z^{-1})g(z^{-1})\gamma - \gamma \leq \epsilon \tag{4.38}$$

provided that the weight $\bar{\mathbf{W}}_{\Delta}$ is diagonal.

2. For a structured uncertainty, $\boldsymbol{\Gamma} = \mathrm{diag}\{\gamma_m\}$ and it follows from (4.28) that there exists $\gamma_m > 0$ and $\epsilon > 0$ such that

$$\mathbf{P}^2\boldsymbol{\Sigma}^{-2}\bar{\mathbf{W}}_{\Delta}^2\mathbf{Q}^*(z^{-1})\mathbf{Q}(z^{-1})g^*(z^{-1})g(z^{-1})\boldsymbol{\Gamma} - \boldsymbol{\Gamma} \leq \epsilon\mathbf{I} \tag{4.39}$$

for the system to be guaranteed stable. The inequality in (4.39) is true if and only if

$$p_m^2\sigma_m^{-2}\bar{w}_{\Delta_m}^2 q_m^*(z^{-1})q_m(z^{-1})g^*(z^{-1})g(z^{-1})\gamma_m - \gamma_m \leq \epsilon \tag{4.40}$$

for all $m = 1, \ldots, M$ where $q_m^*(z^{-1})$, $q_m(z^{-1})$ and $\bar{w}_{\Delta_m}^2$ are the m^{th} diagonal entries of $\mathbf{Q}^*(z^{-1})$, $\mathbf{Q}(z^{-1})$ and $\bar{\mathbf{W}}_\Delta$ respectively.

The stability criteria (4.40) allows a different γ_m for every mode making the test completely decoupled. However for (4.38), a unique γ is required for all modes resulting in a partially decoupled test [Morales and Heath, 2011].

4.4 Storage Ring Controller Design and Implementation

Using the first order plus delay transfer function given in (3.4) and the parameters in Table 2.6, the discrete time dynamic process model for the storage ring is

$$g_{SR}(z^{-1}) = z^{-7}\frac{0.356z^{-1}}{1 - 0.644z^{-1}} \tag{4.41}$$

where $d = 7$ is chosen. The controller described by (4.17) requires two matrix multiplications i.e. multiplication by $\mathbf{\Phi}^{\mathrm{T}}$ to convert the measurements from the sensors into mode space to which the dynamics are applied, then a second matrix multiplication by $\mathbf{\Psi}_1$ to convert from mode space to input space. Given that $\mathbf{R}$ has dimensions 172×172, the two matrix multiplications require a significant amount of computation to be achieved within the 10kHz sampling rate for the Diamond control network. Motivated by the requirement to reduce computation, a common value of λ is used for all modes and the bandwidth of each mode is adjusted by applying a different gain p_m to individual modes - a method that has been used extensively for electron orbit control. The IMC structure for this approach is shown in Fig. 4.10 where the controller is represented as

$$\mathbf{C}(z^{-1}) = c_m(z^{-1})\mathbf{C} \tag{4.42}$$

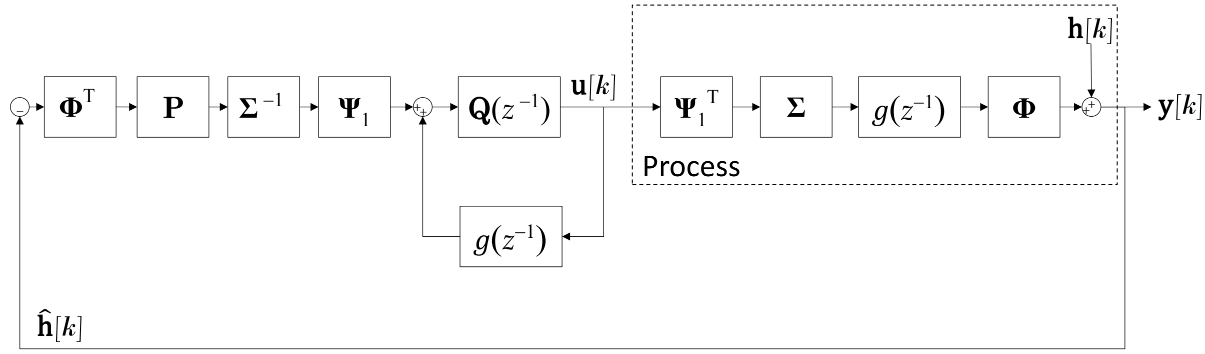

Fig. 4.10: Alternative IMC structure to reduce computation for implementation.

where $\mathbf{C} \in \mathbb{R}^{N \times M}$ is

$$\mathbf{C} = \mathbf{\Psi}_1 \mathbf{P} \mathbf{\Sigma}^{-1} \mathbf{\Phi}^{\mathrm{T}} \tag{4.43}$$

with $\mathbf{P} = \mathrm{diag}_{m=1,\ldots,M}\{p_m\}$. In this case, the scalar control dynamics for all spatial modes become

$$\begin{aligned} c_m(z^{-1}) &= \frac{q_m(z^{-1})}{1 - g(z^{-1})q_m(z^{-1})} \\ &= \frac{p_m}{\sigma_m} \frac{1-\lambda}{b_0 + b_1} \frac{1 - a_1 z^{-1}}{1 - \lambda z^{-1} - z^{-d}(1-\lambda)\tilde{B}(z^{-1})} \end{aligned} \tag{4.44}$$

where the controller is designed by selecting a single λ for all modes and a suitable value of μ that will result in different controller gains on all modes. Since the denominator polynomial is the same as in (4.14), the controller includes integral action. Multiplying the measurements from the sensors $\mathbf{y}[k]$ by $\mathbf{C}$ converts directly from output space to input space and the controller dynamics are then applied in the input space. This structure means that only one matrix multiplication is required when generating the control actions. The control design needs to balance the conflicting requirements of robustness and performance which reduces to the choice of a suitable ζ (and hence λ) that will provide sufficient bandwidth to attenuate the disturbances and values of p_m that will focus the control effort on the lower order modes. However the controller also needs to provide attenuation at low frequencies for all modes, in order to respond to the slow drift in the electron beam. It is

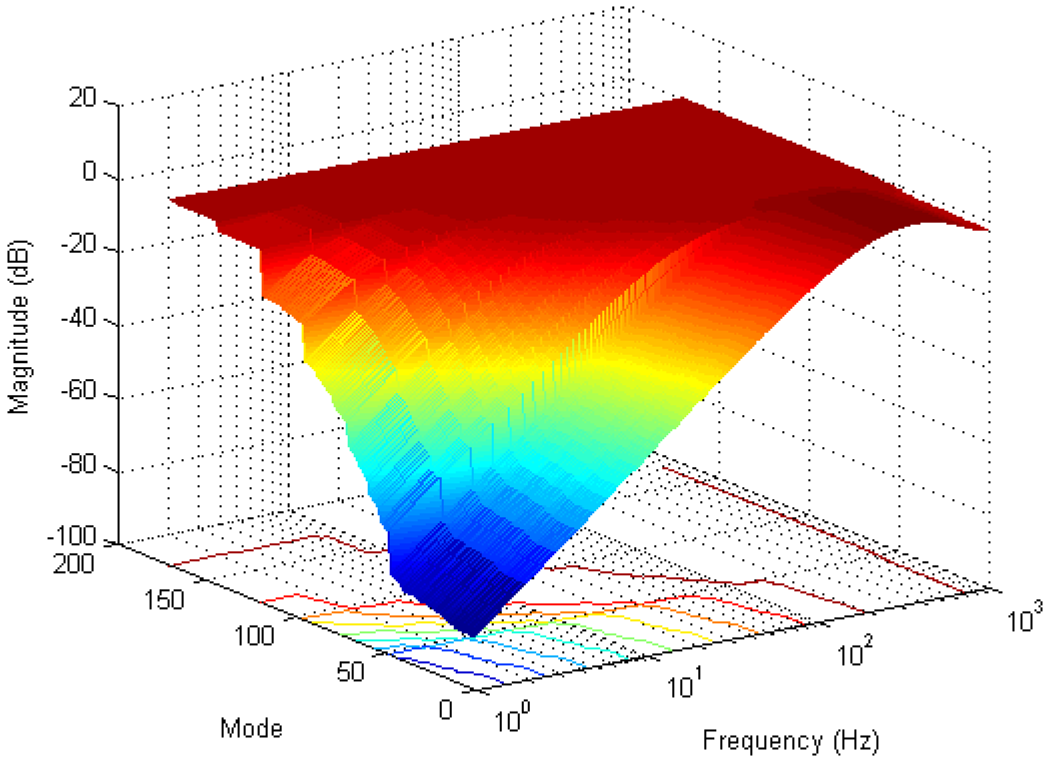

Fig. 4.11: Storage ring vertical sensitivity function in both spatial and temporal frequency domains.

appropriate to select ζ such that the time constant of the closed loop response is equivalent to the delay, so that $\zeta = 1/\tau_d$ which gives $\lambda = e^{-T_s/\tau_d}$ [Morari and Zafiriou, 1989]. This corresponds to a closed loop bandwidth of $\zeta = 1.43 \times 10^3$ rad.s^{-1} or 227 Hz. For this choice of ζ, given (4.11), the IMC controller becomes

$$q_{SR}(z^{-1}) = \frac{0.374 - 0.241z^{-1}}{1 - 0.867z^{-1}} \tag{4.45}$$

To select appropriate controller gains, the sensitivity function at each mode is considered, which is given as

$$\bar{s}_m(z^{-1}) = \frac{1 - \lambda z^{-1} - z^{-d}(1-\lambda)\tilde{B}(z^{-1})}{1 - \lambda z^{-1} - z^{-d}(1-p_m)(1-\lambda)\tilde{B}(z^{-1})} \tag{4.46}$$

The sensitivity function in both spatial and temporal frequency domains is shown

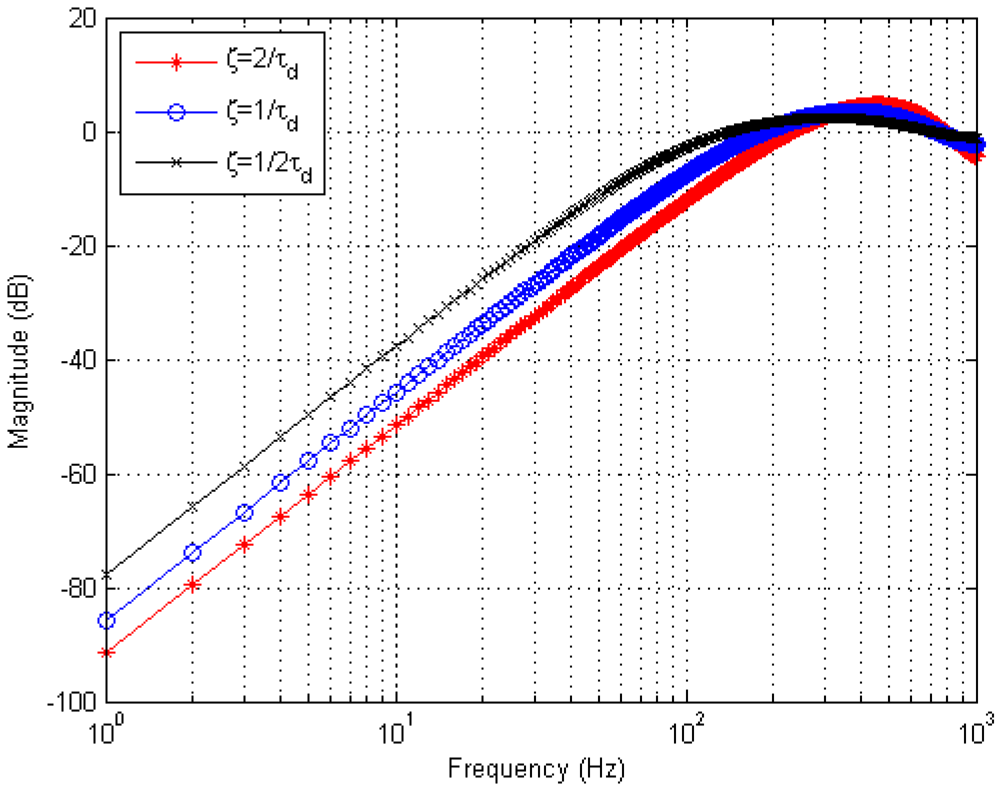

Fig. 4.12: Storage ring vertical sensitivity function observed at 1st mode for $\zeta = 2/\tau_d = 454$Hz ('$*$' red), $\zeta = 1/\tau_d = 227$Hz ('o' blue) and $\zeta = 1/2\tau_d = 113$Hz ('x' black).

in Fig. 4.11 where $\zeta = 1/\tau_d$ and $\mu = 1$ are chosen. The sensitivity is shaped to target specific dynamic frequencies (through the choice of ζ) and specific modes (through the choice of μ). Given $\zeta = 1/\tau_d$, the disturbance attenuation is focused at the low frequencies ($<$ 100Hz) where the bulk of the disturbance is concentrated. A larger ζ results in a more aggressive sensitivity function with increased low frequency attenuation but at the cost of amplifying disturbances at high frequencies. The tradeoff is demonstrated in Fig. 4.12, where the effect of ζ on the sensitivity function, observed at a single mode is shown and it can be seen that decreasing ζ results in a less aggressive sensitivity function. For the given choice of regularisation parameter, $\mu = 1$, the gain p_m is close to 1 for the first 48 modes on the vertical plane and p_m is close to 0 for the remaining modes as shown in Fig. 4.13. Likewise on the horizontal plane, the gain p_m is close to 1 for the first 72 modes. This choice of μ offers a

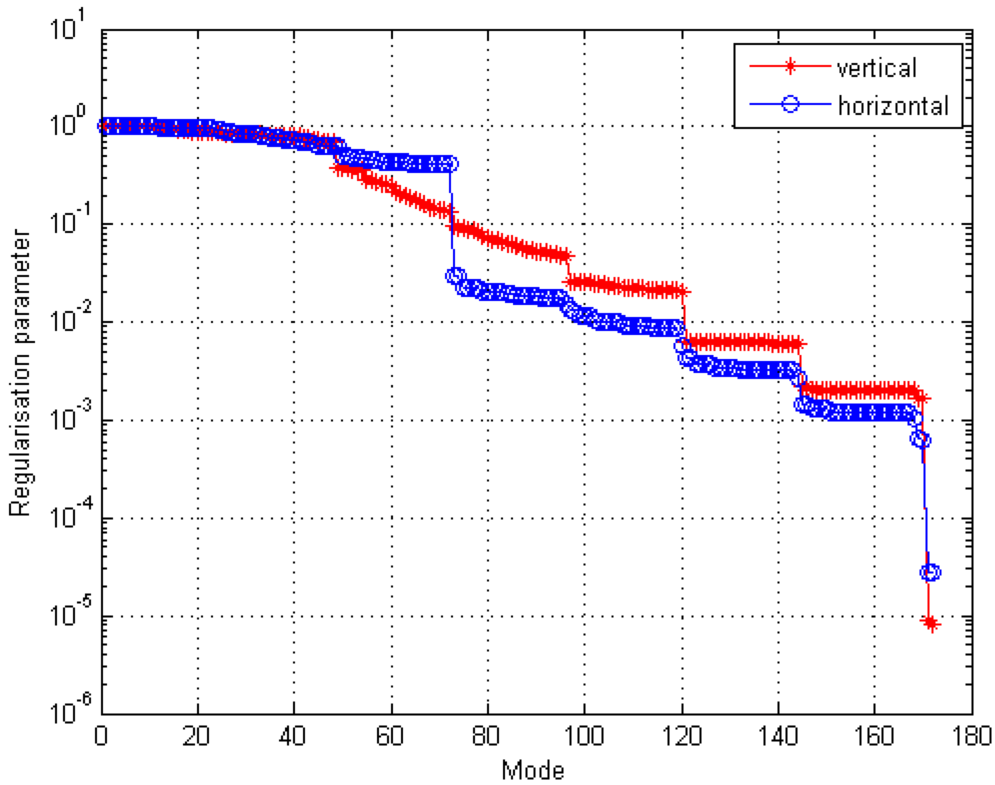

Fig. 4.13: Storage ring vertical ('$*$' red) and horizontal ('o' blue) regularisation parameter, p_m for each mode when $\mu = 1$.

natural separation of the modes, since the first 48 vertical and first 72 horizontal modes have the most significant singular values. The sensitivity function in Fig. 4.11 is shaped so that the maximum disturbance attenuation is focused at the low order modes and at high order modes, the disturbance attenuation is reduced. The 0dB contours of the sensitivity function, shown in Fig. 4.11 can be projected onto the two-dimensional disturbance map to better understand the effect of the parameters ζ and μ. In Fig. 4.14, for a constant μ, ζ is varied which determines the controller bandwidth at a given mode. By contrast, decreasing μ extends control to the high order modes for each dynamic frequency for a given ζ, as shown in Fig. 4.15 and when $\mu = 0$, the control action at all modes is equal.

In order to guarantee robust stability of the closed loop with a particular choice of ζ and μ, the robust stability test in Section 4.3 is used. The controller structure in

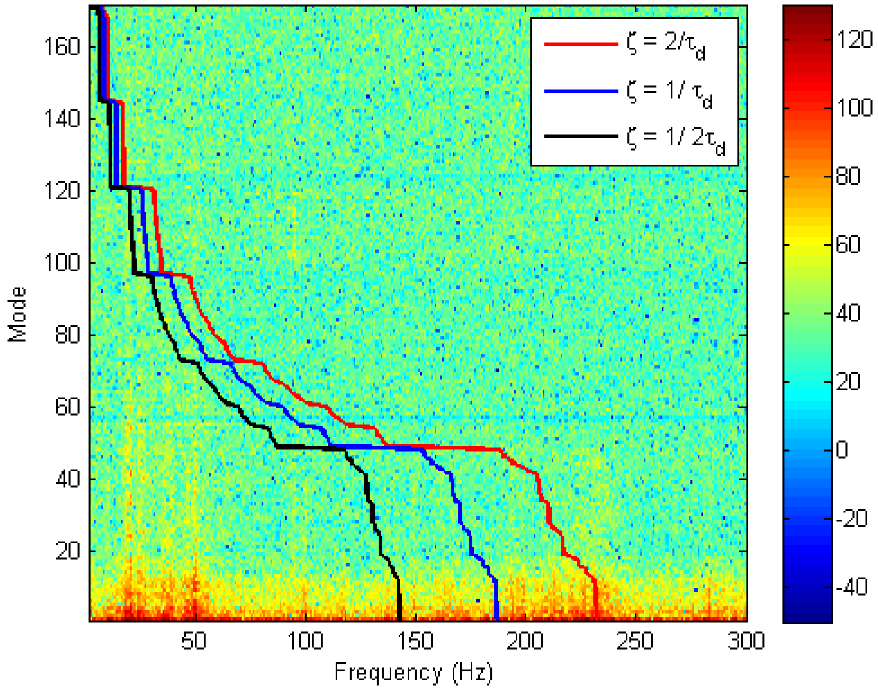

Fig. 4.14: Storage ring sensitivity 0dB contour for $\zeta = 2/\tau_d$ (red), $\zeta = 1/\tau_d$ (blue) and $\zeta = 1/2\tau_d$ (black) shown with the average power (in dB) for each mode against frequency (Hz).

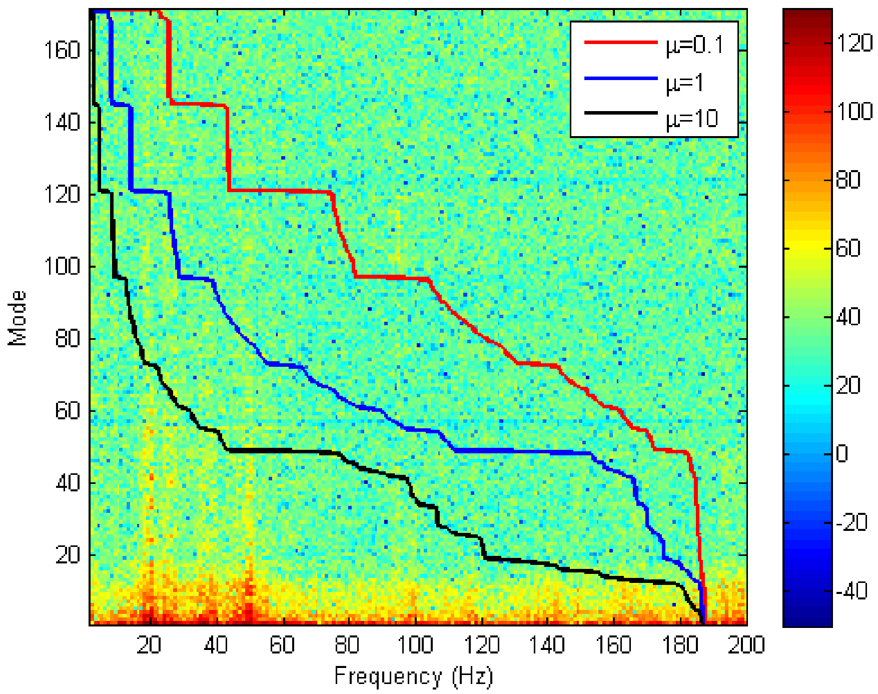

Fig. 4.15: Storage ring sensitivity 0dB contour for μ=0.1 (red), μ=1 (blue) and μ=10 (black) shown with the average power (in dB) for each mode against frequency (Hz).

Fig. 4.10 is represented as the feedback interconnection of $\mathbf{X}(z^{-1})$ and a diagonal additive operator $\bar{\boldsymbol{\Delta}}$ on the singular values of the response matrix. This is not a realistic uncertainty representation for the response matrix, since the actual uncertainty includes actuator and sensor errors and is therefore unstructured, however in Chapter 5 a more realistic uncertainty description is developed. To demonstrate a meaningful comparison between robustness and performance, a simple uncertainty description is addressed here. In this case, the robust stability test can be decomposed and performed on a mode by mode basis to determine whether $\boldsymbol{\mathcal{G}}$ in (4.35) exists for a given $\mathbf{X}(z^{-1})$ and $\bar{\boldsymbol{\Delta}}$. A search for a robust controller is achieved through the LMI feasibility test via the KYP lemma, using a standard semidefinite programming solver, SDPT3 [Toh et al., 1999]. For each mode, a search for the upper bound of the l_2 gain that satisfies the LMI feasibility condition in (4.35) is performed and the result is shown in Fig. 4.16. All modes of the process are found to be stable for the various values of μ shown in Fig. 4.16. As a further result, it is found that, for a given mode, a larger value of μ results in a larger allowable uncertainty which means that the mode becomes less sensitive to uncertainty in the singular value associated with that mode (i.e. the mode is more robust). Therefore, if no robust controller can be found, then p_m should be decreased by increasing μ.

Using the robust stability result, μ was changed from the initial setting of $\mu = 1$ to $\mu = 10$ and the observed vertical integrated beam motion for both choices are shown in Fig. 4.17. While $\mu = 1$ offers less robustness than $\mu = 10$, particularly at high order modes, the smaller value of $\mu = 1$ provides better performance i.e. when $\mu = 1$, the integrated beam motion at each frequency is less than that observed when $\mu = 10$. Because $\mu = 1$ provides better disturbance rejection while still ensuring closed loop robust stability, it is chosen for the storage ring controller.

As a further comparison, the integrated beam motion on the storage ring is shown in Fig. 4.18 for various controller bandwidths with $\mu = 1$. By decreasing the controller

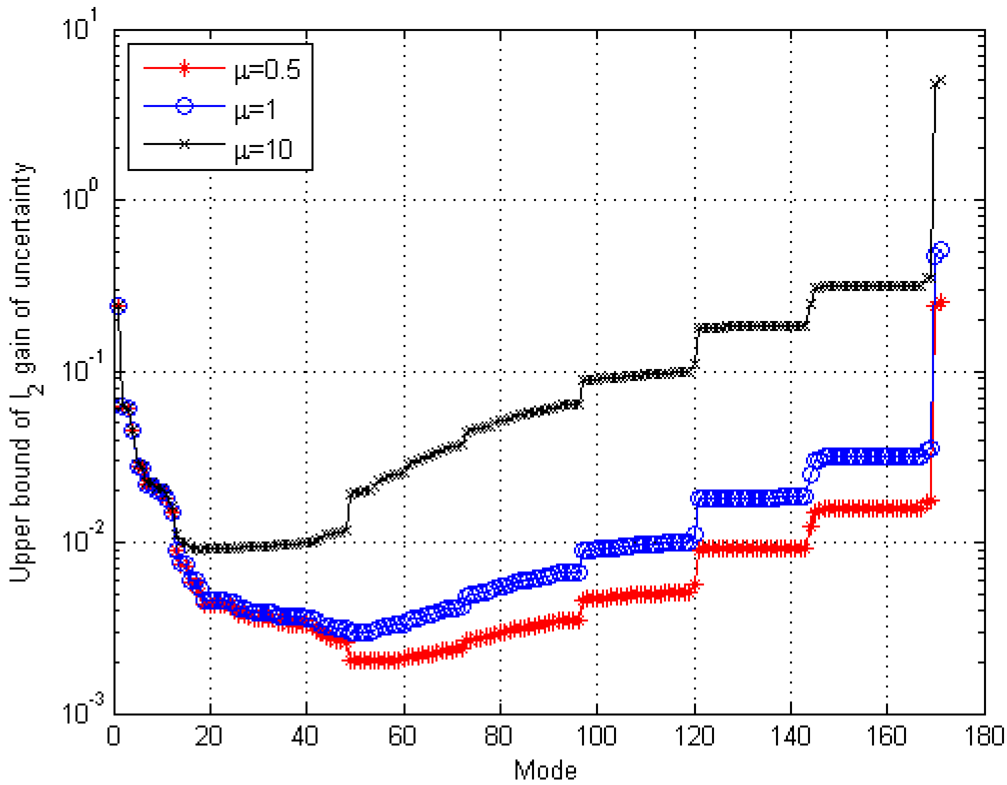

Fig. 4.16: Allowable size of uncertainty on singular values for vertical storage ring controller where $\zeta = 2/\tau_d$ and $\mu = 0.5$ ('$*$' red), $\mu = 1$ ('o' blue) and $\mu = 10$ ('x' black).

bandwidth so that $\zeta = 1/2\tau_d$, the high frequency beam motion is reduced but the low frequency performance deteriorates. This is expected given the sensitivities in Fig. 4.12. However choosing a larger controller bandwidth, $\zeta = 2/\tau_d$ gives improved performance for frequencies $<$ 100Hz which is desirable for the storage ring as this is where the main harmonics of the disturbances lie. Increasing the closed loop bandwidth also results in greater amplification of the beam motion at higher frequencies but the amplification at frequencies above 1kHz is acceptable for the Diamond storage ring since it is indistinguishable from sensor noise and cannot be detected by beamlines. Therefore $\zeta = 2/\tau_d$ is chosen for the storage ring controller. By considering both performance and robustness, $\zeta = 2/\tau_d$ and $\mu = 1$ are selected for the storage ring, where the 10% beam size requirement for stability means that the allowed RMS motion is 12.3μm horizontally and 0.6μm

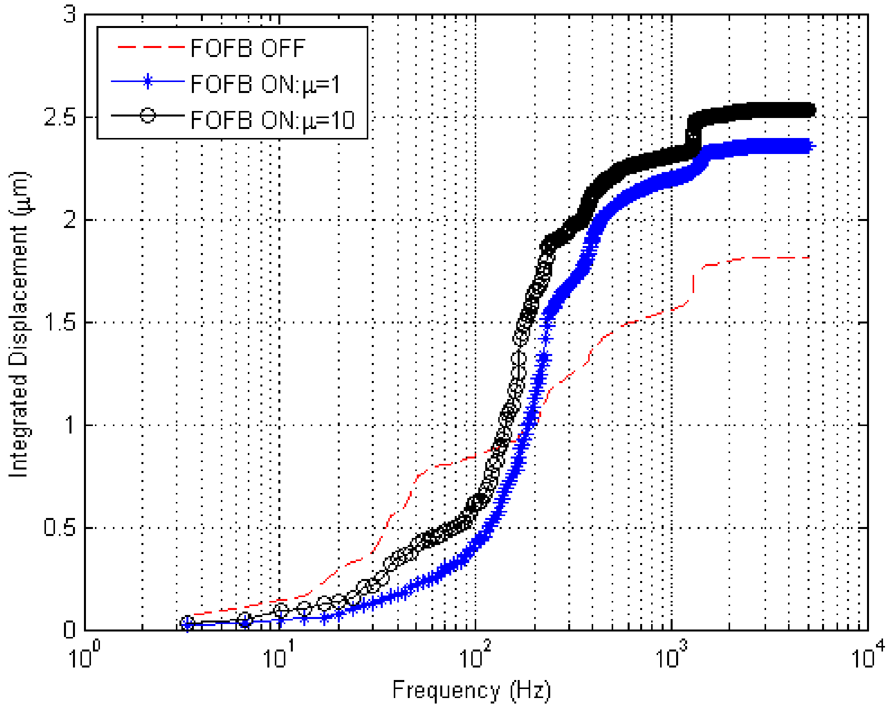

Fig. 4.17: Storage ring vertical integrated beam motion for the uncorrected beam ('- -' red), and the corrected beam for $\mu = 1$ ('$*$' blue) and $\mu = 10$ ('o' black). For all cases $\zeta = 2/\tau_d$.

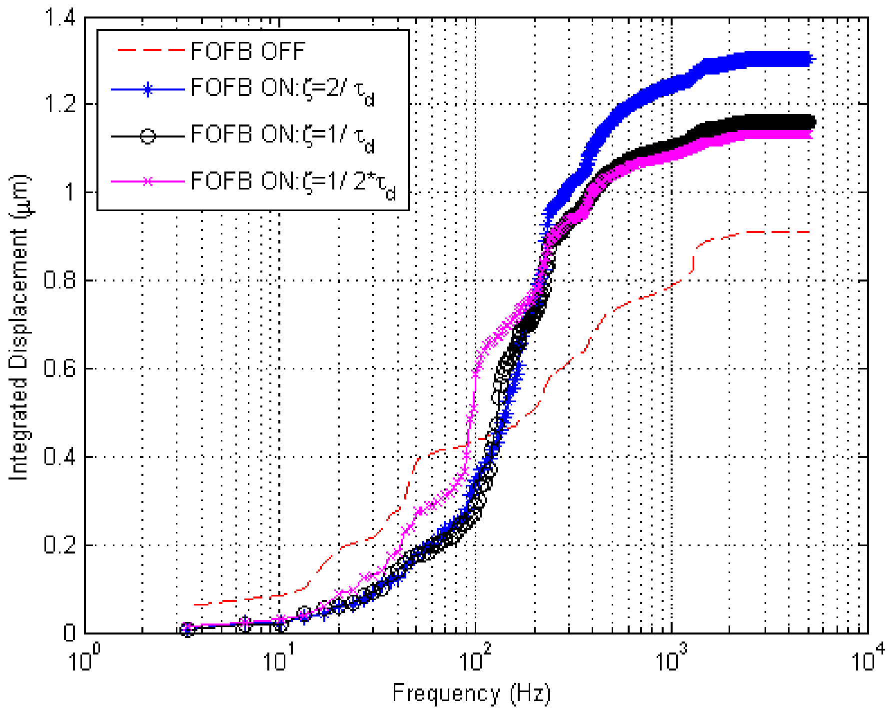

Fig. 4.18: Storage ring vertical integrated beam motion for the uncorrected beam ('- -' red), the corrected beam with $\zeta = 2/\tau_d$ ('$*$' blue), $\zeta = 1/\tau_d$ ('o' black) and $\zeta = 1/2\tau_d$ ('x' magenta). For all cases $\mu = 1$.

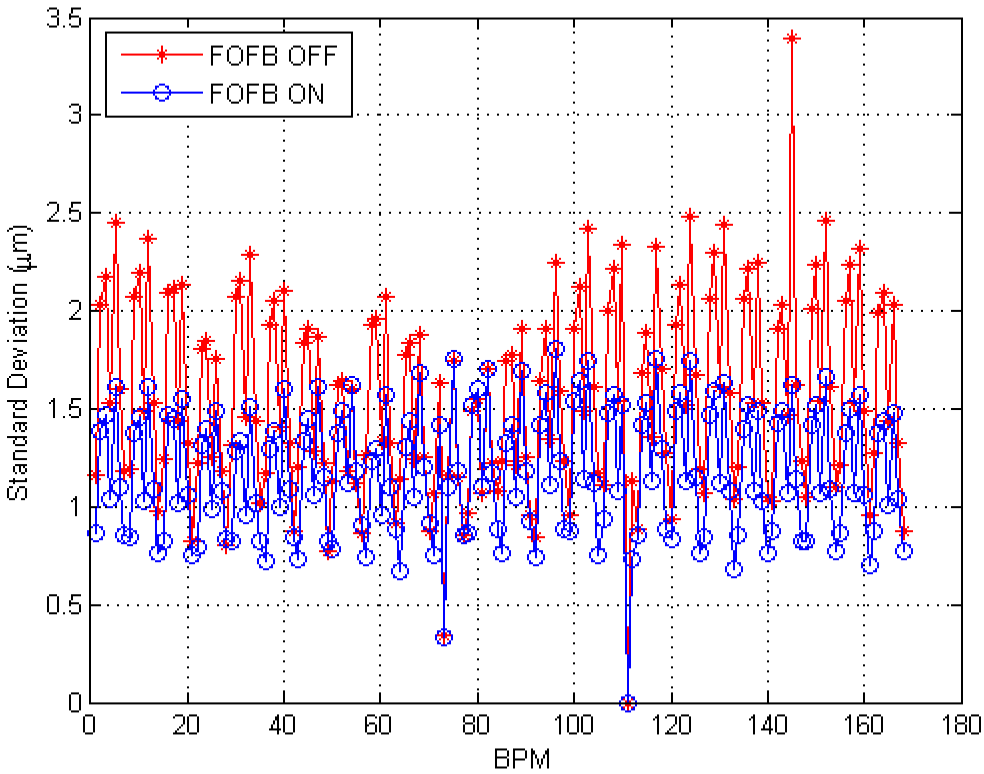

Fig. 4.19: Storage ring vertical standard deviation of uncontrolled variations ('$*$' red) and controlled beam ('o' blue) for each sensor when $\zeta = 2/\tau_d$ and $\mu = 1$.

vertically. In order to evaluate whether the specifications for stability are met, the integrated beam motion shown in Fig. 4.18 where $\zeta = 2/\tau_d$ and $\mu = 1$ demonstrates that the achieved vertical RMS motion is 0.30μm at 100Hz, giving $< 5\%$ beam stability, so the specification is achieved. Additionally, the effect of the controller on the standard deviation of the uncontrolled variation is shown in Fig. 4.19 and it can be seen that the controller significantly reduces the beam position variations, though the effect of the disturbance varies considerably between sensors because the level of uncertainty of the underlying disturbance depends upon the location of the sensor around the ring. The periodic pattern observed in Fig. 4.19 arises from the 24 repeated cells that form the closed ring. As a final comparison, the beam profile in both space and time is given in Fig. 4.20 and Fig. 4.21. The uncorrected beam position for 20 samples is shown in Fig. 4.20 at all BPMs and the corrected beam

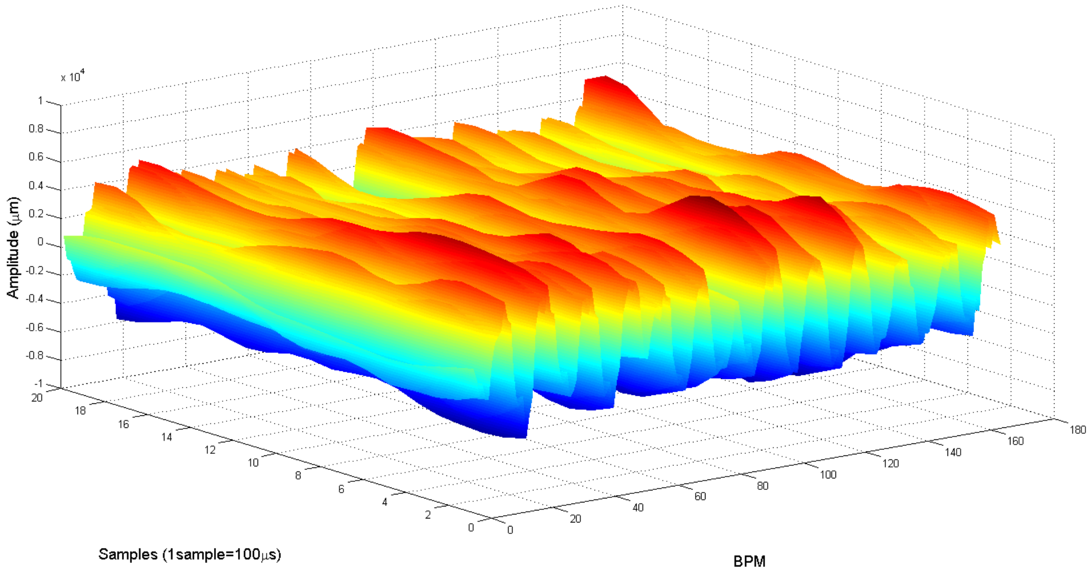

Fig. 4.20: Storage ring vertical uncorrected beam motion observed at all BPMs taken over 2ms i.e. 20 samples.

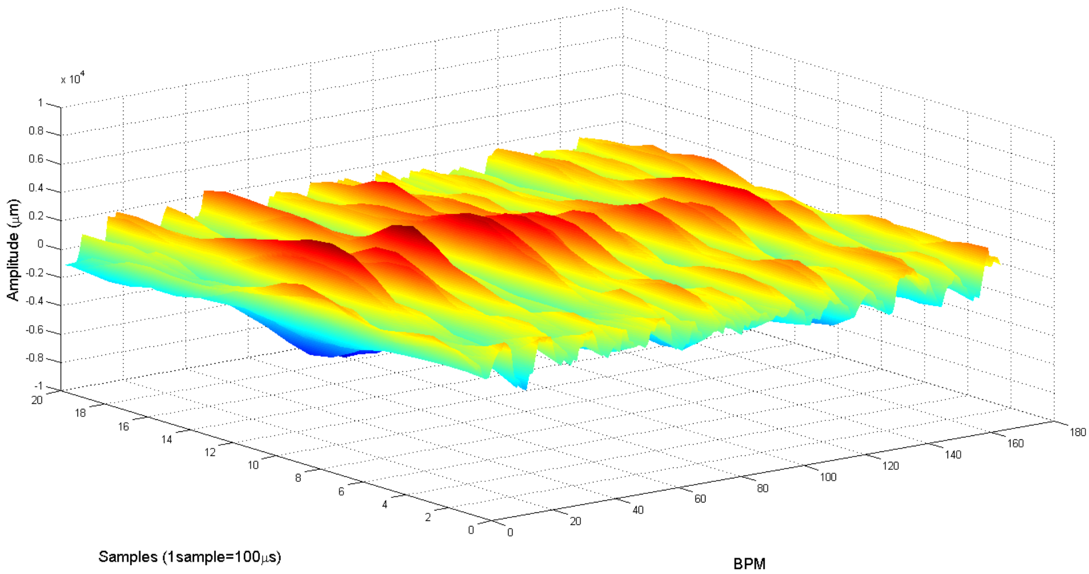

Fig. 4.21: Storage ring vertical corrected beam motion observed at all BPMs taken over 2ms i.e. 20 samples.

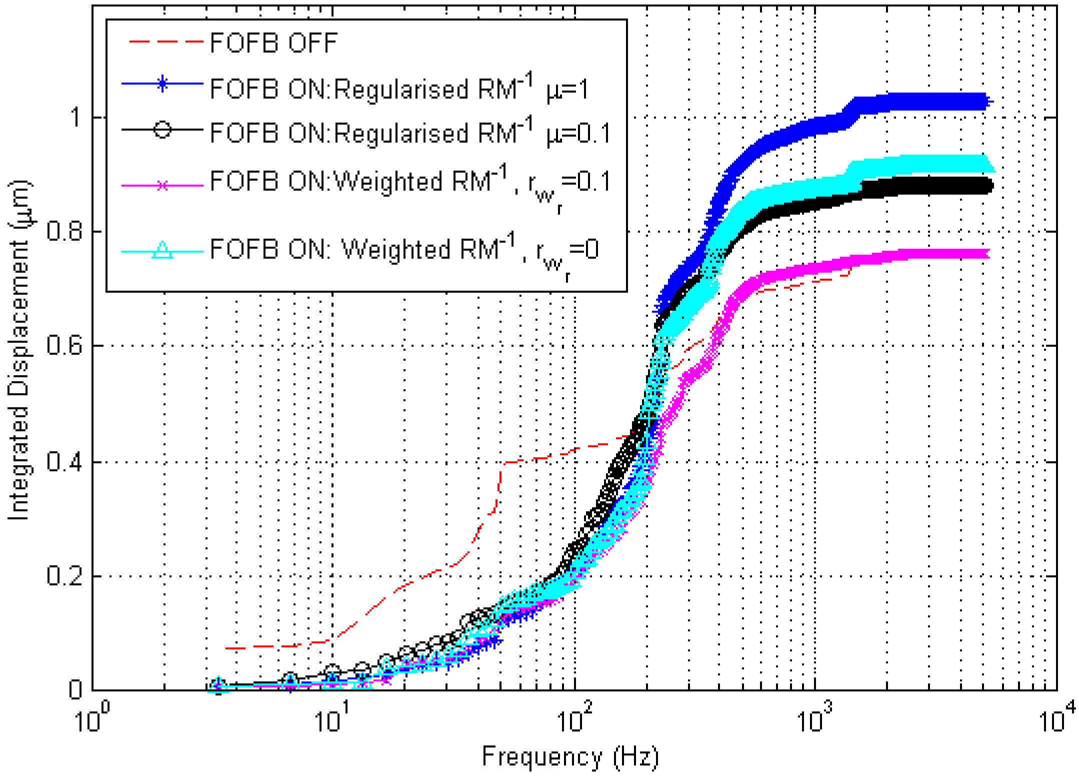

Fig. 4.22: Storage ring vertical integrated beam motion observed at a primary BPM, for the uncorrected beam ('- -' red), the corrected beam using the regularised inverse response matrix when $\mu = 1$ ('$*$' blue) and when $\mu = 0.1$ ('o' black) compared to using the weighted inverse response matrix when non-primary BPMs are given a weight of $r_{w_r} = 0.1$ ('x' magenta) and a weight of $r_{w_r} = 0$ ('$\triangle$' cyan).

position is shown in Fig. 4.21. The reduction in beam size both in the spatial and temporal domains is evident.

So far, the approach taken has been to filter the singular values. As an alternative, the integrated beam motion when only 52 modes are used is shown in Fig. 4.22. The 52 selected modes are associated with 'primary' BPMs i.e. the BPMs positioned at the two ends of straight sections of the storage ring which are particularly important since these are the positions where the photon beams are taken off for experiments. By using a weighted response matrix inversion which allows preferential weighting at specific sensors, rather than modes, the new response matrix becomes

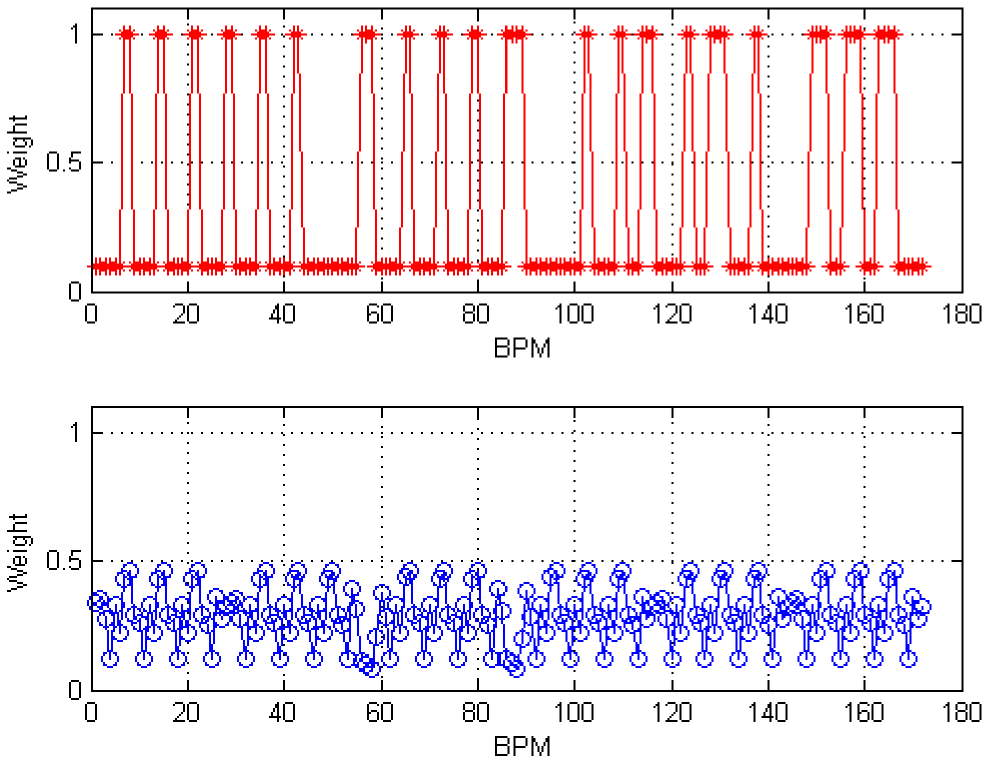

Fig. 4.23: Weights on storage ring inverse response matrix when non-primary BPMs are given a weight of $r_{w_r} = 0.1$ and primary BPMs a weight of $r_{w_p} = 1$ ('$*$' red) compared to the equivalent weighting for a regularised response matrix when $\mu = 1$ ('o' blue).

$$\tilde{\mathbf{R}}^{-1} = \mathbf{R}_W \mathbf{\Phi}^{\mathrm{T}} \mathbf{\Sigma}^{-1} \mathbf{\Psi}_1 \tag{4.47}$$

where $\mathbf{R}_W = \mathrm{diag}_{1,\ldots,M}\{r_{w_{p,r}}\}$ where r_{w_p} is the weight on the primary BPM and r_{w_r} is the weight on the regular BPM and $r_{w_p} > r_{w_r}$ i.e. the weights imposed on 'primary' BPMs are greater than those on the regular BPMs. So by setting $r_{w_p} = 1$ for all primary BPMs and $r_{w_r} = 0$ for all non-primary BPMs, particular modes are discarded. As a comparison, selecting a very large μ in the former approach of filtering the singular values will also clamp or turn-off modes, however, the modes that are being discarded are different. The integrated beam motion shown in Fig. 4.22 is obtained by observing the effect at a primary BPM when $r_{w_p} = 1$ and for two choices of weights on the regular BPMs; $r_{w_r} = 0.1$ and $r_{w_r} = 0$ and it is observed that including the modes that are discarded when $r_{w_r} = 0$ improves performance even when a small weight is assigned these modes.

Fig. 4.23 shows $\mathbf{R}_W$ when the regular BPMs weights are $r_{w_r} = 0.1$ compared to the equivalent $\mathbf{R}_W$ when $\mu = 1$ is chosen for the regularised inverse response matrix given by (4.43). At BPMs where the weights are largest correspond to the primary BPMs for both methods, however it can be seen that by using the regularisation parameter μ, the weights are ordered for the regular BPMs where typically BPMs associated with the center of straight sections are given the lowest weighting. A smaller μ will result in a larger weight on the primary BPMs and results in better performance as shown in Fig. 4.22. Therefore, because the regularisation parameter offers a natural weighting of the BPMs, improved performance can be achieved by either selecting a small μ (provided robust stability conditions are met) or using a weighted inverse response matrix to select the weights given to each BPM.

4.5 Booster Controller Design and Implementation

Using the first order plus delay transfer function given in (3.4) and the parameters in Table 2.6, the discrete time dynamic process model for the booster is

$$g_{BR}(z^{-1}) = z^{-7}\frac{0.467z^{-1}}{1-0.534z^{-1}} \tag{4.48}$$

On the booster, it was feasible to perform the two matrix multiplications shown in Fig. 4.2 so that the controller is in the form where the dynamics are given by (4.17) and are different for individual modes. This is reasonable since there is a small number of modes (M=22). In Fig. 4.24, the integrated beam motion when the controller is off is shown for all 22 modes, which is different at each mode

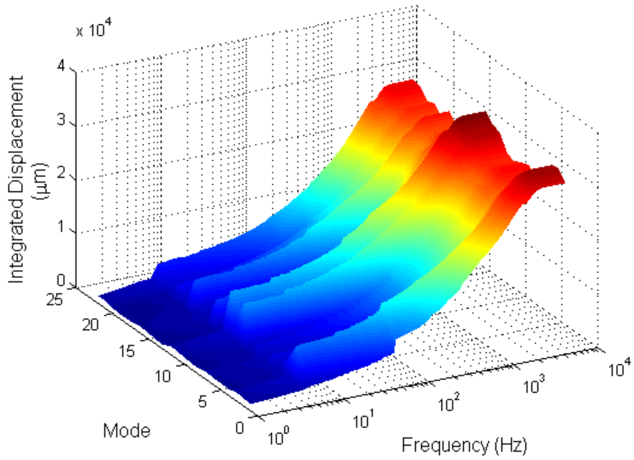

Fig. 4.24: Booster vertical uncorrected integrated beam motion at all modes.

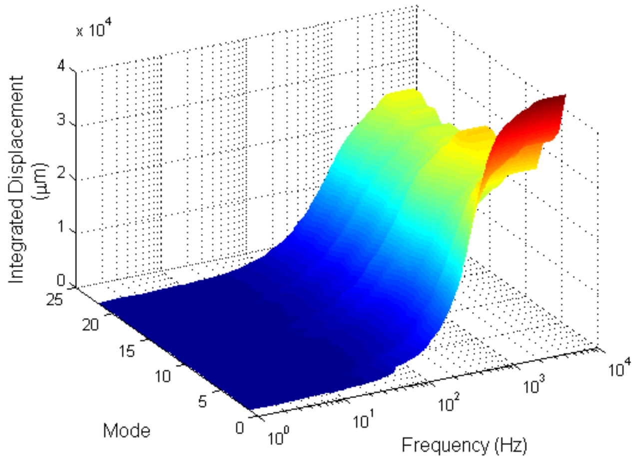

Fig. 4.25: Booster vertical corrected integrated beam motion at all modes where the same dynamics are selected for each mode which is detuned by a different gain.

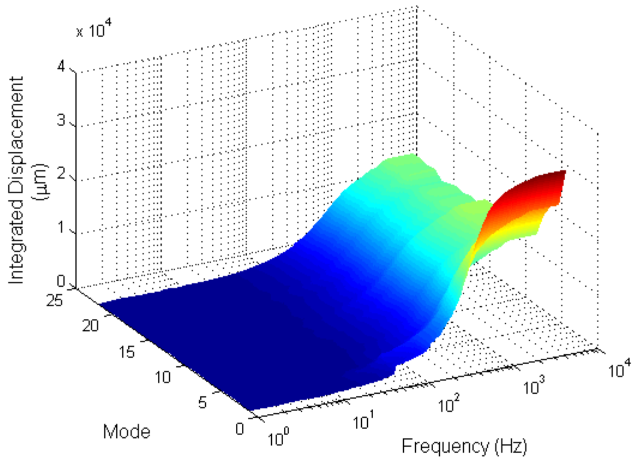

Fig. 4.26: Booster vertical corrected integrated beam motion at all modes where different dynamics are selected for individual modes.

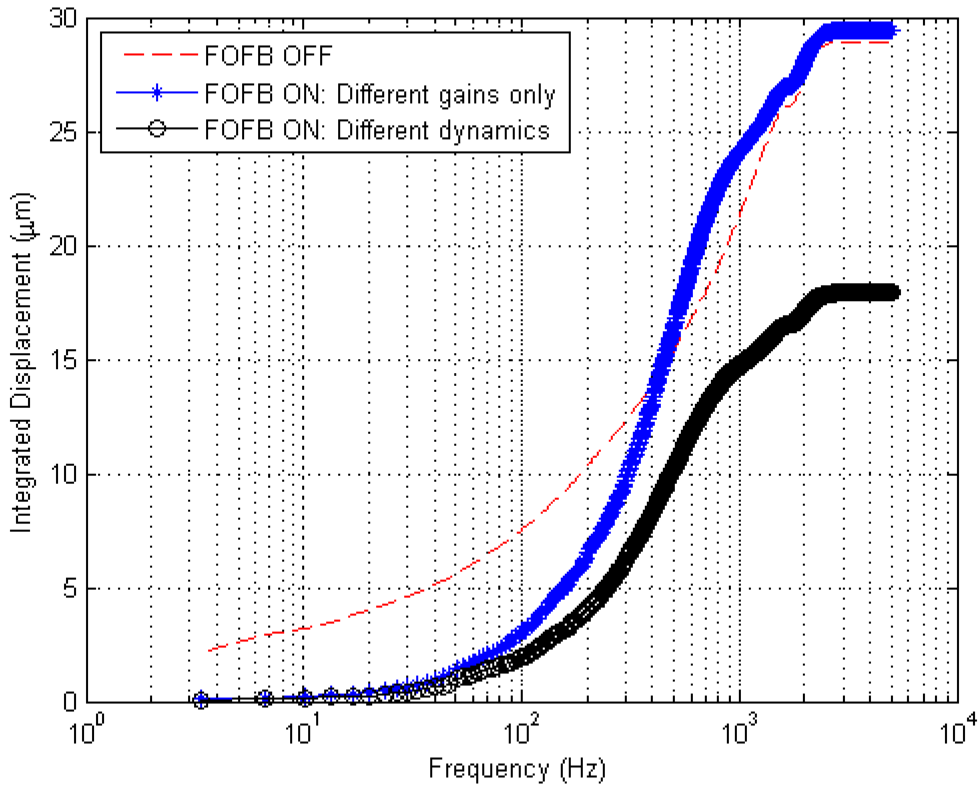

Fig. 4.27: Booster vertical uncorrected integrated beam motion ('- -' red) and corrected integrated beam motion when different gains only are applied to individual modes ('$*$' blue) and when different dynamics are applied to individual modes ('o' black).

and therefore it is sensible to design the sensitivity to match the effect of the disturbance on a mode by mode basis. In Fig. 4.25 the integrated beam motion where a single $\zeta = 1/\tau_d$ is selected for all modes and by choosing $\mu = 1$, the controller dynamics are detuned for each mode. The beam stability specifications are met with this design, however Fig. 4.26 shows the performance when $\mu = 1$ is also used but the controller bandwidths for the first 15 modes are chosen to be 189Hz whereas the bandwidth of the high order modes is chosen to be 227Hz. The former approach may reduce the computation for the controller and is practical, but improved beam stability is achieved when different dynamics are designed for the individual modes. The integrated beam motion at a single BPM is shown in Fig. 4.27 which compares the two methods, where it is evident the improvement of

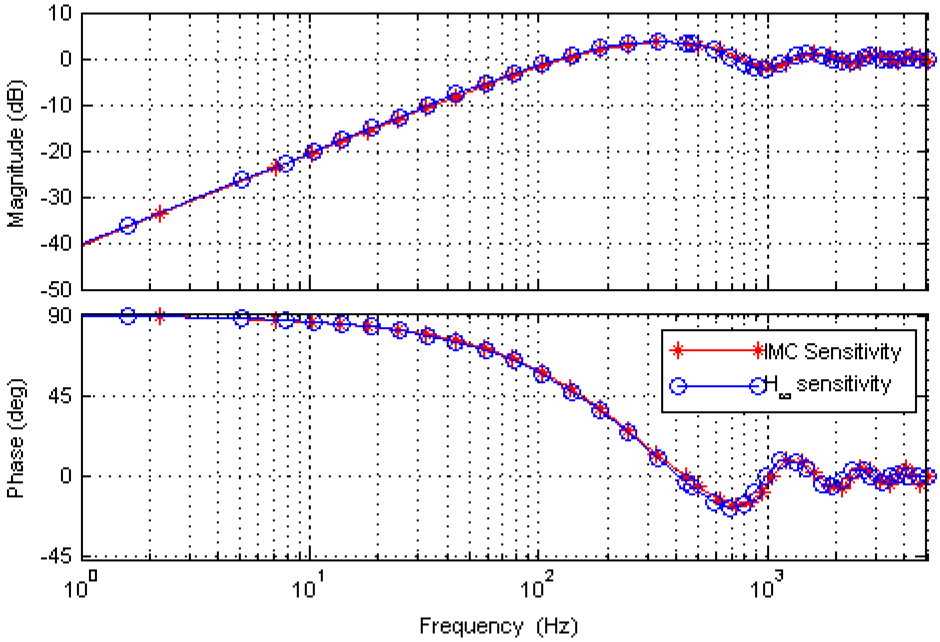

Fig. 4.28: Booster vertical closed loop sensitivity with IMC controller ('$*$' red) compared to the H_∞ controller ('o' blue).

different dynamics on each mode (or groups of modes) which gives greater flexibility in design and enhanced performance because using different dynamics allows shaping the sensitivity to match the disturbance content.

4.6 H_∞ Optimal Controller Design

An H_∞ design method that explicitly addresses the robust stability concerns within a single framework can be adopted. A spatial uncertainty operator is considered, where $\bar{\mathbf{v}}_\Delta = \bar{\mathbf{W}}_\Delta\bar{\mathbf{\Delta}}(\bar{\mathbf{u}}_\Delta)$. Similar to the IMC design, $\bar{\mathbf{\Delta}}$ is considered as a diagonal additive operator on the singular values of the response matrix with a weighting $\bar{\mathbf{W}}_\Delta$ and $\|\bar{\mathbf{\Delta}}\|_\infty \leq 1$. Approximate integral control is introduced by a performance weight such that $\bar{\mathbf{z}}_y[k] = \bar{\mathbf{W}}_y(z^{-1})\bar{\mathbf{y}}[k]$ which is given by

$$\bar{\mathbf{W}}_y(z^{-1}) = \frac{(1-\epsilon_y)z^{-1}}{1-\epsilon_y z^{-1}}\mathbf{I} \tag{4.49}$$

where $\epsilon_y > 0$ is sufficiently small. Additionally, a weighted sensitivity on each mode is considered given as

$$\bar{\mathbf{y}}[k] = \bar{\mathbf{W}}_h(z^{-1})\bar{\mathbf{h}}[k] \tag{4.50}$$

The design problem is to find a controller $\mathbf{C}(z^{-1})$ to minimise the norm from $\tilde{\mathbf{v}}[k]$ to $\tilde{\mathbf{u}}[k]$ defined by

$$\tilde{\mathbf{u}} = \begin{bmatrix} \bar{\mathbf{z}}_y[k] \\ \bar{\mathbf{u}}_\Delta[k] \\ \bar{\mathbf{y}}[k] \end{bmatrix} \quad \tilde{\mathbf{v}} \ = \begin{bmatrix} \bar{\mathbf{h}}[k] \\ \bar{\mathbf{v}}_\Delta[k] \\ \bar{\mathbf{u}}[k] \end{bmatrix} \tag{4.51}$$

where

$$\begin{aligned} \begin{bmatrix} \bar{\mathbf{z}}_y[k] \\ \bar{\mathbf{u}}_\Delta[k] \\ \bar{\mathbf{y}}[k] \end{bmatrix} &= \begin{bmatrix} \mathbf{W}_y(z^{-1})\mathbf{W}_h(z^{-1}) & \mathbf{W}_y(z^{-1})g(z^{-1}) & \mathbf{W}_y(z^{-1})\mathbf{\Sigma}g(z^{-1}) \\ \mathbf{0} & \mathbf{0} & \mathbf{W}_\Delta \\ \mathbf{W}_h(z^{-1}) & g(z^{-1})\mathbf{I} & \mathbf{\Sigma}g(z^{-1}) \end{bmatrix} \begin{bmatrix} \bar{\mathbf{h}}[k] \\ \bar{\mathbf{v}}_\Delta[k] \\ \bar{\mathbf{u}}[k] \end{bmatrix} \\ &:= \mathbf{T}_{\tilde{u}\tilde{v}} \begin{bmatrix} \bar{\mathbf{h}}[k] \\ \bar{\mathbf{v}}_\Delta[k] \\ \bar{\mathbf{u}}[k] \end{bmatrix} \end{aligned} \tag{4.52}$$

For the booster, a sensitivity weight, $\mathbf{W}_h(z^{-1})$ is chosen to be equivalent to the IMC filter, $(1 - f_{q_m}(z^{-1}))$ and is different for each mode. The weighted sensitivity of the resulting H_∞ controller compared to the IMC controller is shown in Fig. 4.28 which are equivalent for a particular uncertainty. Additionally, the step response shown in Fig. 4.29 of the resulting H_∞ controller demonstrates that integral action is achieved by including the weight $\mathbf{W}_y(z^{-1})$. If however the size of the uncertainty is increased, a more conservative controller is found, which results in less attenuation of low frequency disturbances and a lower bandwidth as shown in Fig. 4.30. By using an H_∞ approach, the effect of the size of the uncertainty can be explicitly accounted for in the controller design. While the choice of an IMC implementation is motivated by ease of implementation and tuning, the H_∞ approach can be used to design

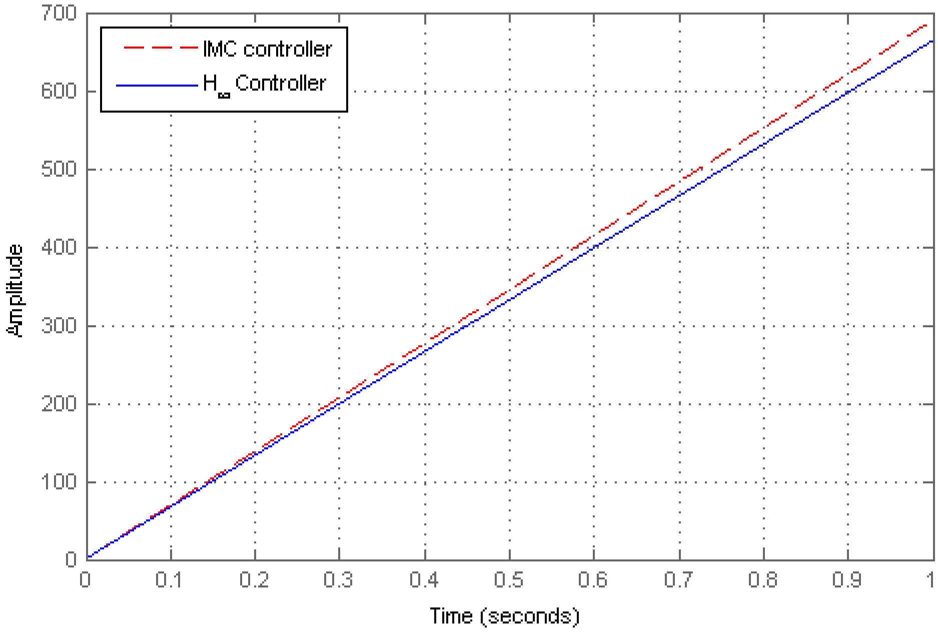

Fig. 4.29: Booster vertical controller step response of the IMC controller ('- -' red) compared to the H_∞ controller ('-' blue).

an equivalent filter $f_{q_m}(z^{-1})$ and therefore an equivalent IMC controller. The more conservative H_∞ controller was implemented on the booster and the integrated beam motion is shown in Fig. 4.31 compared with the more aggressive IMC controller. The effect of reducing the attenuation at low frequencies is evident from the more integrated motion at these frequencies, however the high frequency amplification is removed with this choice of weighted sensitivity.

4.7 Conclusion

An IMC controller structure is developed where two parameters are used to tune the controller dynamics in both spatial and temporal domains respectively. By considering the power distribution of the underlying disturbance, the controller bandwidth for each mode is selected. In this chapter an additive, structured uncertainty was used considered in the controller design. However while this simple uncertainty

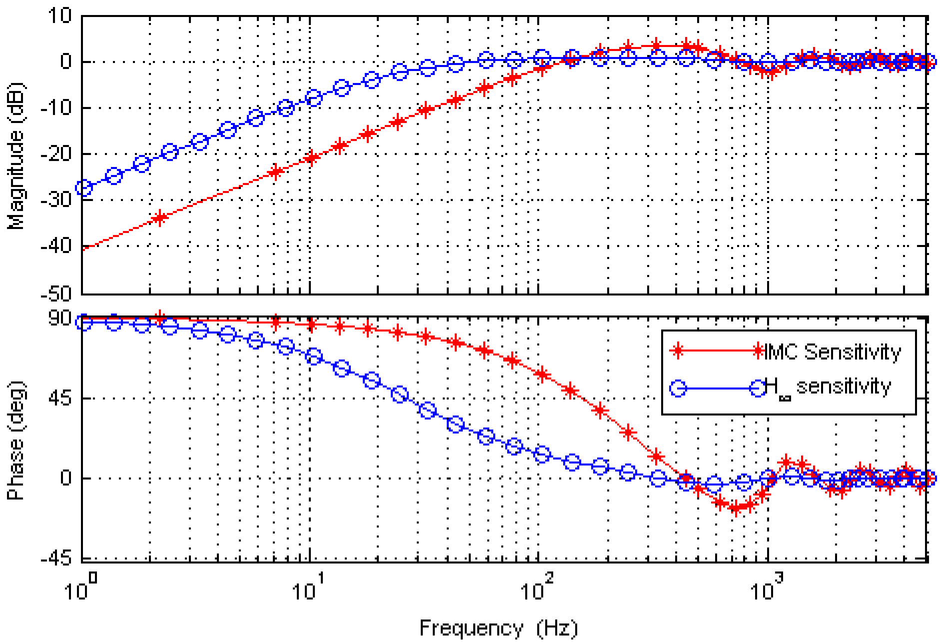

Fig. 4.30: Booster vertical closed loop sensitivity with IMC controller ('$*$' red) compared to H_∞ controller ('o' blue) for a larger uncertainty for each mode.

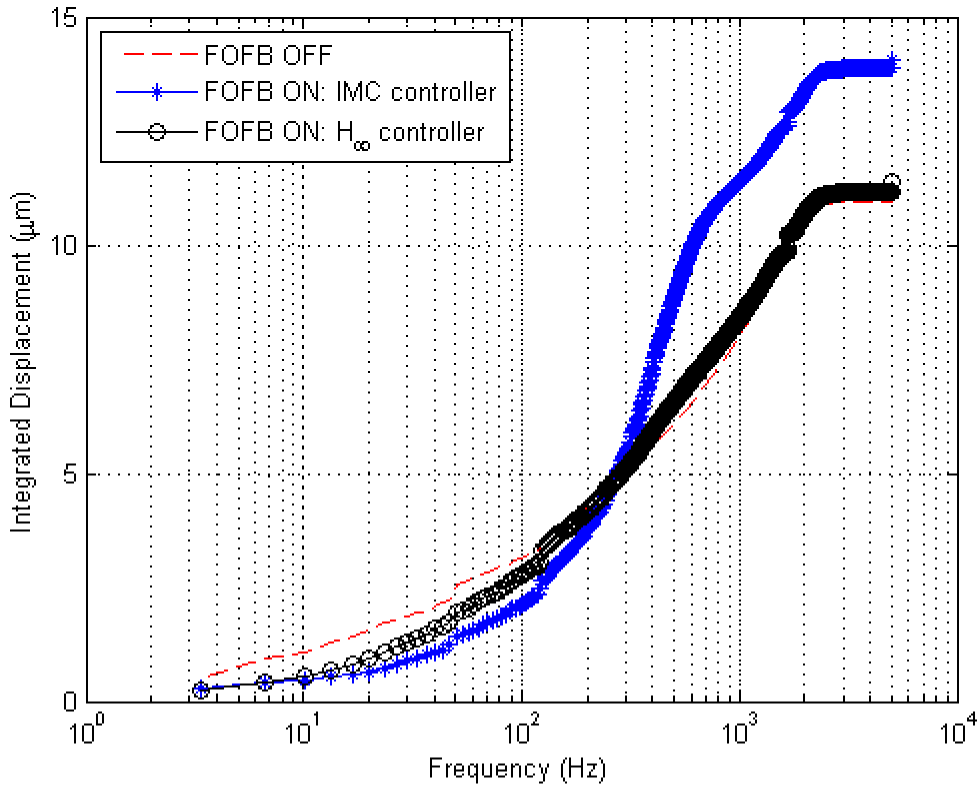

Fig. 4.31: Booster integrated beam motion at first vertical sensor for the uncontrolled beam ('- -' red) and the controlled beam using the IMC controller ('$*$' blue) and the H_∞ controller ('o' black).

model was useful to understand the tradeoffs of the design parameters in terms of performance and robustness, it is not realistic, namely because it does not account for errors in the sensors and actuators, which is addressed in the following chapter.

A robust stability test was developed in this chapter using the structured uncertainty representation by representing the spatial uncertainty with IQCs and the stability criteria was expressed in the form of an LMI feasibility problem by using the KYP lemma and the controller gain at each mode was tuned in order to meet robust stability criteria.

While modal truncation is motivated by the requirement to ensure robust stability and computational efficiency, two approaches offer increased flexibility in design and performance. The first being that by designing the controller to be aggressive in the low order modes and conservative at the high order modes, all modes of the process can be used for control to ensure maximum disturbance correction. This is achieved through a pseudo-inverse response matrix and the IQC stability test can be used to design this matrix to guarantee robust stability. Secondly, by selecting controller dynamics on a mode-by-mode basis, better performance is achieved because the dynamics are designed match the disturbance spectrum at that mode.

Finally, while the IMC structure is practical for implementation, an H_∞ control strategy can be used to design an equivalent IMC controller for some performance criteria since the weighted sensitivity selected for the H_∞ control strategy is directly related to the IMC filter parameter. Furthermore, both designs seek to minimise the effect of the disturbances on performance and ensure closed loop stability in the presence of spatial uncertainty.

Chapter 5

Fourier Decomposition and Uncertainty Modelling

In the Chapter 4, a robust stability test was used to determine the stability of the closed loop in the presence of uncertainty in the singular values. The test was used to indicate the allowable size of the uncertainty for each mode and it was demonstrated how the mode can be made less sensitive to errors in the singular values by changing the regularisation parameter μ. Though this result is useful, spatial uncertainty includes several sources, such as

- BPM scaling errors which originate from imperfect calibration of the sensors which are either static or changing slowly with time [Pfingstner and Snuverink, 2012].
- Actuator scaling errors which also come from calibration errors or magnetic field drift and are either static or changing slowly with time [Pfingstner and Snuverink, 2012].
- Drifts in the tune arising from any gradient errors which changes the pattern of the betatron function. These gradient errors can come from different sources

such as fabrication errors of the magnetic elements in quadrupoles, quadrupole power supply fluctuation or hysteresis during energy ramping, misalignment of sextupole magnets and even significant closed orbit perturbations [Jena et al., 2013].

Using the SVD approach these uncertainties will appear in the left and right singular vector matrices as well as the singular values. Therefore considering only uncertainty in the singular values is not realistic and in this chapter more realistic uncertainty models are presented where the three sources of uncertainty are decoupled and each maintains a direct physical interpretation.

5.1 Harmonic Modal Decomposition

The equation of the vertical disturbed closed orbit of Chapter 2 can be expressed as

$$\mathcal{Y}_c(\mathcal{Z}) = \frac{\theta_c\sqrt{\beta_0(\mathcal{Z})}\sqrt{\beta(\mathcal{Z})}}{2\sin\pi\mathcal{Q}}\cos\left(\mathcal{Q}\pi - (|\eta(\mathcal{Z}) - \eta_0(\mathcal{Z})|)\right) \tag{5.1}$$

and by introducing the Courant-Snyder variables [Courant and Snyder, 1958]

$$\begin{aligned}\tilde{\mathcal{Y}}_c &= \frac{\mathcal{Y}}{\sqrt{\beta}} \\ \tilde{\eta} &= \frac{\eta}{\mathcal{Q}}\end{aligned} \tag{5.2}$$

(5.1) can be written as

$$\tilde{\mathcal{Y}}_c(\mathcal{Z}) = \frac{\theta_c\sqrt{\beta_0(\mathcal{Z})}}{2\sin\pi\mathcal{Q}}\cos\mathcal{Q}\left(\pi - (|\tilde{\eta}(\mathcal{Z}) - \tilde{\eta}_0(\mathcal{Z})|)\right) \tag{5.3}$$

Fourier analysis of (5.3) gives (where the $\mathcal{Z}$ operator is omitted for clarity) [Yu et al., 1989]

$$\tilde{\mathcal{Y}}_c = \frac{\theta_c\beta_0}{2\sin\pi\mathcal{Q}}\sum_{f=0}^{\infty}\hat{\sigma}_f\cos f(\tilde{\eta} - \tilde{\eta}_0) \tag{5.4}$$

where

$$
\begin{aligned}
\hat{\sigma}_{f_0} &= \frac{1}{2\pi}\int_{-\pi}^{\pi} \cos \mathcal{Q}\tilde{\eta}\,\mathrm{d}\tilde{\eta} = \frac{1}{\mathcal{Q}}\frac{\sin \mathcal{Q}\pi}{\pi} \\
\hat{\sigma}_{f} &= \frac{(-1)^f}{\pi}\int_{-\pi}^{\pi} \cos f\tilde{\eta} \cos \mathcal{Q}\tilde{\eta}\,\mathrm{d}\tilde{\eta} = \frac{2\mathcal{Q}}{\mathcal{Q}^2 - f^2}\frac{\sin \mathcal{Q}\pi}{\pi} \quad (f = 1, 2, \dots)
\end{aligned}
\tag{5.5}
$$

The expression in (5.4) can be further simplified by

$$
\tilde{\mathcal{Y}}_c = \theta_c \beta_0 \sum_{f=0}^{\infty} \hat{\sigma}_f \cos f(\tilde{\eta} - \tilde{\eta}_0) \tag{5.6}
$$

where the Fourier coefficients are redefined as

$$
\begin{aligned}
\hat{\sigma}_{f_0} &= \frac{1}{2\pi}\frac{1}{\mathcal{Q}} \\
\hat{\sigma}_{f} &= \frac{1}{2\pi}\frac{2\mathcal{Q}}{\mathcal{Q}^2 - f^2} \quad (f = 1, 2, \dots)
\end{aligned}
\tag{5.7}
$$

and therefore each element of the response matrix defined as $\mathcal{Y}_c/\theta_c$ is given by

$$
\begin{aligned}
r_n(\tilde{\eta}_m) &= \sqrt{\beta_m}\sqrt{\beta_n} \sum_{f=-F}^{F} \hat{\sigma}_f \cos f(\tilde{\eta}_m - \tilde{\eta}_n) \\
&= \sqrt{\beta_m}\sqrt{\beta_n} \sum_{f=-F}^{F} \hat{\sigma}_f \mathrm{e}^{if\tilde{\eta}_m} \mathrm{e}^{-if\tilde{\eta}_n}
\end{aligned}
\tag{5.8}
$$

for $f = [-F, \dots, F]$ where F is chosen so that $F \leq M \leq N$. The Fourier coefficients defined in (5.7) are shown in Fig. 5.1a and Fig. 5.1b for the vertical and horizontal responses of the storage ring respectively. The resonance properties of the disturbed closed orbit are evident. The orbit is most sensitive to those Fourier components of the perturbation whose order is close to the tune, $\mathcal{Q}$. Furthermore, (5.8) shows that the Fourier components must be taken with respect to the phase variable $\tilde{\eta}$ rather than the geometrical variable $\mathcal{Z}$ [Courant and Snyder, 1958].

In matrix form (5.8) becomes

$$
\mathbf{R} = \hat{\mathbf{\Phi}}\hat{\mathbf{\Sigma}}\hat{\mathbf{\Psi}}^{\mathrm{T}} \tag{5.9}
$$

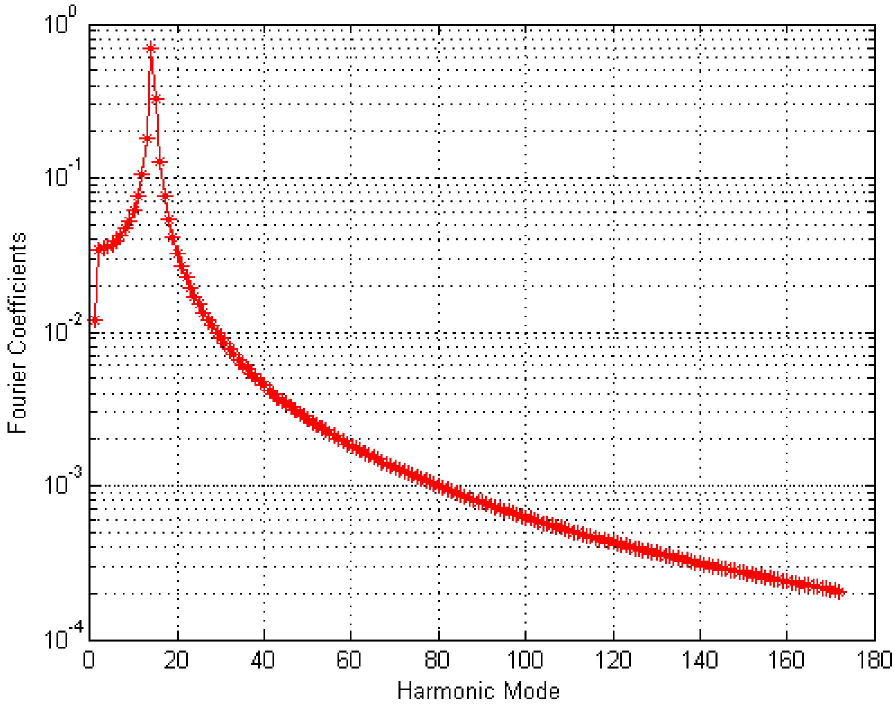

(a) Vertical Fourier coefficients $|\hat{\sigma}_f|$ of the storage ring for the vertical tune $\mathcal{Q}_{\mathcal{Y}} = 13.324$.

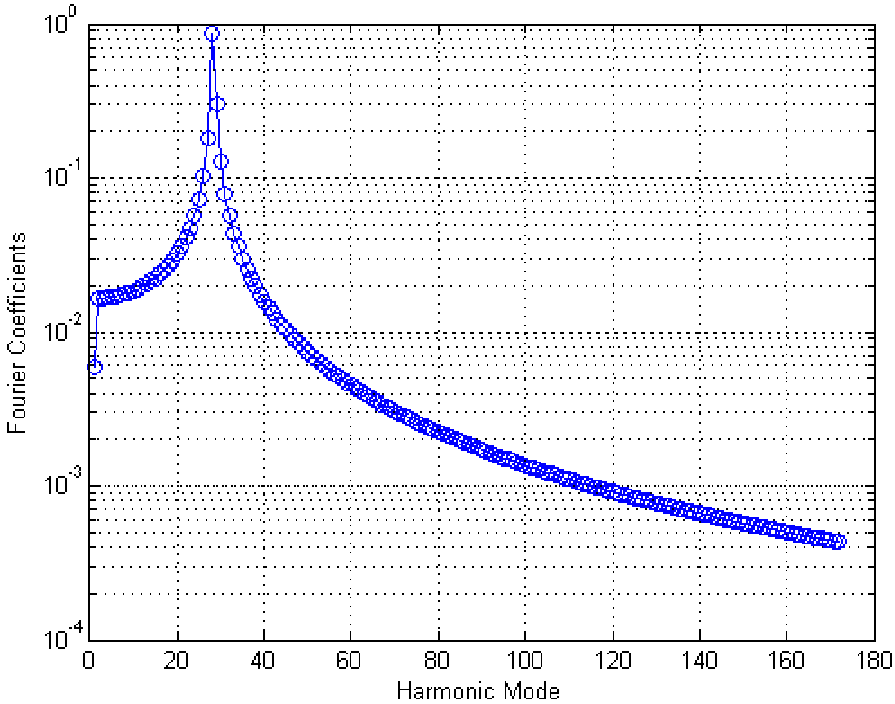

(b) Horizontal Fourier coefficients $|\hat{\sigma}_f|$ of the storage ring for the horizontal tune $\mathcal{Q}_{\mathcal{X}} = 27.266$.

Fig. 5.1: Storage ring Fourier coefficients.

where

$$\begin{aligned}
\hat{\boldsymbol{\Sigma}} &= \operatorname{diag}_{f=-F,\ldots,F}\{\hat{\sigma}_f\} \\
\hat{\boldsymbol{\Phi}} &= \operatorname{diag}_{m=1,\ldots,M}\{\sqrt{\beta_m}\}\left[\mathrm{e}^{if\tilde{\eta}_m}\right]_{mf} \\
\hat{\boldsymbol{\Psi}} &= \operatorname{diag}_{n=1,\ldots,N}\{\sqrt{\beta_n}\}\left[\mathrm{e}^{-if\tilde{\eta}_n}\right]_{nf}
\end{aligned} \tag{5.10}$$

and $\hat{\boldsymbol{\Phi}} \in \mathbb{C}^{M\times(2F+1)}$, $\hat{\boldsymbol{\Sigma}} \in \mathbb{C}^{(2F+1)\times(2F+1)}$ and $\hat{\boldsymbol{\Psi}} \in \mathbb{C}^{N\times(2F+1)}$ [Gayadeen and Duncan, 2012]. The Fourier coefficients in $\hat{\boldsymbol{\Sigma}}$ are completely determined by the tune of the machine and the matrices $\hat{\boldsymbol{\Phi}}$ and $\hat{\boldsymbol{\Psi}}$ are determined by the betatron phases of the BPMs and corrector magnets, which in turn depends solely on the position of the BPMs and the strengths of the corrector magnets respectively. The columns of $\hat{\boldsymbol{\Phi}}$ and $\hat{\boldsymbol{\Psi}}$ are therefore not orthogonal because of the uneven spacing of BPMs and corrector magnets. However, the matrices are block orthogonal due to the repetition of cells and symmetry of the ring.

5.2 Uncertainty Modelling

Using the harmonic decomposition of the response matrix developed in Section 5.1, the spatially uncertain response can be expressed as

$$\mathbf{y}[k] = \left[\mathbf{I} + \mathbf{W}_{\hat{\Phi}}\boldsymbol{\Delta}_{\hat{\Phi}}\right]\hat{\boldsymbol{\Phi}}g(z^{-1})\hat{\boldsymbol{\Sigma}}\left[\mathbf{I} + \mathbf{W}_{\hat{\Sigma}}\boldsymbol{\Delta}_{\hat{\Sigma}}\right]\left[\mathbf{I} + \mathbf{W}_{\hat{\Psi}}\boldsymbol{\Delta}_{\hat{\Psi}}\right]\hat{\boldsymbol{\Psi}}^{-\mathrm{T}}\mathbf{u}[k] + \mathbf{h}[k] \tag{5.11}$$

In this expression, $\boldsymbol{\Delta}_{\hat{\Phi}}$ represents errors in the BPM positions and $\boldsymbol{\Delta}_{\hat{\Psi}}$ represents variations in the strengths of the corrector magnets. The weights $\mathbf{W}_{\hat{\Phi}}$ and $\mathbf{W}_{\hat{\Psi}}$ are normalisation weights so that $\|\boldsymbol{\Delta}_{\hat{\Phi}}\|_\infty \leq 1$ and $\|\boldsymbol{\Delta}_{\hat{\Psi}}\|_\infty \leq 1$. These uncertainties were measured on the storage ring and the structures are shown in Fig. 5.2 and Fig. 5.3. Because $\hat{\boldsymbol{\Phi}}$ and $\hat{\boldsymbol{\Psi}}$ are determined solely by the position of the BPMs and strengths of the corrector for each component, and there is no coupling between the BPMs and correctors, both $\boldsymbol{\Delta}_{\hat{\Phi}}$ and $\boldsymbol{\Delta}_{\hat{\Psi}}$ can described by diagonally structured

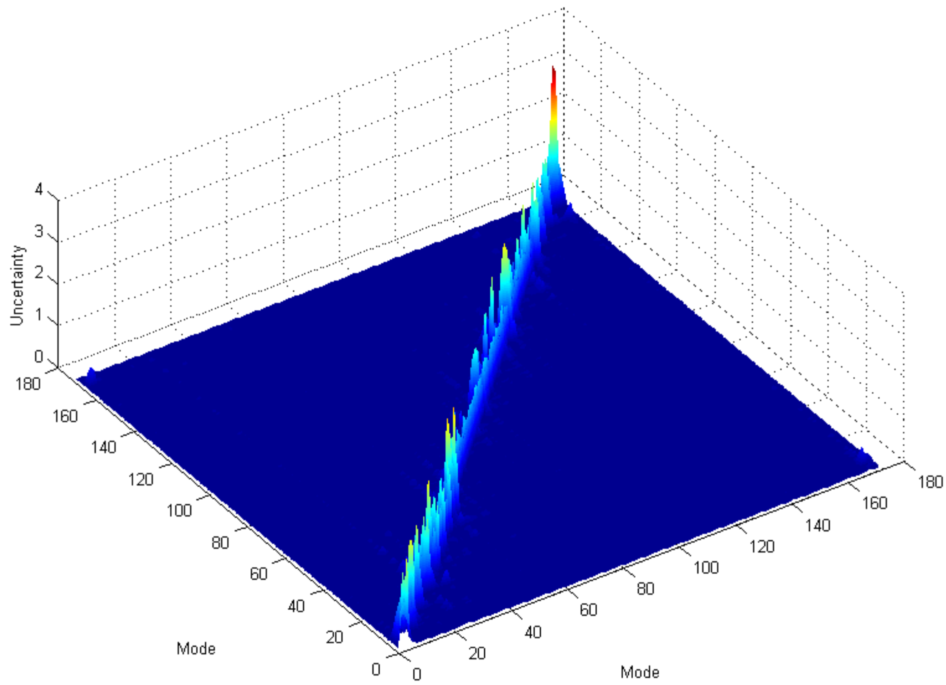

Fig. 5.2: Storage ring uncertainty $|\mathbf{W}_{\hat{\Phi}}\boldsymbol{\Delta}_{\hat{\Phi}}|$ in BPM positions between measured vertical response matrix and ideal vertical response matrix.

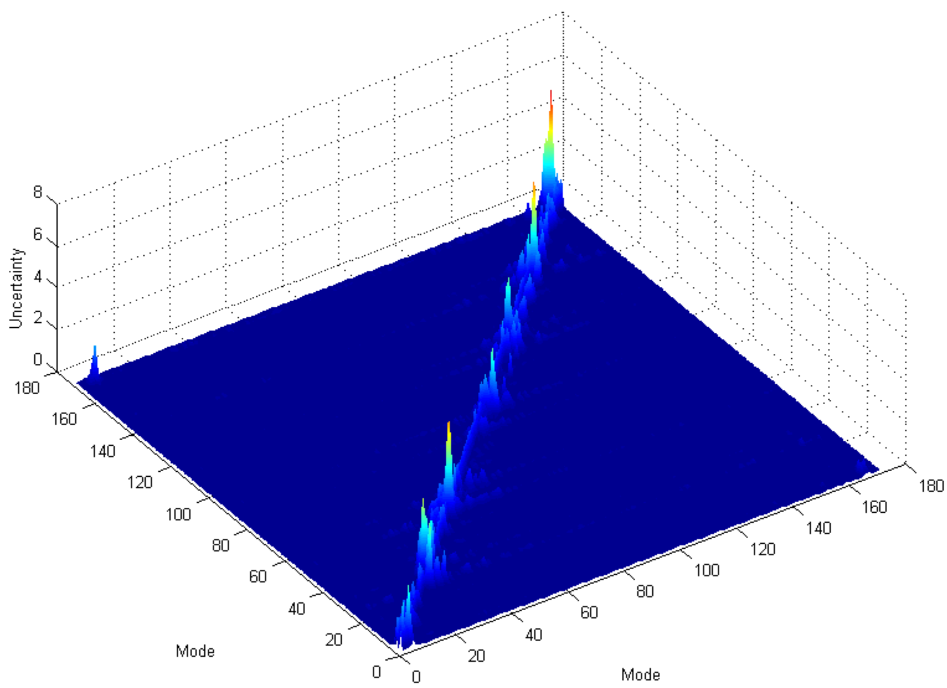

Fig. 5.3: Storage ring uncertainty $|\mathbf{W}_{\hat{\Psi}}\boldsymbol{\Delta}_{\hat{\Psi}}|$ in corrector magnet strengths between measured vertical response matrix and ideal vertical response matrix.

operators such that

$$\begin{aligned} \boldsymbol{\Delta}_{\hat{\Phi}} &= \text{diag}\{\delta_{\hat{\Phi}_f}\} \\ \boldsymbol{\Delta}_{\hat{\Psi}} &= \text{diag}\{\delta_{\hat{\Psi}_f}\} \end{aligned} \tag{5.12}$$

with $\|\delta_{(\hat{\Phi},\hat{\Psi})_f}\|_\infty \leq 1$, $\forall f \in [-F, \dots, F]$.

Likewise, the uncertainty $\boldsymbol{\Delta}_{\hat{\Sigma}}$ represents the error in the Fourier coefficients and given (5.7), it is related to the uncertainty in the tune, where for each harmonic mode

$$\Delta_{\hat{\Sigma}_f} \approx \left.\frac{\delta \hat{\sigma}_f}{\delta \mathcal{Q}}\right|_{\mathcal{Q}=\mathcal{Q}_0} \Delta_{\mathcal{Q}} \tag{5.13}$$

where

$$\left.\frac{\delta \hat{\sigma}_f}{\delta \mathcal{Q}}\right|_{\mathcal{Q}=\mathcal{Q}_0} = \frac{\hat{\sigma}_f}{\mathcal{Q}_0}\left[\frac{f^2 + {\mathcal{Q}_0}^2}{f^2 - {\mathcal{Q}_0}^2}\right] \tag{5.14}$$

and $\mathcal{Q}_0$ is the nominal tune. Therefore, $\boldsymbol{\Delta}_{\hat{\Sigma}}$ is dependent only on the tune and can be represented by a multiplicative operator

$$\boldsymbol{\Delta}_{\hat{\Sigma}} = \text{diag}\{\Delta_{\hat{\Sigma}_f}\} \tag{5.15}$$

where $\|\Delta_{\hat{\Sigma}_f}\|_\infty \leq 1$ and

$$\boldsymbol{\Delta}_{\hat{\Sigma}} = \text{diag}\left\{\frac{\hat{\sigma}_f}{\mathcal{Q}_0}\left[\frac{f^2 + {\mathcal{Q}_0}^2}{f^2 - {\mathcal{Q}_0}^2}\right]\right\} \boldsymbol{\Delta}_{\mathcal{Q}} \tag{5.16}$$

The tune of the machine is a measurable parameter and severe drift of the tune will cause the electron oscillations of the perturbed beam to grow rapidly to amplitudes larger than normal creating dangerous resonances. The increase in beam size may cause loss of electrons or decrease the beam density, reducing the effective emittance [Sands, 1970]. Representing the uncertainty as errors in the tune is more intuitive than using Fourier coefficients as it maintains a direct physical interpretation, similar to the uncertainties in the BPM positions, $\boldsymbol{\Delta}_{\hat{\Phi}}$ and corrector magnets strengths $\boldsymbol{\Delta}_{\hat{\Psi}}$.

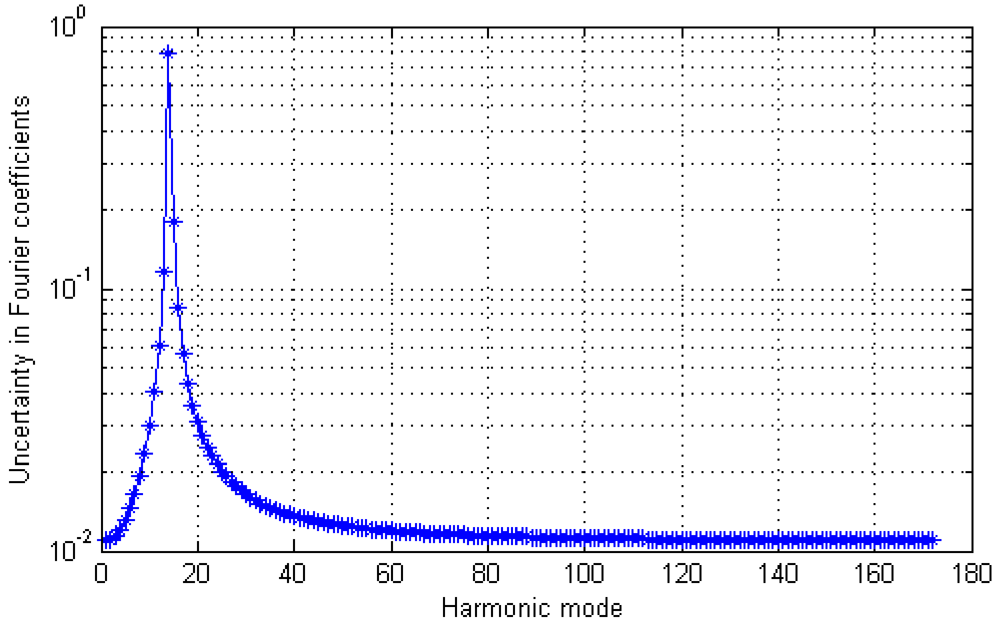

Fig. 5.4: Storage ring uncertainty $|\mathbf{\Delta}_{\hat{\Sigma}}|$ between measured vertical response matrix and ideal vertical response matrix for a 1% change in tune.

Therefore, with

$$\mathbf{W}_{\hat{\Sigma}} = \mathrm{diag}\left\{\frac{\mathcal{Q}_0}{\hat{\sigma}_f}\left[\frac{f^2 - {\mathcal{Q}_0}^2}{f^2 + {\mathcal{Q}_0}^2}\right]\right\} \tag{5.17}$$

uncertainty in the tune can be expressed in the form

$$\mathbf{W}_{\hat{\Sigma}}\mathbf{\Delta}_{\hat{\Sigma}} = \mathbf{\Delta}_{\mathcal{Q}} \tag{5.18}$$

The size of the uncertainty in the Fourier coefficients is shown in Fig. 5.4 for a change in the vertical tune from the ideal 13.324 to 13.18 (i.e $\approx$ 1% change). The largest error is associated with the harmonic mode closest to the tune and the errors furthest away from the tune are almost negligible in comparison.

5.3 Harmonic Robust Stability Analysis

The three norm-bounded uncertainty operators in (5.11) can be combined and represented as $\mathbf{\Delta}_F = \mathrm{diag}\{\mathbf{\Delta}_{\hat{\Phi}}, \mathbf{\Delta}_{\hat{\Sigma}}, \mathbf{\Delta}_{\hat{\Psi}}\}$. If $\mathbf{\Delta}_{\hat{\Phi}} \in \mathrm{IQC}(\mathbf{\Pi}_{\mathbf{\Delta}_{\hat{\Phi}}})$, $\mathbf{\Delta}_{\hat{\Sigma}} \in \mathrm{IQC}(\mathbf{\Pi}_{\mathbf{\Delta}_{\hat{\Sigma}}})$

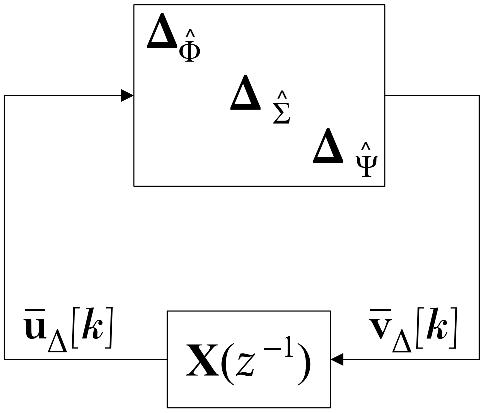

Fig. 5.5: The closed loop system represented in standard feedback configuration where three uncertainties are considered as described by (5.11).

and $\mathbf{\Delta}_{\hat{\Psi}} \in \mathrm{IQC}(\mathbf{\Pi}_{\mathbf{\Delta}_{\hat{\Psi}}})$ the following multipliers can be chosen

$$\begin{aligned}
\mathbf{\Pi}_{\Delta_{\hat{\Phi}}} &= \begin{bmatrix} \mathbf{\Gamma}_{\hat{\Phi}} & \\ & -\mathbf{\Gamma}_{\hat{\Phi}} \end{bmatrix} \\
\mathbf{\Pi}_{\Delta_{\hat{\Sigma}}} &= \begin{bmatrix} \mathbf{\Gamma}_{\hat{\Sigma}} & \\ & -\mathbf{\Gamma}_{\hat{\Sigma}} \end{bmatrix} \\
\mathbf{\Pi}_{\Delta_{\hat{\Psi}}} &= \begin{bmatrix} \mathbf{\Gamma}_{\hat{\Psi}} & \\ & -\mathbf{\Gamma}_{\hat{\Psi}} \end{bmatrix}
\end{aligned} \tag{5.19}$$

In particular, for diagonally structured uncertainties

$$\begin{aligned}
\mathbf{\Gamma}_{\hat{\Phi}} &= \mathrm{diag}\{\gamma_{\hat{\Phi}_f}\} \\
\mathbf{\Gamma}_{\hat{\Sigma}} &= \mathrm{diag}\{\gamma_{\hat{\Sigma}_f}\} \\
\mathbf{\Gamma}_{\hat{\Psi}} &= \mathrm{diag}\{\gamma_{\hat{\Psi}_f}\}
\end{aligned} \tag{5.20}$$

where $\gamma_{\hat{\Phi}_f} > 0$, $\gamma_{\hat{\Sigma}_f} > 0$ and $\gamma_{\hat{\Psi}_f} > 0$, $\forall f \in [-F, \ldots, F]$. If $\mathbf{\Delta}_F \in \mathrm{IQC}(\mathbf{\Pi}_{\mathbf{\Delta}_F})$ then

$$\mathbf{\Pi}_{\mathbf{\Delta}_F} = \mathrm{daug}\left(\mathbf{\Pi}_{\Delta_{\hat{\Phi}}}, \mathbf{\Pi}_{\Delta_{\hat{\Sigma}}}, \mathbf{\Pi}_{\Delta_{\hat{\Psi}}}\right) \tag{5.21}$$

where daug$(\cdot)$ represents the diagonal augmentation of the submultipliers described in [El Ghaoui and Niculescu, 2000] such that

$$\mathbf{\Pi}_{\mathbf{\Delta}_F} = \left[\begin{array}{ccc|ccc} \mathbf{\Gamma}_{\hat{\Phi}} & & & & & \\ & \mathbf{\Gamma}_{\hat{\Sigma}} & & & & \\ & & \mathbf{\Gamma}_{\hat{\Psi}} & & & \\ \hline & & & -\mathbf{\Gamma}_{\hat{\Phi}} & & \\ & & & & -\mathbf{\Gamma}_{\hat{\Sigma}} & \\ & & & & & -\mathbf{\Gamma}_{\hat{\Psi}} \end{array}\right] \tag{5.22}$$

The closed loop system with uncertainty can be completely represented in the standard feedback form shown in Fig. 5.5 where

$$\begin{bmatrix} \bar{\mathbf{u}}_{\hat{\Phi}}[k] \\ \bar{\mathbf{u}}_{\hat{\Sigma}}[k] \\ \bar{\mathbf{u}}_{\hat{\Psi}}[k] \end{bmatrix} = \begin{bmatrix} \mathbf{X}_{11}(z^{-1}) & \mathbf{X}_{12}(z^{-1}) & \mathbf{X}_{13}(z^{-1}) \\ \mathbf{X}_{21}(z^{-1}) & \mathbf{X}_{22}(z^{-1}) & \mathbf{X}_{23}(z^{-1}) \\ \mathbf{X}_{31}(z^{-1}) & \mathbf{X}_{32}(z^{-1}) & \mathbf{X}_{33}(z^{-1}) \end{bmatrix} \begin{bmatrix} \bar{\mathbf{v}}_{\hat{\Phi}}[k] \\ \bar{\mathbf{v}}_{\hat{\Sigma}}[k] \\ \bar{\mathbf{v}}_{\hat{\Psi}}[k] \end{bmatrix} \tag{5.23}$$

where

$$\begin{aligned} \mathbf{X}_{11}(z^{-1}) &= -\mathbf{PQ}(z^{-1})g(z^{-1})\mathbf{W}_{\hat{\Phi}} \\ \mathbf{X}_{12}(z^{-1}) &= \hat{\mathbf{\Sigma}}g(z^{-1})\hat{\mathbf{\Phi}}\left[\mathbf{I} - \mathbf{PQ}(z^{-1})g(z^{-1})\right]\mathbf{W}_{\hat{\Phi}} \\ \mathbf{X}_{13}(z^{-1}) &= \hat{\mathbf{\Phi}}\hat{\mathbf{\Sigma}}g(z^{-1})\hat{\mathbf{\Psi}}^{-\mathrm{T}}\left[\mathbf{I} - \mathbf{PQ}(z^{-1})g(z^{-1})\right]\mathbf{W}_{\hat{\Phi}} \\ \mathbf{X}_{21}(z^{-1}) &= -\hat{\mathbf{\Phi}}^{-1}\mathbf{P}\hat{\mathbf{\Sigma}}^{-1}\mathbf{Q}(z^{-1})\mathbf{W}_{\hat{\Sigma}} \\ \mathbf{X}_{22}(z^{-1}) &= -\mathbf{PQ}(z^{-1})g(z^{-1})\mathbf{W}_{\hat{\Sigma}} \\ \mathbf{X}_{23}(z^{-1}) &= \hat{\mathbf{\Phi}}^{-1}\left[\mathbf{I} - \mathbf{PQ}(z^{-1})g(z^{-1})\right]\mathbf{W}_{\hat{\Sigma}} \\ \mathbf{X}_{31}(z^{-1}) &= \hat{\mathbf{\Phi}}^{-1}\mathbf{P}\hat{\mathbf{\Sigma}}^{-1}\mathbf{Q}(z^{-1})\hat{\mathbf{\Psi}}\mathbf{W}_{\hat{\Psi}} \\ \mathbf{X}_{32}(z^{-1}) &= -\hat{\mathbf{\Psi}}\mathbf{PQ}(z^{-1})g(z^{-1})\mathbf{W}_{\hat{\Psi}} \\ \mathbf{X}_{33}(z^{-1}) &= -\mathbf{PQ}(z^{-1})g(z^{-1})\mathbf{W}_{\hat{\Psi}} \end{aligned} \tag{5.24}$$

where the regularisation gain matrix $\mathbf{P}$ has diagonal elements $p_f = \hat{\sigma}_f^2/(\hat{\sigma}_f^2 + \mu)$.

5.4 Storage Ring Robust Stability in the Presence of Tune Drift

The benefit of using a Fourier decomposition technique, over the traditional singular value decomposition is the relationship between the spatial modes and a meaningful physical interpretation. Harmonic coefficients are related to the tune (described by (5.7)) which is a measurable beam parameter that is crucial to optimal performance of the accelerator. When SVD is used for modal decomposition, the uncertainty associated with the singular values is not diagonally structured since it combines errors in the tune, strengths of corrector magnets and positions of BPMs. A meaningful comparison between the Fourier coefficients and singular values can be made by reordering the Fourier coefficients in descending order. Fig. 5.6a shows the reordered Fourier coefficients compared to the singular values plotted in Fig. 5.6b. It is reasonable then to associate the largest singular value with the tune - a relationship which is not obvious.

If harmonic decomposition of the response matrix is chosen for implementation of the controller rather than a singular value decomposition, the design procedure presented in Chapter 4 can be followed. In this case, a regularisation parameter μ can also be applied to the Fourier coefficients to make the controller more aggressive at particular modes. For the SVD, the regularisation parameter was used to limit control effort on the high order modes defined by low-gain directions. However, a harmonic decomposition results in modes with low gains that are furthest away from the tune and the regularisation parameter is used to limit control on modes further from the tune. The effect of the regularisation parameter on the controller gain using harmonic analysis is shown in Fig. 5.7 and similar to the singular value modes, large values of μ effectively switches off the low-gain directions.

Similarly, the distribution of the disturbance content in harmonic mode space is

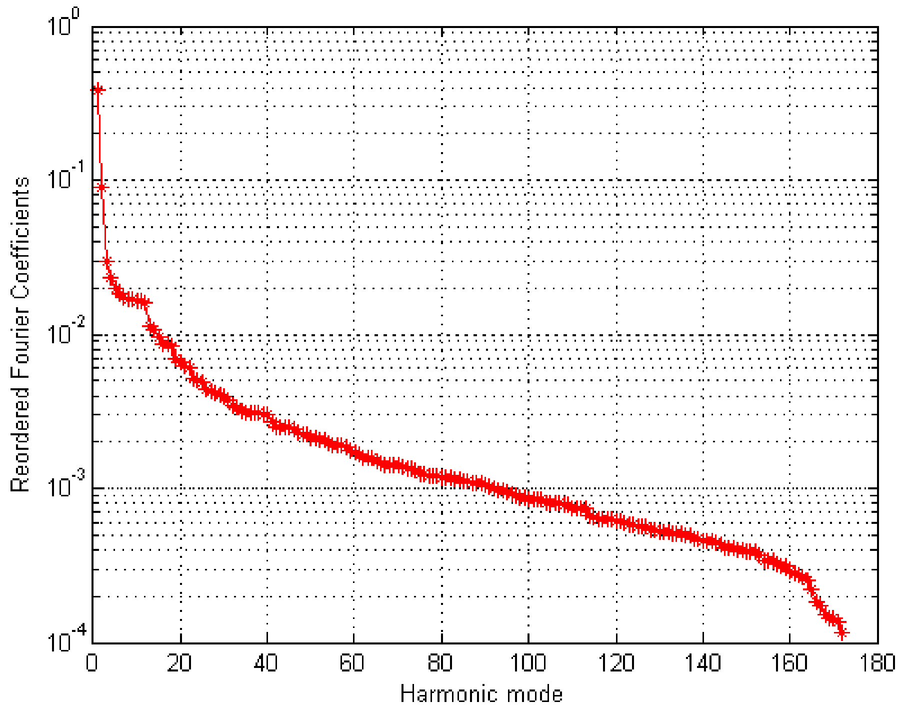

(a) Storage ring vertical Fourier coefficients reordered in descending order

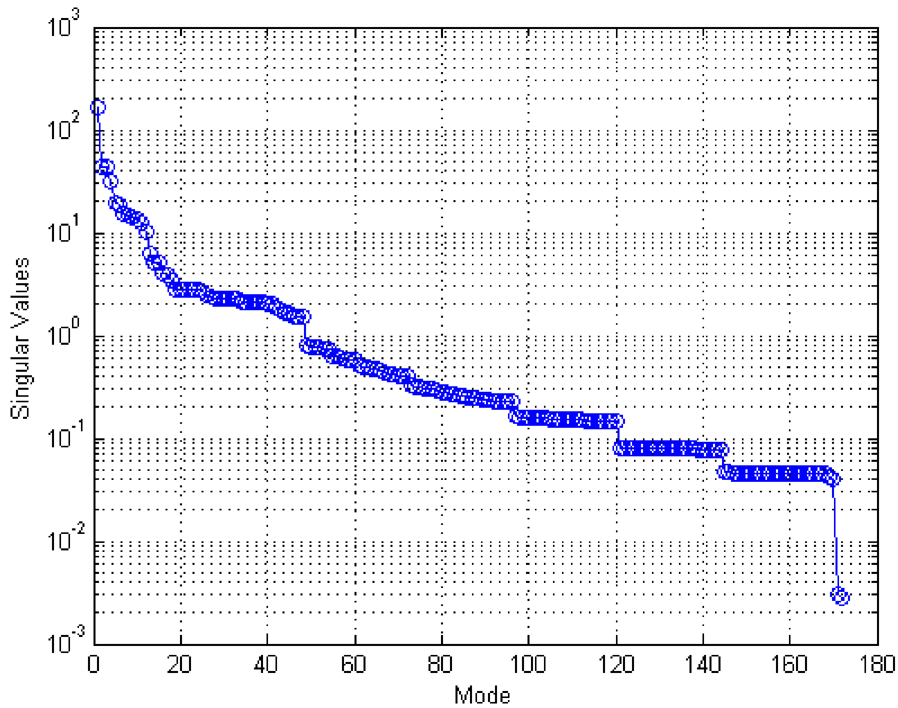

(b) Storage ring vertical singular values

Fig. 5.6: Comparison of re-ordered Fourier coefficients and singular values.

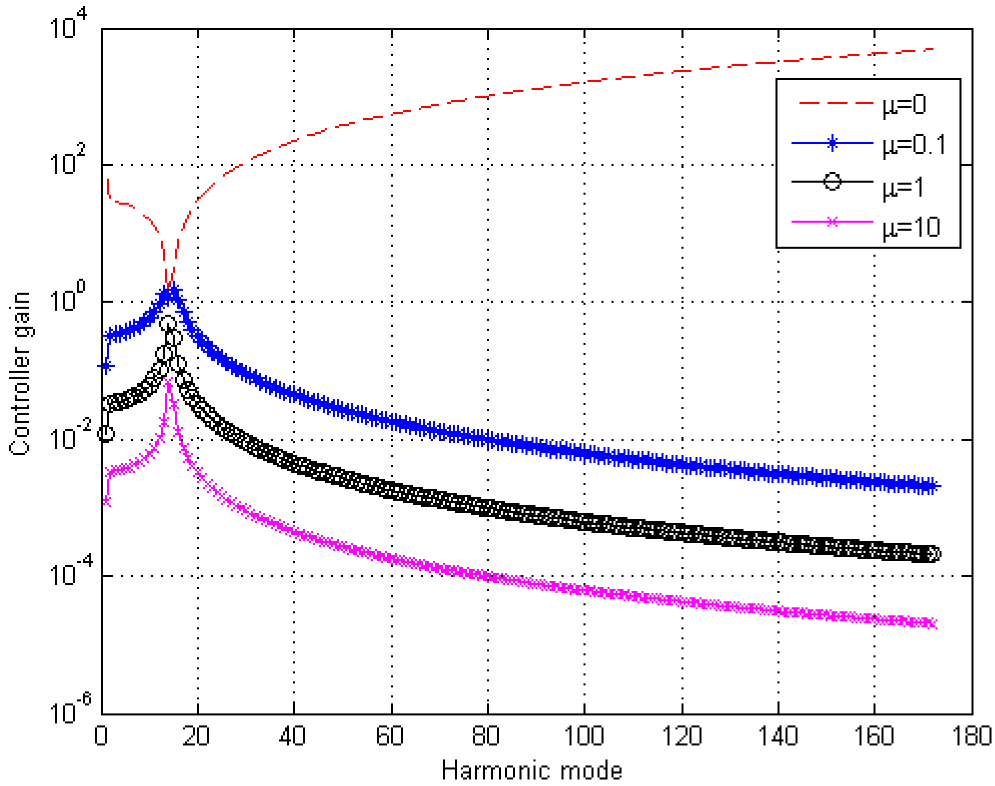

Fig. 5.7: The inverse Fourier coefficients for the vertical response matrix of storage ring ('- -' red) (corresponding to $\mu = 0$) shown with the regularised controller gain, $p_f \hat{\sigma}_f^{-1}$ for each mode where $\mu = 0.1$ ('$*$' blue), $\mu = 1$ ('o' black) and $\mu = 10$ ('x' magenta).

used to select appropriate controller bandwidths for each mode. Fig. 5.8 shows the disturbance content for the first 40 harmonic modes which not only shows the 20Hz disturbance peak but also that the bulk of the disturbance power is concentrated around the modes associated with the tune (where $\mathcal{Q}_{\mathcal{Y}} = 13.324$). Therefore, these modes constitute the low order singular value modes and, for a harmonic modal approach, the two-dimensional sensitivity is designed to focus disturbance attenuation at low frequencies (i.e. < 100Hz), as is the case when using SVD but instead the sensitivity function is smallest at modes close to the tune value, as shown in Fig. 5.9.

Using the robust stability analysis, the closed loop stability in the presence of tune drift can be quantified. Using the harmonic decomposition of the response matrix,

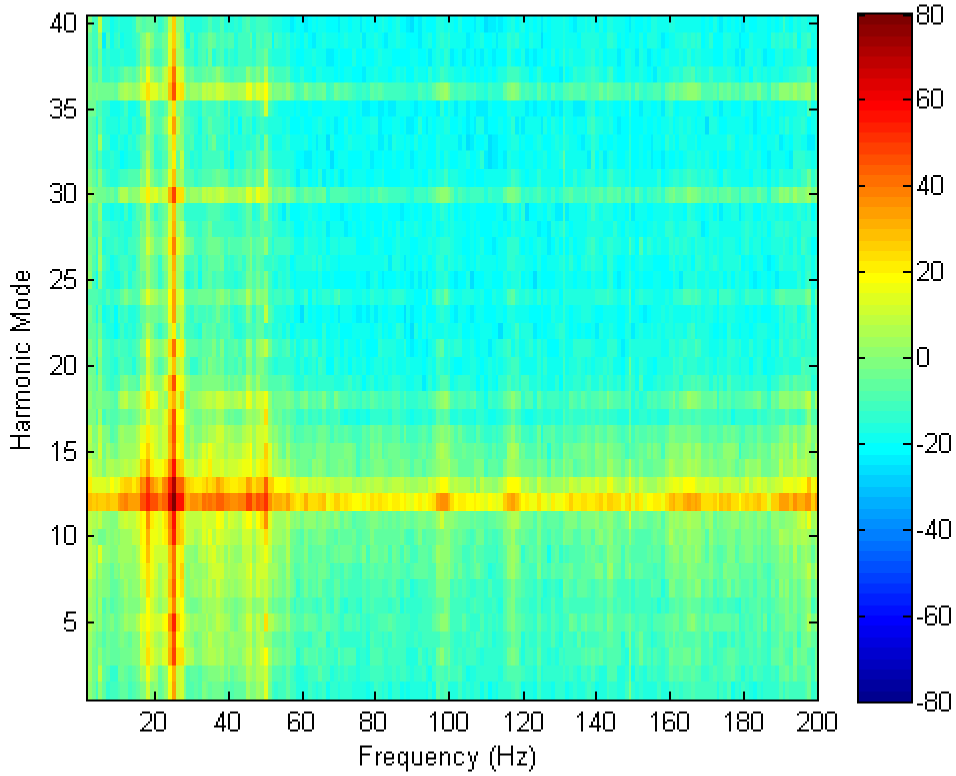

Fig. 5.8: Colormap of average power (dB) for each harmonic mode against frequency (Hz).

the robust stability test is decoupled on a mode-by-mode basis and for each mode there exists some $\gamma_{\hat{\Sigma}_f} > 0$ so that feasibility condition becomes

$$p_f^2 \hat{\sigma}_f^{-2} w_{\hat{\Sigma}_f} q_f^*(z^{-1}) q_f(z^{-1}) g^*(z^{-1}) g(z^{-1}) \gamma_{\hat{\Sigma}_f} - \gamma_{\hat{\Sigma}_f} \leq \epsilon \tag{5.25}$$

where the weight at each vertical harmonic mode $w_{\hat{\Sigma}_m}$ is determined from measured response matrices and is shown in Fig. 5.10. The robust analysis was performed to determine the allowable size of the uncertainty in the Fourier coefficients for each mode. However, using the relationship between the Fourier coefficients and the tune, the least upper bound on the uncertainty in the Fourier coefficients was used to determine the bound on the tune, which is shown in Fig. 5.11 for various values of μ. The allowable size of the error in the tune can be compared to measured results. For example, in Fig. 5.12 the drift in the tune over an hour of operation is

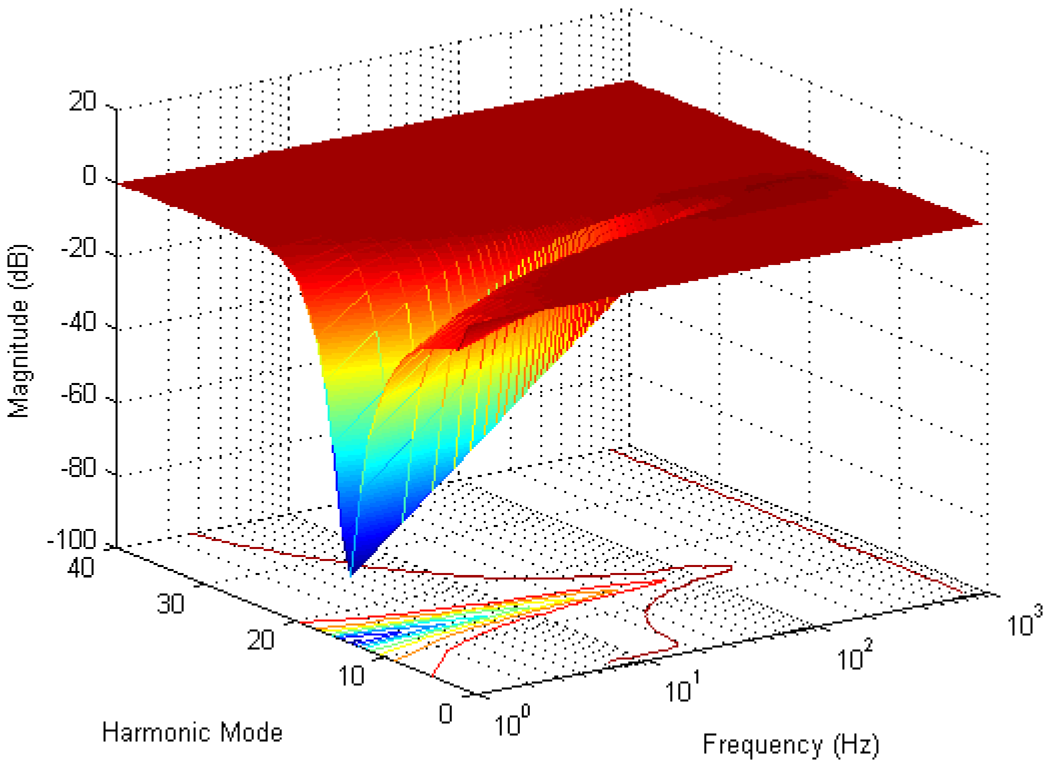

Fig. 5.9: Storage ring vertical sensitivity function in both harmonic spatial and temporal frequency domains.

shown where the maximum change in the tune is 0.0012. From Fig. 5.11, for $\mu = 10$, the allowable size of drift in the tune for the mode associated with the tune (the 13th mode) is found to be 0.006. Therefore, for the expected drift in tune during operation, the closed loop is expected to be stable in the case where the errors in tune are the only source of uncertainty. From Fig. 5.11, a smaller regularisation parameter makes the closed loop less sensitive to changes in the tune.

5.5 Conclusion

The Fourier analysis of the disturbed closed orbit yields a harmonic decomposition of the response matrix, similar to the SVD of the response matrix. There are differences though, namely that the left and right harmonic matrices are determined

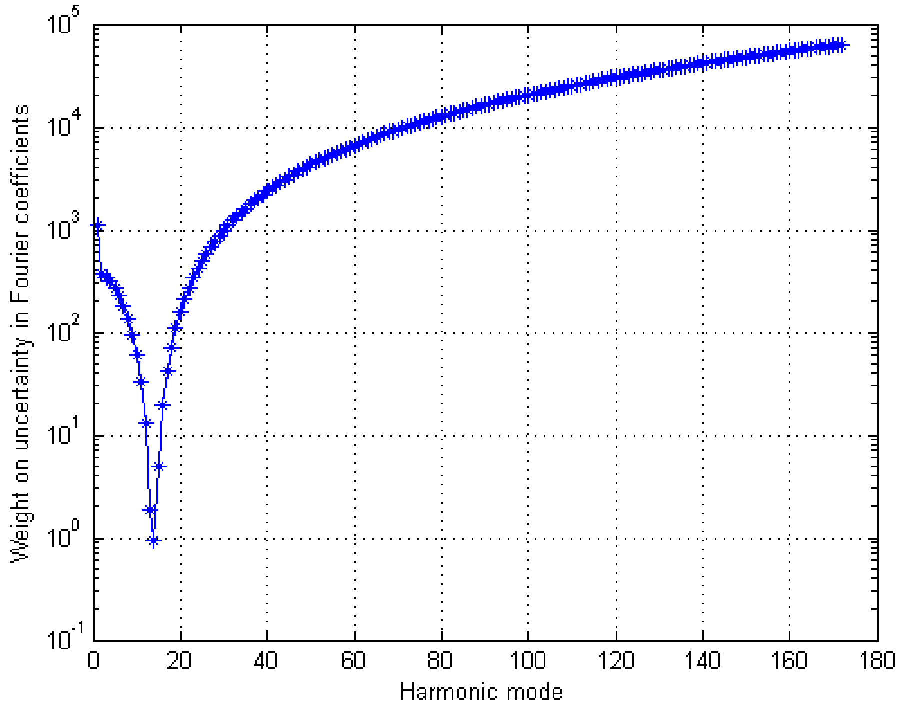

Fig. 5.10: Weight on uncertainty on Fourier coefficients for each vertical mode.

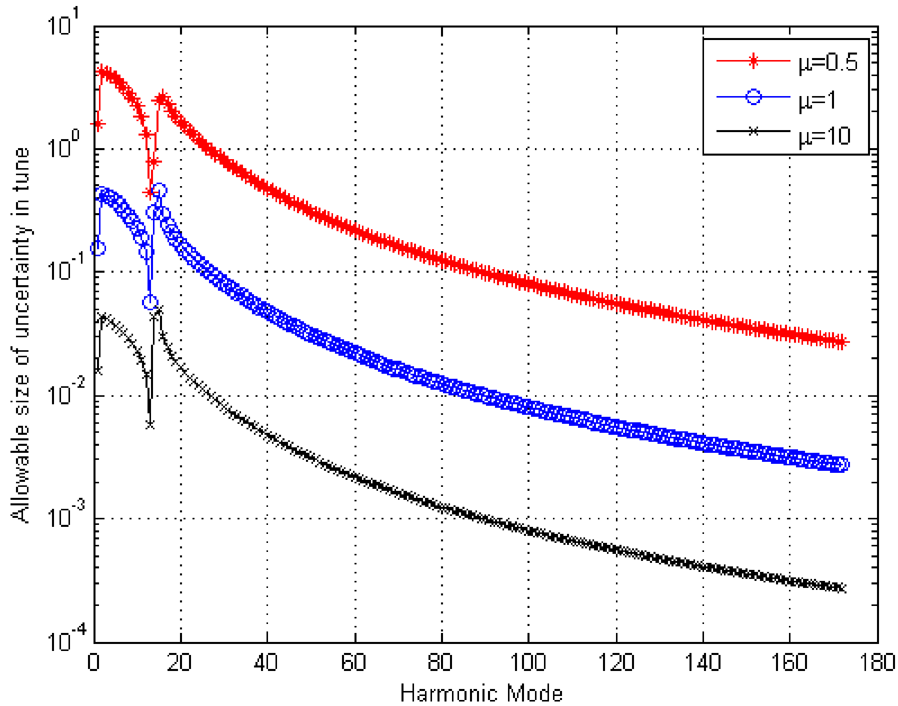

Fig. 5.11: Allowable size of uncertainty in the storage ring vertical tune where $\mu = 0.5$ ('$*$' red), $\mu = 1$ ('o' blue) and $\mu = 10$ ('x' black).

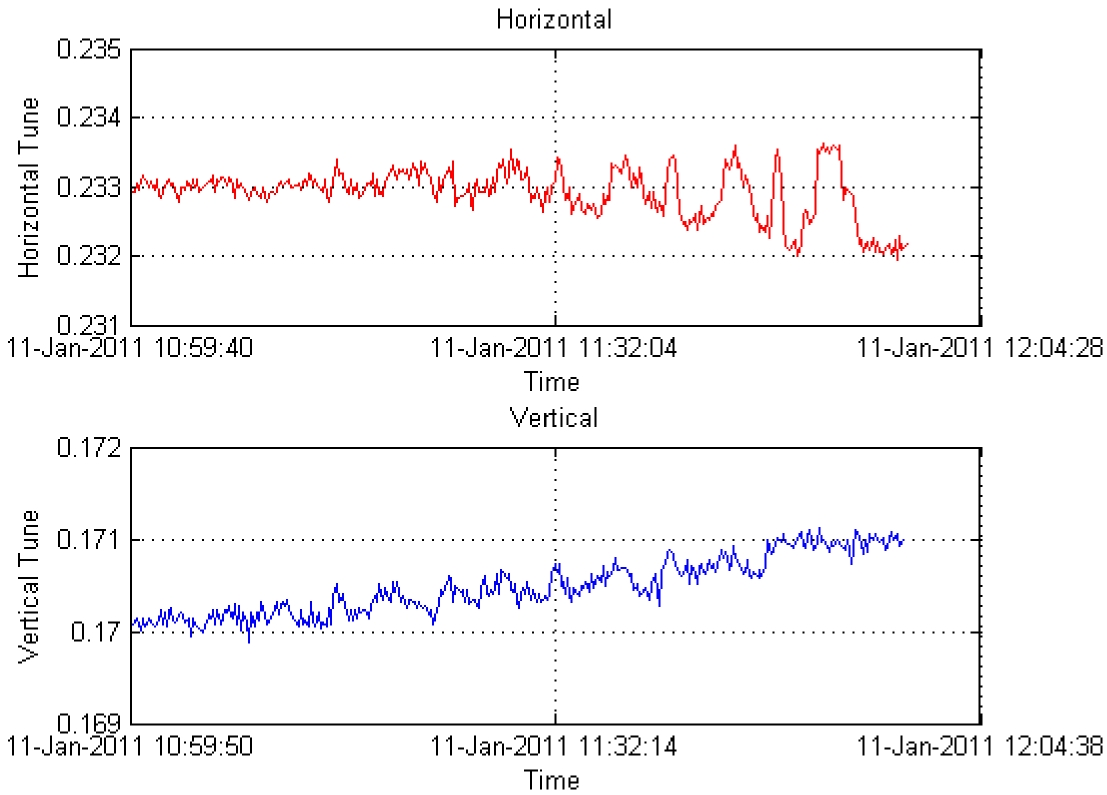

Fig. 5.12: Measured drift in tune on the storage ring over an hour. Both horizontal (red) and vertical (blue) fractional tunes are shown where the ideal tunes are $\mathcal{Q}_{\mathcal{X}} = 27.23$ and $\mathcal{Q}_{\mathcal{Y}} = 13.18$.

solely by the BPM positions and corrector magnet strengths respectively and as a result are not orthogonal and the Fourier coefficients are determined solely by the tune. By using these relationships, the associated uncertainties can be described in a diagonally structured form and the IQC robust stability test can be decoupled on a mode-by-mode basis. A further result is that the robust stability results can be used to determine bounds on meaningful beam parameters such as the acceptable drifts in tune during operation.

Chapter 6

Anti-Windup Design for Internal Model Control

The power supply units, discussed in Section 2.4.1 have slew rate limits to impose voltage limitations to protect the corrector magnet. In current operation at Diamond, the closed loop is unconstrained, however in future operation, it is expected that the rate limits would be introduced and therefore a constrained control strategy would be required. In principle, an MPC scheme could be used to design control inputs that accommodate these constraints, but the size of the control problem (172 actuators by 172 sensors) and fast sample rate (1kHz) mean that robust constrained MPC is not feasible because of the computational burden given the current control network architecture at Diamond. Anti-windup compensation is therefore an appropriate choice when the electron beam feedback system is rate constrained, with the aim of reducing the deviation between the linear and nonlinear control signal rate. The term 'windup' refers to the severe degradation in performance that occurs when any saturation nonlinearity is inserted at the plant input, in an otherwise linear feedback control loop. 'Anti-windup' therefore refers to the augmentation of a controller in a feedback loop that is prone to windup so that [Zaccarian and Teel, 2011]:

- the closed-loop performance is unaltered when saturation does not occur, in other words, the augmentation has no effect for small signals;
- acceptable performance is achieved, to the extent that is possible, even when actuator saturation occurs.

Anti-windup synthesis refers to the design of such augmentation.

An IMC anti-windup technique used for the design of magnitude constrained cross-directional controllers are addressed in [Heath and Wills, 2004, Heath et al., 2005, Morales and Heath, 2011] where the linear IMC controller is designed, neglecting the nonlinearity and then an anti-windup compensation scheme is added. Standard IMC was not intended to operate as an anti-windup scheme and therefore gives poor performance for saturating systems, therefore a common anti-windup treatment in an IMC framework for saturating actuators is to factorise the unconstrained IMC controller into a forward controller and a feedback term around the saturation [Goodwin et al., 1993, Zheng et al., 1993]. This technique however is not straightforward for the rate limiter under consideration because it already contains an internal feedback loop which represents an inherent factorisation of the unconstrained controller. In this chapter, an IMC anti-windup compensation technique based on the factorisation of the unconstrained controller is presented for the rate limited closed loop which is adapted from techniques used for saturation limits. The goals of the anti-windup compensation are:

- *Small signal preservation*

  To make the response of the anti-windup augmented closed-loop system match the response of the unconstrained closed-loop system whenever the unconstrained control input response is in the region where the saturation nonlinearity equals the identity. The unconstrained closed loop response is reproducible

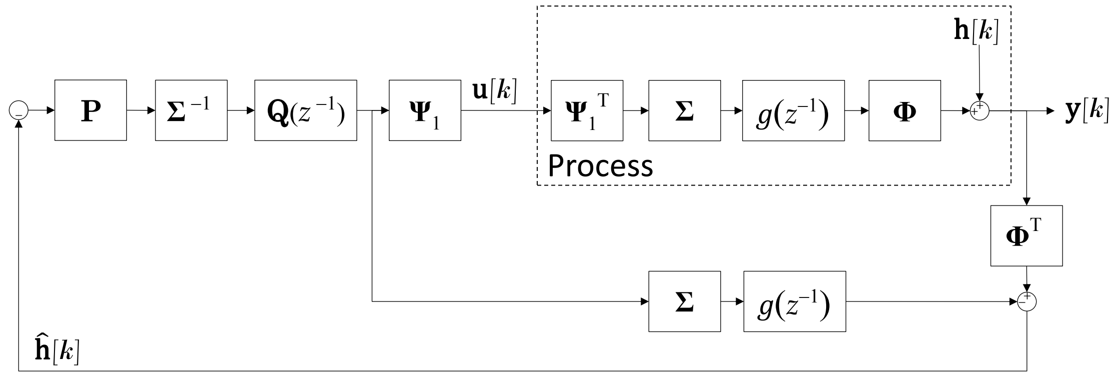

Fig. 6.1: The standard IMC structure.

and should be preserved, at least when the initial state of the anti-windup augmentation (if it exist) is zero. This behaviour is called the small signal preservation property. This is enforced by the structure of the anti-windup augmentation [Zaccarian and Teel, 2011].

- *Internal stability*

  To make, in the absence of exogenous inputs, a desired constant operating point asymptotically stable with a basin of attraction at least as big as the set of states over which the system is expected to operate [Zaccarian and Teel, 2011]. This property is enforced by the unconstrained controller for the unconstrained closed-loop system and should be maintained for the anti-windup augmentation.

- *External stability*

  To induce a bounded response for initial states and exogenous inputs that are expected during operation.

- *Unconstrained response recovery*

  To recover the unconstrained closed-loop response asymptotically when rate constrained. The performance of the anti-windup augmented closed loop is assessed on how closely it emulates the unconstrained closed loop response. Internal and external stability becomes relevant in this case.

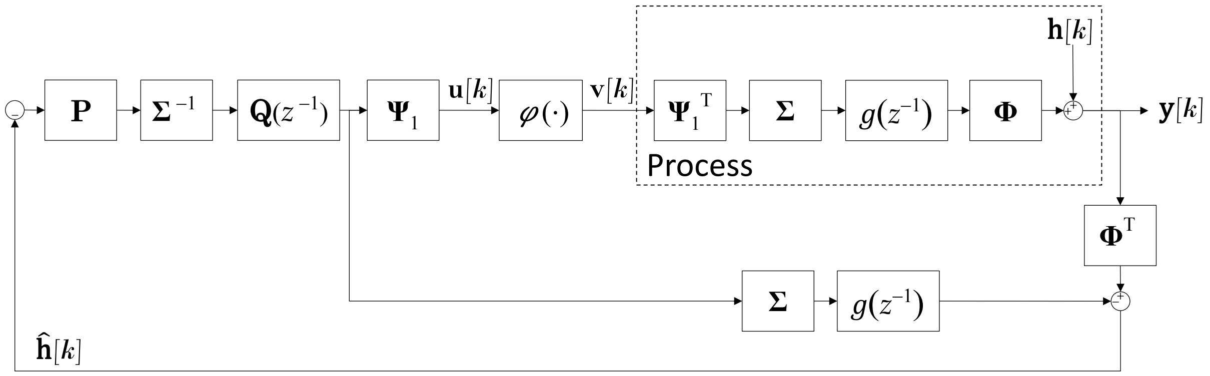

Fig. 6.2: The IMC structure with nonlinearity without anti-windup.

In this chapter, the unconstrained system is augmented to achieve the goals of the anti-windup compensation and the performance and stability of the constrained system are discussed.

6.1 Structure of Rate Limiter

From Chapter 4, the closed loop equations for the standard IMC structure, shown in Fig. 6.1 are given by

$$\begin{aligned} \bar{\mathbf{u}}[k] &= -\mathbf{Q}(z^{-1})\mathbf{\Sigma}^{-1}\mathbf{P}\bar{\mathbf{h}}[k] \\ \bar{\mathbf{y}}[k] &= \left(\mathbf{I} - g(z^{-1})\mathbf{Q}(z^{-1})\mathbf{P}\right)\bar{\mathbf{h}}[k] \end{aligned} \tag{6.1}$$

However for a rate limited actuator, the system is shown in Fig. 6.2 where

$$\bar{\mathbf{u}}[k] = -\mathbf{Q}(z^{-1})\mathbf{\Sigma}^{-1}\mathbf{P}\bar{\mathbf{h}}[k] - g(z^{-1})\mathbf{Q}(z^{-1})\mathbf{P}\left(\bar{\mathbf{u}}[k] - \bar{\mathbf{v}}[k]\right) \tag{6.2}$$

and $v_n[k] = \varphi(u_n[k])$ where $\varphi(\cdot)$ represents the rate limit nonlinearity.

The rate limiter used at Diamond is implemented as a cascaded saturation function with an integrator and a gain enclosed within a feedback loop. This structure is depicted in Fig. 6.3 and is a common representation of rate limiters in aircraft

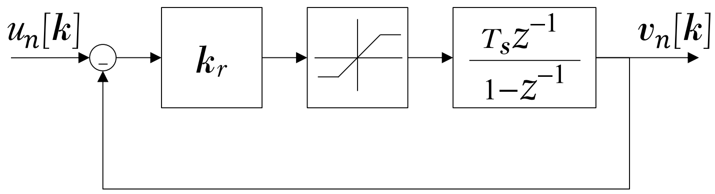

Fig. 6.3: Rate limiter structure.

applications [Brieger et al., 2007, Rundqwist and Stahl-Gunnarsson, 1996, Sofrony et al., 2009, 2010]. Typically, the input signal $u_n[k]$ applied to each actuator is rate constrained such that

$$u_{rl}^{min} \leq u_n[k] - u_n[k-1] \leq u_{rl}^{max} \tag{6.3}$$

and for each actuator

$$\dot{v}_n[k] = k_r \text{sat}(u_n[k] - v_n[k]) \tag{6.4}$$

with sat$(\cdot)$ being a saturation function defined by

$$\text{sat}(u_n[k]) = \begin{cases} u_n[k] & |u_n[k]| \leq u_{sat} \\ u_{sat} \times \text{sign}(u_n[k]) & |u_n[k]| > u_{sat} \end{cases} \tag{6.5}$$

where u_{sat} is the magnitude at which the input signal saturates and k_r is a gain. When the nonlinearity is not active, the system behaves linearly and the closed loop is asymptotically stable and well-posed. When the rate limits have not been reached (i.e. the saturation block acts as the identity), the rate limiter is defined by

$$\varphi_n(z^{-1}) = \frac{k_r T_s z^{-1}}{1 + (k_r T_s - 1)z^{-1}} \tag{6.6}$$

so that it behaves as a low pass filter with cut-off frequency determined by k_r when $k_r T_s < 1$. For the Diamond storage ring and booster $k_r = 1/T_s$, so when the rate limits have not been reached, the rate limiters acts as a pure delay term. When the rate limits have been reached the rate limiter is interpreted as a restricted tracking

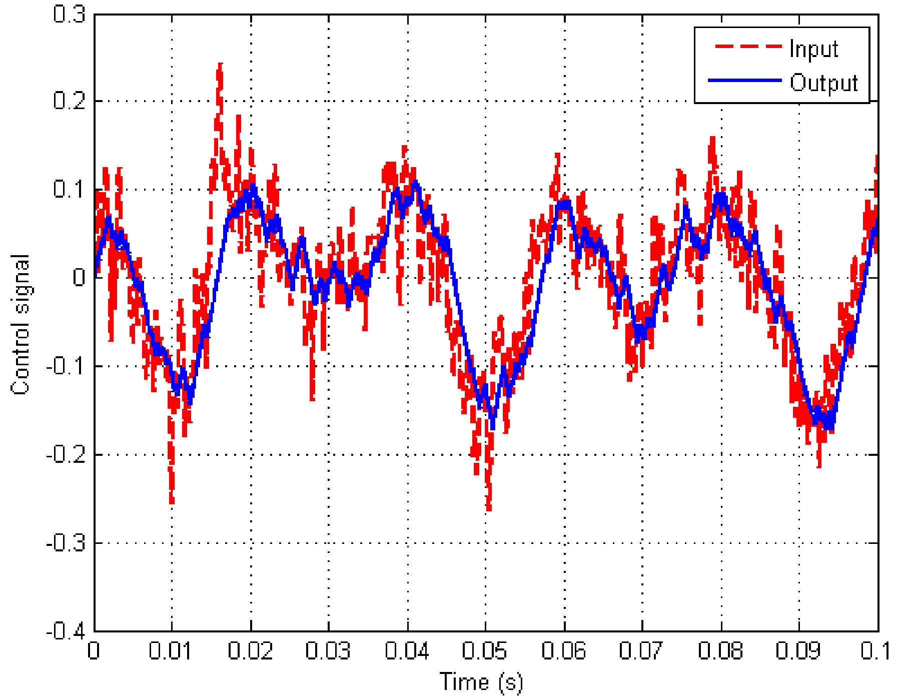

Fig. 6.4: Input signal ('- -' red) and output signal ('-' blue) of the rate limiter observed at 1st BPM over 0.1s.

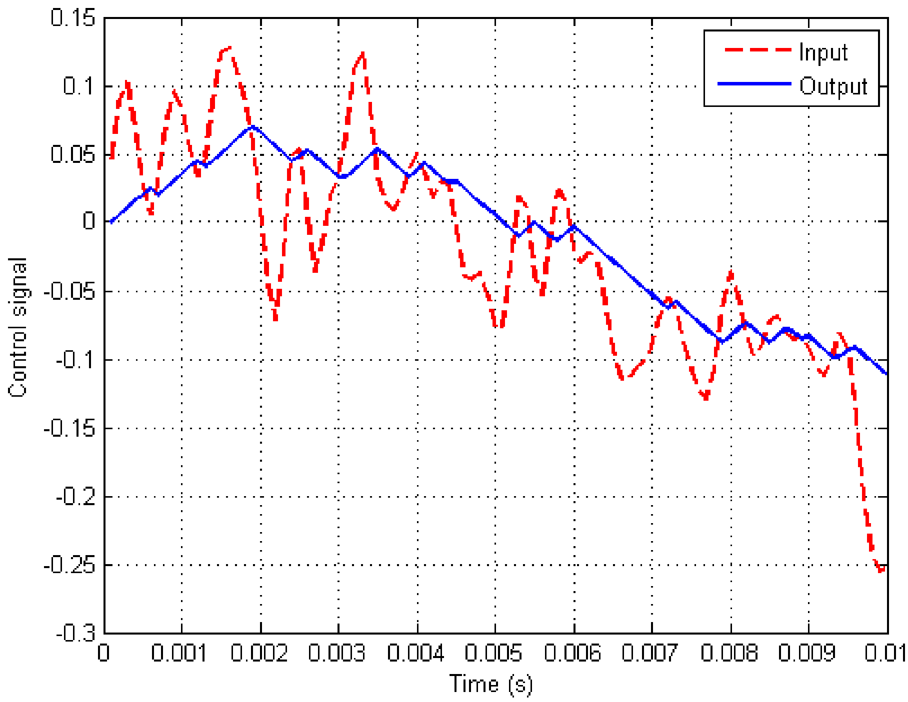

Fig. 6.5: Input signal ('- -' red) and output signal ('-' blue) of the rate limiter observed at 1st BPM over the first 0.01s.

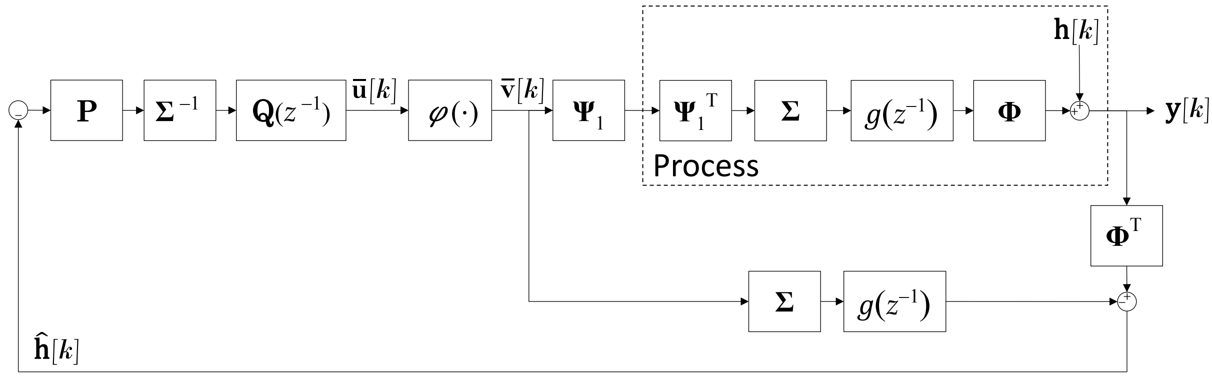

Fig. 6.6: The conventional IMC anti-windup structure.

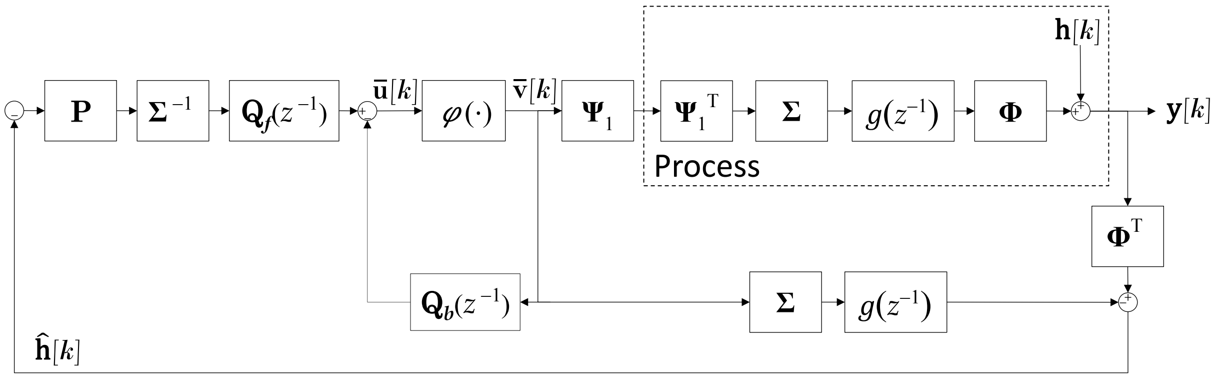

Fig. 6.7: The modified IMC anti-windup structure.

problem [Sofrony et al., 2010]. This effect is demonstrated in Fig. 6.4, for $k_r = 1/T_s$ (and in detail in Fig. 6.5) where the input and output of the rate limiter is compared.

6.2 Internal Model Control Anti-windup Structures for Rate Limiters

For the standard IMC implementation with rate limited actuators, shown in Fig. 6.2, it can be seen from (6.2) that the plant and the model are driven by different inputs causing plant-model mismatch. Therefore for anti-windup compensation it is desirable to include a model of the rate limiter in the path of the plant model which is achieved in the form shown in Fig. 6.6 and the rate constraints may be introduced to the controller with the condition,

$$u_{rl}^{min} \leq [\mathbf{\Psi}_1 \bar{\mathbf{u}}[k]]_n - [\mathbf{\Psi}_1 \bar{\mathbf{u}}[k-1]]_n \leq u_{rl}^{max} \tag{6.7}$$

Therefore, to preserve the original constraints on *each actuator*, the projection matrices $\mathbf{\Psi}_1$ and $\mathbf{\Psi}_1^{\mathrm{T}}$ must be included at the input and output of the rate limiter structure. For the IMC anti-windup structure in Fig. 6.6

$$\begin{aligned} \bar{\mathbf{u}}[k] &= -\mathbf{Q}(z^{-1})\mathbf{\Sigma}^{-1}\mathbf{P}\bar{\mathbf{h}}[k] \\ \bar{\mathbf{y}}[k] &= \bar{\mathbf{h}}[k] + g(z^{-1})\mathbf{\Sigma}\bar{\mathbf{v}}[k] \end{aligned} \tag{6.8}$$

where the plant and model are driven by the same inputs but the effect of the nonlinearity on the plant output is not fed back directly to the controller. However in [Zheng et al., 1993], it is shown that improved dynamic response is gained by including a feedback term around the non-linearity when the non-linear element is a saturation. One way of achieving this with an IMC structure for saturating nonlinearities is by factorising the unconstrained controller, $q_m(z^{-1})$ for each mode, as

$$q_m(z^{-1}) = q_{f_m}(z^{-1})\left[1 + q_{b_m}(z^{-1})\right]^{-1} \tag{6.9}$$

where $q_{b_m}(z^{-1})$ is in a feedback loop around the saturation. For the rate limiter, this factorisation is shown in Fig. 6.7 where the control action is given by

$$\begin{aligned} \bar{\mathbf{u}}[k] &= -\mathbf{Q}_f(z^{-1})\mathbf{\Sigma}^{-1}\mathbf{P}\bar{\mathbf{h}}[k] - \mathbf{Q}_b(z^{-1})\bar{\mathbf{v}}[k] \\ \bar{\mathbf{u}}[k] &= -\mathbf{Q}_f(z^{-1})\mathbf{\Sigma}^{-1}\mathbf{P}\bar{\mathbf{y}}[k] + \left[g(z^{-1})\mathbf{Q}_f(z^{-1})\mathbf{P} - \mathbf{Q}_b(z^{-1})\right]\bar{\mathbf{v}}[k] \end{aligned} \tag{6.10}$$

In this case, the controller not only takes into account the disturbance but also the effect of the nonlinearity on the control action. For a saturating nonlinearity, it follows trivially that when unconstrained, $\mathbf{Q}_f(z^{-1}) = \mathbf{Q}(z^{-1})$ and $\mathbf{Q}_b(z^{-1}) = \mathbf{0}$ and (6.8) and (6.10) are equivalent and thus ensuring small signal preservation. However the rate limiter already has an internal feedback loop and in the following section the technique used for saturation limits is extended for rate limiters.

6.3 Internal Model Control Anti-Windup Compensation Design

The IMC anti-windup compensation design is based on the factorisation of the unconstrained controller $q_m(z^{-1})$. The structure of the anti-windup compensation takes the form shown in Fig. 6.8 for the rate limiter under consideration. The input signal to the saturation element is given by

$$\begin{aligned}
\bar{\mathbf{u}}[k] &= -\mathbf{P}\boldsymbol{\Sigma}^{-1}\mathbf{Q}_f(z^{-1})\bar{\mathbf{y}}[k] + \left[\mathbf{P}g(z^{-1})\mathbf{Q}_f(z^{-1}) - \mathbf{Q}_b(z^{-1})\right]\bar{\mathbf{v}}[k] \\
\bar{\mathbf{v}}[k] &= \boldsymbol{\Psi}_1^{\mathrm{T}}\frac{T_s z^{-1}}{1 - z^{-1}}\mathbf{v}_{NL}[k] \\
\mathbf{u}_{NL}[k] &= \mathbf{K}_r\boldsymbol{\Psi}_1\left(\bar{\mathbf{u}}[k] - \bar{\mathbf{v}}[k]\right) \\
&= -\mathbf{K}_r\boldsymbol{\Psi}_1\mathbf{P}\boldsymbol{\Sigma}^{-1}\mathbf{Q}_f(z^{-1})\bar{\mathbf{y}}[k] \\
&\quad + \mathbf{K}_r\boldsymbol{\Psi}_1\left[\mathbf{P}g(z^{-1})\mathbf{Q}_f(z^{-1}) - \mathbf{Q}_b(z^{-1}) - \mathbf{I}\right]\boldsymbol{\Psi}_1^{\mathrm{T}}\frac{T_s z^{-1}}{1 - z^{-1}}\mathbf{v}_{NL}[k]
\end{aligned} \tag{6.11}$$

where $\mathbf{K}_r = \mathrm{diag}\{k_r\}$. The factorisation given in (6.9) must be modified for the rate limited system since the unconstrained controller is actually given by

$$\frac{k_r T_s z^{-1}}{1 - (1 - k_r T_s)z^{-1}} q_m(z^{-1}) \tag{6.12}$$

Therefore the factorisation into a forward and feedback controller for anti-windup compensation, where the feedback term is considered around the entire nonlinearity is given by

$$q_{f_m}(z^{-1})\frac{k_r T_s z^{-1}}{1 - (1 - k_r T_s - k_r T_s q_{b_m}(z^{-1}))z^{-1}} \tag{6.13}$$

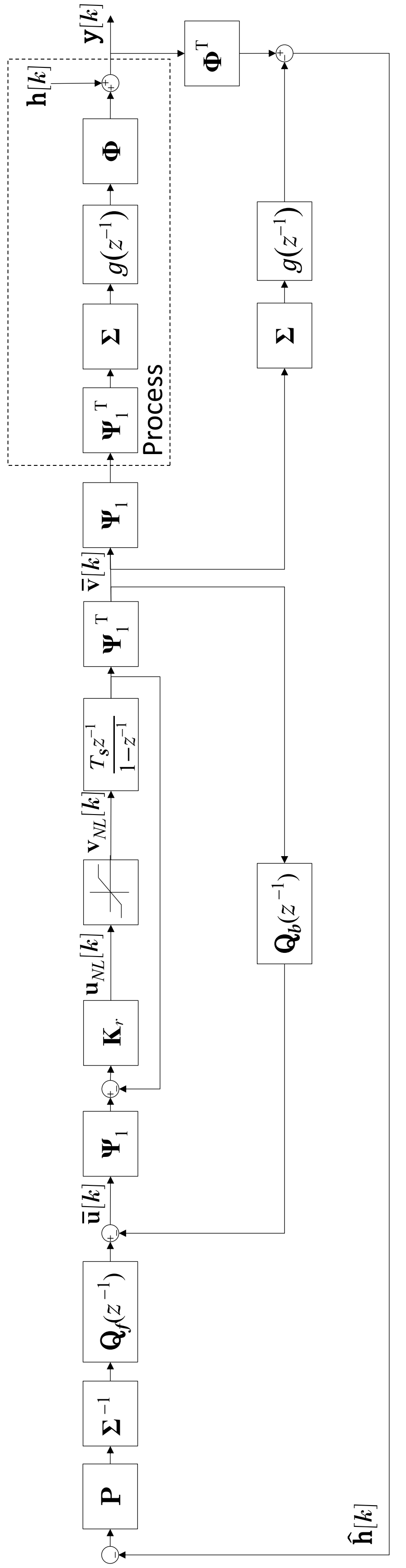

Fig. 6.8: IMC anti-windup compensation structure.

Therefore for any proper $q_{f_m}(z^{-1})$ and any k_r,

$$q_{b_m}(z^{-1}) = \left[q_{f_m}(z^{-1})q_m(z^{-1})^{-1} - 1\right]\left[1 - (1 - k_r T_s)z^{-1}\right]\left[k_r T_s z^{-1}\right]^{-1} \tag{6.14}$$

where $q_{b_m}(z^{-1})$ is proper. This choice of $q_{b_m}(z^{-1})$ ensures small signal preservation, so that, when the system is unconstrained the anti-windup compensation controllers, $q_{f_m}(z^{-1})$ and $q_{b_m}(z^{-1})$ are equivalent to the unconstrained controller and the anti-windup augmentation does not affect the closed loop behaviour. The following sections discuss various approaches for the design of $q_{f_m}(z^{-1})$ and $q_{b_m}(z^{-1})$.

6.3.1 Weighting Factorisation

A simple factorisation is given by

$$q_{f_m}(z^{-1}) = \upsilon_{w_m} q_m(z^{-1}) + (1 - \upsilon_{w_m})q_m(0) \tag{6.15}$$

where υ_{w_m} is a weight on each mode, with $\upsilon_{w_m} \in [0, 1]$. This factorisation can be directly applied to the rate limiter case where the feedback anti-windup compensator, $q_{b_m}(z^{-1})$ is given directly by (6.14). The choice of $\upsilon_{w_m} = 1$ results in the conventional IMC structure, which is not guaranteed to result in enhanced performance during rate saturation but is nominally stable (since $q_{f_m}(z^{-1}) = q_m(z^{-1})$). Conversely, the choice of $\upsilon_{w_m} = 0$ corresponds to $q_{f_m} = q_m(0)$, which is the factorisation proposed in [Goodwin et al., 1993]. It is important to note that for this choice, the factorisation is dependent on the design of the unconstrained controller which already takes into account whether $g(z^{-1})$ is minimum phase or not.

For a measured disturbance on the storage, the integrated vertical beam motion is simulated in Fig. 6.9, for these two choices of υ_{w_m}. When $\upsilon_{w_m} = 1$, the constrained performance is not improved by the anti-windup structure since it is nominally

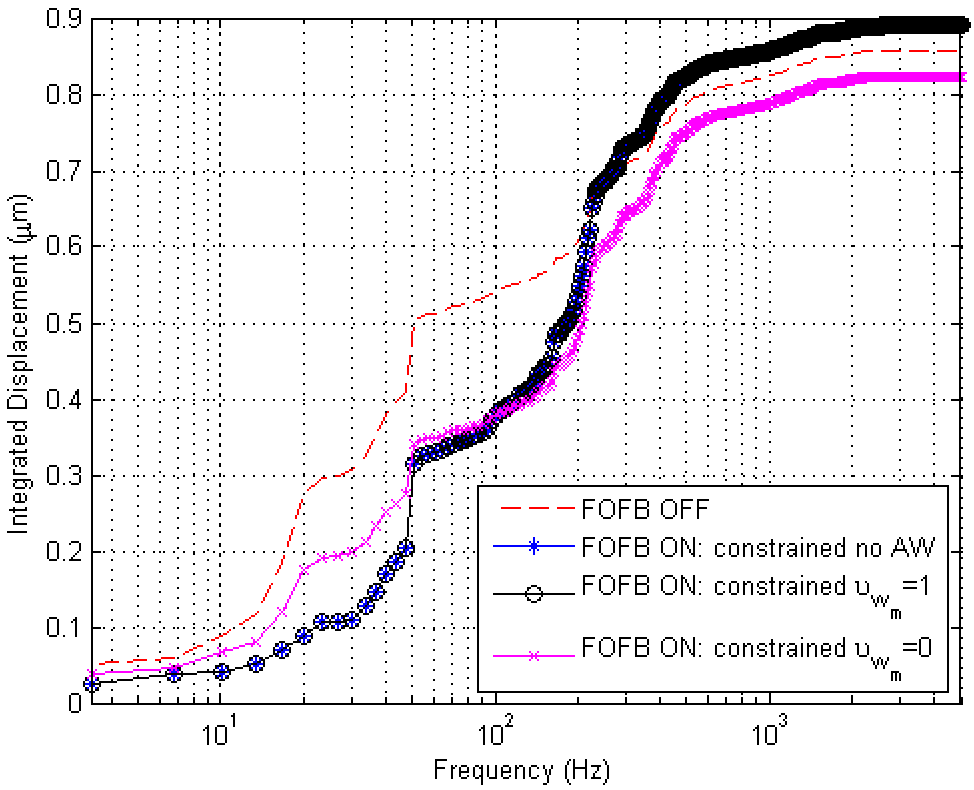

Fig. 6.9: Storage ring vertical integrated beam motion at 1st BPM showing the uncontrolled beam ('- -' red), the constrained controlled beam with no anti-windup ('$*$' blue), the constrained controlled beam with anti-windup where $\upsilon_{w_m} = 1$ ('o' black) and $\upsilon_{w_m} = 0$ ('x' magenta).

equivalent to the conventional IMC form, which offers no anti-windup compensation. However when $\upsilon_{w_m} = 0$, the effects of the anti-windup compensation can be seen at high frequencies, where the effect of the rate limiter is greatest and the tracking problem becomes more difficult. However at frequencies below 100Hz, the anti-windup compensation is not effective. In fact, the improved performance at higher frequencies is at the expense of the performance at lower frequencies. The tradeoff between the performance at low and high frequencies can be made through the choice of $0 < \upsilon_{w_m} < 1$. Although the constrained performance is improved at high frequencies when $\upsilon_{w_m} = 0$, nominal stability is not necessarily guaranteed even in the absence of uncertainty [Akkermans et al., 2004]. Also, $\upsilon_{w_m} = 0$ does not necessarily correspond to the maximum achievable nonlinear performance. Therefore the choice of υ_{w_m} is a tradeoff between constrained performance and stability and is restrictive since the anti-windup design is reduced to a line search over the interval $[0, 1]$ which imposes stability and performance limits [Adegbege, 2011].

6.3.2 Filter Factorisation

A more general factorisation proposed in [Zheng et al., 1993] can be adapted for a non-minimum phase process and is given by

$$q_{f_m}(z^{-1}) = \upsilon_{a_m}(z^{-1})g^{-}(z^{-1})q_m(z^{-1}) \tag{6.16}$$

where

$$g(z^{-1}) = g^{+}(z^{-1})g^{-}(z^{-1}) \tag{6.17}$$

such that $g^{+}(z^{-1})$ contains all the non-minimum phase characteristics of $g(z^{-1})$. With this factorisation, $\upsilon_{a_m}(z^{-1})$ must be chosen such that $\upsilon_{a_m}(z^{-1})g^{-}(z^{-1})q_m(z^{-1})$ is minimum phase and as before, $q_{b_m}(z^{-1})$ is given by (6.14) and $q_{b_m}(z^{-1})$ is guaranteed proper. For the choice of filter

$$\upsilon_{a_m}(z^{-1}) = \frac{1 - 0.7z^{-1}}{0.356z^{-1}} \tag{6.18}$$

for all $m = [1, \ldots, M]$, the simulated performance on the storage ring in terms of the integrated beam motion is shown in Fig. 6.10. Unlike the weighting factorisation in (6.15), the factorisation in (6.16) results in improved performance at the high frequencies when rate constrained without the deterioration of low frequency performance through a suitable choice of υ_{a_m}. This is because the design is not as restrictive as the weighting option in (6.15) and trivially the choice of $\upsilon_{a_m} = [g^{-}]^{-1}$ is equivalent to choosing $\upsilon_{w_m} = 1$. However selecting an optimal υ_{a_m} is not straightforward and in Section 6.3.3, a method for choosing υ_{a_m} is presented.

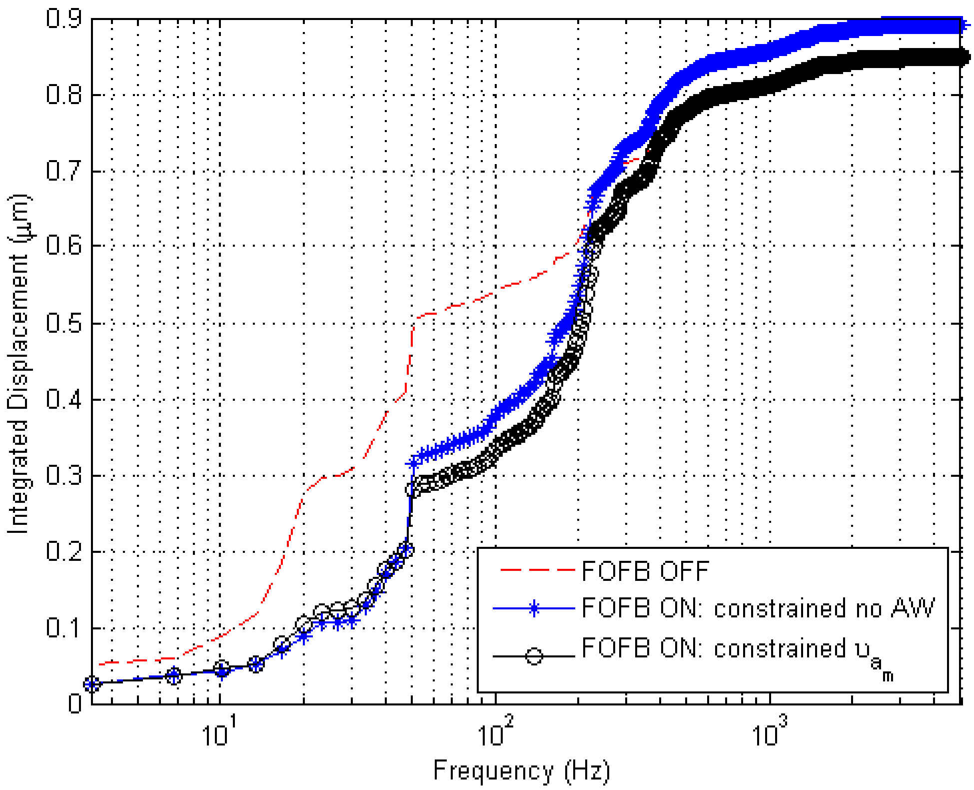

Fig. 6.10: Storage ring vertical integrated beam motion at 1st BPM showing the uncontrolled beam ('- -' red), the constrained controlled beam with no anti-windup ('$*$' blue) and the constrained controlled beam with anti-windup where v_{a_m} is chosen in (6.18) ('o' black).

6.3.3 Riccati-based Factorisation

LMI based anti-windup synthesis schemes have been suggested to design optimal anti-windup compensators for particular performance objectives [Massimetti et al., 2009, Sofrony et al., 2009, Turner et al., 2003]. In [Sofrony et al., 2010], a Riccati based solution was proposed in favour of an LMI based formulation which is easy to tune and feature a single parameter which captures the trade-off between performance and robustness. Since the saturation nonlinearity internal to the rate limiter is the only nonlinearity, it was suggested in [Sofrony et al., 2010] that the plant and the controller can be augmented to represent the problem as an equivalent magnitude limit problem where a modified plant $\tilde{\mathbf{G}}(z^{-1})$ and a modified unconstrained controller $\tilde{\mathbf{C}}(z^{-1})$ are defined as

$$\begin{aligned}
\begin{bmatrix} \bar{\mathbf{y}}[k] \\ \bar{\mathbf{v}}[k] \end{bmatrix} &= \underbrace{\begin{bmatrix} \boldsymbol{\Sigma} g(z^{-1}) \frac{T_s z^{-1}}{1-z^{-1}} \\ \frac{T_s z^{-1}}{1-z^{-1}} \mathbf{I} \end{bmatrix}}_{\tilde{\mathbf{G}}(z^{-1})} \bar{\mathbf{v}}_{NL}[k] + \begin{bmatrix} \mathbf{I} \\ \mathbf{0} \end{bmatrix} \bar{\mathbf{h}}[k] \\
\bar{\mathbf{u}}_{NL}[k] &= \underbrace{\mathbf{K}_r \begin{bmatrix} -\mathbf{P}\boldsymbol{\Sigma}^{-1}\mathbf{C}(z^{-1}) & -\mathbf{I} \end{bmatrix}}_{\tilde{\mathbf{C}}(z^{-1})} \begin{bmatrix} \bar{\mathbf{y}}[k] \\ \bar{\mathbf{v}}[k] \end{bmatrix}
\end{aligned} \tag{6.19}$$

The anti-windup compensation schemes in [Massimetti et al., 2009, Sofrony et al., 2010, Turner et al., 2003] take the form shown in Fig. 6.11 and is described by

$$\begin{aligned}
\mathbf{u}_{NL}[k] &= \boldsymbol{\Psi}_1 \left[\mathbf{u}_{lin}[k] - \mathbf{v}_d[k]\right] \\
\mathbf{v}_d[k] &= (\mathbf{X}_r(z^{-1}) - \mathbf{I})\boldsymbol{\Psi}_1^{\mathrm{T}} \left(\mathbf{u}_{NL}[k] - \mathbf{v}_{NL}[k]\right) \\
\mathbf{u}_{lin}[k] &= \mathbf{K}_r \left(\bar{\mathbf{u}}[k] - \mathbf{v}_{lin}[k]\right) \\
\bar{\mathbf{u}}[k] &= \mathbf{C}(z^{-1})(\mathbf{y}_d[k] + \bar{\mathbf{y}}[k]) \\
\mathbf{v}_{lin}[k] &= \mathbf{v}_{rm}[k] + \mathbf{v}_{rd}[k] \\
\mathbf{y}_d[k] &= \boldsymbol{\Sigma} g(z^{-1})\mathbf{X}_r(z^{-1})\boldsymbol{\Psi}_1^{\mathrm{T}} \frac{T_s z^{-1}}{1-z^{-1}} \left(\mathbf{u}_{NL}[k] - \mathbf{v}_{NL}[k]\right) \\
\mathbf{v}_{rm}[k] &= \boldsymbol{\Psi}_1^{\mathrm{T}} \frac{T_s z^{-1}}{1-z^{-1}} \mathbf{v}_{NL}[k] \\
\mathbf{v}_{rd}[k] &= \frac{T_s z^{-1}}{1-z^{-1}} \mathbf{X}_r(z^{-1})\boldsymbol{\Psi}_1^{\mathrm{T}} \left(\mathbf{u}_{NL}[k] - \mathbf{v}_{NL}[k]\right)
\end{aligned} \tag{6.20}$$

For a single mode, the modified plant, $\tilde{\mathbf{G}}(z^{-1})$ is given by

$$\tilde{g}_m(z^{-1}) = \begin{bmatrix} \sigma_m g(z^{-1}) \frac{T_s z^{-1}}{1-z^{-1}} \\ \frac{T_s z^{-1}}{1-z^{-1}} \end{bmatrix} \tag{6.21}$$

where the state space realisation is given as

$$\tilde{g}_m(z^{-1}) \sim \left[\begin{array}{c|c} \boldsymbol{\mathcal{A}}_{\tilde{G}} & \boldsymbol{\mathcal{B}}_{\tilde{G}} \\ \hline \boldsymbol{\mathcal{C}}_{\tilde{G}} & \boldsymbol{\mathcal{D}}_{\tilde{G}} \end{array}\right] \tag{6.22}$$

the anti-windup compensator in [Sofrony et al., 2010] is based on the co-prime factorisation of the plant and has the structure

$$\begin{bmatrix} x_{r_m}(z^{-1}) - 1 \\ \tilde{g}_m(z^{-1})x_{r_m}(z^{-1}) \end{bmatrix} \sim \left[\begin{array}{c|c} \boldsymbol{\mathcal{A}}_{\tilde{G}} + \boldsymbol{\mathcal{B}}_{\tilde{G}}\boldsymbol{\mathcal{J}}_{\tilde{G}} & \boldsymbol{\mathcal{B}}_{\tilde{G}} \\ \hline \boldsymbol{\mathcal{J}}_{\tilde{G}} & \mathbf{0} \\ \boldsymbol{\mathcal{C}}_{\tilde{G}} + \boldsymbol{\mathcal{D}}_{\tilde{G}}\boldsymbol{\mathcal{J}}_{\tilde{G}} & \boldsymbol{\mathcal{D}}_{\tilde{G}} \end{array}\right] \tag{6.23}$$

This formulation is parameterised by the free parameter $\boldsymbol{\mathcal{J}}_{\tilde{G}}$ such that $\boldsymbol{\mathcal{A}}_{\tilde{G}} + \boldsymbol{\mathcal{B}}_{\tilde{G}}\boldsymbol{\mathcal{J}}_{\tilde{G}}$ is Hurwitz [Sofrony et al., 2010]. The mapping $\mathbf{T}_{AW_m} : u_{lin_m} \mapsto y_{d_m}$ is selected as the measure of the performance of the anti-windup compensator, where the gain of $\mathbf{T}_{AW_m}$ dictates how much the linear performance degrades in the presence of the rate constraint. Therefore if

$$\|\mathbf{T}_{AW_m}\|_2 \leq \gamma_{AW_m} \tag{6.24}$$

the goal is to establish stability of $\mathbf{T}_{AW_m}$ and minimise the upper bound, γ_{AW_m}, by choosing an appropriate $\boldsymbol{\mathcal{J}}_{\tilde{G}}$. In [Sofrony et al., 2010] a systematic way of computing $\boldsymbol{\mathcal{J}}_{\tilde{G}}$ (and hence $x_{r_m}(z^{-1})$) is determined and the discrete-time counterpart is presented here. In [Sofrony et al., 2010], there exists a full order anti-windup compensator,

$$\begin{bmatrix} x_{r_m}(z^{-1}) - 1 \\ \tilde{g}_m(z^{-1})x_{r_m}(z^{-1}) \end{bmatrix} \tag{6.25}$$

which solves the anti-windup problem if there exists a matrix $\boldsymbol{\mathcal{G}}_{AW} = \boldsymbol{\mathcal{G}}_{AW}^{\mathrm{T}} > 0$ and positive real scalars $\epsilon_{AW} \in [0, 1]$ (where sat $\in$ sector$[0, \epsilon_{AW}]$) and $\chi_{AW} > 0$ such that

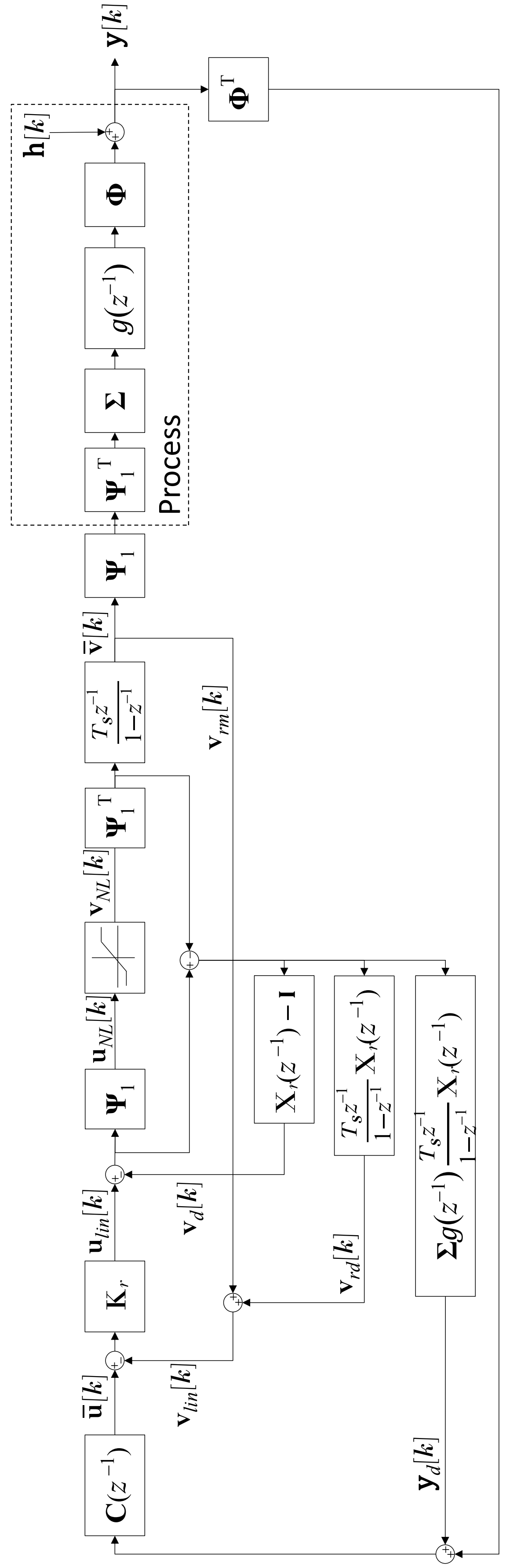

Fig. 6.11: Closed loop system structure for Riccati-based formulation

the following Riccati equation is satisfied

$$\begin{aligned}&\boldsymbol{\mathcal{A}}_{\tilde{G}}{}^{\mathrm{T}}\boldsymbol{\mathcal{G}}_{AW}\boldsymbol{\mathcal{A}}_{\tilde{G}} - \boldsymbol{\mathcal{G}}_{AW} - \boldsymbol{\mathcal{A}}_{\tilde{G}}{}^{\mathrm{T}}\boldsymbol{\mathcal{G}}_{AW}\boldsymbol{\mathcal{B}}_{\tilde{G}}\left(\chi_{AW} + \boldsymbol{\mathcal{B}}_{\tilde{G}}{}^{\mathrm{T}}\boldsymbol{\mathcal{G}}_{AW}\boldsymbol{\mathcal{B}}_{\tilde{G}}\right)^{-1}\boldsymbol{\mathcal{B}}_{\tilde{G}}{}^{\mathrm{T}}\boldsymbol{\mathcal{G}}_{AW}\boldsymbol{\mathcal{A}}_{\tilde{G}}\\ &+\boldsymbol{\mathcal{C}}_{\tilde{G}}{}^{\mathrm{T}}\boldsymbol{\mathcal{C}}_{\tilde{G}} = \mathbf{0}\end{aligned} \tag{6.26}$$

If (6.26) is satisfied, a suitable compensator achieving $\|\mathbf{T}_{AW_m}\|_2 \leq \gamma_{AW_m}$ is obtained by calculating the matrix gain $\boldsymbol{\mathcal{J}}_{\tilde{G}}$ as

$$\boldsymbol{\mathcal{J}}_{\tilde{G}} = -\left(1 - \epsilon_{AW}\right)^{-1}\chi_{AW}\boldsymbol{\mathcal{B}}_{\tilde{G}}{}^{\mathrm{T}}\boldsymbol{\mathcal{G}}_{AW}\boldsymbol{\mathcal{A}}_{\tilde{G}} \tag{6.27}$$

where $\gamma_{AW_m} = \sqrt{1/\chi_{AW}}$. Therefore there are two tuning parameters: $\epsilon_{AW} \in (0, 1)$ and $\chi_{AW} > 0$ for each mode. Furthermore, the Riccati equation in (6.26) is just a function of χ_{AW} and an explicit bound on the local l_2 gain given is by γ_{AW_m}. For a given χ_{AW} and therefore for a given performance bound and region of attraction, there exists a family of compensator gains $\boldsymbol{\mathcal{J}}_{\tilde{G}}$ parameterised by ϵ_{AW}. The best performance i.e. smallest γ_{AW_m} is achieved when $\epsilon_{AW} \to 0$, and conversely worst performance i.e. $\gamma_{AW_m} \to \infty$ is achieved for $\epsilon_{AW} \to 1$, since this corresponds to no added anti-windup compensation. Furthermore, as χ_{AW} is reduced, the norm of $\boldsymbol{\mathcal{J}}_{\tilde{G}}$ is also reduced and a larger γ_{AW_m} is also achieved.

The controller architecture in Fig. 6.11 is difficult to realise for physical rate limits and for the case at Diamond and other synchrotrons, the saturation block cannot be easily accessed. Therefore the approach taken in this thesis is to develop an anti-windup structure that can be placed around the entire rate limit nonlinearity rather than the saturation only. To do this, the controller can be designed for the modified system in (6.19) with the structure proposed in Fig. 6.11 and the equivalent IMC controllers $q_{f_m}(z^{-1})$ and $q_{b_m}(z^{-1})$ are found. This is reasonable because the structure in Fig. 6.11 is equivalent to the IMC structure in Fig. 6.8 for some choice of $\mathbf{X}(z^{-1})$, $\mathbf{Q}_f(z^{-1})$ and $\mathbf{Q}_b(z^{-1})$. By comparing (6.11) and (6.20), the IMC anti-windup augmented closed loop is equivalent to the structure in Fig. 6.11 if $\mathbf{X}_r(z^{-1})$ is invertible and

$$\begin{aligned}\mathbf{P}\mathbf{\Sigma}^{-1}\mathbf{Q}(z^{-1}) &= -\mathbf{C}(z^{-1})\bar{\varphi}(z^{-1})\left[\mathbf{I}+\bar{\varphi}(z^{-1})\left(\mathbf{I}-g(z^{-1})\mathbf{C}(z^{-1})\right)\right]^{-1}\\ \mathbf{Q}_f(z^{-1}) &= \mathbf{Q}(z^{-1})\left[\bar{\varphi}(z^{-1})\right]^{-1}\left[\mathbf{X}_r(z^{-1})\right]^{-1}\\ \mathbf{Q}_b(z^{-1}) &= \left[\bar{\varphi}(z^{-1})\right]^{-1}\left(\left[\mathbf{X}_r(z^{-1})\right]^{-1}-1\right)-\mathbf{I}\end{aligned} \tag{6.28}$$

where

$$\bar{\boldsymbol{\varphi}}(z^{-1}) = \mathbf{\Psi}_1^{\mathrm{T}}\mathbf{K}_r\frac{T_s z^{-1}}{1-z^{-1}}\mathbf{\Psi}_1 \tag{6.29}$$

Furthermore, for a given mode, if $x_{r_m}(z^{-1})$ is chosen as

$$x_{r_m}(z^{-1}) = \frac{1-z^{-1}}{1-(1-k_rT_s)z^{-1}} \tag{6.30}$$

the standard IMC structure (with no anti-windup compensation) is recovered i.e.

$$\begin{aligned}q_{b_m}(z^{-1}) &= 0\\ q_{f_m}(z^{-1}) &= q_m(z^{-1})\frac{1-(1-k_rT_s)z^{-1}}{k_rT_s z^{-1}}\end{aligned} \tag{6.31}$$

The IMC factorisation based on the filter, $\upsilon_{a_m}(z^{-1})$ given by (6.16) can also be interpreted in terms of the parametrisation in (6.23) where

$$\upsilon_{a_m}(z^{-1}) = \left[g^{-}(z^{-1})\bar{\varphi}(z^{-1})x_{r_m}\right]^{-1} \tag{6.32}$$

Therefore by using the Riccati-based synthesis method, $\upsilon_{a_m}(z^{-1})$ can be designed to meet performance and stability criteria.

6.4 Stability of the Anti-Windup Augmented Closed Loop

The internal and external stability goals of the anti-windup augmented closed loop can be addressed via the minimisation of the l_2 gain, however due to the presence of the integrator term in the rate limiter model, the interconnection of the rate limiter is not l_2 stable. The condition of l_2 stability is required for stability analysis within the IQC framework [Megretski and Rantzer, 1997] which is utilised in this thesis. In [Megretski, 2001], the l_2 stability problem is resolved by connecting the rate limiter in series with a filter so that $w_n[k] = \rho(z^{-1})v_n[k]$, where the modified rate limiter is defined as

$$\tilde{\varphi}(z^{-1}) = \varphi(z^{-1})\rho(z^{-1}) \tag{6.33}$$

For the Diamond storage ring and booster $k_r = 1/T_s$, so that when the saturation acts as the identity

$$\tilde{\varphi}(z^{-1}) = z^{-1}\rho(z^{-1}) \tag{6.34}$$

and an appropriate choice for the filter is $\rho(z^{-1}) = 1/z^{-1}$. The l_2 stability of the modified rate limiter with this choice can be determined following the analysis in [Megretski, 2001].

Lemma 1 (l_2 stability of discrete rate limiter)**.** *For the semiconcave function* sat *with* $\dot{\text{sat}}(0) = \kappa$ *for* $0 < \kappa < \infty$*, define* $\tilde{\varphi}$ *as the system* $u_n[k] \to w_n[k]$ *where*

$$\begin{aligned} \dot{v}_n[k] &= \text{sat}(u_n[k] - v_n[k]) \\ w_n[k] &= v_n[k] + \text{sat}(u_n[k] - v_n[k]) \end{aligned} \tag{6.35}$$

and $v_n(0) = 0$*, the system is stable and the induced* l_2 *gain in the channel* $u_n[k] \to w_n[k]$ *does not exceed* $\max\{\kappa, \sqrt{2}\}$.

Proof. For the rate limiter with filter $\rho(z^{-1})$ connected to the output,

$$\begin{aligned} \dot{v}_n[k] &= \mathrm{sat}(u_n[k] - v_n[k]) \\ w_n[k] &= \rho(z^{-1}) \frac{k_r T_s z^{-1}}{1 - z^{-1}} \dot{v}_n[k] \end{aligned} \tag{6.36}$$

Substituting for k_r and $\rho(z^{-1})$ gives

$$w_n[k](1 - z^{-1}) = \mathrm{sat}(u_n[k] - v_n[k]) \tag{6.37}$$

Since $w_n[k] = \rho(z^{-1})v_n[k]$ then

$$w_n[k] - v_n[k] = \mathrm{sat}(u_n[k] - v_n[k]) \tag{6.38}$$

Proving an upper bound, γ_φ, on the system $u_n[k] \to w_n[k]$ is equivalent to proving the IQC of the form

$$0 \leq \gamma_\varphi^2 \|u_n[k]\|^2 \|w_n[k]\|^2 = \gamma_\varphi^2 \|v_n[k] + (u_n[k] + v_n[k])\|^2 - \|v_n[k] + (w_n[k] - v_n[k])\|^2 \tag{6.39}$$

which refers to

$$\begin{aligned} &\gamma_\varphi^2 |v_n[k] + (u_n[k] - v_n[k])|^2 - |v_n[k] + (w_n[k] - v_n[k])|^2 = \\ &\begin{bmatrix} v_n[k]' & (u_n[k] + v_n[k])' & (w_n[k] - v_n[k])' \end{bmatrix} \begin{bmatrix} \Gamma_{\varphi_{11}} & \Gamma_{\varphi_{12}} & \Gamma_{\varphi_{13}} \\ \Gamma_{\varphi_{21}} & \Gamma_{\varphi_{22}} & \Gamma_{\varphi_{23}} \\ \Gamma_{\varphi_{31}} & \Gamma_{\varphi_{32}} & \Gamma_{\varphi_{33}} \end{bmatrix} \begin{bmatrix} v_n[k]' \\ (u_n[k] - v_n[k])' \\ (w_n[k] - v_n[k])' \end{bmatrix} \end{aligned} \tag{6.40}$$

which gives

$$
\begin{aligned}
\Gamma_{\varphi_{11}} &= \gamma_\varphi^2 - 1 \\
\Gamma_{\varphi_{12}} &= \Gamma_{\varphi_{21}} = \Gamma_{\varphi_{22}} = \gamma_\varphi^2 \\
\Gamma_{\varphi_{13}} &= \Gamma_{\varphi_{31}} = \Gamma_{\varphi_{33}} = -1 \\
\Gamma_{\varphi_{23}} &= \Gamma_{\varphi_{32}} = 0
\end{aligned} \tag{6.41}
$$

For inequality (6.39) to hold, the following inequalities must hold [Megretski, 2001]

$$
\begin{aligned}
&\begin{bmatrix} \Gamma_{\varphi_{11}} & \Gamma_{\varphi_{12}} \\ \Gamma_{\varphi_{21}} & 2\Gamma_{\varphi_{22}} \end{bmatrix} \geq 0 \\
&\Gamma_{\varphi_{22}} + 2\kappa\Gamma_{\varphi_{23}} + \kappa^2\Gamma_{\varphi_{33}} \geq 0
\end{aligned} \tag{6.42}
$$

The first inequality in (6.42) yields $\gamma_\varphi^2 \geq 2$ while the second gives $\gamma_\varphi^2 \geq \kappa^2$ which results in the upper bound $\gamma_\varphi = \max\{\kappa, \sqrt{2}\}$. □

In order to perform robust stability analysis, the rate limiter was modified in (6.33) and in order to preserve the original problem, the plant model must be adjusted to reflect the modified rate limiter. Therefore a filter, $1/\rho(z^{-1})$ is introduced at the input to the plant such that

$$
g_{rl}(z^{-1}) = z^{-1}g(z^{-1}) \tag{6.43}
$$

since $\rho(z^{-1}) = 1/z^{-1}$. The control law for the modified rate limiter and plant within the IMC structure in Fig. 6.8 becomes,

$$
\begin{aligned}
\bar{u}_m[k] &= -p_m{\sigma_m}^{-1}q_{f_m}(z^{-1})\hat{h}_m[k] \\
\hat{h}_m[k] &= \bar{y}_m[k] - \sigma_m g_{rl}(z^{-1})\bar{w}_m[k] \\
\bar{w}_m[k] &= \rho(z^{-1})\bar{v}_m[k] \\
\bar{v}_m[k] &= \frac{z^{-1}}{1-z^{-1}}\text{sat}\left(\bar{u}_m[k] - \bar{v}_m[k]\right)
\end{aligned} \tag{6.44}
$$

However, given (6.43) and the choice of $\rho(z^{-1})$, $\bar{u}_m[k]$ for the modified system is equivalent to the original problem. Therefore $q_m(z^{-1})$ is designed for the modified rate limiter and the plant, which gives the desired input for the original problem. For the IMC structure, $q_m(z^{-1})$ would normally be chosen as the approximate inverse of the plant dynamics as in Chapter 4, but because of the modified rate limiter, $q_m(z^{-1})$ is chosen as the inverse of the minimum-phase part of $g_{rl}(z^{-1})$. However, given (6.43), the minimum-phase part of the plant dynamics remains the same, so that $q_m(z^{-1})$ is chosen as before in (4.11).

To guarantee external stability of the IMC anti-windup augmented closed loop against spatial uncertainty and the presence of the rate limiter, both the uncertainty and the nonlinearity can be expressed in an IQC framework. For the following perturbed system,

$$\mathbf{y}[k] = \mathbf{\Phi} g(z^{-1}) \left[\mathbf{\Sigma} + \bar{\mathbf{\Delta}} \right] \mathbf{\Psi}_1^{\mathrm{T}} \mathbf{u}[k] + \mathbf{h}[k] \tag{6.45}$$

the operator $\bar{\mathbf{\Delta}}$ is considered to be diagonal to represent independent variations in each mode. As in Chapter 4, for stability analysis the closed loop system is expressed in the standard feedback loop configuration, and given that $\bar{\mathbf{v}}_\Delta[k] = \bar{\mathbf{\Delta}} \bar{\mathbf{u}}_\Delta[k]$ and $\bar{\mathbf{w}}[k] = \tilde{\boldsymbol{\varphi}} \bar{\mathbf{u}}[k]$, the closed loop system is completely characterized by

$$\begin{aligned} \begin{bmatrix} \bar{\mathbf{u}}[k] \\ \bar{\mathbf{u}}_\Delta[k] \end{bmatrix} &= \mathbf{X}(z^{-1}) \begin{bmatrix} \bar{\mathbf{w}}[k] \\ \bar{\mathbf{v}}_\Delta[k] \end{bmatrix} \\ \begin{bmatrix} \bar{\mathbf{w}}[k] \\ \bar{\mathbf{v}}_\Delta[k] \end{bmatrix} &= \mathbf{\Delta}_T \left(\begin{bmatrix} \bar{\mathbf{u}}[k] \\ \bar{\mathbf{u}}_\Delta[k] \end{bmatrix} \right) \end{aligned} \tag{6.46}$$

where the operator $\mathbf{\Delta}_T$ encapsulates the rate limiter and the uncertainty such that, $\mathbf{\Delta}_T = \mathrm{diag}\{\tilde{\boldsymbol{\varphi}}, \bar{\mathbf{\Delta}}\}$ and the LTI transfer matrix $\mathbf{X}(z^{-1})$ is given as,

$$\mathbf{X}(z^{-1}) = \begin{bmatrix} -\mathbf{Q}_b(z^{-1}) & -\mathbf{P}\boldsymbol{\Sigma}^{-1}\mathbf{Q}_f(z^{-1}) \\ \mathbf{I} & \mathbf{0} \end{bmatrix} \tag{6.47}$$

For mixed uncertainty, $\bar{\boldsymbol{\Delta}} \in \text{IQC}(\boldsymbol{\Pi}_{\bar{\Delta}})$ and $\tilde{\boldsymbol{\varphi}} \in \text{IQC}(\boldsymbol{\Pi}_{\tilde{\varphi}})$ and in this case, the uncertainty is represented as $\bar{\boldsymbol{\Delta}} = \text{diag}\{\bar{\delta}_m\}$ with $\|\bar{\delta}_m\|_\infty \leq 1$, $\forall m = 1 \ldots M$. Therefore

$$\boldsymbol{\Pi}_{\bar{\Delta}} = \begin{bmatrix} \Gamma_{\bar{\Delta}} & \mathbf{0} \\ \mathbf{0} & -\Gamma_{\bar{\Delta}} \end{bmatrix} \tag{6.48}$$

is a suitable choice where $\Gamma_{\bar{\Delta}} = \text{diag}\{\gamma_{\bar{\Delta}_m}\}$ and $\gamma_{\bar{\Delta}_m} > 0$.

To model the modified rate limiter (when the saturation is modeled as a [0,1] sector bounded nonlinearity), the following IQC multipliers are suitable:

- An IQC multiplier can be derived from the relationship between the gain from $\bar{u}_m[k]$ to $\bar{w}_m[k]$ which is shown to not exceed $\sqrt{2}$:

$$\boldsymbol{\Pi}_{\tilde{\varphi}_1} = \begin{bmatrix} 2\mathbf{I} & \mathbf{0} \\ \mathbf{0} & -\mathbf{I} \end{bmatrix} \tag{6.49}$$

- An IQC multiplier can be derived from the relationship from the input to the saturation block to the output can be modeled as a [0,1] sector bounded nonlinearity:

$$\boldsymbol{\Pi}_{\tilde{\varphi}_2} = \begin{bmatrix} \mathbf{0} & \mathbf{I} \\ \mathbf{I} & -2\mathbf{I} \end{bmatrix} \tag{6.50}$$

- Any conic combination of the above two multipliers are also considered as appropriate :

$$\boldsymbol{\Pi}_{\tilde{\varphi}} = \sum_{i=1}^{2} k_\Pi \boldsymbol{\Pi}_{\tilde{\varphi}_i} \tag{6.51}$$

  for any $k_\Pi \geq 0$ [Chakraborty et al., 2011].

The feasibility condition in (4.35) is used to determine stability of the closed loop in the presence of the rate limiter and uncertainty where $\mathbf{X}(z^{-1})$ is given by (6.47) and $\tilde{\mathbf{\Pi}}$ is

$$\begin{aligned}
\tilde{\mathbf{\Pi}}_{11} &= \boldsymbol{\mathcal{C}}_X^{\mathrm{T}}\mathbf{\Pi}_{\Delta_T 11}\boldsymbol{\mathcal{C}}_X \\
\tilde{\mathbf{\Pi}}_{12} = \tilde{\mathbf{\Pi}}_{21}^{*} &= \boldsymbol{\mathcal{C}}_X^{\mathrm{T}}\mathbf{\Pi}_{\Delta_T 12}\boldsymbol{\mathcal{C}}_X + \boldsymbol{\mathcal{C}}_X^{\mathrm{T}}\mathbf{\Pi}_{\Delta_T 11}\boldsymbol{\mathcal{D}}_X \\
\tilde{\mathbf{\Pi}}_{22} &= \mathbf{\Pi}_{\Delta_T 22} + \mathbf{\Pi}_{\Delta_T 21}\boldsymbol{\mathcal{D}}_X + \boldsymbol{\mathcal{D}}_X^{\mathrm{T}}\mathbf{\Pi}_{\Delta_T 21} + \boldsymbol{\mathcal{D}}_X^{\mathrm{T}}\mathbf{\Pi}_{\Delta_T 11}\boldsymbol{\mathcal{D}}_X
\end{aligned} \tag{6.52}$$

where $\mathbf{\Pi}_{\Delta_T} = \mathrm{daug}\{\mathbf{\Pi}_{\tilde{\varphi}}, \mathbf{\Pi}_{\bar{\Delta}}\}$.

6.5 Booster Anti-Windup Design and Implementation

The IMC anti-windup compensation structure was implemented on the booster and the factorisation of $q_{f_m}(z^{-1})$ and $q_{b_m}(z^{-1})$ were designed using two techniques:

- Weighting factorisation: $q_{f_m}(z^{-1}) = \upsilon_{w_m} q_m(z^{-1}) + (1-\upsilon_{w_m})q_m(0)$
- Filter factorisation: $q_{f_m}(z^{-1}) = \upsilon_{a_m}(z^{-1})g^{-}(z^{-1})q_m(z^{-1})$

and the integrated beam motions observed on the process from each design are shown in Fig. 6.12 and Fig. 6.13 respectively. By comparing the constrained performance with the unconstrained performance, unconstrained response recovery is determined, that is, how close the anti-windup augmented closed loop system performance emulates the response of the unconstrained closed-loop system. When the constraints are active, there is a deterioration in performance compared to the performance of the unconstrained system. However, the goal of the anti-windup is to as best as possible recover the unconstrained performance. Fig. 6.12 shows the integrated beam motion where $\upsilon_{w_m} = 0$ is compared to the unconstrained performance since this choice of υ_{w_m} is expected to give the best constrained performance when using the weighting factorisation technique. The results are similar to the simulations of the storage ring system where this choice of anti-windup results in improved performance at high frequencies but worse performance at frequencies below 100Hz which is undesirable as the bulk of the disturbance lies at these frequencies.

As an alternative, the filter factorisation technique given by (6.16) was also implemented where the Riccati-based synthesis was used to find an appropriate $\upsilon_{a_m}(z^{-1})$ given by

$$\upsilon_{a_m}(z^{-1}) = \frac{1 - 0.09z^{-1} + 0.91z^{-2}}{1 + 0.91z^{-1} - 0.09z^{-2}} \tag{6.53}$$

The resulting beam motion is shown in Fig. 6.13 and similar to the simulation result on the storage ring, this choice of factorisation results in improved performance at all frequencies when rate constrained.

To determine the upper bound of the l_2 gain of the uncertainty, $\bar{\boldsymbol{\Delta}}$ in the presence of the rate limiter for both techniques, the robust stability test was used. It is found that the closed loop system is stable in the presence of the rate limiter and spatial uncertainty and the allowable size of the uncertainty is shown in Fig. 6.14 for each mode. As a final comparison, Fig. 6.14 shows that the factorisation determined by (6.53) gives greater stability than the simple weighting factorisation when $\upsilon_{w_m} = 0$. This result demonstrates that while $\upsilon_{w_m} = 0$ gives satisfactory anti-windup compensation at certain frequencies, the performance of this augmentation is neither optimal nor does it offer better robust stability over the less restrictive factorisation given by the judicial choice of $\upsilon_{a_m} = 0$ in (6.16).

6.6 Conclusion

A rate limit constraint is introduced to the closed loop and the IMC unconstrained controller was augmented to provide acceptable closed loop performance during constrained operation. The augmentation involves factorising the unconstrained

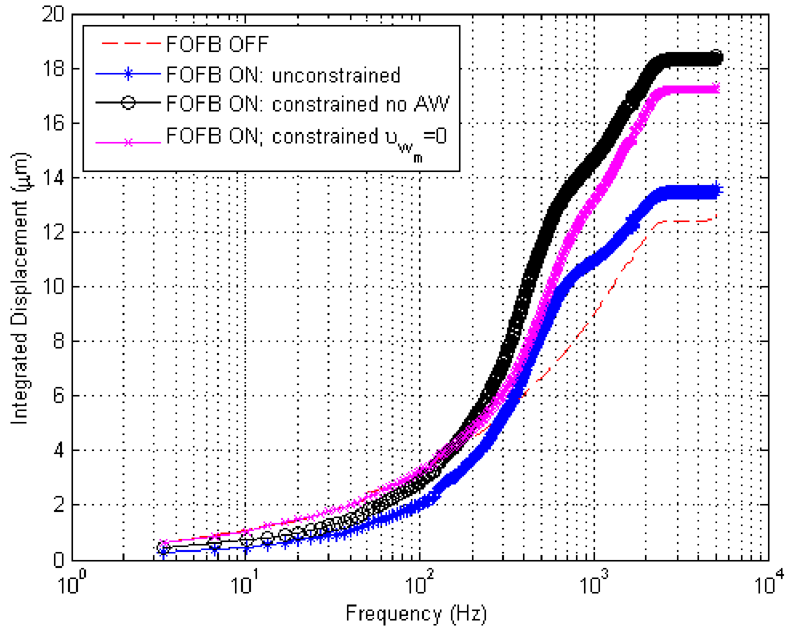

Fig. 6.12: Uncontrolled integrated beam motion at 1st vertical BPM on the booster ('- -' red), controlled integrated beam motion for the unconstrained system ('$*$' blue), the rate constrained system with no anti-windup ('o' black) and rate constrained system with anti-windup using (6.15) where $\upsilon_{w_m} = 0$ ('x' magenta) where a rate limit of 1.5A/s is used.

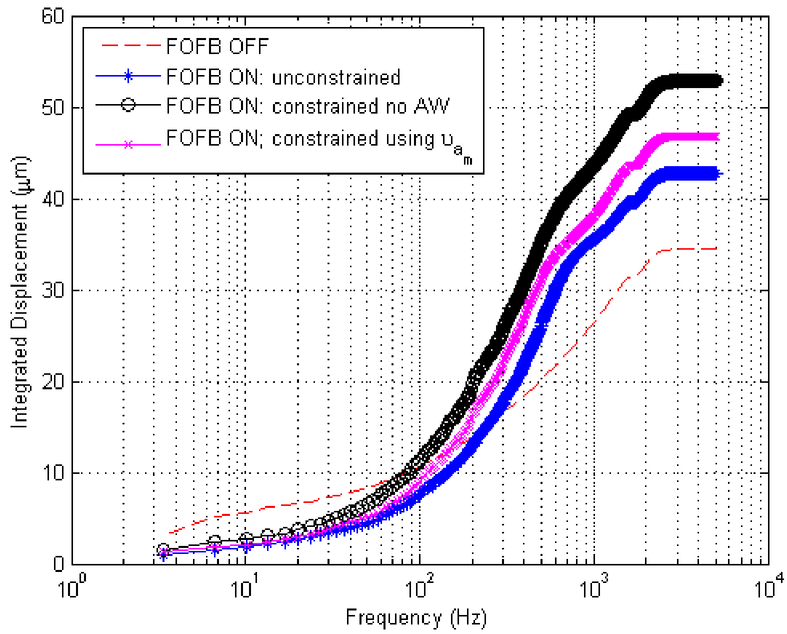

Fig. 6.13: Uncontrolled integrated beam motion at 1st vertical BPM on the booster ('- -' red), controlled integrated beam motion for the unconstrained system ('$*$' blue), the rate constrained system with no anti-windup ('o' black) and rate constrained system with anti-windup using (6.16) where $\upsilon_{a_m}(z^{-1})$ is chosen in (6.53) ('x' magenta) where a rate limit of 1.5A/s is used.

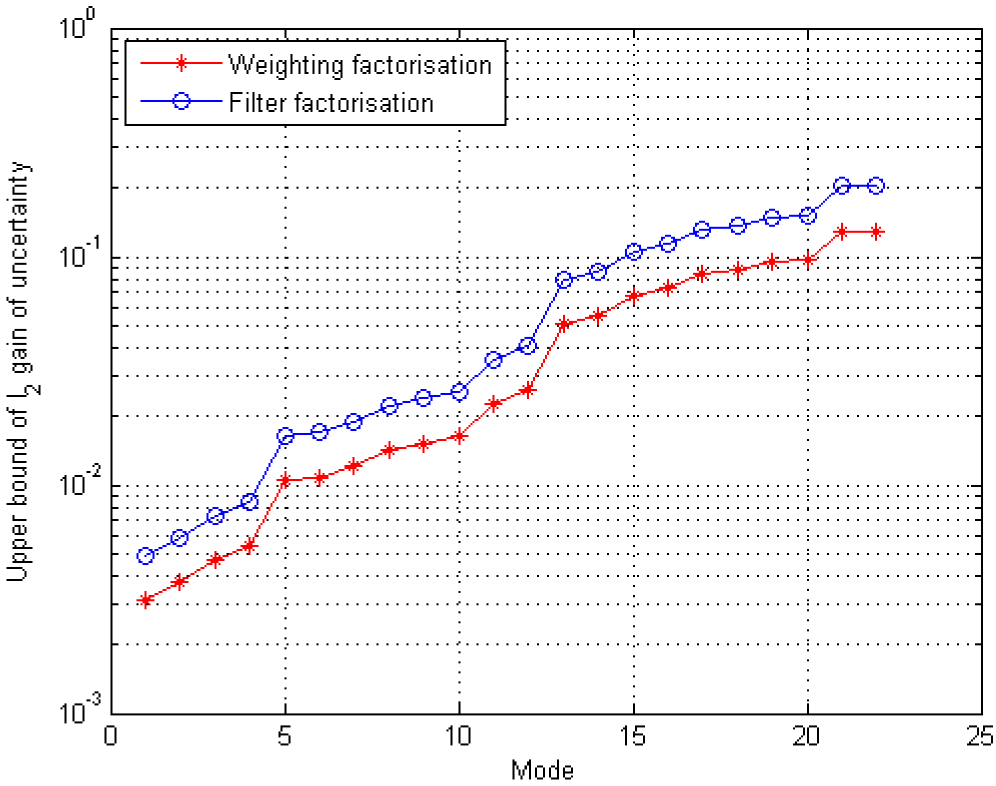

Fig. 6.14: Allowable size of uncertainty in the booster for each mode for the rate constrained system with anti-windup where $\upsilon_{w_m} = 0$ ('$*$' red) and with anti-windup where $\upsilon_{a_m}(z^{-1})$ is given in (6.53) ('o' blue). In both cases, $\mu = 1$.

controller to include an anti-windup term which must be chosen to ensure small signal preservation and internal stability. The IQC robust stability test was extended to incorporate both the rate constraint and spatial uncertainty to ensure that the augmented closed loop system is robustly stable. To determine stability in an l_2 sense, the rate limiter and the plant must be modified. The unconstrained response recovery for common factorisation choices are compared and while a simple weighting factorisation recovers the high frequency unconstrained response, a less restrictive filter factorisation offers better constrained performance. A further observation is that an optimal choice of the filter for factorisation can be synthesised using an Riccati-based technique that is reformulated for use in an IMC structure.

Chapter 7

Multiple Actuator Array Control

The work presented in this section is motivated by the fact that historically at synchrotrons, slow drifts in the location of the electron beam at frequencies below 1Hz were corrected by a separate control system while disturbances above 1Hz were corrected by the 'fast' feedback system; hence the use of the term 'fast orbit feedback (FOFB)'. Some machines continue to use a fast and slow orbit feedback system, where correctors with strong magnetic fields are used for slow correction, but the use of these correctors located over high conductivity vacuum chambers produce eddy currents that limit the feedback bandwidth to a few Hertz [Hubert et al., 2009]. Therefore a set of fast correctors is required to compensate for high frequency disturbances meaning that some storage rings use two arrays of corrector magnets, respectively referred to as 'strong' and 'fast' correctors [Chiu et al., 2013, Hubert et al., 2009, Plouvier et al., 2011, Steier et al., 2004]. At storage rings like that at Diamond, the FOFB system utilises one set of corrector magnets that are responsible for correcting disturbances below 1Hz as well. However future development at Diamond may introduce corrector magnets with different dynamics than those currently used and the starting assumption in this thesis that all correctors have the same dynamics will no longer be valid. In this chapter, an approach to orbit control where there are two arrays of actuators with different dynamics is presented that preserves as much as possible the IMC structure and analysis presented in previous chapters.

The control problem at facilities using two arrays of correctors, is the design of two global feedback systems that work together. An early approach has been to design the two feedback controllers separately, but when the controllers share a common frequency range, they fight against each other, resulting in the saturation of the faster correctors. Consequently several approaches are proposed to deal with this problem, one of which is the use of a 'frequency deadband' to separate the fast and slow systems so that the two systems are independent [Schwartz and Emery, 2001]. However, beam spectrum components within the frequency deadband are not corrected. This is undesirable as there are components of the disturbance that cannot be left without correction within the deadband frequency range, such as transient orbit distortions from insertion devices, which change the magnetic field as part of an experiment. Another approach is to use the fast feedback system alone with an active frequency range down to DC, which solves the uncorrected perturbations at low frequencies, but in some cases this presents a limitation due to the relative weakness of fast correctors. Because the fast correctors are designed to regulate small perturbations at high speeds and therefore have limited amplitude ranges, the correctors tend to saturate [Hubert et al., 2009]. In some machines, this is compensated for by using the slow correctors to periodically remove the DC components of the fast correctors so that the fast correctors do not saturate even after long term drift of the closed orbit [Yu et al., 2008]. Other solutions seek to use the slow system to predict the different orbit at the next iteration and transfer it as a new reference to the fast system. As a consequence, the fast system will not see the perturbation created by the slow correction and will not try to compensate for it [Schwartz and Emery, 2001, Steier et al., 2004]. However this approach has caused closed loop instabilities on systems where the dynamics of the fast correctors are sufficiently different from the slow ones [Hubert et al., 2009]. Some machines combine some of these approaches [Hubert et al., 2009].

Several control designs based on large-scale optimisation have been used to handle multi-array cross-directional problems which use long horizon MPC [Backström et al., 2001]. The size of the control problem in industrial cross-directional systems is usually overcome by reducing the model size or using a fast quadratic programming algorithm [Fan et al., 2004]. However, for this application, the goal is to provide heuristics for the given control structures already in place at synchrotrons, that is either PI or IMC controllers to handle the multiple actuator array problem.

In this chapter, the aim is to design a controller which uses both corrector magnet arrays to meet the electron beam stability requirements and guarantee closed loop stability in the presence of spatial uncertainty so that:

1. The time taken for online computation is not greater than that of the single array system.
2. The tuning for performance and robustness is intuitive.
3. The specific dynamics and constraints of each array are addressed.

In order to meet these goals, a method of exploiting the knowledge of the spatial responses of the arrays of correctors is used to determine the interaction between the controllable subspaces. As a result the problem can be decomposed into a series of single-input, single-output (SISO), multiple-input, single-output (MISO) and multiple-input, multiple-output (MIMO) problems [Duncan and Heath, 2010, Duncan et al., 2008]. As a consequence, the online computation is minimised by selecting appropriate control directions when subspaces of the two arrays overlap. In particular, if the control directions of the two arrays are orthogonal, then the problem can be interpreted as a decoupled two-input, two-output (TITO) structure (i.e. two SISO structures) and the design and analysis techniques presented in the previous chapters of this thesis are applicable. If however, the control directions align, the problem has a two-input, single-output (TISO) structure, and mid-ranging control can be used.

The term mid-ranging control typically refers to the class of control problems where two actuators are manipulated to control one measured variable. Furthermore there is the condition that one input should return to its midpoint or some setpoint. The inputs usually differ in their dynamic effect on the output and in the relative cost of manipulating each one, with the fast input normally being more costly to use than the slow input [Henson et al., 1995]. Therefore mid-ranging control schemes seek to manipulate both inputs upon an upset but then gradually reset or mid-range the fast input to its desired setpoint [Allison and Ogawa, 2003, Gayadeen and Heath, 2009]. Mid-ranging control therefore is suitable for the fast and strong corrector problem. Though it may be possible to manipulate each actuator separately, for electron beam control it is desirable to simultaneously manipulate both inputs, as the strong correctors are bandwidth limited. Additionally, an important characteristic of mid-ranging applications is that input constraints are often encountered [Allison and Ogawa, 2003], which is the case with most fast corrector magnets. There are several approaches to designing mid-ranging controllers [Allison and Ogawa, 2003, Henson et al., 1995], but in [Gayadeen and Heath, 2009] an IMC structure is used, which is adopted in this thesis since it is consistent with the design for a single array of actuators, presented in previous chapters.

More recently in [Gallieri and Maciejowski, 2011], a dual-mode MPC approach based on sum-of-norms regularisation is used to develop a smart allocation policy to use the least number of actuators. However with this design, actuators are set to zero for extensive periods. For the electron beam motion control such an approach is inappropriate, as it is desirable to maximise the use of all actuators to ensure that the maximum DC correction is achieved. The IMC approach to the multi-array problem with a mid-ranging strategy is proposed not only to achieve comparable computation times as with the single array system but also to allow explicit design trade-offs and to take advantage of the different actuator characteristics such as dynamics and saturation limits.

7.1 Multi-Array Controller Design

For a system with two arrays of actuators where N_f and N_s are the number of actuators in each array, the dynamics of each array is given by

$$\begin{aligned} g_s(z^{-1}) &= z^{-d_s}\frac{b_{0_s} + b_{1_s}z^{-1}}{1 - a_{1_s}z^{-1}} \\ g_f(z^{-1}) &= z^{-d_f}\frac{b_{0_f} + b_{1_f}z^{-1}}{1 - a_{1_f}z^{-1}} \end{aligned} \tag{7.1}$$

where, without loss of generality, it is assumed that

1. $g_s(1) = 1$ and $g_f(1) = 1$ i.e. the DC gains of the dynamics can be taken as unity.

2. the dynamics of $g_f(z^{-1})$ are faster than $g_s(z^{-1})$.

3. all the actuators of a given array have the same dynamics.

The position measured at M BPMs is described by

$$\mathbf{y}[k] = g_s(z^{-1})\mathbf{R}_s\mathbf{u}_s[k] + g_f(z^{-1})\mathbf{R}_f\mathbf{u}_f[k] + \mathbf{h}[k] \tag{7.2}$$

where $\mathbf{u}_s[k] \in \mathbb{R}^{N_s}$ and $\mathbf{u}_f[k] \in \mathbb{R}^{N_f}$ represent the inputs applied to the two distinct arrays of actuators. The response matrices for each array is represented by $\mathbf{R}_s$ and $\mathbf{R}_f$ where $N_s = \text{rank}(\mathbf{R}_s)$ and $N_f = \text{rank}(\mathbf{R}_f)$ and $N_f \leq N_s$. The response matrices of each array, $\mathbf{R}_s$ and $\mathbf{R}_f$ can each be expressed in terms of reduced singular value decompositions so that,

$$\begin{aligned}\mathbf{R}_s &= \mathbf{\Phi}_s\mathbf{\Sigma}_s\mathbf{\Psi}_s^{\mathrm{T}}\\ \mathbf{R}_f &= \mathbf{\Phi}_f\mathbf{\Sigma}_f\mathbf{\Psi}_f^{\mathrm{T}}\end{aligned} \tag{7.3}$$

where $\mathbf{\Phi}_s \in \mathbb{R}^{M\times N_s}$, $\mathbf{\Sigma}_s \in \mathbb{R}^{N_s\times N_s}$, $\mathbf{\Psi}_s \in \mathbb{R}^{N_s\times N_s}$, $\mathbf{\Phi}_f \in \mathbb{R}^{M\times N_f}$, $\mathbf{\Sigma}_f \in \mathbb{R}^{N_f\times N_f}$ and $\mathbf{\Psi}_f \in \mathbb{R}^{N_f\times N_f}$. The columns of $\mathbf{\Psi}_s$ and $\mathbf{\Psi}_f$ in (7.3) represent the controllable subspaces of the response matrices and even though $\mathbf{R}_s$ and $\mathbf{R}_f$ are independent, there may be some overlap between the controllable subspaces where the relationship between the subspaces of $\mathbf{R}_s$ and $\mathbf{R}_f$ can be found by comparing the subspaces of $\mathbf{\Phi}_s$ and $\mathbf{\Phi}_f$ which are both orthogonal and can be determined from Algorithm 12.4.3 in [Golub and Van Loan, 1996] such that

$$\mathbf{\Phi}_s^{\mathrm{T}}\mathbf{\Phi}_f = \mathbf{A} \tag{7.4}$$

and the singular value decomposition of $\mathbf{A}$ is given by

$$\mathbf{A} = \mathbf{\Phi}_A \begin{bmatrix}\mathbf{\Sigma}_A\\ \mathbf{0}\end{bmatrix} \mathbf{\Psi}_A^{\mathrm{T}} \tag{7.5}$$

with left matrix, $\mathbf{\Phi}_A \in \mathbb{R}^{N_s\times N_s}$, right matrix $\mathbf{\Psi}_A \in \mathbb{R}^{N_f\times N_f}$ and $\mathbf{\Sigma}_A \in \mathbb{R}^{N_f\times N_f}$ such that

$$\mathbf{\Sigma}_A = \begin{bmatrix}\cos(\theta_{A_1}) & & \\ & \ddots & \\ & & \cos(\theta_{A_{N_f}})\end{bmatrix} \tag{7.6}$$

where θ_{A_i} is the angle between the principal vectors spanning $\mathbf{\Phi}_f$ and $\mathbf{\Phi}_s$ which span the controllable subspaces of $\mathbf{R}_s$ and $\mathbf{R}_f$.

An internal model controller for such a multi-array system takes the form

$$\begin{aligned}
\mathbf{u}_s[k] &= -\tilde{\mathbf{Q}}_s(z^{-1})\hat{\mathbf{h}}(z^{-1}) \\
\mathbf{u}_f[k] &= -\tilde{\mathbf{Q}}_f(z^{-1})\hat{\mathbf{h}}(z^{-1}) \\
\hat{\mathbf{h}}(z^{-1}) &= \mathbf{y}[k] - g_s(z^{-1})\mathbf{R}_s\mathbf{u}_s[k] - g_f(z^{-1})\mathbf{R}_f\mathbf{u}_f[k]
\end{aligned} \tag{7.7}$$

so that the nominal closed loop response is

$$\mathbf{y}[k] = \left[\mathbf{I} - g_s(z^{-1})\mathbf{R}_s\tilde{\mathbf{Q}}_s(z^{-1}) - g_f(z^{-1})\mathbf{R}_f\tilde{\mathbf{Q}}_f(z^{-1})\right]\mathbf{h}(k) \tag{7.8}$$

which can be expressed as,

$$\mathbf{y}[k] = \left[\mathbf{I} - [\mathbf{\Phi}_s \;\; \mathbf{\Phi}_f]\begin{bmatrix} g_s(z^{-1})\mathbf{\Sigma}_s\mathbf{\Psi}_s^{\mathrm{T}}\tilde{\mathbf{Q}}_s(z^{-1}) \\ g_f(z^{-1})\mathbf{\Sigma}_f\mathbf{\Psi}_f^{\mathrm{T}}\tilde{\mathbf{Q}}_f(z^{-1}) \end{bmatrix}\right]\mathbf{h}(k) \tag{7.9}$$

where

$$\begin{aligned}
\tilde{\mathbf{Q}}_s(z^{-1}) &= \mathbf{\Psi}_s\mathbf{\Sigma}_s^{-1}\mathbf{Q}_s(z^{-1})\tilde{\mathbf{\Phi}}_s \\
\tilde{\mathbf{Q}}_f(z^{-1}) &= \mathbf{\Psi}_f\mathbf{\Sigma}_f^{-1}\mathbf{Q}_f(z^{-1})\tilde{\mathbf{\Phi}}_f
\end{aligned} \tag{7.10}$$

for some diagonal $\mathbf{Q}_s(z^{-1})$ and $\mathbf{Q}_f(z^{-1})$ and for $\tilde{\mathbf{\Phi}}_s \in \mathbb{R}^{N_s \times M}$ and $\tilde{\mathbf{\Phi}}_f \in \mathbb{R}^{N_f \times M}$. Therefore (7.9) can be expressed as

$$\mathbf{y}[k] = \left[\mathbf{I} - [\mathbf{\Phi}_s \;\; \mathbf{\Phi}_f]\begin{bmatrix} g_s(z^{-1})\mathbf{Q}_s(z^{-1})\tilde{\mathbf{\Phi}}_s \\ g_f(z^{-1})\mathbf{Q}_f(z^{-1})\tilde{\mathbf{\Phi}}_f \end{bmatrix}\right]\mathbf{h}[k] \tag{7.11}$$

If the diagonal transfer function matrices $\mathbf{Q}_f(z^{-1})$ and $\mathbf{Q}_s(z^{-1})$ are chosen to have unity DC gain, then for steady state

$$\mathbf{y}_{ss} = \left[\mathbf{I} - [\mathbf{\Phi}_s \;\; \mathbf{\Phi}_f]\begin{bmatrix} \tilde{\mathbf{\Phi}}_s \\ \tilde{\mathbf{\Phi}}_f \end{bmatrix}\right]\mathbf{h}_{ss} \tag{7.12}$$

Pre-multiplying both sides by $[\boldsymbol{\Phi}_s \;\; \boldsymbol{\Phi}_f]^{\mathrm{T}}$, projects the response into modal space so that

$$\begin{bmatrix} \boldsymbol{\Phi}_s^{\mathrm{T}} \\ \boldsymbol{\Phi}_f^{\mathrm{T}} \end{bmatrix} \mathbf{y}_{ss} = \begin{bmatrix} \boldsymbol{\Phi}_s^{\mathrm{T}} \\ \boldsymbol{\Phi}_f^{\mathrm{T}} \end{bmatrix} \mathbf{h}_{ss} - \begin{bmatrix} \boldsymbol{\Phi}_s^{\mathrm{T}} \\ \boldsymbol{\Phi}_f^{\mathrm{T}} \end{bmatrix} \begin{bmatrix} \boldsymbol{\Phi}_s & \boldsymbol{\Phi}_f \end{bmatrix} \begin{bmatrix} \tilde{\boldsymbol{\Phi}}_s \\ \tilde{\boldsymbol{\Phi}}_f \end{bmatrix} \mathbf{h}_{ss} \tag{7.13}$$

and defining

$$\begin{bmatrix} \tilde{\boldsymbol{\Phi}}_s \\ \tilde{\boldsymbol{\Phi}}_f \end{bmatrix} = \boldsymbol{\Omega} \begin{bmatrix} \boldsymbol{\Phi}_s^{\mathrm{T}} \\ \boldsymbol{\Phi}_f^{\mathrm{T}} \end{bmatrix} \tag{7.14}$$

where $\boldsymbol{\Omega}$ is a decoupling matrix, with $\boldsymbol{\Omega}_{11} \in \mathbb{R}^{N_s \times N_s}$, $\boldsymbol{\Omega}_{12} \in \mathbb{R}^{N_s \times N_f}$, $\boldsymbol{\Omega}_{21} \in \mathbb{R}^{N_f \times N_s}$ and $\boldsymbol{\Omega}_{22} \in \mathbb{R}^{N_f \times N_f}$, so that

$$\begin{aligned} \bar{\mathbf{y}}_{ss} &= \begin{bmatrix} \boldsymbol{\Phi}_s^{\mathrm{T}} \\ \boldsymbol{\Phi}_f^{\mathrm{T}} \end{bmatrix} \mathbf{y}_{ss} \\ \bar{\mathbf{h}}_{ss} &= \begin{bmatrix} \boldsymbol{\Phi}_s^{\mathrm{T}} \\ \boldsymbol{\Phi}_f^{\mathrm{T}} \end{bmatrix} \mathbf{h}_{ss} \end{aligned} \tag{7.15}$$

and

$$\bar{\mathbf{y}}_{ss} = \left[\mathbf{I} - \begin{bmatrix} \mathbf{I} & \boldsymbol{\Phi}_s^{\mathrm{T}} \boldsymbol{\Phi}_f \\ \boldsymbol{\Phi}_f^{T} \boldsymbol{\Phi}_s & \mathbf{I} \end{bmatrix} \begin{bmatrix} \boldsymbol{\Omega}_{11} & \boldsymbol{\Omega}_{12} \\ \boldsymbol{\Omega}_{21} & \boldsymbol{\Omega}_{22} \end{bmatrix} \right] \bar{\mathbf{h}}_{ss} \tag{7.16}$$

From the relationship in (7.4), then

$$\begin{bmatrix} \mathbf{I} & \boldsymbol{\Phi}_s^{T} \boldsymbol{\Phi}_f \\ \boldsymbol{\Phi}_f^{T} \boldsymbol{\Phi}_s & \mathbf{I} \end{bmatrix} = \begin{bmatrix} \mathbf{I} & \mathbf{A} \\ \mathbf{A}^{\mathrm{T}} & \mathbf{I} \end{bmatrix} \tag{7.17}$$

and given (7.5)

$$\begin{bmatrix} \mathbf{I} & \boldsymbol{\Phi}_s^{T} \boldsymbol{\Phi}_f \\ \boldsymbol{\Phi}_f^{T} \boldsymbol{\Phi}_s & \mathbf{I} \end{bmatrix} = \begin{bmatrix} \boldsymbol{\Phi}_A & \\ & \boldsymbol{\Psi}_A \end{bmatrix} \left[\begin{array}{cc|c} \mathbf{I} & \mathbf{0} & \boldsymbol{\Sigma}_A \\ \mathbf{0} & \mathbf{I} & \mathbf{0} \\ \hline \boldsymbol{\Sigma}_A & \mathbf{0} & \mathbf{I} \end{array} \right] \begin{bmatrix} \boldsymbol{\Phi}_A & \\ & \boldsymbol{\Psi}_A \end{bmatrix}^{\mathrm{T}} \tag{7.18}$$

The ideal design would be to make $\mathbf{\Omega}$ equal to the inverse of the matrix in (7.18) and because it has a block diagonal structure, this gives

$$\mathbf{\Omega} = \begin{bmatrix} \mathbf{\Phi}_A & \\ & \mathbf{\Psi}_A \end{bmatrix} \tilde{\mathbf{\Omega}} \begin{bmatrix} \mathbf{\Phi}_A & \\ & \mathbf{\Psi}_A \end{bmatrix}^{\mathrm{T}} \tag{7.19}$$

where

$$\tilde{\mathbf{\Omega}} = \begin{bmatrix} \tilde{\mathbf{\Sigma}}_A & \mathbf{0} & \tilde{\mathbf{\Sigma}}_A \\ \mathbf{0} & \mathbf{I} & \mathbf{0} \\ \tilde{\mathbf{\Sigma}}_A & \mathbf{0} & \tilde{\mathbf{\Sigma}}_A \end{bmatrix} \odot \begin{bmatrix} \mathbf{I} & \mathbf{0} & -\mathbf{\Sigma}_A \\ \mathbf{0} & \mathbf{I} & \mathbf{0} \\ -\mathbf{\Sigma}_A & \mathbf{0} & \mathbf{I} \end{bmatrix} \tag{7.20}$$

and $\tilde{\mathbf{\Sigma}}_A \in \mathbb{R}^{N_f \times N_f}$ is a diagonal matrix with elements

$$\left[\tilde{\mathbf{\Sigma}}_A\right]_{ii} = \frac{1}{1 - \cos^2 \theta_{A_i}} \tag{7.21}$$

and $\odot$ denotes element-wise multiplication [Duncan and Heath, 2010]. Difficulties with this choice arise when $\cos(\theta_{A_i}) \approx 1$ which occurs when the angle between the subspaces is small. Instead, heuristic choices for the elements of $\tilde{\mathbf{\Omega}}$ can be made, which are described below:

1. Define the following:

$$\begin{aligned} \tilde{\mathbf{\Omega}}_{11} &= \begin{bmatrix} \tilde{\mathbf{\Sigma}}_A & \mathbf{0} \\ \mathbf{0} & \mathbf{I} \end{bmatrix} \\ \tilde{\mathbf{\Omega}}_{12} &= \begin{bmatrix} -\tilde{\mathbf{\Sigma}}_A \mathbf{\Sigma}_A \\ \mathbf{0} \end{bmatrix} \\ \tilde{\mathbf{\Omega}}_{21} &= \begin{bmatrix} -\tilde{\mathbf{\Sigma}}_A \mathbf{\Sigma}_A & \mathbf{0} \end{bmatrix} \\ \tilde{\mathbf{\Omega}}_{22} &= \tilde{\mathbf{\Sigma}}_A \end{aligned} \tag{7.22}$$

2. When $\cos(\theta_{A_i}) = 0$, the directions $\mathbf{\Phi}_s(:, i)$ and $\mathbf{\Phi}_f(:, i)$ are orthogonal so that the system is considered as a decoupled two-input, two-output system i.e. two

SISO structures. The relationships in (7.22) give this automatically where the corresponding elements of $\tilde{\mathbf{\Omega}}_{11}$ and $\tilde{\mathbf{\Omega}}_{22}$ are set to 1 and $\tilde{\mathbf{\Omega}}_{12}$ and $\tilde{\mathbf{\Omega}}_{21}$ are set to 0 so that the two directions are controlled independently.

3. When $0 < \cos(\theta_{A_i}) < 1$, (7.22) automatically splits the effort between the two actuators.

4. When $\cos(\theta_{A_i})$ is close to 1, the directions $\mathbf{\Phi}_s(:,i)$ and $\mathbf{\Phi}_f(:,i)$ almost line up and choosing to control in one direction is appropriate. This is achieved by set the corresponding elements of either $\tilde{\mathbf{\Omega}}_{11}$ or $\tilde{\mathbf{\Omega}}_{22}$ to 1 and the other to 0. In this case, the corresponding elements of $\tilde{\mathbf{\Omega}}_{12}$ and $\tilde{\mathbf{\Omega}}_{21}$ are set to 0.

5. When $\cos(\theta_{A_i}) = 1$, the directions $\mathbf{\Phi}_s(:,i)$ and $\mathbf{\Phi}_f(:,i)$ align, giving a TISO structure. In this case, mid-ranging control is appropriate due to the actuator characteristics and the corresponding diagonal elements of $\tilde{\mathbf{\Omega}}_{11}$ and $\tilde{\mathbf{\Omega}}_{22}$ are transfer functions. The design of $\tilde{\mathbf{\Omega}}_{11}$ and $\tilde{\mathbf{\Omega}}_{22}$ in this case is discussed in Section 7.3.2.

7.2 Stability of the Multi-Array Design

Suppose that the true plant behaviour is given by

$$\mathbf{y}[k] = g_s(z^{-1})\left[\mathbf{R}_s + \mathbf{\Delta}_s^{\mathbf{\Phi}}\right]\mathbf{u}_s[k] + g_f(z^{-1})\left[\mathbf{R}_f + \mathbf{\Delta}_f^{\Phi}\right]\mathbf{u}_f[k] + \mathbf{h}[k] \tag{7.23}$$

where $\mathbf{\Delta}_s^{\mathbf{\Phi}} \in \mathbb{R}^{M\times N_S}$ and $\mathbf{\Delta}_s^{\mathbf{\Phi}} \in \mathbb{R}^{M\times N_S}$ are additive uncertainties in the spatial responses of the two arrays. The uncertainty operators in the two arrays can be written as

$$\begin{bmatrix} \mathbf{\Phi}_s^{\mathrm{T}} \\ \mathbf{\Phi}_f^{\mathrm{T}} \end{bmatrix} \begin{bmatrix} \mathbf{\Delta}_s^{\mathbf{\Phi}} & \mathbf{\Delta}_f^{\mathbf{\Phi}} \end{bmatrix} \begin{bmatrix} \mathbf{\Psi}_s & \\ & \mathbf{\Psi}_f \end{bmatrix} = \mathbf{W}^l \begin{bmatrix} \tilde{\mathbf{\Delta}}_{11}^{\mathbf{\Phi}} & \tilde{\mathbf{\Delta}}_{12}^{\mathbf{\Phi}} \\ \tilde{\mathbf{\Delta}}_{21}^{\mathbf{\Phi}} & \tilde{\mathbf{\Delta}}_{22}^{\mathbf{\Phi}} \end{bmatrix} \mathbf{W}^r \tag{7.24}$$

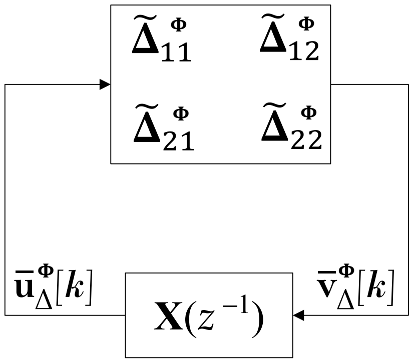

Fig. 7.1: The closed loop with uncertainty represented in the standard feedback configuration.

where $\mathbf{W}^l = \text{diag}\{\mathbf{W}^l_s, \mathbf{W}^l_f\}$ and $\mathbf{W}^r = \text{diag}\{\mathbf{W}^r_s, \mathbf{W}^r_f\}$ with $\tilde{\boldsymbol{\Delta}}^{\boldsymbol{\Phi}}_{11} \in \mathbb{R}^{N_s \times N_s}$, $\tilde{\boldsymbol{\Delta}}^{\boldsymbol{\Phi}}_{12} \in \mathbb{R}^{N_s \times N_f}$, $\tilde{\boldsymbol{\Delta}}^{\boldsymbol{\Phi}}_{21} \in \mathbb{R}^{N_f \times N_s}$ and $\tilde{\boldsymbol{\Delta}}^{\boldsymbol{\Phi}}_{22}$ representing the plant uncertainty lying within the subspace that is controllable by the combination of the two actuator arrays. The weights $\mathbf{W}^l$ and $\mathbf{W}^r$ are known matrices that characterize the uncertainty in the modal space [Duncan and Heath, 2010].

The closed loop system with uncertainty can be completely represented in the standard feedback form shown in Fig. 7.1 where

$$\mathbf{X}(z^{-1}) = \mathbf{W}^r \begin{bmatrix} -\tilde{\mathbf{Q}}_s(z^{-1}) \\ -\tilde{\mathbf{Q}}_f(z^{-1}) \end{bmatrix} \begin{bmatrix} g_s(z^{-1}) & g_f(z^{-1}) \end{bmatrix} \mathbf{W}^l \tag{7.25}$$

and

$$\begin{bmatrix} \tilde{\mathbf{Q}}_s(z^{-1}) \\ \tilde{\mathbf{Q}}_f(z^{-1}) \end{bmatrix} = \begin{bmatrix} \boldsymbol{\Psi}_s \boldsymbol{\Sigma}_s^{-1} \mathbf{Q}_s(z^{-1}) & \mathbf{0} \\ \mathbf{0} & \boldsymbol{\Psi}_f \boldsymbol{\Sigma}_f^{-1} \mathbf{Q}_f(z^{-1}) \end{bmatrix} \boldsymbol{\Omega} \begin{bmatrix} \boldsymbol{\Phi}_s^{\mathrm{T}} \\ \boldsymbol{\Phi}_f^{\mathrm{T}} \end{bmatrix} \tag{7.26}$$

and for any uncertainty satisfying

$$\left\| \begin{bmatrix} \tilde{\boldsymbol{\Delta}}^{\boldsymbol{\Phi}}_{11} & \tilde{\boldsymbol{\Delta}}^{\boldsymbol{\Phi}}_{12} \\ \tilde{\boldsymbol{\Delta}}^{\boldsymbol{\Phi}}_{21} & \tilde{\boldsymbol{\Delta}}^{\boldsymbol{\Phi}}_{22} \end{bmatrix} \right\|_{\infty} \leq 1 \tag{7.27}$$

a sufficient condition to ensure closed loop stability is that $\|\mathbf{X}(z^{-1})\|_{\infty} < 1$ which

Parameter	Slow Array	Fast Array
a (rad.s^{-1})	$2\pi \times 2$	$2\pi \times 1000$
τ_d (μs)	700	600

Table 7.1: Values of parameters for slow and fast processes.

gives

$$\left\| \mathbf{W}^r \begin{bmatrix} \mathbf{\Sigma}_s^{-1}\mathbf{Q}_s g_s(z^{-1}) & \\ & \mathbf{\Sigma}_f^{-1}\mathbf{Q}_f g_f(z^{-1}) \end{bmatrix} \begin{bmatrix} \tilde{\mathbf{\Omega}}_{11} & \tilde{\mathbf{\Omega}}_{12} \\ \tilde{\mathbf{\Omega}}_{21} & \tilde{\mathbf{\Omega}}_{22} \end{bmatrix} \left[\begin{array}{cc|c} \mathbf{I} & \mathbf{0} & \tilde{\mathbf{\Sigma}}_A \\ \mathbf{0} & \mathbf{I} & \mathbf{0} \\ \hline \tilde{\mathbf{\Sigma}}_A & \mathbf{0} & \mathbf{I} \end{array} \right] \mathbf{W}^l \right\|_\infty < 1 \tag{7.28}$$

7.3 Booster Multi-Array Design

7.3.1 Choice of Control Directions

In this section a simulation study is presented for the booster, where two arrays of actuators are considered. One array contains 'slow' corrector magnets which are bandwidth limited and the second array uses 'fast' corrector magnets which are amplitude limited where $N_s = 17$ and $N_f = 5$. Using the first order plus delay transfer function given in (3.4) and the parameters of the dynamics in Table 7.1, the frequency responses for the two arrays are shown in Fig. 7.2. The cosine of the angles between the first 5 columns of $\mathbf{\Phi}_s$ and $\mathbf{\Phi}_f$ are determined by (7.5) and are listed in Table 7.2. The following strategy is used for control:

- For $i = 1$ to 3, the control directions almost line up, so mid-ranging control is used. The design for the mid-ranging case is presented in Section 7.3.2.
- For $i = 4$, the control effort is split using $\tilde{\mathbf{\Omega}}$ in (7.20).
- For $i = 5$ to 17, $\cos(\theta_{A_i}) = 0$ meaning that the directions are decoupled and

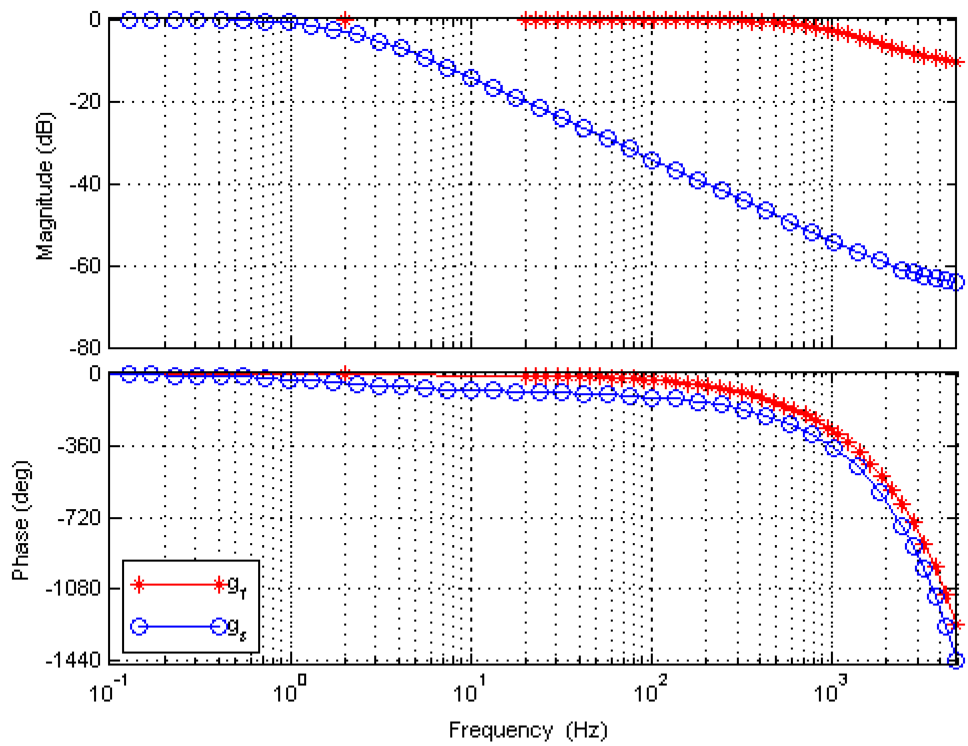

Fig. 7.2: Frequency responses of fast ('$*$' red) and slow actuators ('o' blue).

SISO structures are used. The controllers for each SISO loop are designed according to techniques described in Chapter 4. For $i = 5$, both the fast and slow actuators are used and for $i = 6$ to 17, slow actuators are used.

7.3.2 Mid-ranging Controller Design

The two-input, single-output problem is considered where the output is expressed as

$$\begin{aligned} y[k] = & \left[1 - g_s(z^{-1})q_{mr_s}(z^{-1}) - g_f(z^{-1})q_{mr_f}(z^{-1})\right] h[k] + \\ & \left[g_s(z^{-1})q_{p_s}(z^{-1}) + g_f(z^{-1})q_{p_f}(z^{-1})\right] u_r[k] \end{aligned} \tag{7.29}$$

where $g_s(z^{-1})$ and $g_f(z^{-1})$ are the slow and fast process models respectively and $q_{mr_s}(z^{-1})$ and $q_{mr_f}(z^{-1})$ are the associated IMC controllers. The mid-ranging objective is to use both inputs to control $y[k]$ and return the fast input to its setpoint

	$i=1$	$i=2$	$i=3$	$i=4$	$i=5$
$\cos(\theta_{A_i})$	0.99	0.98	0.91	0.59	0

Table 7.2: Angles between controllable subspaces of $\mathbf{R}_s$ and $\mathbf{R}_f$.

$u_r[k]$ where the pre-filters $q_{p_s}(z^{-1})$ and $q_{p_f}(z^{-1})$ are designed to obtain a desired response from $u_r[k]$ to $y[k]$ [Gayadeen and Heath, 2009]. Therefore, the corresponding elements of $\tilde{\mathbf{\Omega}}_{11}$ and $\tilde{\mathbf{\Omega}}_{22}$ in (7.22) are $[q_{s_i}(z^{-1})]^{-1}\, q_{mr_s}(z^{-1})$ and $[q_{f_i}(z^{-1})]^{-1}\, q_{mr_f}(z^{-1})$ respectively. The control signals to the two actuators are

$$\begin{aligned} u_s[k] &= q_{mr_s}(z^{-1})h[k] + q_{p_s}(z^{-1})u_r[k] \\ u_f[k] &= q_{mr_f}(z^{-1})h[k] + q_{p_f}(z^{-1})u_r[k] \end{aligned} \tag{7.30}$$

The mid-ranging design specifies not only the complementary sensitivity with both actuators, $T_{fast}(z^{-1})$, but also the complementary sensitivity corresponding to the control action with the slow actuator alone, $T_{slow}(z^{-1})$ which are defined as follows,

$$\begin{aligned} T_{fast}(z^{-1}) &= g_s(z^{-1})q_{mr_s}(z^{-1}) + g_f(z^{-1})q_{mr_f}(z^{-1}) \\ T_{slow}(z^{-1}) &= g_s(z^{-1})q_{mr_s}(z^{-1}) \end{aligned} \tag{7.31}$$

To achieve the control objectives,

$$\begin{aligned} T_{fast}(z^{-1})|_{ss} &= 1 \\ T_{slow}(z^{-1})|_{ss} &= 1 \end{aligned} \tag{7.32}$$

and the decoupling between the setpoint on the faster input, $u_r[k]$ and $y[k]$ is achieved through the use of pre-filters which must satisfy the condition,

$$g_s(z^{-1})q_{p_s}(z^{-1}) + g_f(z^{-1})q_{p_f}(z^{-1}) = 0 \tag{7.33}$$

Because $g_f(z^{-1})$ and $g_s(z^{-1})$ both include delay terms, $T_{slow}(z^{-1})$ is chosen as

$$T_{slow}(z^{-1}) = T^{-}_{slow}(z^{-1})T^{+}_{slow}(z^{-1}) \tag{7.34}$$

where $T^{+}_{slow}(z^{-1})$ includes the delays of both $g_f(z^{-1})$ and $g_s(z^{-1})$ so that $T_{slow}(z^{-1})/g_f(z^{-1})$ and $T_{slow}(z^{-1})/g_s(z^{-1})$ are both causal and stable. So in this case,

$$T_{slow}(z^{-1}) = z^{-(d_s+d_f)}\frac{1-\lambda_s}{1-\lambda_s z^{-1}} \tag{7.35}$$

and the controller for the slow array is given by

$$q_s(z^{-1}) = T_{slow}(z^{-1})g_s(z^{-1})^{-1} \tag{7.36}$$

Likewise the fast sensitivity can be written as

$$T_{fast}(z^{-1}) = T^{-}_{fast}(z^{-1})T^{+}_{fast}(z^{-1}) \tag{7.37}$$

where $T^{+}_{fast}(z^{-1})$ includes the non-minimum phase components of $g_f(z^{-1})$ only so that $T_{fast}(z^{-1})/g_f(z^{-1})$ is causal and stable. The controller for the fast array is determined by

$$q_f(z^{-1}) = \left[T_{fast}(z^{-1}) - T_{slow}(z^{-1})\right]\left[g_f(z^{-1})\right]^{-1} \tag{7.38}$$

Design of the pre-filters are described in [Gayadeen and Heath, 2009] however a simple choice is

$$\begin{aligned} q_{p_f}(z^{-1}) &= \tilde{q}_p(z^{-1})g^{+}_s(z^{-1}) \\ q_{p_s}(z^{-1}) &= -\tilde{q}_p(z^{-1})\frac{g_f(z^{-1})}{g^{-}_s(z^{-1})} \end{aligned} \tag{7.39}$$

where $\tilde{q}_p(z^{-1})g^{+}_s(z^{-1})|_{ss} = 1$ for some filter $\tilde{q}_p(z^{-1})$.

For the dynamics given in Table 7.1, the chosen complementary sensitivities are shown in Fig. 7.3 which results in the closed loop sensitivities in Fig. 7.4. When the fast actuator is unconstrained, the resulting integrated beam motion is shown

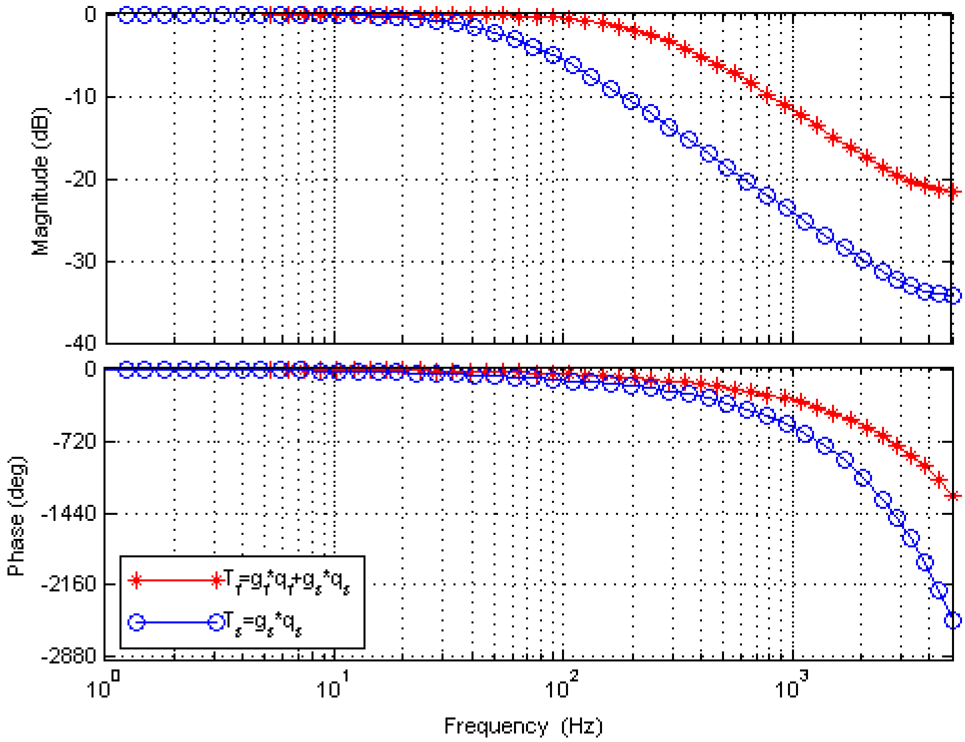

Fig. 7.3: Fast ('$*$' red) and slow ('o' blue) complementary sensitivities for the mid-ranging design

in Fig. 7.5. The mid-ranging controller gives satisfactory performance and can be tuned to further suppress the low frequency integrated beam motion. The benefit of the mid-ranging control approach is demonstrated in Fig. 7.6. Firstly, the effect of a step change in the disturbance is shown at 80μs where fast actuator saturation is avoided when mid-ranging control is used. The response of the control signals to changes in the disturbance is determined solely through the choice of $q_{mr_s}(z^{-1})$ and $q_{mr_f}(z^{-1})$ as given by (7.30). Furthermore, a step change in the fast actuator setpoint is also shown in Fig. 7.6 at 170μs. The choice of pre-filters is used to minimise the effect of changes to the fast actuator setpoint on the output response. Mid-ranging control is therefore used to obtain a desired response from $y[k]$ to $h[k]$, from $u_r[k]$ to $u_f[k]$ and a decoupled response from $u_f[k]$ to $y[k]$.

On the booster, five response matrices measured off the machine over a five month

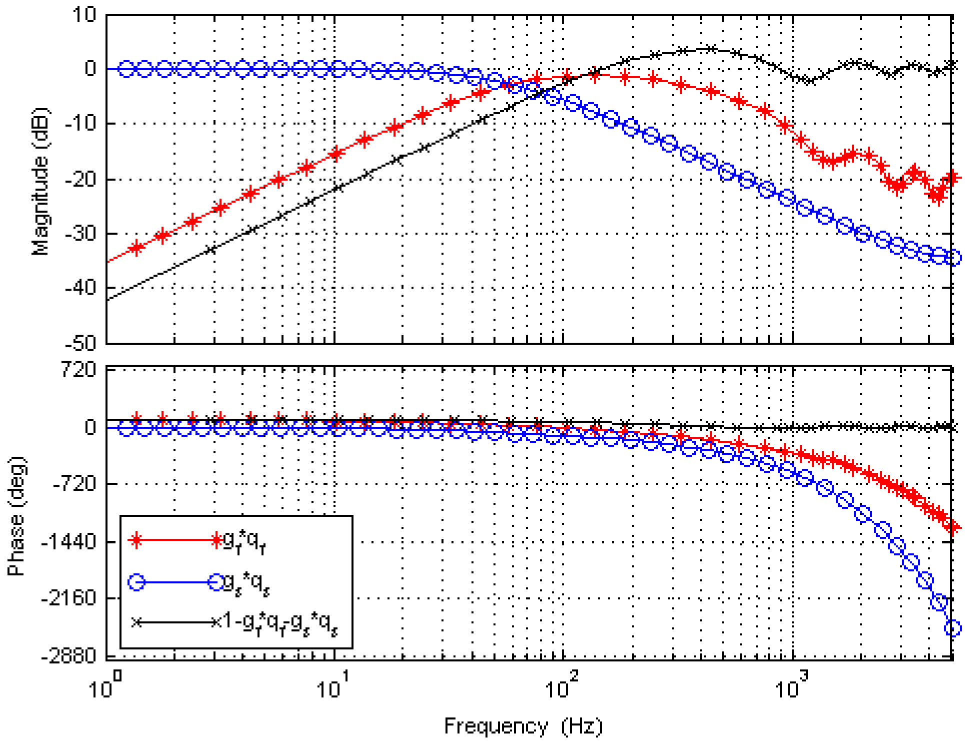

Fig. 7.4: Fast controller sensitivity ('$*$' red), slow controller sensitivity ('o' blue) and closed loop sensitivity ('x' black) for the mid-ranging design

period were compared with the ideal response matrices for both arrays to determine $\boldsymbol{\Delta}_s^{\boldsymbol{\Phi}}$ and $\boldsymbol{\Delta}_f^{\boldsymbol{\Phi}}$. It was found that the stability condition in (7.28) is satisfied for all measured responses indicating that the closed loop system is stable in the presence of spatial uncertainties. It is straightforward to check that the design ensures that the stability condition is met since $\cos(\theta_{A_i})$ is not inverted which would result in an ill-conditioned matrix when $\cos(\theta_{A_i})$ is close to zero.

7.4 Conclusion

For a system with two arrays of actuators for electron beam control, the extent of the overlap of the controllable subspaces of each array can be used to find modes where the problem can be split into SISO, MISO or decoupled MIMO blocks. By

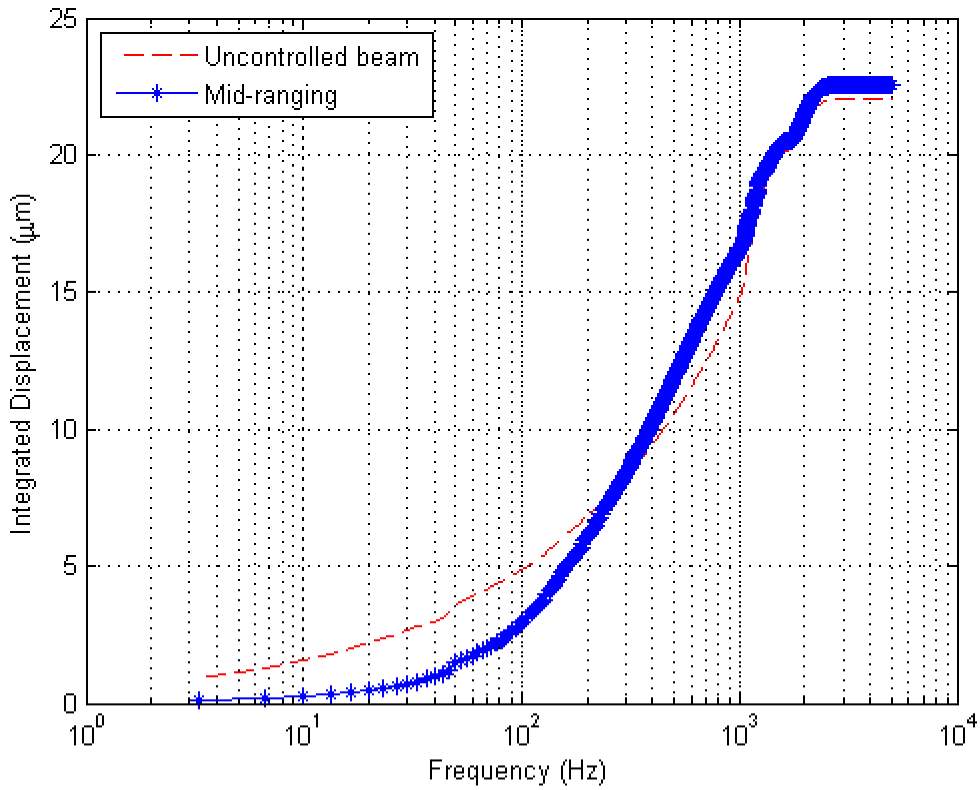

Fig. 7.5: Integrated beam motion for the uncontrolled beam, ('- -' red) and the controlled beam when the both actuators are used designed with mid-ranging objectives ('$*$' blue).

preserving the IMC structure, simple robustness measures can be applied to ensure closed loop stability in the presence of the spatial uncertainties. For the TISO case, mid-ranging control is appropriate given the distinct characteristics of the two actuators and results in a control strategy that uses both inputs in such a way as to meet performance specifications without violating the constraints of each actuator.

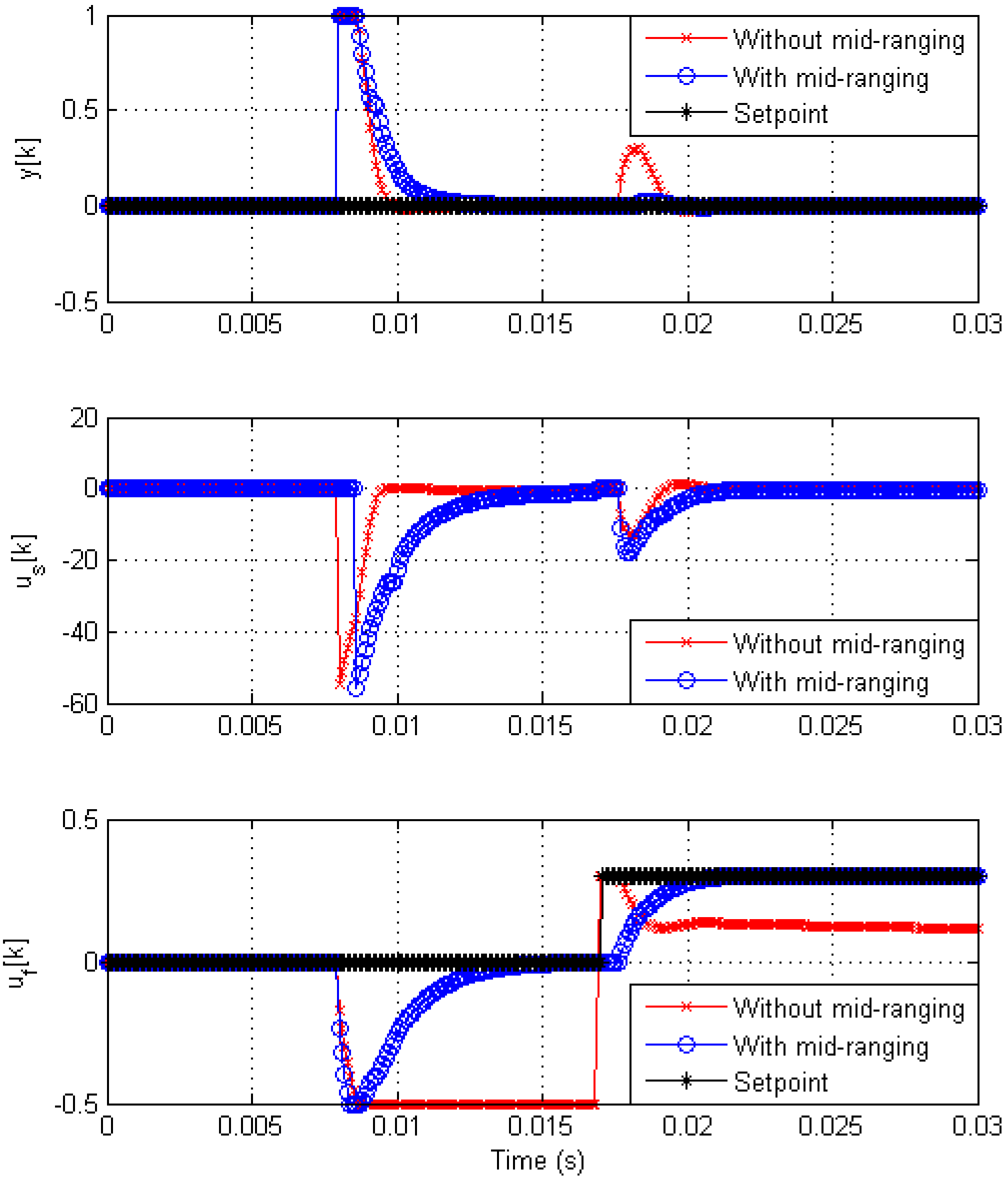

Fig. 7.6: At 0.008s the response to a step change in disturbance is shown when both actuators are used without mid-ranging control ('$*$' red) and with mid-ranging control ('o' blue). The reference for the output $y[k]$ and $u_f[k]$ are shown ('x' black). At 0.017s the response to a step change in the fast actuator setpoint is shown. (At 0.017s the saturated signal $u_f[k]$ shown in red is reset to zero to show the effect of the step change.)

Chapter 8

Conclusions and Future Work

In this thesis, the design and analysis of controllers used to stabilise electron beams in synchrotrons was presented. An IMC controller design was presented based on the starting assumptions that all the actuators have the same dynamics and that there are no constraints on the actuators. The presence of spatial uncertainty was considered and techniques for tuning the controller for performance and robustness were discussed. A more realistic uncertainty description was introduced and physical insight to the robust stability analysis of the system was presented. Next, rate limits on the actuators were introduced and constrained control augmentations to the unconstrained controller were presented. As a further alternative, the case where the actuators no longer have the same dynamics was considered. In particular, the common configuration of two arrays of actuators with different dynamic characteristics was presented. The approaches taken in this thesis were motivated by the requirement to ensure feasible online implementation within the current constraints of controller implementations at synchrotrons. To conclude, the main contributions of each chapter are summarised and some future research directions are outlined.

8.1 Summary

The following results have been presented in this thesis:

- In Chapter 4, an unconstrained controller design is proposed and tradeoffs between performance and robustness were demonstrated. The spatial and dynamic responses of the actuators are decoupled and therefore control is decoupled as well. Furthermore, the multivariate control problem is diagonalised using SVD, such that an IMC controller is designed for each spatial mode. The controller gain and dynamics are selected by considering the two-dimensional distribution of the disturbance. A robust stability test is developed by representing the uncertainty with IQCs and using the KYP lemma, the stability criteria is expressed in the form of an LMI feasibility problem. In this chapter, the design and implementation on the storage ring and booster are presented. While the strategy on the storage ring is motivated by the requirement of computational efficiency, it is demonstrated that the electron beam stability requirements are achieved and the closed loop system is stable. As a comparison, both different dynamics and gains are applied to each mode on the booster using the two-dimensional sensitivity shaping approach. Though this approach requires twice the computation as the suboptimal strategy on the storage ring, significantly better performance was achieved. While the IMC structure is practical, as a final option, it is demonstrated how an H_∞ control strategy is used to design an equivalent IMC controller.

- In Chapter 5, a harmonic analysis framework for modelling the spatial uncertainties is developed. The goal of this approach was to develop models of the main sources of spatial uncertainties that maintain physical interpretations so that bounds on the deviations of meaningful beam parameters and sensor and actuator inaccuracies can be determined to ensure closed loop stability. Fourier analysis of the disturbed closed orbit leads to a harmonic decomposition of the response matrix where the decomposed response matrix, maintains a physical interpretation, unlike the SVD approach. The main result being the relationship between the Fourier coefficients of the disturbed closed orbit and the tune. Furthermore, the main sources of spatial uncertainties are decoupled from one another and are diagonally structured which means that the robust stability tests can be performed on a mode-by-mode basis. By applying the robust stability test, on each harmonic mode, bounds on the sensor and actuator inaccuracies and the machine tune are determined.

- In Chapter 6, methods for augmenting the unconstrained controller to provide anti-windup compensation and ensure closed loop stability, in the presence of rate limit constraints on the actuators, are presented. The IQC robust stability test was extended to incorporate both the rate constraint and spatial uncertainty to ensure that the augmented closed loop system is robustly stable. A Riccati-based synthesis that guarantees constrained closed loop specifications is reformulated for the IMC anti-windup structure and is shown to give improved performance over traditional IMC anti-windup designs. The preservation of the IMC structure allows for minor modifications to be made to the unconstrained system in order to provide acceptable constrained performance when the actuator rate limits are active. Furthermore, the IMC anti-windup approach does not require signals from within the rate limiter structure to be accessed, which is of practical importance for this application.

- In Chapter 7, an IMC design for the case where there are two arrays of actuators with different dynamics is addressed. Modes in which the subspaces of each array overlap are identified and for these modes, appropriate control directions are chosen, thereby decomposing the problem into a series of SISO and TISO problems. For the TISO case, a mid-ranging control technique is utilised, which exploits the characteristics of each actuator to achieve performance specifications while avoiding actuator saturation.

8.2 Future Research Directions

- It would be a significant advance in the synchrotron community to apply the technique where different gains and dynamics are selected for individual modes based on shaping the two-dimensional sensitivity function. Similarly, it would be of interest to implement the multi-array controller proposed in this thesis on machines that use the two arrays and compare the performance to current solutions. The most significant factor in moving towards the implementation of these techniques is the migration of existing control networks at synchrotron facilities to architectures that can accommodate significantly more computation. However new facilities, such as the NSLSII may be capable of handling the two matrix multiplications involved and it would be a promising direction to apply optimal techniques to these systems which are not as computationally limited as older machines.

- It has been suggested that a quadratic programme (QP) can be incorporated within a constrained IMC structure in order to achieve optimal steady state behaviour [Heath and Wills, 2004]. Unlike MPC algorithms, QP does not require any horizon (prediction or control) and this approach is straightforward to implement. However, it requires the solution of an online optimisation problem that becomes computationally infeasible for most existing synchrotron controller infrastructures, which are still limited by the two matrix multiplications needed to project into mode space. If it were possible to efficiently solve the QP online, then improved steady state constrained performance can be achieved. A study into the tradeoff between any added delay introduced by either incorporating QP within the IMC structure or using MPC and the improvement on performance would be of significant benefit for the synchrotron community. An interesting path is to tackle efficient online optimisation (either as an IMC with QP or as an MPC problem) for electron beam stabilisation which focuses on development of customised solvers for MPC problems both in terms of software and hardware. The computational burden of solving convex MPC problems online can be significantly reduced by exploiting the inherent problem structure. Using a solver tailored to the specific optimization problem, such as CVXGEN [Mattingley et al., 2011] is impressive for small-scale systems but there are severe limitations on the problem sizes that can be handled. In [Domahidi et al., 2012] implementation strategies for efficient primal-dual interior point methods are discussed which aim to extend the set of MPC formulations that can be solved very efficiently. The fastest achieved computation time of 90μs was reported for an MPC problem with 4 states, 1 output and a length 10 prediction horizon. In terms of hardware development, in [Wills et al., 2012] the implementation of linear MPC at millisecond range, or faster, sampling rates was addressed. The design was implemented using FPGAs and employs parallelism, pipelining, and specialized numerical formats [Wills et al., 2012] and a 23 state model and length 12 prediction horizon, with 200μs sampling period was used to demonstrate that 30μs was necessary for computing the control action. There has been recent work that considers embedded MPC using FPGAs and efficient solvers for convex programs [Jerez et al., 2013]. Achievable rates of 1MHz was obtained for a 12th order LTI SISO system using a 16 sample control horizon utilising parallelism. Currently the positional data at Diamond is converted from fixed point to floating point notation by the power PC, enabling the use of fast matrix multiplications which currently take 4μs. Therefore any MPC will require a computation time of 4μs. The majority of fast MPC implementations using FPGAs make use of fixed-point arithmetic rather than floating point. In [Jerez et al., 2013] it was demonstrated that the round-off errors leads to reduced accuracy but not instability. The NSLSII new FOFB architecture will use FPGAs (Virtex 6) to enable corrections within mode space [Tian and Hua, 2011] but it is unclear whether the loss of accuracy in using FPGA fixed point calculation is tolerable for this application.

- The multi-array problem can be formulated as a constrained large scale multivariable control problem; in this case long horizon MPC is appropriate. A computationally efficient solution would be a significant advancement to the fast and slow corrector magnet problem. Additionally, the IQC framework to analyse robust stability can be extended to the multi-array case for not only uncertainty in the singular values but also in the singular vectors of each array.

Bibliography

M. G. Abbott, G. Rehm M. T., and I. S. Uzun. The Diamond Light Source control system interface to the LIBERA electron beam position monitors. In *International Conference on Accelerator and Large Experimental Physics Control Systems*, pages 694–696, Kobe, Japan, 2009. 35, 36

A. Adegbege. *Constrained Internal Model Control*. PhD thesis, School of Electrical and Electronic Engineering, University of Manchester, 2011. 140

J. A. G. Akkermans, A. G. Wills, and W. P. Heath. Robust cross-directional control of paper making machines with saturating actuators. In *Control Systems*, Québec, Canada, 2004. 139

B. Allison and S. Ogawa. Design and tuning of valve position controllers with industrial applications. *Transactions of the Institute of Measurement and Control*, 25:3–16, 2003. 159

M. Ariola and A. Pironti. Plasma shape control for the JET tokamak: an optimal output regulation approach. *IEEE Control Systems*, 25:65 – 75, 2005. 67

J. U. Backström, C. Gheorghe, G. E. Stewart, and R. N. Vyse. Constrained model predictive control for cross-directional multi-array processes. *Pulp and Paper Canada*, 102:T128–T131, 2001. 158

B. Bamieh, F. Paganini, and M. A. Dahleh. Distributed control of spatially invariant systems. *IEEE Transactions on Automatic Control*, 47(7):1091–1107, 2002. 57

M. Boge, M. Dehler, T. Schilcher, V. Schlott, and R. Ursic. Fast closed orbit control in the SLS storage ring. In *Particle Accelerator Conference*, volume 2, pages 1129–1131, 1999. 60

O. Brieger, M. Kerr, D. Leissling, I. Postlethwaite, J. Sofrony, and M. C. Turner. Anti-windup compensation of rate saturation in an experimental aircraft. In *American Control Conference*, pages 924–929, New York, N.Y., 2007. 132

A. Chakraborty, P. Seiler, and G. J. Balas. Local performance analysis of uncertain polynomial systems with applications to actuator saturation. In *IEEE Conference on Decision and Control and European Control Conference*, pages 8176–8181, Orlando, FL, 2011. 151

P. C. Chiu, C. H. Kuo, K. H. Hu, C. Y. Wu, and K. T. Hsu. Fast orbit feedback scheme and implementation for Taiwan Photon Source. In *International Particle Acclerator Conference*, pages 1146–1148, Shanghai, China, 2013. 5, 156

C. Christou, M. T. Heron, J. Rowland, and S. Gayadeen. Studies to optimize the Diamond Light Source booster synchrotron as a 100Mev Storage Ring. In *International Particle Acclerator Conference*, pages 3053–3055, San Sebastián, Spain, 2011. 29

K. W. Corscadden and S. R. Duncan. Multivariable disturbance modelling for web processes. *International Journal of Systems Science*, 31(1):97–106, 2000. 39

E. B. Courant and H. S. Snyder. Theory of the alternating gradient synchrotron. *Annals of Physics*, 3:1–48, 1958. 112, 113

E. B. Dahlin. Designing and tuning digital controllers. *Instrumentation & Control Systems*, 41(6):77, 1968. 78

G. De Tommasi, S. Galeani, A. Pironti, G. Varano, and L. Zaccarian. Nonlinear dynamic allocator for optimal input/output performance trade-off: Application to the JET tokamak shape controller. *Automatica*, 47(5):981–987, 2011. 67

A. Domahidi, A. Zgraggen, M. N. Zeilinger, M. Morari, and C. N. Jones. Efficient interior point methods for multistage problems arising in receding horizon control. In *IEEE 51st Annual Conference on Decision and Control*, pages 668 – 674, Maui, HI, 2012. 179

S. R. Duncan. *The cross-directional control of web forming processes*. PhD thesis, Department of Electrical Engineering, University of London, 1989. 2

S. R. Duncan. The design of a fast orbit beam stabilisation system for the Diamond synchrotron. Technical Report 2296/07, Department of Engineering Science, University of Oxford, 2007. 58, 68, 72, 78

S. R. Duncan and G. F. Bryant. The spatial bandwidth of cross-directional control systems for web processes. *Automatica*, 33(2):139–153, 1997. 2, 3, 57, 61

S. R. Duncan and W. P. Heath. The robustness of multi-array cross-directional control systems. In *Control Systems Conference*, pages 180–185, Stockholm, Sweden, 2010. 158, 164, 166

S. R. Duncan, W. P. Heath, A. Halouskova, and M. Karny. Application of basis functions to the cross-directional control of web processes. In *UKACC International Conference on Control*, volume 2, pages 1278–1283, 1996. 59

S. R. Duncan, W. P. Heath, and A. R. Taylor. A new approach to multi-array cross-directional control. In *PAPTAC Control Systems Conference*, pages 69–74, Vancouver, BC, Canada, 2008. 158

L. El Ghaoui and S. I. Niculescu, editors. *Advances in Linear Matrix Inequality Methods in Control: Advances in Design and Control*. SIAM, 2000. 120

F. R. Elder, A. M. Gurewitsch, R. V. Langmuir, and H. C. Pollock. Radiation from electrons in a synchrotron. *Physical Review*, 71:829–830, 1947. 10

J. Fan, G. E. Stewart, and G. A. Dumont. Two-dimensional frequency analysis for unconstrained model predictive control of cross-directional processes. *Automatica*, 40(11):1891–1903, 2004. 158

A. P. Featherstone, J. G. VanAntwerp, and R. D. Braatz. *Identification and Control of Sheet and Film Processes*. Springer, 2000. 2, 39, 66

M. Gallieri and J. M. Maciejowski. ℓ_{asso} MPC: Smart regulation of over-actuated systems. In *American Control Conference*, pages 1217–1222, Montréal, Canada, 2011. 159

S. Gayadeen and S. R. Duncan. Uncertainty modeling and robust stability analysis of a synchrotron electron beam stabilisation control system. In *IEEE 51st Annual Conference on Decision and Control*, pages 931–936, Maui, HI, 2012. 6, 7, 68, 115

S. Gayadeen and S. R. Duncan. Anti-windup compensation for electron beam stabilisation control systems on synchrotrons with rate constrained actuators. In *European Control Conference*, pages 2752–2757, Zürich, Switzerland, 2013. 7, 68

S. Gayadeen and S. R. Duncan. Design of an electron beam stabilisation controller for a synchrotron. *Control Engineering Practice*, 26:201–210, 2014. 6, 7

S. Gayadeen and W. P. Heath. An Internal Model Control approach to mid-ranging control. In *IFAC International Symposium on Advanced Control of Chemical Processes*, Istanbul, July, 2009. 159, 169, 170

S. Gayadeen, S. R. Duncan, C. Christou, M. T. Heron, and J. Rowland. Diamond Light Source Booster fast orbit feedback system. In *International Conference on Accelerator and Large Experimental Physics Control Systems*, pages 160–163, Grenoble, France, 2011. 6

S. Gayadeen, S. R. Duncan, and W. P. Heath. Design of multi-array controllers for electron beam stabilisation on synchrotrons. In *American Control Conference*, pages 1201–1206, Washington, D.C., 2013a. 7

S. Gayadeen, S. R. Duncan, and M. T. Heron. Fast Orbit Feedback Control in mode space. In *International Conference on Accelerator and Large Experimental Physics Control Systems*, pages 1082–1085, San Francisco, CA, 2013b. 6, 7

G. H. Golub and C. F. Van Loan. *Matrix computations (3rd ed.)*. Johns Hopkins University Press, 1996. 161

G. H. Golub and C. F. Van Loan. Tikhonov regularization and total least squares. *SIAM Journal on Matrix Analysis and Applications*, 21(1), 1999. 80

G. C. Goodwin, S. E. Graebe, and W. S. Levine. Internal model control of linear systems with saturating actuators. In *Proceedings of the European Control Conference*, pages 1072–1077, Groningen, Netherlands, 1993. 129, 138

W. P. Heath. Orthogonal functions for cross-directional control of web forming processes. *Automatica*, 32(2):183–198, 1996. 2, 57, 60, 61

W. P. Heath and A. G. Wills. Design of cross-directional controllers with optimal steady state performance. *European Journal of Control*, 10(1):15–27, 2004. 57, 62, 79, 129, 178

W. P. Heath, A. G. Wills, and J. A. G. Akkermans. A sufficient condition for the stability of optimizing controllers with saturating actuators. *International Journal of Robust and Nonlinear Control*, 15(12):515–529, 2005. 129

M. A. Henson, B. A. Ogunnaike, and J. Schwaber. Habituating control strategies for process control. *AIChE Journal*, 41(3):604–618, 1995. 159

M. T. Heron, M. G. Abbott, J. A. Dobbing, G. Rehm, J. Rowland, and I. S. Uzun. Diamond Light Source electron beam position feedback: Design, realisation and performance. In *International Conference on Accelerator and Large Experimental Physics Control Systems*, pages 650–652, Kobe, Japan, 2009. 38

M. Hovd, R. D. Braatz, and S. Skogestad. SVD controllers for H_2, H_∞ and μ-optimal control. *Automatica*, 33(3):433–439, 1997. 57

N. Hubert, L. Cassinari, J-C. Denard, A. Nadji, and L. Nadolski. Global orbit feedback systems down to DC using fast and slow correctors. In *9th European Workshop on Beam Diagnostics and Instrumentation for Particle Accelerators*, pages 27–31, Basel, Switzerland, 2009. 5, 156, 157, 158

S. Jena, S. Yadav, R. K. Agrawal, A. D. Ghodke, P. Fatnani, and T. A. Puntambekar. Stabilization of betatron tune in Indus-2 storage ring. Submitted to Chinese Physics C, 2013. 112

J. L. Jerez, P. J. Goulart, S. Richter, G. A. Constantinides, E. C. Kerrigan, and M. Morari. Embedded predictive control on an FPGA using the fast gradient method. In *European Control Conference*, pages 2752–2757, Zürich, Switzerland, 2013. 179, 180

U. Jonsson. Lecture notes on Integral Quadratic Constraints, 2001. 87, 88, 89

S. H. Kim. Calculation of pulsed kicker magnetic field attenuation inside beam chambers. Technical Report LS-291, Advanced Proton Source, 2001. 34

M. Massimetti, L. Zaccarian, T. Hu, and A. R. Teel. Linear discrete-time global and regional anti-windup: an LMI approach. *International Journal of Control*, 82 (12):2179–2192, 2009. 141, 142

G. Materlik. Diamond Light Source Review 2012/2013. Technical report, Diamond Light Source Ltd., 2013. 1

J. Mattingley, W. Yang, and S. Boyd. Receding horizon control. *IEEE Control Systems*, 31(3):52–65, June 2011. 179

A. Megretski. New IQC for quasi-concave nonlinearities. *International Journal of Robust and Nonlinear Control*, 11(7):603–620, 2001. 147, 149

A. Megretski and A. Rantzer. System analysis via Integral Quadratic Constraints. *IEEE Transactions on Automatic Control*, 42(6):819–830, 1997. 82, 85, 87, 89, 147

R. M. Morales and W. P. Heath. The robustness and design of constrained cross-directional control via Integral Quadratic Constraints. *IEEE Transactions on Control Systems Technology*, 19(6):1421–1432, 2011. 90, 129

M. Morari and E. Zafiriou. *Robust Process Control*. Prentice-Hall, 1989. 4, 76, 77, 78, 92

J. J. Moré. *The Levenberg-Marquardt algorithm: Implementation and theory*, volume 630 of *Lecture Notes in Mathematics*. Springer Berlin Heidelberg, 1978. 48

A. Napier, S. Gayadeen, and S. R. Duncan. Fast orbit beam stabilisation for a synchrotron. In *IEEE International Conference on Control Applications*, pages 1770–1775, Denver, CO, 2011. 6, 68

A. Neumaier. Solving ill-conditioned and singular linear systems: A tutorial on regularization. *SIAM Review*, 40(3):636, 1998. 80

S. Pfeiffer, C. Schmidt, G. Lichtenberg, and H. Werner. Grey box identification for the Free Electron Laser FLASH exploiting symmetries of the RF-system. In *18th IFAC World Congress*, pages 10770–10775, Milano, Italy, 2011. 67

S. Pfeiffer, G. Lichtenberg, C. Schmidt, H. Schlarb, and H. Werner. Design of an optimal and robust controller for a free-electron laser exploiting symmetries of the RF-system. In *IEEE 51st Annual Conference on Decision and Control*, pages 4253–4258, Maui, HI, 2012. 67

J. Pfingstner and J. Snuverink. Analytic robust stability analysis of svd orbit feedback. Technical Report CERN-OPEN-2012-019. CLIC-Note-946, CERN, 2012. 111

E. Plouvier, F. Epaud, J. M. Koch, and K. B. Scheidt. The New Fast Orbit Correction System of the ESRF Storage Ring. In *10th European Workshop on Beam Diagnostics and Instrumentation for Particle Accelerators*, pages 694–697, Hamburg, Germany, 2011. 5, 156

E. Plouvier, F. Epaud, F. Farvacque, and J. M. Koch. Optimisation of the svd treatment in the fast orbit correction of the ESRF storage ring. In *International Beam Instrumentation Conference (IBIC)*, pages 215–217, Oxford, UK, 2013. 60

A. Rantzer and A. Megretski. System analysis via Integral Quadratic Constraints - Part II. *IEEE Transactions on Automatic Control*, 42:819–830, 1997. 85

G. Rehm. Achieving and measuring sub-micrometer beam stability at 3rd generation light sources. *Journal of Physics: Conference Series*, 425(4), 2013. 52, 54

L. Rundqwist and K. Stahl-Gunnarsson. Phase compensation of rate limiters in unstable aircraft. In *Proceedings of the IEEE International Conference on Control Applications*, pages 19–24, Dearborn, MI, 1996. 132

J. Safranek. Linear optics from closed orbits (LOCO)-An introduction. *ICFA Beam Dynamics Newsletter*, (44):43–49, 2007. 48

M. Sands. The physics of electron storage rings, an introduction. Technical Report SLAC-121, SLAC, 1970. 26, 46, 47, 117

C. Schwartz and L. Emery. Compensating the frequency deadband of the APS real-time and DC transverse orbit correction systems. In *Particle Accelerator Conference*, pages 1234 –1236, Chicago, IL, 2001. 157

D. Seborg, T. Edgar, D. Mellichamp, and F. Doyle III. *Process Dynamics and Control*. John Wiley and Sons, 2011. 79

S. Skogestad and I. Postlethwaite. *Multivariable feedback control - analysis and design (2nd edition)*. Wiley, 2005. 2, 61

S. Skogestad, M. Morari, and J. C. Doyle. Robust control of ill-conditioned plants: high-purity distillation. *IEEE Transactions on Automatic Control*, 33(12):1092–1105, 1988. 61

J. Sofrony, M. C. Turner, and I. Postlethwaite. A simple anti-windup compensation scheme for systems with rate-limited actuators. In *ICCAS-SICE*, pages 3311 – 3316, Fukuoka, Japan, 2009. 132, 141

J. Sofrony, M. C. Turner, and I. Postlethwaite. Anti-windup synthesis for systems with rate-limits using riccati equations. *International Journal of Control*, 83(2): 233–245, 2010. 132, 134, 141, 142, 143

C. Steier, E. Domning, T. Scarvie, and E. Williams. Operational experience integrating slow and fast orbit feedbacks at the ALS. In *9th European Particle Accelerator Conference*, pages 2786–2788, Lucerne, Switzerland, 2004. 5, 156, 157

R. J. Steinhagen. Real-time feedback on beam parameters. In *Asian Particle Accelerator Conference*, pages 295–299, Indore, India, 2007. 53

G. E. Stewart. *Two dimensional loop shaping: Controller design for paper machine cross-directional processes*. PhD thesis, Department of Electrical and Computer Engineering, University of British Columbia, 2000. 2, 62

G. E. Stewart, D. M. Gorinevsky, and G. A. Dumont. Two-dimensional loop shaping. *Automatica*, 39(5):779–792, 2003. 57, 66

Y. Tian and L. Hua. NSLS-II fast orbit feeback with individual eigenmode compensation. In *International Conference on Accelerators and Large Experimental Physics Control Systems*, pages 1488–1490, Grenoble, France, 2011. 60, 180

K. C. Toh, M. J. Todd, and R. H. Tutuncu. SDPT3- a matlab software package for semidefinite programming. *Optimization Methods and Software*, 11(12):545–581, 1999. 96

M. C. Turner, G. Herrmann, and I. Postlethwaite. Discrete time antiwind-up - part 1: Stability and performance. In *European Control Conference*, Cambridge, UK, 2003. 141, 142

H. Wiedemann. Storage ring design as a syncrhotron light source. Technical report, Stanford University, 2002. 14, 17

H. Wiedemann. *Particle Accelerator Physics*. Springer, 2007. 27

R. G. Wilhelm. On the controllability of cross-direction variations of sheet properties. In *Tappi Engineering Conference*, pages 621–629, Boston, MA, 1984. 39

K. Wille. *The Physics of Particle Accelerators: An Introduction*. Oxford University Press, 1996. 10, 21, 22, 23

A. G. Wills, G. Knagge, and B. Ninness. Fast linear model predictive control via custom integrated circuit architecture. *IEEE Transactions on Control Systems Technology*, 20(1):59–71, 2012. 179

E. Wilson. *An Introduction to Particle Accelerators*. Oxford University Press, 2001. 10, 22, 23

H. Winick. Fourth generation light sources. Technical Report SLAC-PUB-7525, SLAC National Accelerator Laboratory, 1997. 12

L. H. Yu, E. Bozoki, J. Galayda, S. Krinsky, and G. Vignola. Real time harmonic closed orbit correction. *Nuclear Instruments and Methods in Physics Research Section A*, 284(23):268–285, 1989. 112

L. H. Yu, S. Krinsky, O. Singh, and F. Willeke. The performance of a fast closed orbit feedback system with combined fast and slow correctors. In *11th European Particle Accelerator Conference*, pages 3315–3317, Genoa, Italy, 2008. 157

L. Zaccarian and A. R. Teel. *Modern Anti-windup Synthesis:Control Augmentation for Actuator Saturation.* Princeton Series in Applied Mathematics. Princeton University Press, 2011. 128, 130

A. Zheng, M. V. Kothare, and M. Morari. Anti-windup design for internal model control. *International Journal of Control*, 60(5):1015–1024, 1993. 129, 135, 140